SPECTRAL ESTIMATES AND FLOW CHARACTERISTICS FROM NON-UNIFORMLY SAMPLED LDV DATA IN A TURBULENT JUNCTION VORTEX

by

Subhra K. Nath

Dissertation submitted to the Faculty of the

Virginia Polytechnic Institute and State University

in partial fulfillment of the requirements for the degree of

DOCTOR OF PHILOSOPHY

in

Mechanical Engineering

APPROVED:

F. J. Pierce, Chairman

H. L. Moses

T. E. Diller

D. J. Nelson

G. W. Swift

April, 1989

Blacksburg, Virginia

SPECTRAL ESTIMATES AND FLOW CHARACTERISTICS FROM NON-UNIFORMLY SAMPLED LDV DATA IN A TURBULENT JUNCTION VORTEX

by

Subhra K. Nath

F. J. Pierce, Chairman

Mechanical Engineering

(ABSTRACT)

The strongly time variant flow in an incompressible, turbulent junction vortex formed at the base of a streamlined cylinder with a circular leading edge placed normal to a flat surface was investigated. The investigation centered around spectral analysis and time resolved measurements of the velocity fluctuations to characterize the time variant flow on the plane of symmetry. All the measurements were performed with a two-color, two-component, frequency shifted laser Doppler velocimeter.

Spectral analysis methods for randomly sampled data occuring from the LDV were evaluated under various simulated and real flow situations. The real flow situations studied were the vortex shedding flow behind a cylinder and the two-dimensional turbulent boundary layer. The spectral estimates obtained from the discretized lag product method were found to be better than those obtained from the direct transform method. It was found that the exact lag product method does not offer significant improvements in the spectral estimates to offset its computational slowness.

The mean velocity vectors in the junction vortex showed a single vortex on the plane of symmetry and a singular separation point upstream of the cylinder.

The time resolved measurements showed the instantaneous separation point on the plane of symmetry to be randomly oscillating between two limits. Maximum possible excursions of the junction vortex position and size were also obtained form the time resolved measurements.

The turbulence intensities in the junction vortex were found to be at least two to three times higher than typical two-dimensional boundary layer values. The histograms of instantaneous velocity fluctuations deviated from the expected Gaussian distributions and were found to have multiple peaks.

The spectral content of the junction vortex flow was investigated. The overall character of the junction vortex flow was found to be similar to a two-dimensional turbulent boundary layer, with greater amplification perceived in the lower frequencies relative to the higher frequencies. The spectra at locations above the time mean center of the junction vortex showed distinct peaks around 20-30 Hz, unlike boundary layer flows.

Acknowledgements

It is a great pleasure to be able to thank all the people who have helped me in one way or another during my stay at Virginia Polytechnic Institute and State University.

Foremost, my sincerest appreciation goes to Dr. F. J. Pierce for his patience, tolerance, and constant encouragement throughout the course of this work. I also thank him for providing me this wonderful opportunity of working in a superior environment and seeing this part of the world.

I would also like to thank all the shop personnel in the Mechanical Engineering department for their help on numerous occasions.

Lastly, I thank all my friends in Blacksburg and elsewhere in the USA who helped to make my stay here a very enjoyable one.

Table of Contents

List of Illustrations

List of Tables

Nomenclature

B	Bandwidth or Resolution
e	2.71828 ....
E	Expectation operator
d_f	Distance between the fringes
f	Frequency
f_D	Unshifted Doppler frequency
f_{Nyq}	Nyquist frequency
$G(f)$	One-sided spectral density
I_o	Light intensity at the center of the laser beam
I_u, I_v	Reverse flow intermittencies
j	Imaginary number
L	Length
m	Maximum lag number
N	Total number of points
N_n	No. of points in each slot
P	Probability distribution function or probability
P_k	Total pressure from the Kiel probe
Q	Dynamic pressure
Q_*	Dynamic pressure at the throat
r	Lag number
R	Gas constant for air
Re	Reynolds number
$R(\tau)$	Autocorrelation function
$S(f)$	Two-sided spectral density
T	Record length

U,V	Non-dimensionalized mean velocity components
u,v	Instantaneous velocities
$\hat{u}, \hat{v}$	Non-dimensionalized turbulence intensities
u', v'	Fluctuating components of u and v
$\overline{u}, \overline{v}$	Mean velocities
V_n	Velocity normal to the fringes
V_∞	Mean velocity at wind tunnel throat
Var	Variance
$w(t)$	Window function
$W(f)$	Fourier transform of $w(t)$
W_{rect}	Fourier transform of rectangular window
W_{Hann}	Fourier transform of Hanning window
x	streamwise coordinate
$x(t)$	Function of t
$X(f)$	Fourier transform of $x(t)$
y	Vertical coordinate

Greek Symbols

δ	Boundary layer thickness
Δt	Sampling interval or slot width
ε	Realtive error
θ	Half-angle between the laser beams
λ	Wavelength or mean sampling rate
μ	Viscosity of air
ρ	Density of air
ρ_∞	Density of air at T_∞
σ	Standard deviation

τ	time or time lag
τ_m	Maximum time lag

1.0 Introduction

The flow field in and around a turbulent junction vortex has been the subject of extensive investigations recently. The flow in the turbulent junction vortex is highly complex. There is a separation of the flow, accompanied by a prominent vortex (or system of vortices) with a large region of reverse flow, and the flow is highly three dimensional in nature. Accurate numerical simulation of such a flow is very difficult because of a variety of reasons, the most important reason being the lack of adequate turbulence models. The main thrust of the investigation of the junction vortex flow has thus been an experimental one. Most of the experiments were concerned with documenting and understanding of the mean flow field. A few investigations were aimed at determining the characteristics of the three dimensional turbulent boundary layer and the Reynolds stresses. Many were just flow visualization studies. The experimental results for the mean flow field generally show a single well defined vortex embedded in the lower regions of the boundary layer and a singular separation point upstream from the leading edge of the body.

But the actual flow in the junction vortex proves to be much more complicated than what the mean flow and the turbulent stresses can describe. Hints of a very complex flow phenomena were first obtained from real time smoke flow visualizations. The smoke flow visualizations revealed that the junction vortex is not such a well defined static structure as suggested by the mean flow results, but appears to be a very dynamic structure. Close observations of the smoke flow visualizations show the whole vortex structure to be in constant, apparently random movement, changing its size and position every instant. The motion of the vortex seems

quite irregular, although clearly discernible to the naked eye in the flow visualizations. This extremely dynamic nature of the junction vortex was attributed to the strong time variance of the junction vortex flow. It should be noted here that any turbulent flow is time variant in nature. The difference between the time variance of a typical turbulent flow and the time variance of the junction vortex flow appears to be mainly one of magnitude. The fluctuations of the junction vortex flow were considered to be much stronger than the typical fluctuations expected in turbulent boundary layers. To describe this very dynamic nature of the junction vortex flow, the words 'strong time variance' or 'strongly time variant' will be used throughout this report.

The strongly time variant behavior of the junction vortex flow led to questions as to whether the flow is dominated by a characteristic frequency (as in the case of shedding vortices from a cylinder) or a range of frequencies, and the spatial extent and the time variant position of the vortex. The present investigation attempts to shed some light on this very complicated time variant aspect of the flow through real time measurements.

1.1 Flow Geometry

The complex separated turbulent flow under investigation is the three-dimensional separated turbulent flow centered about a junction or horseshoe vortex system. This type of flow field is typically generated around an obstacle protruding through a turbulent boundary layer. The dominant feature of this type of flow is a horseshoe shaped vortex (or system of vortices) found near the intersection of the protruding obstacle and the flat surface on which the turbulent boundary layer is growing. The flow in the present investigation is generated by placing a streamlined cylinder normal to a flat surface in a thick turbulent boundary layer as shown in Fig. 1.1. The physical mechanism responsible for the formation of this vortex is the total pressure gradient near the leading edge of the obstacle resulting from the upstream boundary layer flow.

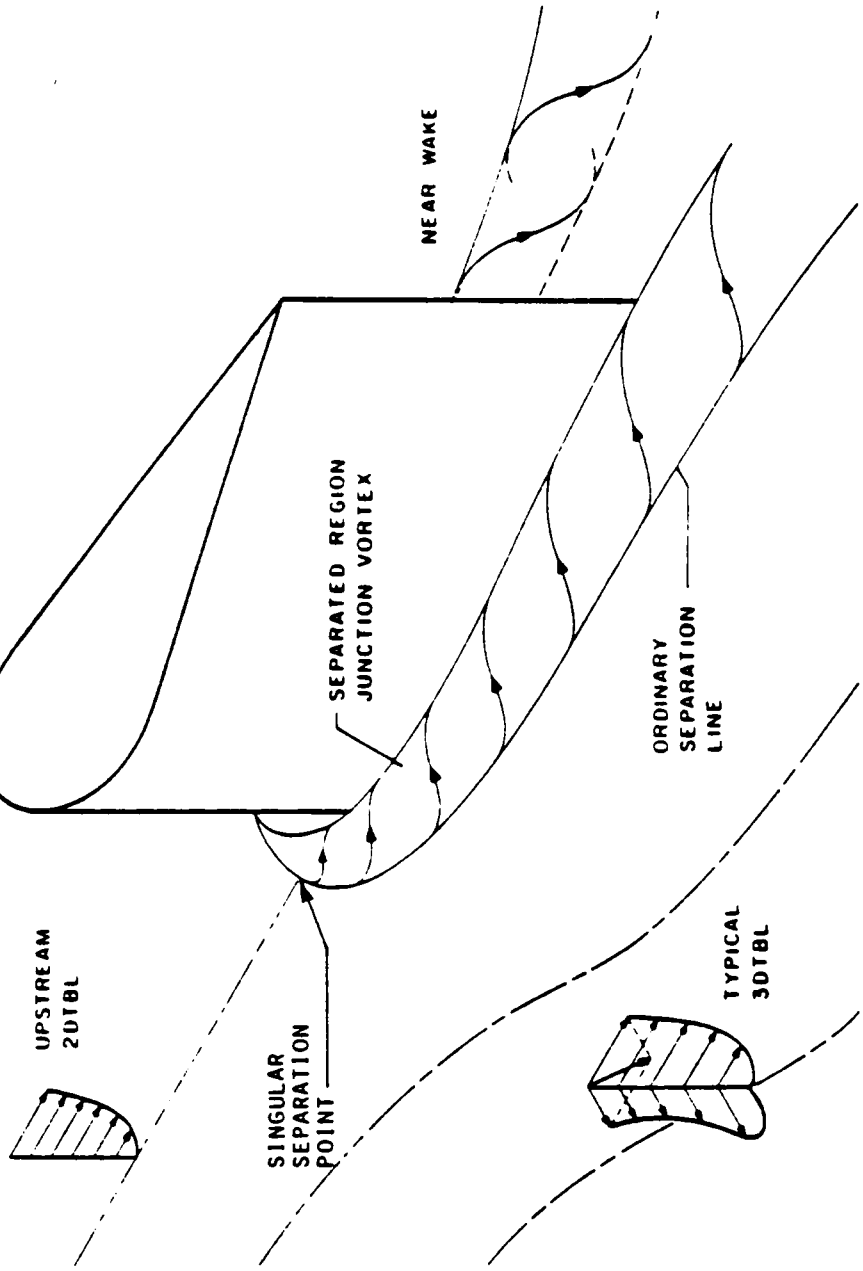

Figure 1.1. The Flow Field Around a Turbulent Junction Vortex

This type of flow is encountered frequently in a wide variety of real world flow circumstances. Among these are the flow around bridge piers in rivers, around buildings and structures in an atmospheric boundary layer, at wing-fuselage junctions, at strut-surface junctions, control surface-body junctions, at strut-surface junctions in turbomachine flow passages, at the leading edge junction between turbomachine blades and end walls, around submarine sail-hull and control surface junctions, and in and around ship hull-strut intersections.

For ease of reference, the total flow system is arbitrarily divided into four regions, which include :

1. The three-dimensional pressure-driven turbulent boundary layer-like flow upstream and around the body but excluding the separated flow.

2. The three-dimensional separation region including the separation sheet/envelope and the three-dimensional junction vortex system which is contained between the separation sheet and the body itself, including the flow forward of and around the body sides to the trailing edge.

3. The near-wake flow dominated by the strong mixing of the tails of the junction vortex system coming off the two sides of the body, as well as the wake from the boundary layers developed on the body sides and mixing with the adjacent boundary layer-like more remote floor flow.

4. The far-wake flow where the various complex turbulent flows in region three continue to mix and homogenize to some extent toward a more typical boundary layer-like downstream flow.

The present study is conducted in region two in the junction vortex, and is especially concentrated on the flow forward of the leading edge in the plane of symmetry. In connection with

the present work, the word junction vortex will be used to refer to this region under investigation.

1.2 Previous Studies

An extensive body of literature [1-37] exists on the junction vortex flow. Most studies [1-14] concentrated on the mean flow field, surface pressure distributions and surface flow visualizations. Turbulent stresses were also reported along with the mean flow results in some of the investigations [15-23]. The experimental results generally show a single vortex embedded in the boundary layer and a singular separation point upstream of the body. From topological considerations, multiple counter-rotating vortices have been predicted by Hunt, et al. [24], and some evidence of this can be found in Baker [9], Ishii and Honami [12]. The question of multiplicity of vortices is discussed in Pierce and Tree [25].

Computational studies of the junction vortex flow are not very abundant, probably because of the great complexity of the flow field, and the difficulty of finding an appropriate turbulence model. Gorski, et al. [26] attempted to simulate the incompressible turbulent junction vortex flow in the region between the leading edge and the trailing edge of the body. They used a parabolic marching method, using experimental results of Shabaka [16] as the initial conditions. They compared the results from an eddy viscosity turbulence model to the results from the $k-\varepsilon$ model and found that the $k-\varepsilon$ model yielded better results. Smith and Gajjar [27] used triple deck theory to calculate the incompressible laminar flow in a wing-body junction, assuming large Reynolds number flow. Kaul, et al. [28] simulated the incompressible laminar flow around a cylinder-endwall junction by solving the three-dimensional Navier-Stokes equations. A Reynolds number of 1000 based on the cylinder diameter was used in their computations. Briley and McDonald [29] solved the three-dimensional compressible Navier-Stokes equations for a laminar junction vortex created at the intersection of an elliptical strut and a flat plate. Their study was conducted for a Reynolds number of 400 (based on the body

chord) and a Mach number of 0.2. Moore and Moore [30] solved the turbulent junction vortex flow in a turbine cascade. Their numerical solution method used finite difference methods along with a pressure correction procedure. The Prandtl mixing length turbulence model was used. There was a notable lack of any extensive and self consistent data bases against which to compare or calibrate the computational methods. To fulfil this requirement, Pierce, et al. [2,3] have developed a self consistent data base for a turbulent junction vortex flow.

The strongly time variant nature of the junction vortex flow has not received much attention, excepting the investigations of turbulent stresses. Rood [32] investigated the existence of what he termed as 'large scale, time dependent structures' in the junction vortex flow. He argued that the large scale structure can be identified by a phase relationship between the instantaneous velocity fluctuations in the junction vortex. To determine the large scale spatial structure, he mapped contours of correlation values between velocities at two spatially separated points, using the maximum value of the coherence function as a measure of the correlation between two points in the flow field. From the correlation contours, he determined the spatial extent of large scale structures in the junction vortex. This investigation was extended to the wake region by Rood and Keller [33]. Rood [34] also used the correlation technique to investigate the influence of the body leading edge (nose) radius on the spatial extent of the junction vortex in the wake region, when the body was placed at a small angle of incidence. In another investigation, Rood and Anthony [35] studied the effects of different trailing edge profiles on the junction vortex flow in the wake region, again for a body placed at an angle of incidence. Hasan, et al. [36] studied the wall pressure field around a wing-body junction. They analyzed the wall pressure fluctuations for their spectral content and concluded that the effect of the adverse pressure gradient due to the presence of the wing is to increase the low frequency content of the pressure fluctuations while decreasing the high frequency content. An interesting report on the time variant characteristics of a laminar junction vortex flow was presented by Thomas [37]. He presented pictures of hydrogen bubble flow visualizations in the

plane of symmetry upstream of the body. The pictures from the visualizations show evidence of a periodic generating and shedding of vortices from the separation line.

1.3 Present Investigation

The study reported here focuses on the strongly time variant behavior of the flow in a turbulent junction vortex. Understanding of such a flow is important from the basic fluid dynamic point of view insofar as it sheds light on the behavior of large scale vortices embedded in a turbulent flow field. It can be speculated that vortices generated by other flow circumstances may behave in a similar way as the junction vortex. It may also help in improving the understanding the underlying mechanisms producing such strongly time variant flows. This study may also be useful in the selection of an appropriate turbulence model for numerical computations.

It is also speculated that the unsteady flow field in the junction vortex is a possible source of noise, produced by both hydrodynamic sources and surface noise through wall pressure fluctuations. In many practical situations, it is important to control or reduce the noise level. A relevant example is underwater surveillance of submarines. The achievement of a lower noise level would be useful in escaping detection. Also any unique characteristics of the noise generated by the junction vortex would be undesirable as this signature could be used for identification.

It is also expected that the unsteadiness of the junction vortex gives rise to unsteady forces on the body. A characterization of the unsteady forces may be of interest to a designer.

The present study of the strongly time variant flow in the junction vortex consists of spectral analysis and time resolved measurements of the velocity fluctuations. A frequent question concerning a time variant phenomena is whether there are any dominant periodic components. A spectral analysis is usually conducted for this purpose. Conducting a spectral

analysis may be relatively simpler in many situations. In the junction vortex flow many complications arise which make it very difficult to estimate spectra. In the case of velocity spectra, the first difficulty is encountered in the choice of a measurement system for obtaining velocity signals. For reasons which will be discussed later, the only reliable velocity signal obtainable from the junction vortex flow is through the use of a laser Doppler velocimeter. The laser Doppler system used for the experiments was equipped with a burst type counter processor. This compicates the spectral estimation process even further because the signal obtained from a counter processor is not a continuous one. Rather the data is obtained in a random fashion depending on the arrival of the seeding particles. In the usual spectral analysis, it is assumed that the data is available either in a continuous form or in an uniformly sampled manner. The only kind of velocity data available for the junction vortex flow using a LDV is a randomly sampled velocity signal. The problem then is how to estimate spectra from this non-uniformly sampled velocity data.

The various methods available for spectral estimation of non-uniformly sampled data were discussed first. The performance of these methods were then evaluated for various simulated data and real flow circumstances. Based on the results of this evaluation, a best method was chosen and applied for estimating spectrum from the velocity fluctuations in the junction vortex.

The time resolved velocity measurements were made with a laser Doppler velocimeter in the plane of symmetry. From the time resolved velocity measurements, the spectra and various other characteristics of the strongly time variant flow were computed in addition to the mean velocities and turbulent stresses.

The following chapters describe this experimental study of the strongly time variant flow of a turbulent junction vortex. Chapter two contains a description of the equipment used in the experiments and the coordinate system. The methods of spectral analysis for both uniformly and non-uniformly sampled data are described in Chapter three. Chapter four discusses the

experimental methods used. The results of the investigation of the performance of various spectral analysis methods for non-uniformly sampled data are presented in Chapter five. Chapter six contains the results of the spectral analysis and the time resolved measurements of the velocity fluctuations in the junction vortex. A brief summary of the experimental study and the results is given in Chapter seven.

2.0 Facilities

2.1 Cylindric Body

The turbulent junction vortex is generated by placing the streamlined cylindric body shown in Fig. 2.1 in the turbulent boundary layer on the flat floor of the wind tunnel. The flat sides of the cylinder terminate in a sharp trailing edge and are tangent to the circular leading edge of the body. The cylinder has a leading edge diameter (maximum thickness) of 127 mm, an overall length (chord) of 298 mm, and a height of 229 mm.

This particular body geometry was selected by Pierce et al. [2,3] as a standard test case for evaluating predictive capabilities of numerical codes attempting to solve a complex three-dimensional turbulent flow problem. It was selected to generate a strong surrounding three-dimensional turbulent boundary layer and a physically larger junction vortex flow. An extensive data base is available [2,3] for the flow field around this body, as well as in the wake region. The measurements were taken with a five-hole probe. In the plane of symmetry forward to the leading edge, an additional set of LDV measurements made by Tree [23] are also available.

Other bodies with different dimensions have been used by various people to generate the junction vortex flow. For example, Dickinson [10] used a NACA 0020 profile, and Devenport and Simpson [22] used a NACA 0012 profile in their experiments. The body used in the present experiment has a higher thickness to chord ratio than the NACA profiles.

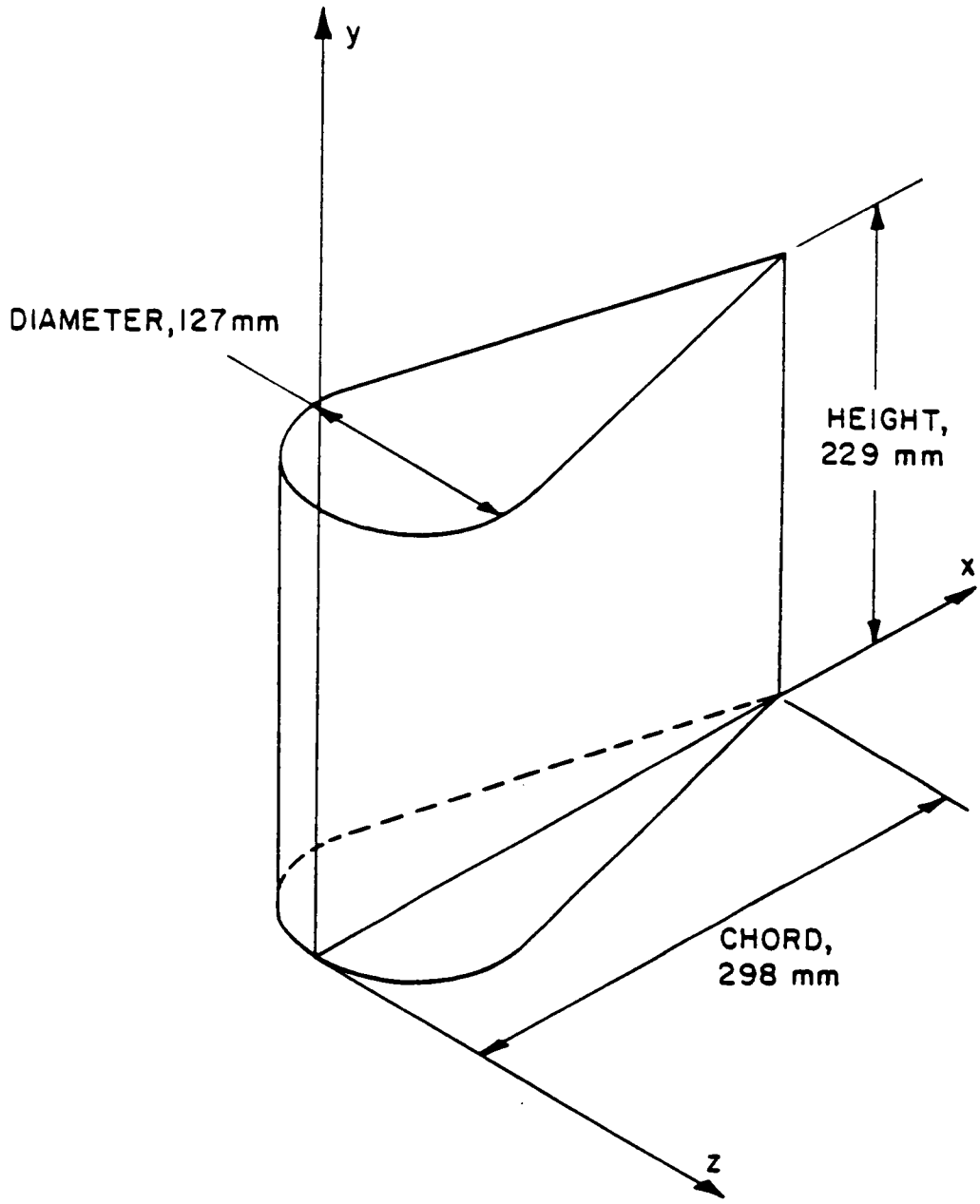

Figure 2.1. Cylindric Body and the Coordinate System

2.2 Coordinate System

The righthand orthogonal coordinate system used to describe this flow is also shown in Fig. 2.1. The origin of the coordinate system is at the intersection of the floor center line with the leading edge of the body. The flow is in the positive x direction. The x direction may sometimes be referred to as the streamwise direction and the y direction as the vertical direction.

2.3 Region Under Investigation and Choice of Equipment

The experiments reported here are concentrated on the upstream plane of symmetry. The measurement area includes the separated region containing the junction vortex. The measurement region extends 83 mm in front of the body leading edge and 51 mm above the wind tunnel floor as shown in Fig. 2.2. The flow field in this region is characterized by the following:

1. The flow is highly turbulent.

2. There are large areas of both instantaneous and mean reverse flow.

3. A large portion of the flow has very high pitch angles. That is, u and v components of the flow are comparable in magnitude.

The use of a pressure probe for flow measurement in this region may be questioned because of problems inherent with any type of physical pressure probe measurements. These include the following:

1. Question of interference with the flow because of the physical insertion of a probe in the flow field.

2. Does not detect flow reversal.

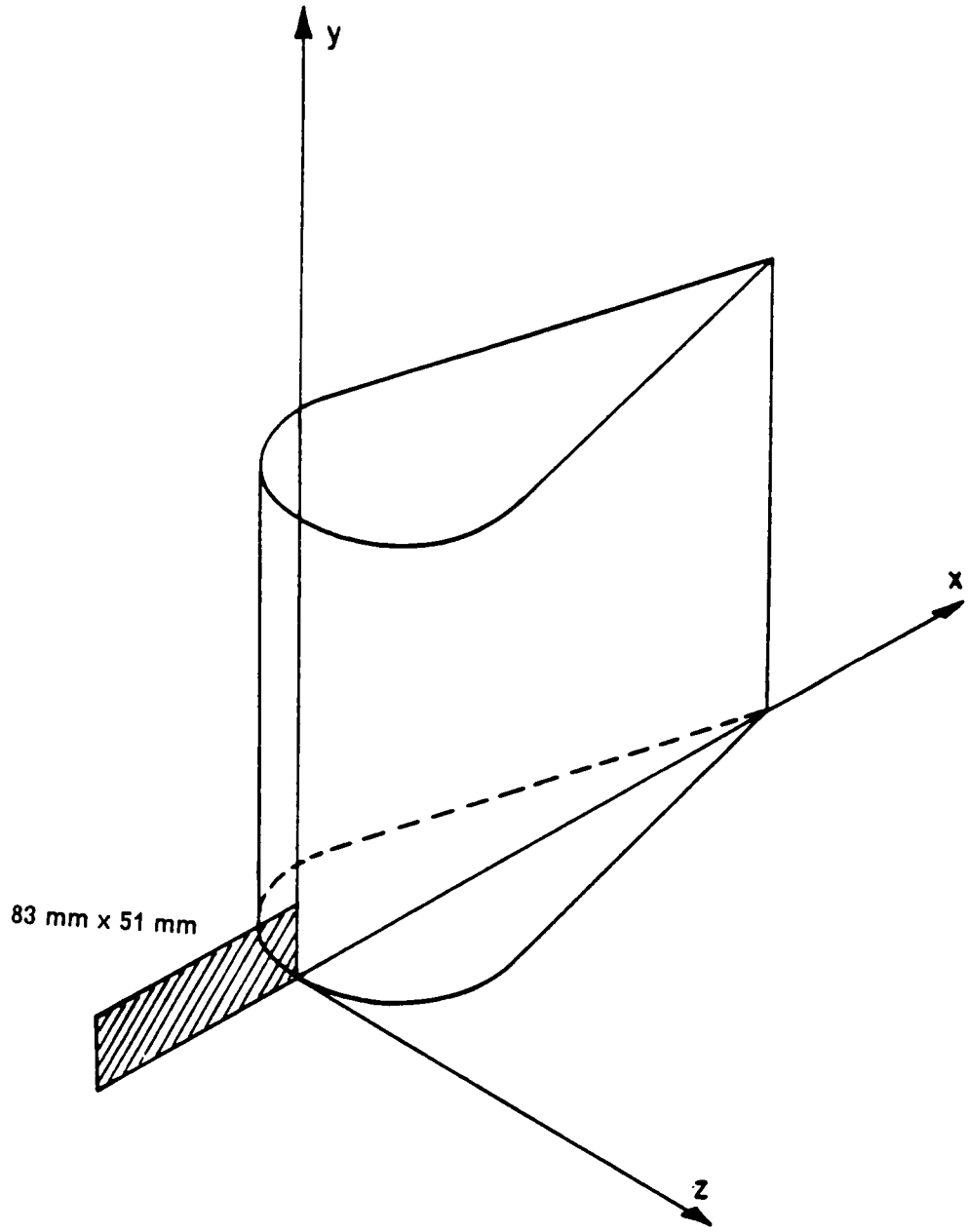

Figure 2.2. Measurement Region

3. Difficult to interpret in zones of high local turbulence intensity.

A hot wire/film anemometer system also suffers from similar disadvantages. In addition, an assumption that the flow is dominant in one direction ($v/u << 1$) has to be made for the sensor analysis of a hot wire anemometer response. In the junction vortex flow, velocities in both the x and y directions are comparable in magnitude and hence a sensor analysis assuming a single dominant flow velocity is not valid. A hot wire anemometer system also has the disadvantage of requiring very careful and frequent calibrations.

To overcome these problems, a frequency shifted LDV was chosen to investigate this region of the plane of symmetry flow field. Being an optical technique, it eliminates probe interference effects. Spatial resolution was significantly improved, and its directional sensitivity allows easy measurements in the reversed flow region. Despite its high cost and the large effort required to set up, the LDV is still the most attractive means of gathering reliable velocity data in this type of complex flow.

2.4 Wind Tunnel

The experiments were conducted in an open circuit, subsonic wind tunnel shown in Fig. 2.3. Air is drawn into the wind tunnel through a rectangular inlet 3.66 m wide and 2.44 m high (flow area equal to 8.92 m^2) and passes through a series of filters and flow straighteners. A 16 : 1 area ratio contraction follows the inlet and is designed to produce a uniform, non-accelerating flow at the exit of the contraction area (henceforth referred to as the throat). The boundary layer is tripped on all four sides of the wind tunnel throat with 2.8 mm diameter rods. A 1.6 mm diameter pitot tube is positioned at the throat to measure the air speed. The wind tunnel has adjustable louvers at the discharge end to control the Reynolds number. Air speeds of up to a maximum of 25 m/s can be attained in this tunnel.

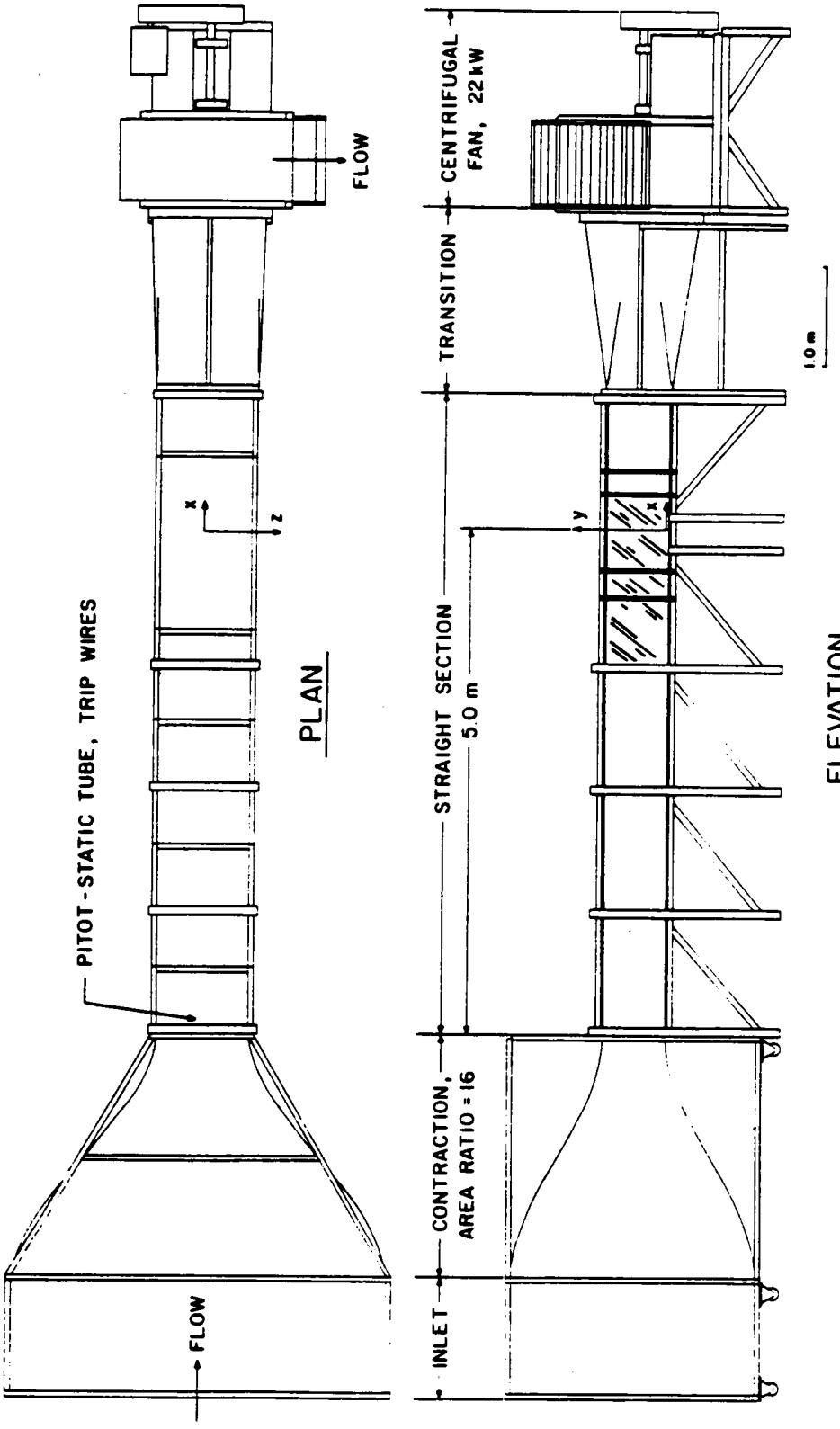

Figure 2.3. Open Circuit, Subsonic Wind Tunnel Used in the Experiments

The test section is a rectangular channel 0.91 m wide, and 0.61 m high (flow area equal to 0.56 m^2, aspect ratio equal to 1.5). The streamlined cylindrical body is placed 5.0 m downstream of the throat of the wind tunnel.

One side wall of the test section is made up of transparent material (plexiglass) to allow access for LDV measurements. Since minor surface scratches in the access wall may degrade the LDV signal to noise ratio, both the inner and the outer surfaces of the side wall were kept polished and scratch-free.

In order to make LDV measurements close to the floor, undesirable diffuse reflections from the floor produced by the laser beam must be eliminated. A highly polished aluminium plate was used as the floor of the test section to reduce diffuse reflections and allow measurements close to the wall.

Dynamic similarity for the low-speed, three-dimensional study was achieved by maintaining a constant Reynolds number at the wind tunnel throat. The Reynolds number per unit length,

$$\frac{Re}{L} = \frac{\rho V_*}{\mu} \tag{2.1}$$

was equal to 1,340,000 per meter, where V_* is the mean velocity at the wind tunnel throat. Table 2.1 summarizes the nominal laboratory and tunnel conditions for the experiments.

2.5 Calibration Wind Tunnel

Hot wire calibrations were conducted in a separate calibration wind tunnel. The calibrations were performed in the center of a large free jet leaving the wind tunnel duct. Air speeds in the core of this large jet ranging from 5 to 40 m/s at a turbulence intensity level of less that 1 percent were possible in this wind tunnel.

Table 2.1. Nominal Laboratory and Wind Tunnel Conditions

Ambient Temperature	25 C
Barometric Pressure	94.5 kPa
Dynamic Pressure at Tunnel Throat	0.274 kPa
Reynolds Number at Throat [1]	980,000
Pressure Drop Through Inlet Section	45 Pa
Flow Parameters at Test Section [2]	
Freestream Turbulence Intensity	0.5% - 0.6%
Freestream Speed/Speed at Throat	1.077
Boundary Layer Thickness	81.6 mm
Displacement Thickness	10.5 mm
Momentum Thickness	8.09 mm
Skin Friction Coefficient	0.00256

[1] Based on the hydraulic diameter

[2] Test section refers to a streamwise position 5.0 m downstream of the wind tunnel throat

2.6 Laser Doppler Velocimeter

A two-color, two-component, frequency shifted laser Doppler velocimeter (referred to as LDV) system was used to gather the experimental data. The laser Doppler velocimeter, sometimes called a laser Doppler anemometer, is a system using optical techniques for measuring instantaneous velocities in fluids. Unlike other flow measuring devices, the LDV has the advantage of being a non-intrusive method. Thus the uncertainty of interfering with the flow field by the introduction of a physical probe is completely eliminated. A LDV is sensitive only to the velocity of the flow and is not affected by fluctuations of temperature, pressure, or fluid properties. The device is also linear, so it does not require extensive and frequent calibrations. In difficult flow measurement situations, such as measurements in recirculating or separated flows, and in flames or combustion gases, the LDV, however complex, often appears as the most reliable method of measurement.

2.6.1 Theory of Laser Doppler Velocimeter Operation

Only a brief review of the theory behind the operation of the LDV is presented here. A number of books [38-40] treat the subject in detail and should be consulted for further reference.

A laser Doppler velocimeter measures the velocity by detecting and measuring the Doppler shift of monochromatic light scattered from a moving object. In velocity measurements, the moving object is generally a particle in the flow. The flow is typically seeded with the particles, although particles naturally present in the flow are often used to scatter the incident light. The particles are assumed to be small enough so that they follow the fluctuations of the flow to a high degree.

A measurement is made when a particle, moving with the flow, scatters the incident light in all directions, and a portion of this scattered light is collected from any direction by a photodetector. The frequency of the scattered light collected by a stationary detector is

Doppler shifted and the shift is referred to as 'the Doppler frequency of the flow'. The Doppler frequency is proportional to the particle velocity and hence, to the flow velocity.

2.6.2 Seeding of the Flow

In laser Doppler velocimetry the velocity actually measured by the instrument is the velocity of small particles suspended in the flow. In order to infer fluid velocities from the measured particle velocities, the particles are assumed to accurately follow the flow. Furthermore, these particles must be good light scatterers, their concentration should be high enough to produce a desirable data rate, they must be conveniently generated at low cost, and they must be non-toxic.

In the present experiment the seed was generated from a seeding solution made from 20 percent cane sugar and 80 percent water (by volume). The solution was atomized and sprayed into the flow by compressed air near the throat of the wind tunnel. The atomized liquid droplets were spherical in shape and were roughly one micron in diameter.

2.6.3 The Fringe Model

This experiment used a dual beam system, a common arrangement where two laser beams of equal intensity are focussed at a point in the flow field. This arrangement has a pair of beams for a single channel system measuring one component of the flow velocity. The operation of the LDV is best explained by a model known as the fringe model.

When two similarly polarized, monochromatic, Gaussian laser beams of equal intensity intersect at an angle (Fig. 2.4), a set of parallel fringe systems are formed at the intersection region. The distance between the fringes, d_f, is given by the equation

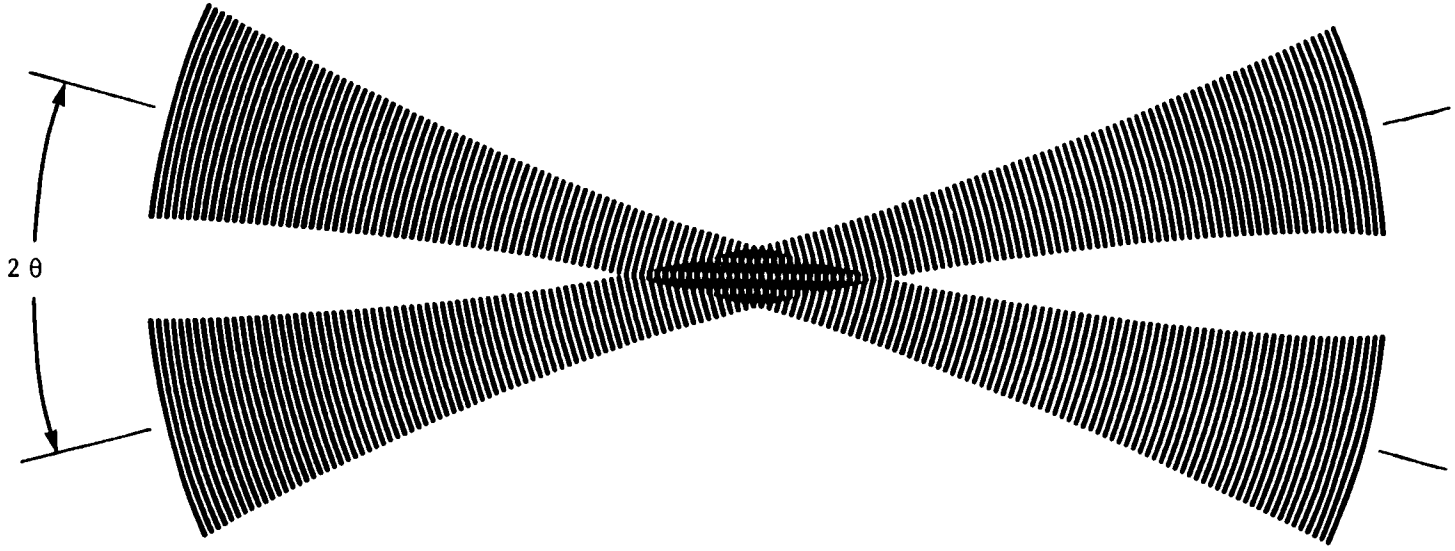

Enlarged View of the Intersection Region

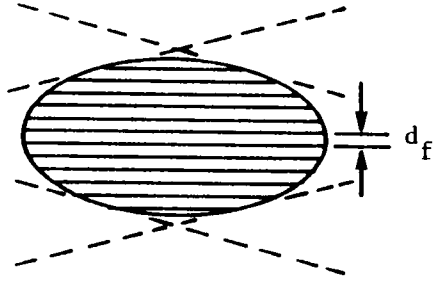

Figure 2.4. Formation of the Fringe Pattern

$$d_f = \frac{\lambda}{2 \sin \theta} \tag{2.2}$$

where λ is the wavelength of the laser light, and θ is the half-angle between the two beams.

2.6.4 The Scattering Volume

The region where the two beams intersect is called the scattering volume. It is ellipsoidal in shape (Fig. 2.5), and its boundary is defined by a surface of constant light intensity, I_0/e^2, where I_0 is the light intensity at the center of the incident beams. When a small particle passes through the scattering volume, it will encounter alternating light and dark regions of the fringes. The light scattered by the particle will vary in proportion to the intensity of the incident light in these light and dark fringes.

2.6.5 The Doppler Burst

The intensity variation of the scattered light is converted by a photodetector into a voltage signal whose amplitude is directly proportional to the scattered light incident on the detector. A representative voltage trace for a single particle going through the scattering volume is shown in Fig. 2.6. It is made up of a sinusoidal ac component superimposed on a Gaussian mean, and it is usually called a Doppler burst. The mean value, resulting from the particles crossing a region with Gaussian-shaped light intensity, is referred to as the pedestal and is removed by high-pass filtering prior to any signal processing. The sinusoidal component has a unique frequency, commonly termed the Doppler frequency, f_D, and is given by

$$f_D = \frac{V_n}{d_f} = \frac{V_n 2 \sin \theta}{\lambda} \tag{2.3}$$

where V_n is component of the velocity normal to the fringes.

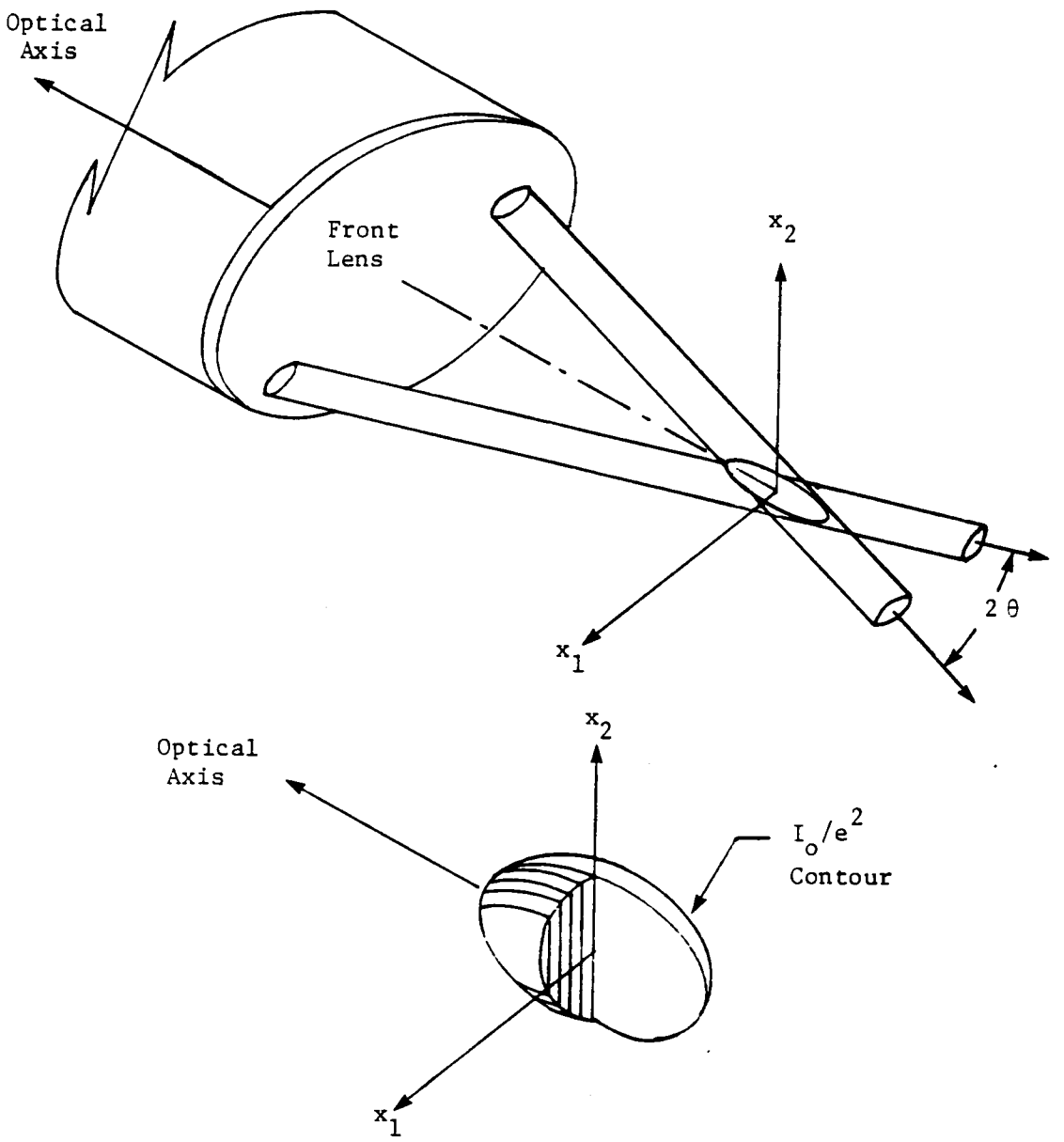

Figure 2.5. Scattering Volume

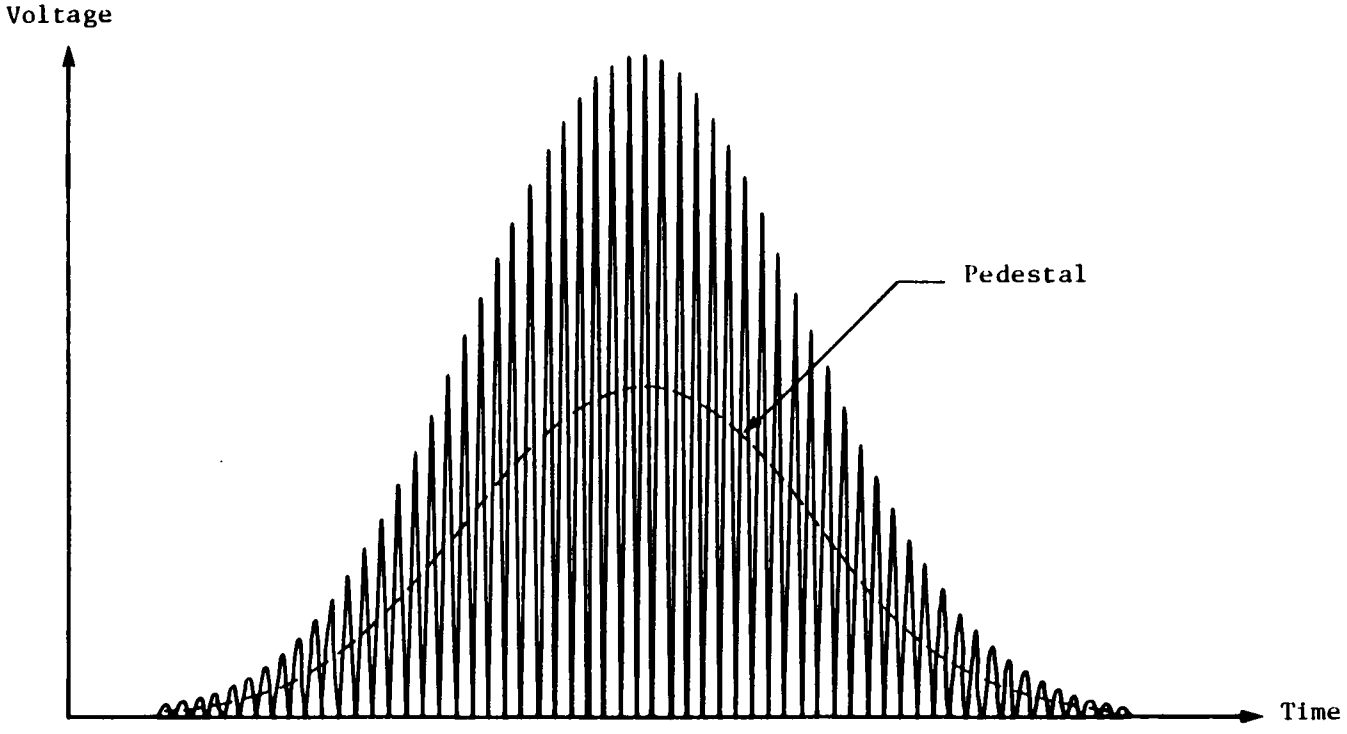

Figure 2.6. Doppler Burst

The velocity of the particle is then given by

$$V_n = \frac{f_D \lambda}{2 \sin \theta} \tag{2.4}$$

Since λ is known for a given type of laser and θ is determined from the geometry of the transmitting optics, measurement of the velocity simply involves the measurement of the Doppler frequency. Furthermore, since λ and θ are fixed for a given experiment, the above equation is linear. Thus, there is no need for a calibration and all the problems associated with calibration can be avoided.

2.6.6 Direction Sensing by Frequency Shift

The symmetry of the photodetector signal generated by a particle going through the scattering volume shows that the frequency of the signal does not indicate whether the particle velocity is positive or negative. The direction of the particle motion is obtained by using a frequency shift system. The addition of the frequency shift system results in a particle with zero velocity generating a photodetector signal having a frequency equal to the shift frequency. From a fringe model viewpoint, the effect of the frequency shift is explained by a set of fringes moving at a velocity consistent with the shift frequency. The motion of the fringes against the direction of motion of the particles gives a higher frequency while motion of the fringes in the direction of motion of the particles gives a lower frequency.

2.6.7 Signal Processing with Counters

A number of methods can be used to determine the Doppler frequency in a Doppler burst. Methods that have been successfully employed include photon correlation, spectrum analysis, frequency tracking and frequency counters. With the rapid advancements in digital electronics in recent years, counters have become the most popular technique. In the LDV set up used for

the current investigation, a commercially available counter made by DISA (now DANTEC) was used.

The counter basically functions as a high-speed electronic stop-watch. Using an internal, high-speed clock the LDV counter measures the time taken for a particle to cross a given number of fringes. From this, the time required to cross one pair of fringes, which is equal to the Doppler period, is computed. The Doppler frequency is then computed simply by inverting the Doppler period.

Counters are generally equipped with validation circuits which perform a check on the data. The purpose of this validation check is to verify the self-consistency within a single Doppler burst. Since a Doppler burst is characterized by a single frequency, the Doppler period computed from 5 fringe crossings and the Doppler period computed from 8 fringe crossings should be approximately the same. This is determined by performing the following comparison in a validation circuit

$$100 \times \frac{\left| \frac{5}{8}\tau_8 - \tau_5 \right|}{\frac{5}{8}\tau_8} \leq \varepsilon \qquad (2.5)$$

The parameter ε is externally user selectable in most counters, and it is usually set in the range of one to ten percent.

It should be noted here that the validation check does not reflect the accuracy of the Doppler frequency measurement. Rather, it indicates the repeatability of the measurement within a single Doppler burst. Any burst that fails this validation check is rejected from further processing. While there are a number of reasons that can lead to a rejected Doppler burst, the primary cause is simultaneous multiple bursts. This condition occurs when multiple particles are present within the scattering volume, and the Doppler burst from one particle is super-

imposed on the Doppler burst generated by another particle or particles. The resultant mixed burst is not characterized by a single frequency and so it is rejected.

2.7 Characteristics of LDV Data from Counters

It is clear from the above descriptions that the following conditions should be met for the LDV system to get an output.

1. A scattering particle goes through the scattering volume and generates a Doppler burst.

2. The Doppler burst is validated by the validation circuitry.

Since the arrival of the particles in the scattering volume is random, the output data from the counters are placed in a random fashion in time. Most counters are also equipped with an analog output. The analog outputs operate essentially with a sample and hold scheme. That is, the output level is kept constant at the previous value until new data arrives. To obtain a reasonable representation of the continuous time series in an analog output, a very high data rate is needed, which is a luxury not practically obtainable in most LDV systems.

2.8 Hot-Wire Anemometer System

A hot wire anemometer system was used for measuring spectra for comparison purposes in a two-dimensional turbulent boundary layer and behind a vortex shedding cylinder. A single hot wire mounted normal to the flow was used for this purpose. The anemometer system utilized a DISA constant temperature anemometer bridge. The output from the bridge was calibrated very carefully in the calibration wind tunnel. The calibrated output was then passed through a linearizer and anti-aliasing filter. The output signal was analyzed for the spectra using a DATA 6000, an advanced digital waveform analyser. The DATA 6000 can acquire data

on two channels simultaneously and perform various mathematical analysis (FFT, autocorrelation etc.). It also has two disk drives which can be used to store the data.

2.9 Computer Data Acquisition and Analysis

Individual Doppler frequencies measured and validated by the counter are available in binary form. An interface is used to transfer this data directly to a DEC PDP11 minicomputer via Direct Memory Access (DMA). The DMA transfer protocol bypasses the CPU and thus achieves a much faster data transfer rate. The data is then stored in a hard disk from where it can be subsequently recalled for analysis.

Data collection was accomplished by DRP3, a commercially available software package marketed by TSI Inc. In addition to data acquisition, the program performs various statistical data analysis and has the capability of graphical display of results.

For the purpose of spectrum analysis, the data was sent to the IBM mainframe computer for further computations. Analyses of the data for evaluating time variant flow properties were done in the minicomputer itself. For this purpose, the program DRP3 was modified and suitable subroutines were incorporated.

2.10 Statistical Bias Errors in LDV Measurement

2.10.1 Velocity Bias

A Burst mode laser velocimeter produces a velocity output whenever a particle is passing through the measurement volume. The arrival rate of measurement particles is not statistically independent of the flow velocity which brings them to the measurement volume. More particles with higher velocities will arrive in the measurement volume. As a result, computed averages are likely to be biased if a simple averaging is used.

To correct for this bias, a residence time weighting technique has been used. This method has been recommended for use with all data densities by the 1985 ASME panel of the Second International Laser Anemometry Symposium [41]. In this method, the amount of time that a particle spends in the measurement volume is measured in addition to the particle velocity. This residence time is then used as a weight to remove the velocity bias. Thus the mean is calculated as

$$Mean = \frac{\sum v_i \tau_i}{\sum \tau_i} \tag{2.6}$$

where v_i is the velocity obtained in the i^{th} measurement and τ_i is the corresponding residence time. Higher moments are calculated in the same fashion.

2.10.2 Fringe Bias

Fringe bias is caused by the fact that real processors cannot measure all speeds at all angles. It is also referred to as angle bias. This bias can be almost completely eliminated in a properly used frequency shifted LDV system. This problem has been discussed in great detail by Tree [23]. His recommendations for eliminating the fringe bias have been followed in the present investigation.

3.0 Spectral Analysis

3.1 Introduction

Spectral analysis of a signal is the use of a processing method which characterizes the frequency content of the signal. Usually, spectral analysis is used to determine the distribution of the mean square value over the range of frequencies of interest. In electrical engineering, the spectrum is often described as a distribution of power, which comes from the fact that the power dissipated in an electrical circuit is proportional to the mean square value of the voltage (or current) applied.

Statistics plays an important role in spectral analysis because, in practice, 1) the signals encountered are inherently random in nature, and 2) only a finite segment of a random signal is available so that only an estimate of the spectrum can be obtained. If the signal is deterministic, that is, a signal which can be predicted for all times, the problem of spectral analysis becomes relatively simpler.

The word 'signal' used in the preceding description is borrowed from electrical engineering terminology. A more general term is a 'time series' and it will be used throughout this report. A time series is defined here as a discrete series obtained by sampling a random or non-deterministic function x of an independent variable t . In most situations, the function $x(t)$ will be a function of time, but in some cases it may be a function of some other physical parameter t , where for example, t could represent a space variable.

3.2 Random Processes

A random variable is a variable whose value cannot be predicted accurately, except to the extent that it may take on one of a set of values, each with some probability. Similarly, a random process is a function $x(t)$ whose value at any point of time cannot be predicted, except probabilistically. A random process is thus essentially described by its probability distribution.

Stationarity is a very important concept for random processes. In a loose and descriptive sense, it means 'unchangingness' in time of the underlying generating mechanism for the random process. The idea of stationarity is that the behavior of a set of random variables at one time is probabilistically the same as the behavior of another set of the same random variables at another time.

Mathematically, in the general case of n random variables, we can capture this property by making the finite dimensional probability distribution time invariant [42]. If the joint probability distribution function is denoted by

$$P[x_1(t_1), x_2(t_2), \ldots, x_n(t_n)],$$

then a random process is strictly stationary if

$$P[x_1(t_1 + \tau), x_2(t_2 + \tau), \ldots, x_n(t_n + \tau)] = P[x_1(t_1), x_2(t_2), \ldots, x_n(t_n)] \tag{3.1}$$

for all possible $t_1, t_2, \ldots, t_n$ and τ .

Thus the probability distribution depends on the relative time separations, $|t_i - t_j|$,of the random variables but not on their absolute time locations $t_1, t_2, \ldots, t_n$. Another way of saying this is that the probability distribution associated with any set of times $t_1, t_2, \ldots, t_n$ is the same as that associated with any other set of times obtained by translating $t_1, t_2, \ldots, t_n$ ahead or backward by an amount τ .

Often a less strict definition of stationarity called weak stationarity is invoked. A random process is called weakly stationary if the mean is a constant and the autocorrelation function is a function of only the time separation. Sometimes other terms as second order stationary or wide sense stationary are also used to denote weak stationarity.

Another important concept is the property of ergodicity. Usually statistical ensemble averaging is used to define the mean, autocorrelation and spectral densities of random processes. However, in practice, an ensemble averaging is often impossible and it is desirable to estimate all statistical properties from a single sample time series $x(t)$ by substituting time averages for ensemble averages. The property of the random process necessary to allow this is called ergodicity. A stationary random process is said to be ergodic if all its statistics can be predicted from a single time series via time averaging, regardless of the origin of the time series. That is, the time averages of all possible single time series are equal to the ensemble average.

A stationary ergodic process will always be assumed in the following discussions. It is also convenient to subtract the mean value from the time series prior to analysis, leaving a stationary ergodic process with zero mean.

3.3 Definitions

There is considerable disagreement in the literature about the terminology in spectral analysis. Different names have been used in the literature for the same term. To avoid confusion, some terms are defined in the following. Various names in use for the same term have been listed in these definitions.

3.3.1 Autocorrelation

For a continuous signal, $x(t)$, from a stationary random process with zero mean, the autocorrelation function, $R(\tau)$, is defined as

$$R(\tau) = \lim_{T \to \infty} \frac{1}{T} \int_0^T x(t)\ x(t+\tau)\ dt \tag{3.2}$$

where T is the total length of the record and τ is the lag time at which the products $x(t)\ x(t+\tau)$ are computed.

The autocorrelation function is usually defined as in Eq. 3.2 in engineering texts [43,44]. Statistics texts [42] sometimes use the term autocovariance function for the definition given in Eq. 3.2 and use the term autocorrelation function for the autocovariance function normalized to have magnitude lying between zero and unity.

Two important properties of the autocorrelation function are worth mentioning. Firstly, the autocorrelation function at zero lag time gives the variance of the signal.

$$R(0) = E[x^2] \tag{3.3}$$

where E denotes the expectation operator.

Secondly, the autocorrelation function is an even function, that is,

$$R(\tau) = R(-\tau) \tag{3.4}$$

3.3.2 Spectrum

The spectrum or spectral density, $S(f)$, is defined from the autocorrelation function by a Fourier transform,

$$S(f) = \int_{-\infty}^{\infty} R(\tau)\ e^{-j2\pi f\tau}\ d\tau \tag{3.5a}$$

The inverse Fourier transform gives back the autocorrelation function,

$$R(\tau) = \int_{-\infty}^{\infty} S(f)\ e^{j2\pi f\tau}\ df \tag{3.5b}$$

Since the autocorrelation function is an even function, Eq. 3.5a can be written as,

$$S(f) = \int_{-\infty}^{\infty} R(\tau)\cos(2\pi f\tau)\ d\tau \tag{3.6}$$

The complex part drops out because of the symmetry of the autocorrelation function. Thus the spectral density is always a real quantity.

Symmetry of $R(\tau)$ also allows Eq. 3.6 to be written as,

$$S(f) = 2\int_{0}^{\infty} R(\tau)\cos(2\pi f\tau)d\tau \tag{3.7}$$

The spectrum, $S(f)$, defined here is sometimes called a two-sided spectrum. That is, the spectrum is defined and assumed to exist for a frequency range extending from $-\infty$ to ∞ .

In practical computations only positive frequencies are encountered and a one sided definition of the spectral density, $G(f)$, where the spectrum extends from 0 to ∞, is used. The relationship between the two definitions is given by

$$\begin{aligned} G(f) &= 2S(f) \quad f \geq 0 \\ &= 0 \qquad f < 0 \end{aligned} \tag{3.8}$$

The one sided definition of spectral density will always be used in the results presented in this report.

According to the above definitions, the unit of spectral density is given by x^2/Hz .

In some of the literature, the angular frequency, ω, is used instead of f in the definition of spectral density. In such cases, a factor of 2π is usually included in or shared by Eq. 3.5a and Eq. 3.5b.

Other terms used for the spectral density are power spectral density, power spectrum, or simply spectrum.

3.4 Spectral Estimation for Uniformly Sampled Data

This section contains a brief description of the spectral estimation methods for uniformly sampled data. A number of good textbooks [42-46] are available on this subject and should be consulted for further reference.

In the classical methods of spectral estimation, the continuous signal is always uniformly sampled. That is, the values of the time series are available at equidistant points in time.

Basically there are three types of approaches for spectral estimation from uniformly sampled data. These are:

1. The correlogram or Blackman-Tukey method. This method involves computing the autocorrelation function of the time series and then taking the Fourier transform of the autocorrelation function.

2. The periodogram or the direct Fourier transform method. The Fourier transform of the original time series is computed, and the square of the magnitude of the Fourier transform gives an estimate of the spectrum.

3. The bandpass filter method. This involves the use of digital bandpass filters (or analog filters if the analog signal is analyzed), one for each frequency range of interest. The output of the filter is squared and averaged to yield the spectrum.

The three different methods of spectral anlysis have been shown to be equivalent (see [45] for further references). It should be noted that the equivalence is valid only under limiting conditions, so that actual results obtained by different methods may not be exactly equal.

The correlogram and the Fourier transform method are described in the following. The bandpass filter method is not very popular for discrete data, and will not be discussed here.

3.4.1 Correlogram Method

This is also known as the Blackman-Tukey method [46]. The autocorrelation function is first estimated and then the spectrum is computed from the Fourier transform of the autocorrelation function.

For a uniformly sampled discrete time series of finite length, the autocorrelation function is estimated by,

$$\hat{R}(\tau) = \hat{R}(r\Delta t) = \frac{1}{N-r}\sum_{n=1}^{N-r} x(n)\ x(n+r), \qquad r = 0,1,2, \ldots ,m \tag{3.9}$$

where $x(n)$ is the time series of N points, Δt being the time interval between points. The lag number is denoted by r and m is the maximun lag up to which computations are performed. Usually the number of points, N, is taken to be at least 10 times the maximum lag, m. The hat will be used throughout this report to denote estimated quantities. It is enough to calculate the autocorrelation function at positive lag values because of the symmetry of the autocorrelation function.

The spectral density was defined as the Fourier transform of the autocorrelation function as shown in Eq. 3.5a. For a discrete time series, the spectral density is given by the discrete time Fourier transform of the autocorrelation function.

$$S(f) = \Delta t \sum_{r=-\infty}^{\infty} R(r\Delta t)\ e^{-j2\pi fr\Delta t} \tag{3.10}$$

or using Eq. 3.6,

$$S(f) = \Delta t \sum_{r=-\infty}^{\infty} R(r\Delta t)\cos(2\pi fr\Delta t) \tag{3.11}$$

The correlogram method of spectral density estimation simply substitutes a finite sequence of autocorrelation estimates for the infinite sequence of unknown true autocorrelation values. For example, substitution of the autocorrelation estimates $\hat{R}(r\Delta t)$ up to a maximum lag m yields the following spectral density estimator,

$$\hat{S}(f) = \Delta t \sum_{r=-m}^{m} \hat{R}(r\Delta t) \cos(2\pi f r \Delta t) \tag{3.12}$$

Using the one sided definition of the spectral density, Eq. 3.12 can be written as,

$$\hat{G}(f) = 2\Delta t \left[\hat{R}(0) + 2 \sum_{r=1}^{m} \hat{R}(r\Delta t) \cos(2\pi f r \Delta t) \right] \tag{3.13}$$

Blackman and Tukey, in their pioneering work [46], computed the spectral density from the autocorrelation function by a slightly different formula,

$$\hat{G}(f) = 2\Delta t \left[\hat{R}(0) + 2 \sum_{r=1}^{m-1} \hat{R}(i) \cos 2\pi f i \Delta t + \hat{R}(m) \cos 2\pi f m \Delta t \right] \tag{3.14}$$

This formula is obtained by using Eq. 3.5 and a trapezoidal integration formula. The two equations differ only by a factor of 2 in the last term of the summation in Eq. 3.13. Results obtained from these two equations will differ by a small amount when no windows are used. If a window function is used, the results will be identical since the window goes to zero for the last term.

The frequencies at which spectra are calculated are given by,

$$f_k = \frac{k}{2m\Delta t}, \quad k = 0,1,2, \ldots ,m \tag{3.15}$$

This produces $(m + 1)$ equally spaced spectral estimates. This frequency spacing was first suggested by Blackman and Tukey from degree of freedom considerations and is conventionally used now.

Equation 3.14 can be rewritten in a computational form as,

$$\hat{G}(f) = 2\Delta t\left[\hat{R}(0) + 2\sum_{i=1}^{m-1}\hat{R}(i)\cos\frac{\pi ik}{m} + \hat{R}(m)\cos\pi m\right], \quad k = 0,1,\ldots,m \tag{3.16}$$

Two other important considerations in the estimation of spectrum are the use of a window function and the upper limit of the frequency up to which spectral estimates can be computed. These topics are discussed in detail later.

3.4.2 Periodogram Method

In this approach the data set is Fourier transformed directly and the squared magnitude of the Fourier transform then gives an estimate of the spectrum [44]. For a finite data set $x(0), x(1), \ldots, x(N-1)$ of N samples, the discrete Fourier transform, $X(f)$, is given by,

$$X(f) = \sum_{r=0}^{N-1} x(r)e^{-j2\pi fr\Delta t} \tag{3.17}$$

The periodogram estimate is then given by

$$\hat{G}(f) = \frac{2\Delta t}{N}\left|X(f)\right|^2 \tag{3.18}$$

The Fourier tansforming is usually performed with a Fast Fourier Transform (FFT) routine. The data set is usually multiplied by a window function prior to the Fourier transformation.

The frequencies at which spectral estimates are calculated are given by

$$f_k = \frac{k}{N\Delta t}, \quad k = 0, 1, \ldots, N \tag{3.19}$$

This produces independent spectral estimates at N equidistant points.

This estimator is known to be inconsistent, that is, the variance does not decrease as the record length is increased. Some sort of averaging procedure must be adopted with this approach to get consistent estimates. The different methods of averaging are discussed in detail later.

3.4.3 Effect of Finite Record Length and Windowing

The definition of a spectrum involves the use of an infinite record length (see Eq. 3.5a). Since only a finite amount of data is available in practice, the effect of a finite record length is important to consider. Suppose in Eq. 3.6, the maximum lag value available is m and the corresponding lag time is τ_m, then the estimate of the spectral density has the form,

$$\hat{S}(f) = \int_{-\tau_m}^{\tau_m} R(\tau) \cos(2\pi f\tau)\ d\tau \tag{3.20}$$

This expression can be rewritten in a form similar to Eq. 3.6, introducing the rectangular window function, $w_{rect}(\tau)$, as

$$\hat{S}(f) = \int_{-\infty}^{\infty} w_{rect}(\tau)\ R(\tau) \cos(2\pi f\tau)\ d\tau \tag{3.21}$$

The rectangular window, $w_{rect}(\tau)$, is then defined as

$$\begin{aligned} w_{rect}(\tau) &= 1 \quad -\tau_m \leq \tau \leq \tau_m \\ &= 0 \quad \textit{otherwise} \end{aligned} \tag{3.22}$$

Since multiplication in the time domain is equivalent to convolution in the frequency domain, the spectral estimate from a finite length data set can be written as [45],

$$\hat{S}(f) = \int_{-\infty}^{\infty} S(\phi)\ W_{rect}(f-\phi)\ d\phi \tag{3.23}$$

where $S(\phi)$ is the spectral density for an infinite record length, and $W_{rect}(f)$ is the Fourier transform of the rectangular window function. The Fourier transform of the window function is also called the spectral window. The spectral window is important in determining the resolution of the spectral analysis method, as discussed later. In this report, a 'window' is used to denote the window function in the time domain, as opposed to 'spectral window', which is used to denote the window function in the frequency domain. Figure 3.1 shows the spectral window for the rectangular window function.

The net effect of this convolution process is the spreading of the mean square value (often called power) from one frequency band to adjacent frequency bands through the sidelobes of $W(f)$. This effect is also known as leakage.

The effect of leakage can be more clearly seen in the case of the spectrum of a sine wave calculated from Eq. 3.23. Thus instead of obtaining a single delta function, the finite record length spreads or smears the main lobe considerably. This is shown in Fig. 3.2. Besides the spreading of the main lobe, there is also an infinite number of smaller side lobes added to the spectral density, with both effects due to the truncation process.

To minimize these problems, window shapes other than the rectangular window have been tried. They obtain their improvements by modifying the rectangular window in the time domain (or an equivalent operation in the frequency domain). There are many possible window shapes, none of which is obviously the best. Each window has its advantages and disadvan-

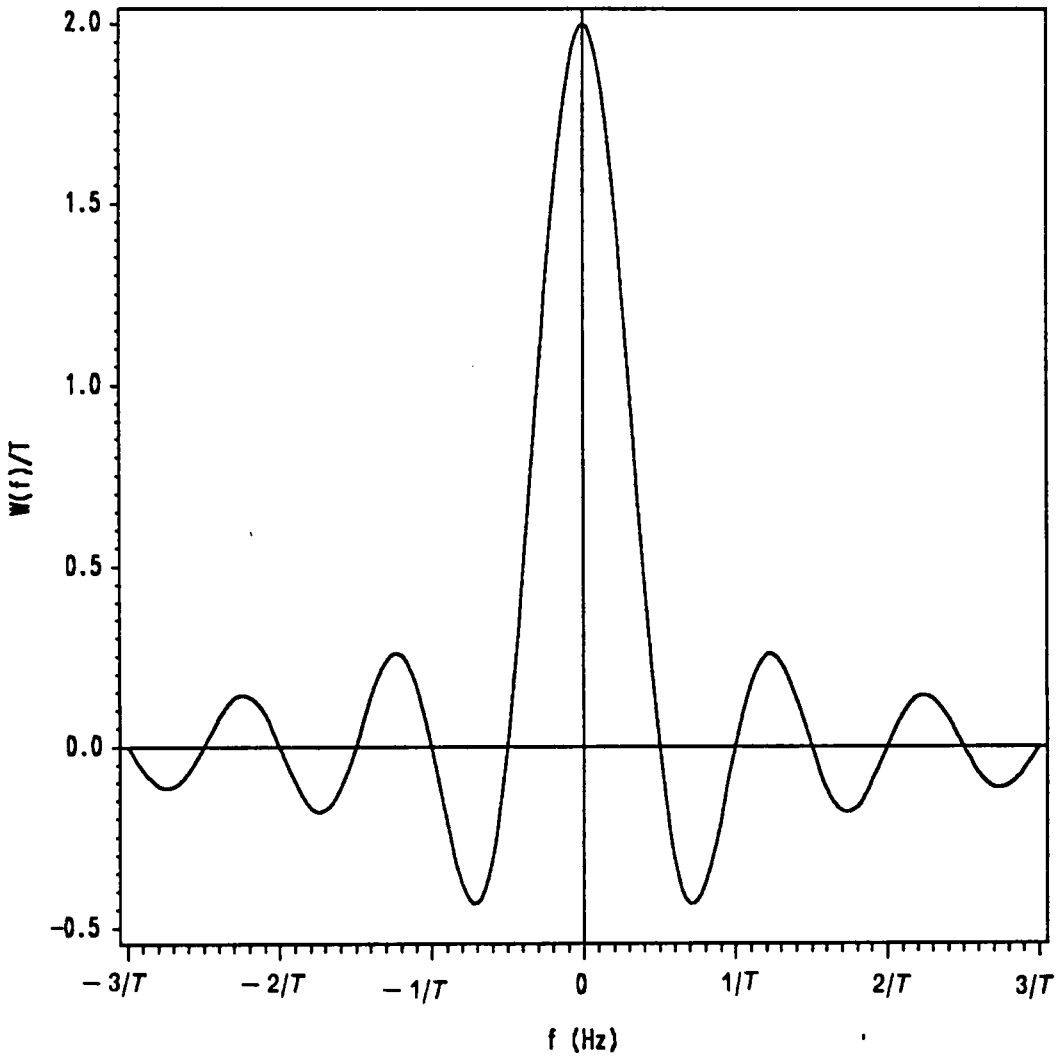

Figure 3.1. Spectral Window of a Rectangular Window in the Time Domain

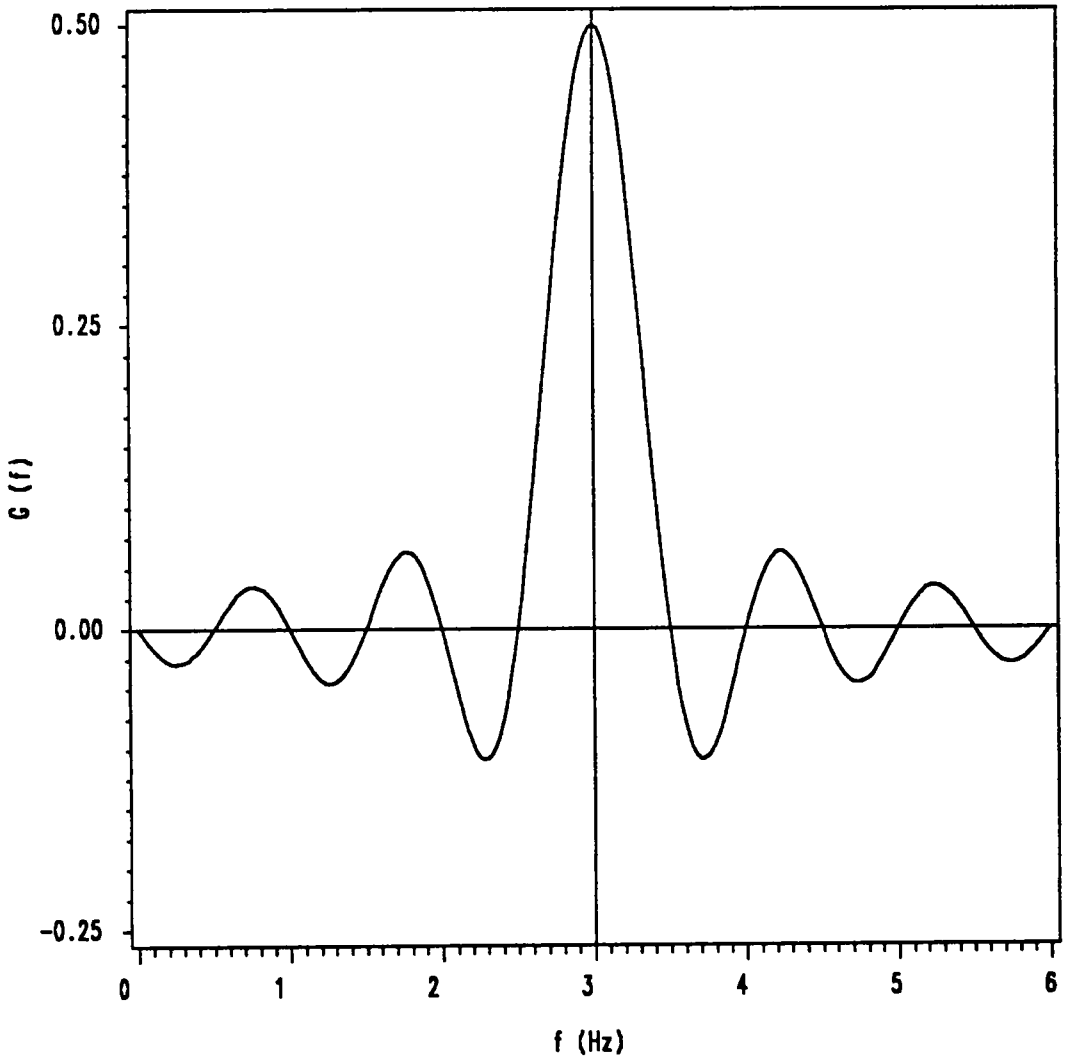

Figure 3.2. Spectrum of a Sine Wave of Frequency = 3 Hz, Amplitude = 1

tages. The window shape used in the present work is called a Hanning window and is given by,

$$\begin{aligned} w_{Hann}(\tau) &= \frac{1}{2}\left[1 + \cos\frac{\pi\tau}{\tau_m}\right] \quad -\tau_m \le \tau \le \tau_m \\ &= 0 \qquad\qquad\qquad\qquad\quad \textit{otherwise} \end{aligned} \tag{3.24}$$

The Fourier transform of the Hanning window, $W_{Hann}(f)$, along with the Fourier transform of the rectangular window, $W_{rect}(f)$, are shown in Fig. 3.3. It can be seen that the Hanning window reduces the side lobes although at the expense of a wider main lobe.

The foregoing discussion about the effect of a finite record length and windowing is also valid for the periodogram method. The main difference is that in the periodogram method, instead of the autocorrelation sequence, the data sequence is being truncated. So the windowing is applied to the data sequence.

3.4.4 Aliasing and the Nyquist Frequency

Aliasing is a problem associated with the sampling of data. If a sine wave whose frequency is greater than $1/2\Delta t$ is sampled at an interval Δt , it appears as a lower frequency in the spectrum. That is, rather than appearing at its true frequency, it appears at its aliased (lower) frequency.

The frequency $1/2\Delta t$ Hz is called the Nyquist frequency and is the maximum frequency that can be correctly detected when data is sampled at a time spacing of Δt . Thus the Nyquist frequency is one-half of the sampling frequency, $1/\Delta t$.

The phenomenon of aliasing is very important when analysing practical data. The Nyquist frequency $1/2\Delta t$ must be high enough to cover the full frequency range present in the time series. This requirement may be impossible to meet in some cases and the use of analog filters called antialiasing filters is common in practice. Such filters try to remove all frequency

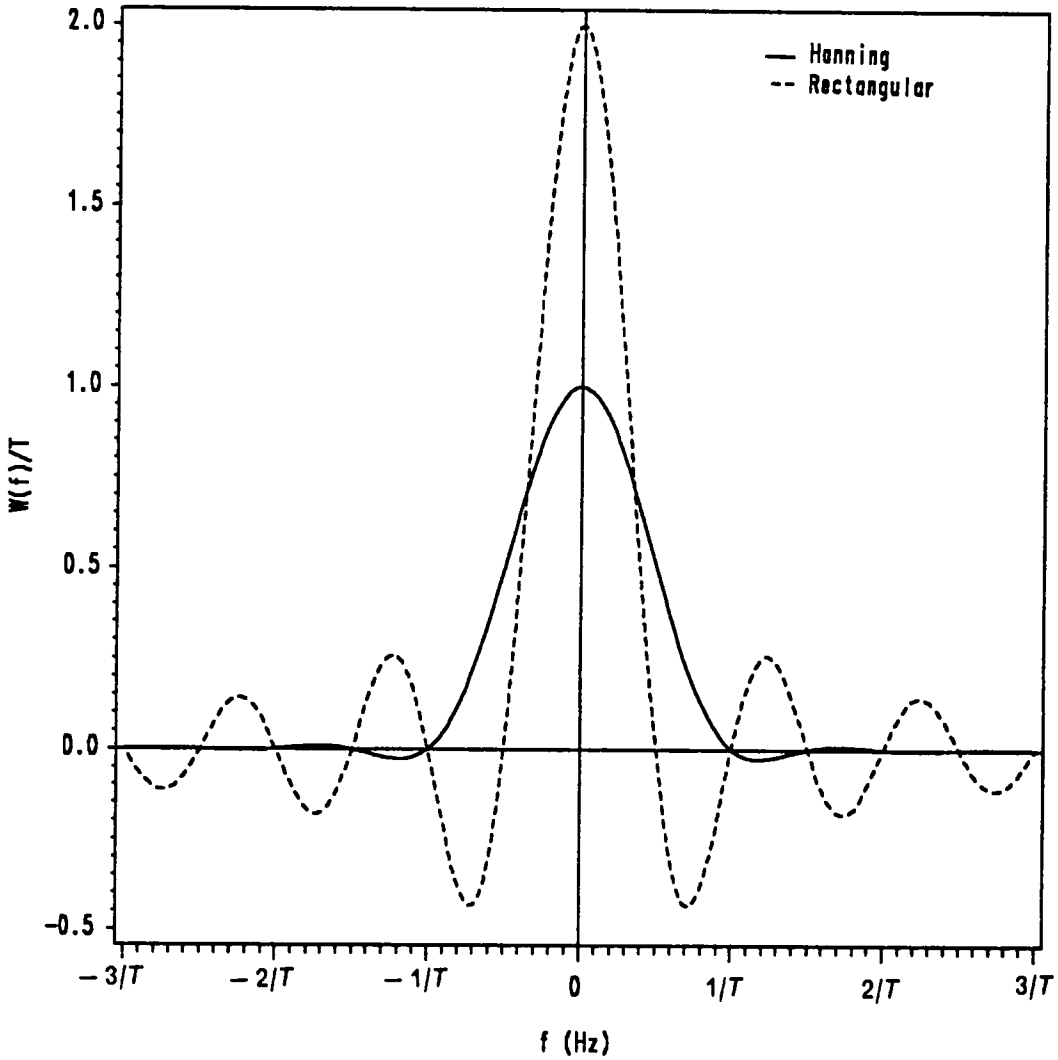

Figure 3.3. Comparison of Hanning and Rectangular Spectral Windows

components higher than the Nyquist frequency. Because of real filter characteristics, it is common to sample at frequencies larger than twice the Nyquist frequency.

3.4.5 Resolution and Bandwidth

The resolution determines the capability of the spectral estimation procedure to resolve fine structures in the frequency properties of the data, such as narrow peaks in the spectrum.

The resolution of a spectral estimator is closely related to the bandwidth of the spectral window. The bandwidth is a property associated with a spectral window used to measure the effective width of the spectral window. For example, the bandwidth of a rectangular spectral window would be the width of the window itself. For a non-rectangular spectral window shape, the bandwidth is usually defined in one of the following two ways:

1. The frequency interval between the half power points in the spectral window.

2. The width of a rectangular spectral window which gives the same mean square value as the spectral window in question.

The bandwidth of the spectral window determines the resolution capability of the spectral estimator. For this reason, resolution and bandwidth are often used synonymously.

It was shown earlier how a single spike in the spectrum (sine wave) is spread out in a broader peak (leakage) due to the finite window width in the time domain. If the spectrum contains two narrow peaks closer together than the bandwidth of the spectral window, the resulting broad peaks in the estimated spectrum overlap and may form a single peak. In this case, it is said that the estimator has failed to resolve the peaks.

It is clear that the bandwidth will be different for different window shapes. It also depends on the definition used. For simplicity, in practical computations an approximate value of resol-

ution or bandwidth is normally used [45] for discrete data. For the correlogram method, the approximate resolution or bandwidth is given by

$$B = \frac{1}{\tau_m} = \frac{1}{m\Delta t} \tag{3.25}$$

where m is the maximum lag number and τ_m is the maximum time delay value in the autocorrelation computation.

The approximate resolution or bandwidth for the periodogram method is given by

$$B = \frac{1}{T} = \frac{1}{N\Delta t} \tag{3.26}$$

where T is the total record length, N is the number of data, and Δt is the time interval between data points.

3.4.6 Statistical Errors

Statistics of spectral estimators describe the behavior of spectral estimators when applied to a stochastic signal. Statistical error, as opposed to instrument error, is the uncertainty in measurements due to the amount of data gathered, the underlying probabilistic nature of the data, and the method used in estimating the desired parameter.

Two important definitions used in describing an estimator are bias and consistency. Suppose that a parameter ϕ is being estimated and the estimate of ϕ is $\hat{\phi}$. Such an estimator is unbiased if

$$E\left[\hat{\phi}\right] = \phi \tag{3.27}$$

where $E[\ ]$ denotes the expectation operator.

The mean square error of the estimate is defined by

$$Mean\ Square\ Error = E\left[\left(\hat{\phi} - \phi\right)^2\right] \tag{3.28}$$

The estimate $\hat{\phi}$ will usually be a function of the record length T. If $\hat{\phi}$ is a consistent estimate of ϕ , then

$$\lim_{T\to\infty} E\left[\left(\hat{\phi} - \phi\right)^2\right] = 0 \tag{3.29}$$

This implies that as the record length becomes larger, the mean square error tends to decrease. It should be noted that the mean square error defined here is the same as the variance and these two terms will be used interchangeably.

The statistics of the periodogram method is considered first. Jenkins and Watts [42] show that the spectral estimator, $\hat{S}(f)$, in the periodogram method is asymptotically (in the limit of infinite record length) unbiased. They also show that the variance is given by

$$var\left[\hat{S}(f)\right] = \sigma^2 = [S(f)]^2 \tag{3.30}$$

where $\hat{S}(f)$ is the estimate of the actual spectrum $S(f)$. It follows that the relative error is

$$\varepsilon = \frac{\sigma}{S(f)} = 1 \tag{3.31}$$

Thus, the rms fluctuations in the estimated spectrum are as large as the mean level of the spectrum itself, a very unsatisfactory result.

Another important relation connecting the relative error to the bandwidth and the record length is given in Newland [43] and Otnes and Enochson [45] as,

$$\varepsilon^2 = \frac{1}{BT} \tag{3.32}$$

where B is the bandwidth and T is the record length. Equation 3.32 is a general relation applicable to any spectral estimation method. It can be seen easily that Eq. 3.32 reduces to Eq. 3.31 for the periodogram method.

3.4.7 Averaging

There are two common methods in use to obtain consistent spectral estimates:

1. Ensemble average independent estimates of the spectrum based on non-overlapping data segments. This technique can be viewed as doing the experiment many times, and can be implemented by subdividing a long record into smaller segments.

2. Use the fact that the estimates at different frequencies are uncorrelated when separated by more than the resolution of the spectral estimation procedure and average over adjacent frequencies. This process is also called smoothing.

The rate of convergence due to the first method is the same as that for any ensemble averaging process. It can be shown that for a spectrum computed by averaging N independent samples, Eq. 3.31 becomes,

$$\varepsilon = \frac{1}{\sqrt{N}} \tag{3.33}$$

This makes the estimate consistent in that by increasing the number of averages, the relative error can be made as small as necessary. The second method of averaging increases the effective bandwidth and as a result, the relative error decreases (Eq. 3.32).

Frequently a combination of the two methods is used. For example, the spectra may be ensemble averaged first and then the neighboring estimates may be averaged to yield the final spectrum.

3.4.8 Bias

The method of averaging over adjacent frequencies effectively increase the bandwidth and decrease the resolution. Besides reducing the ability to resolve sharp features, this method also introduces a bias error. Jenkins and Watts [42] show that the bias error can be related to the curvature of the spectrum. The bias error increases with the extent of the curvature of the spectrum inside the spectral window. If the spectrum is constant inside the spectral window, unbiased estimates are obtained even for large spectral windows. This places a constraint on the maximum bandwidth that can be used.

3.5 Spectral Analysis of Non-Uniformly Sampled Data

Traditionally, spectrum estimation has always been done on periodically sampled data. One reason behind this was computational efficiency, as FFT algorithms can be effectively utilized which make near real-time measurements more readily attainable because of the speed of the FFT algorithms. Signals to be analyzed were mostly analog in nature and a periodic sampling to digitize the signal was convenient.

Unfortunately in the case of LDV signals from a burst type counter processor, the data arrive in a random fashion corresponding to the random arrival of scattering particles in the measurement volume. The standard methods of estimating the spectrum cannot be used with such randomly distributed data.

To illustrate the differences and to give an idea of the difficulties involved with randomly sampled data, two figures showing representative samples of uniformly sampled and randomly sampled data are presented.

Figure 3.4 shows an example of a uniformly sampled time series. This time series was obtained by periodic sampling from a hot wire anemometer output. The form of the time series and the details of the fluctuations can be followed very easily. In comparison, Fig. 3.5 shows an example of a randomly sampled data set. This time series was obtained from LDV measurements under the same circumstances as the hot wire data. In this case of randomly sampled data, some imagination is needed to visualize the nature of the fluctuations.

3.5.1 The Effect of Random Sampling on Aliasing

The effect of random sampling on spectral estimation has been investigated by statisticians since 1960 [47-50]. These investigations were mainly concerned with the establishment of conditions under which alias-free spectral estimation is possible. It was found that certain forms of random sampling may have some advantages in spectral computation.

The effect of various forms of random sampling on spectral aliasing was first studied by Shapiro and Silverman [47]. They showed that in the case of Poisson sampling, in particular, the spectral estimate is free from aliasing effects, irrespective of the average sampling rate. Other sampling schemes are also possible which have this property. This result was arrived at from a strictly theoretical analysis and is valid in an asymptotic sense (infinite amount of data). It should be noted that it is the time between individual samples which followed a Poisson distribution. The value of the random variable itself was assumed to follow a Gaussian distibution. Buetler [48] also presents similar results.

The theoretical result of Shapiro and Silverman that it is possible to obtain alias-free spectra is fundamental to spectral estimation for irregularly sampled data. This phenomenon is well

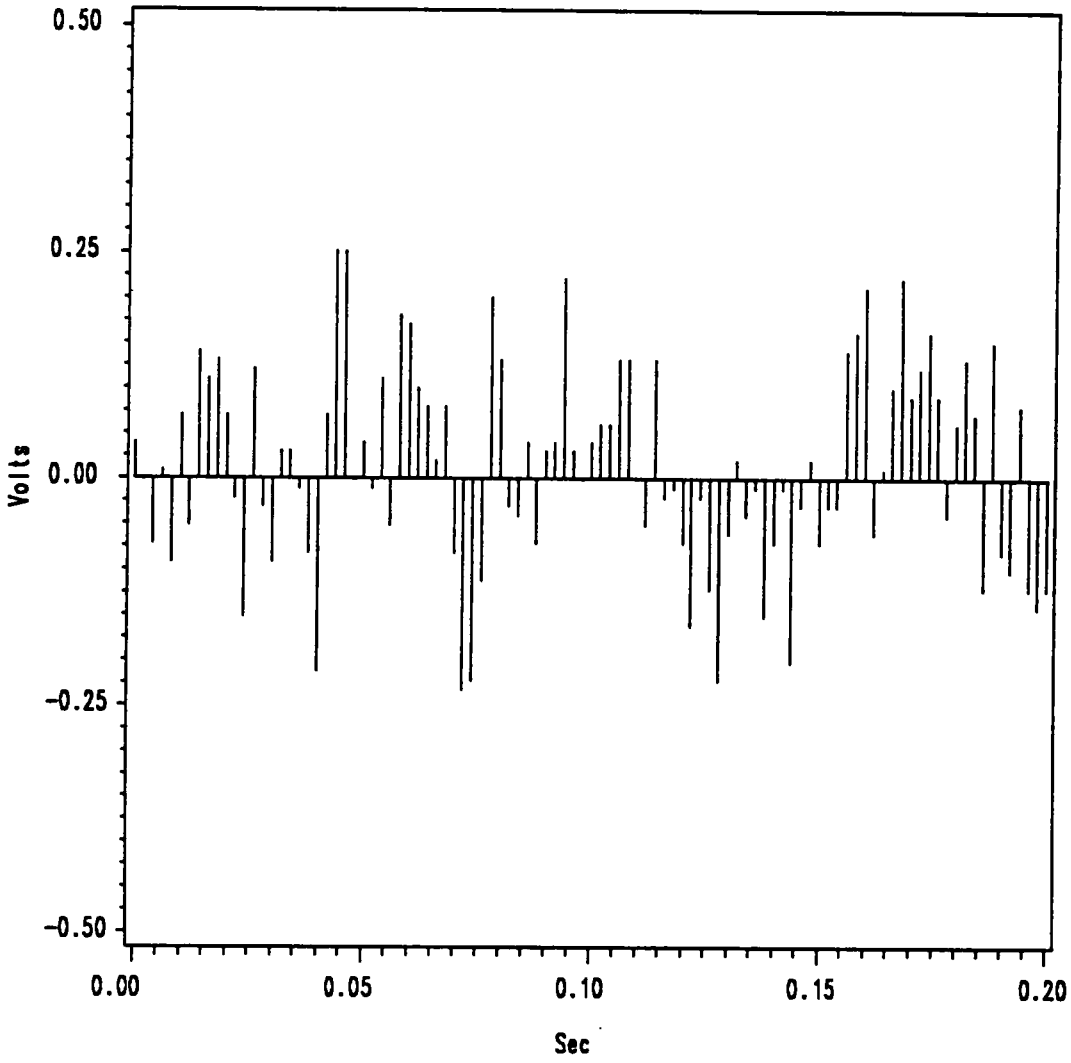

Figure 3.4. Uniformly Sampled Time Series

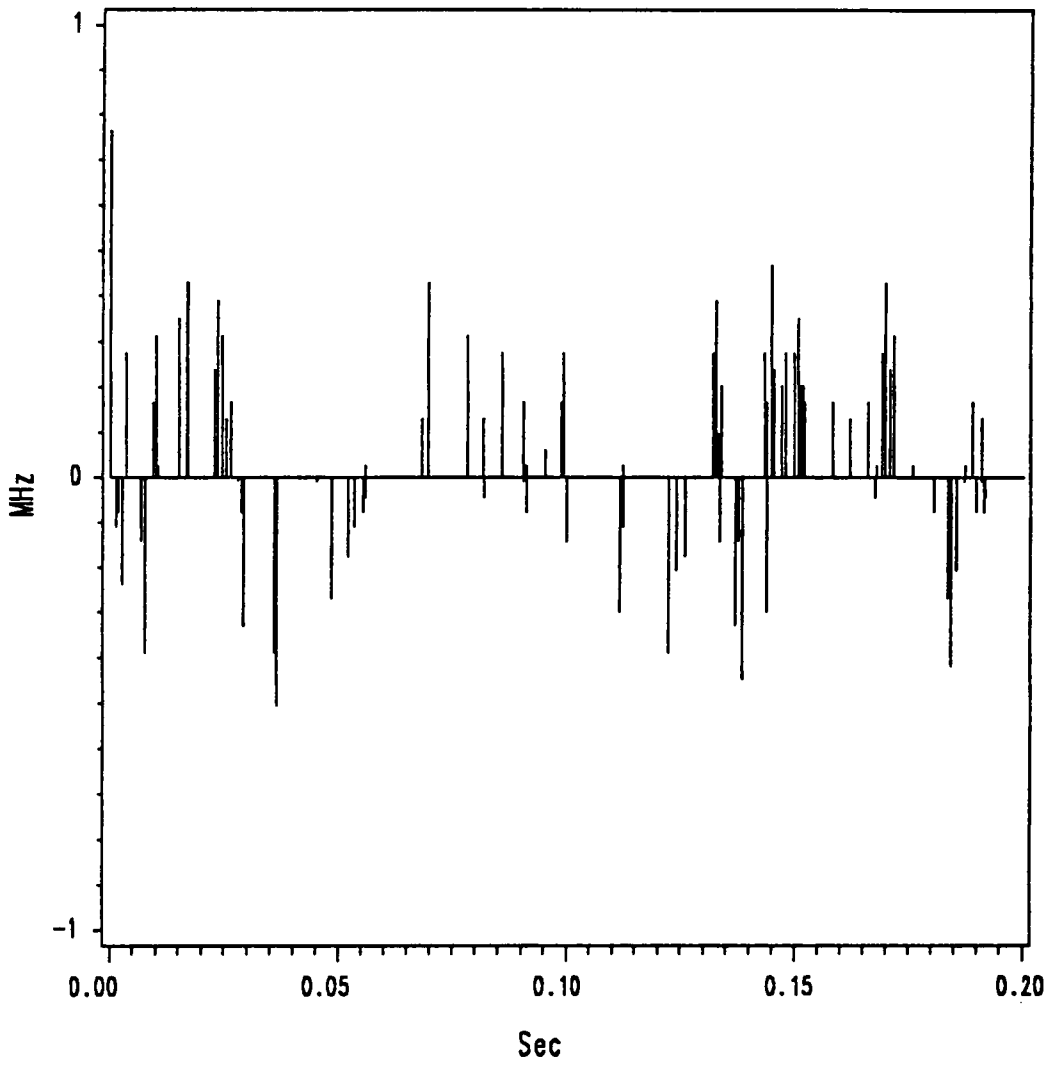

Figure 3.5. Randomly Sampled Time Series

accepted in the statistical literature, although it is surprising to find the problem of aliasing disappear. This is a major advantage of random sampling. On the other hand, it will be shown later that random sampling has the disadvantage of having higher variability in the spectral estimates.

Alias-free spectra is particularly important for LDV data. The maximum data rate obtainable from a well tuned LDV system is usually of the order of 1 KHz. If the data were uniformly sampled, aliasing would restrict spectral estimates to the Nyquist frequency, 500 Hz in this case. For LDV data, which is randomly sampled by nature, spectral estimates can be computed beyond the Nyquist frequency.

3.5.2 Poisson Distribution of LDV Data

In the literature, a Poisson distribution of LDV data is always assumed for theoretical analysis of the spectral estimators and their variances. Alias-free spectra may be calculated well beyond the Nyquist limit on the assumption that the data follows a Poisson distribution. A question can be raised as to the validity of such an assumption. From a statistical standpoint, it can be argued that the very nature of the process would lead to a Poisson distribution. A similar process exists in queing theory, which is successfully modelled using a Poisson distribution. A few investigations [51,52] have shown experimentally that the distribution indeed follows the Poisson distribution closely. The validity of this assumption for the data in this study is investigated in detail and the results are presented in Chapter five.

3.5.3 Performance of Interpolation in Spectral Analysis

Classically, a band limited signal can be sampled at a rate greater than twice the highest frequency contained in the signal (Nyquist criterion) and the characteristics of the continuous signal may be completely recovered (as far as the spectral information is concerned), by using

a linear interpolation filter [53]. The linear interpolator defined in [53] is not the normal linear interpolation, where the function is assumed to vary in a linear fashion between the two points in question. This interpolator is defined by a convolution of all the past values in the time series with a deterministic interpolator function chosen such that it minimizes the mean square error in reconstructing the continuous signal.

Thus it is tempting to try to reconstruct the continuous signal in the randomly sampled case by some form of interpolation. The resulting reconstructed signal then can be sampled periodically, thus avoiding all the difficulties associated with random sampling.

The subject of the error in reconstruction of the time history by interpolation from random samples have been theoretically studied by Leneman and Lewis [53]. They compared mean square errors for different interpolation schemes for three different sampling schemes, including the Poisson sampling. The mean square error for Poisson sampling was large for all the interpolating schemes for sampling rates lower than twice the Nyquist frequency. The errors became smaller as the sampling frequency became greater than twice the Nyquist frequency, but did not become zero (as it does for periodic sampling with an ideal linear interpolation scheme). Even for the best interpolation scheme, the mean square error became zero only after the sampling rate became greater than about six times the Nyquist frequency. This best interpolating scheme was called polygonal hold, which was essentially a linear interpolation between the present value and the next available value in time.

Other interpolation schemes had much larger mean square errors and approached zero only in the limit of infinite sampling frequency. Most important among these interpolation schemes was the sample and hold, which is usually utilized in many LDV systems with analog outputs. In the sample and hold interpolation scheme, the output is held at the present level until the next data arrives. Thus to obtain good spectra from sample and hold signals, a very high data rate is needed.

Adrian and Yao [54] investigated the spectrum obtained from simulated sample and hold signals. They show that the measured spectrum is filtered at the mean sample rate (that is, the process loses information at frequencies above the mean sample rate), and the spectrum contains a white noise spectrum caused by the steps in the sample and hold signal.

3.5.4 Spectral Estimators for Randomly Sampled Data

The traditional methods for spectrum estimation from periodically sampled data follow two basic approaches,

1. The autocorrelation approach, commonly known as Blackman-Tukey algorithm, computes the autocorrelation function first. The spectrum is then obtained by Fourier transforming the autocorrelation function.

2. The periodogram approach, where the data set is Fourier transformed directly. The square of the magnitude of the transform then gives an estimate of the spectrum.

The methods for spectrum estimation from randomly sampled data fall into one of these two categories. Three different methods were identified in the literature. They are,

1. Direct Transform Method (DTM)

2. Discretized Lag Product Method (DLPM)

3. Exact Lag Product Method (ELPM)

All three methods are extensions of the two approaches used in uniform time series work. The direct transform method is similar to the periodogram approach, while the other two methods follow the autocorrelation approach.

The first attempt to define a practical spectrum estimator for randomly sampled data was made by Jones [55,56]. He proposed a time discretizing technique which is very similar to the discretized lag product method. Jones [57] also investigated the effect of aliasing for randomly sampled data when no assumptions are made about the sampling scheme and showed that the random sampling introduced irregular side lobes away from the center of the spectral window.

Thompson [49] discussed a spectral estimator for randomly sampled data similar to the direct transform method. He neglected to subtract the estimate of a white noise term which arises from the random sampling process. Otherwise, he would have discovered the direct transform method proposed by Gaster and Roberts [58,59].

The discretized lag product method was first formally described and used independently by Mayo, Shay and Riter [60], Smith and Meadows [61] and Scott [62].

Gaster and Roberts [63] proposed the exact lag product method and showed that it has the advantage of being asymptotically unbiased. They also describe the discretized lag product method as a special case of the exact lag product method. The exact lag product method has the disadvantage of being extremely slow computationally.

Marquardt and Acuff [64] discussed a spectral estimator which they called a direct quadratic spectrum estimator. This method is very similar to the exact lag product method and will not be discussed separately here.

The spectral estimators for randomly sampled data are described in the following.

3.5.5 Discretized Lag Product Method

This method is similar to the correlogram approach for periodically sampled data. This method is presented in the literature as an algorithm without providing a rigorous theoretical basis by Mayo, et al. [60], Smith and Meadows [61] and Scott [62].

In the correlogram method, an estimate of the autocorrelation function is computed first. The Fourier transform of the autocorrelation function then gives an estimate of the spectrum. Since the data are uniformly sampled, estimates of the autocorrelation function in correlogram method are distributed uniformly in the time lag axis. On the other hand, for randomly sampled data, the estimates of the autocorrelation function are also randomly distributed along the lag axis. The basic idea of discretized lag product method is to form estimates of the autocorrelation function at uniformly distributed points.

In the discretized lag product method, an estimate of the autocorrelation function is first computed and then the spectrum is obtained by Fourier transforming the autocorrelation function. The autocorrelation estimate is formed by dividing the time axis of the autocorrelation function into equidistant intervals, called slots. The randomly sampled data, which consists of discrete points in time along with the time between samples, are then used to compute an estimate of the autocorrelation function. This is accomplished by forming the product of two data points, determining the time difference (lag) between them and then finding the time slot which best approximates the time difference or lag. The sum of these products at each slot is formed for all the data points and the average value of the lagged product within each slot is taken as an estimate of the autocorrelation function at the center of the time slot.

With estimates of the autocorrelation function at uniformly distributed points, one can treat these as if they came from a uniformly sampled data set. In fact, from this point on, the pro-

cedure for obtaining spectra from the autocorrelation function is exactly the same as the correlogram method.

It is useful to remove the mean from the data before any spectral computation is done. The steps involved in spectrum estimation using the discretized lag product method are outlined below :

1. Remove mean from the data.

2. Select maximum lag τ_m and lag increment Δt. The value of maximum lag is selected depending upon the resolution required. The resolution is given by,

$$B = \frac{1}{\tau_m} \tag{3.34}$$

The value of Δt chosen should satisfy the Nyquist criterion. Although theoretically Poisson sampled data should lead to alias-free spectra, the aliasing comes in because of the slotting of the correlation values. Hence the Nyquist criterion should be respected while choosing Δt . The Nyquist frequency is given by,

$$f_{Nyq} = \frac{1}{2\Delta t} \tag{3.35}$$

So now τ_m is divided into m slots of Δt each, where m is given by,

$$\tau_m = m\Delta t \tag{3.36}$$

3. An estimate of the autocorrelation function at a lag of $n\ \Delta t$ is formed by adding cross products between samples $x(t_i)$ and $x(t_j)$ separated by lag times $(t_j - t_i)$ falling in the range $(n\ \Delta t \pm \frac{1}{2}\Delta t)$ and counting the number of such products. The estimate of the autocorrelation function is then given by,

$$\hat{R}(n\,\Delta t) = \frac{1}{N_n} \sum_{i=1}^{N} \sum_{j=1}^{N} x(t_i)\, x(t_j), \qquad j > i \tag{3.37}$$

where, N_n is the number of products such that,

$$(n - 1/2)\,\Delta t < (t_j - t_i) < (n + 1/2)\,\Delta t$$

The summation is carried out over all possible lag products. This provides estimates of the autocorrelation function at uniformly distributed points. From this point on, the procedure is exactly the same as that for uniformly sampled data.

4. A window for the autocorrelation function is now selected. A common window is the Hanning window which is given by,

$$w(n) = \frac{1}{2}\left(1 + \cos\frac{\pi n}{m}\right) \tag{3.38}$$

A corrected autocorrelation function is now computed,

$$\tilde{R}(n\Delta t) = \hat{R}(n\Delta t)\; w(n) \tag{3.39}$$

5. The estimated spectrum is now obtained by Fourier transformation of the autocorrelation function. If the number of autocorrelation estimates are not too large, the estimated spectrum can simply be found by trapezoidal integration following Blackman and Tukey [46] as follows,

$$\hat{G}(f) = 2\,\Delta t \left[\tilde{R}_0 + 2 \sum_{r=1}^{m-1} \tilde{R}_r \cos(2\pi f r \Delta t) + \tilde{R}_m \cos 2\pi f \tau_m \right] \tag{3.40}$$

Here $\hat{G}(f)$ is the one-sided spectrum.

A standard set of frequencies at which spectral estimates are generated are given by,

$$f_k = \frac{k}{2m\Delta t}, \quad k = 0,1,...,m \tag{3.41}$$

The formula for calculating spectral estimates can also be written in a form suitable for computation as,

$$\hat{G}(f) = 2\Delta t \left[\tilde{R}_0 + 2 \sum_{i=1}^{m-1} \tilde{R}_i \cos \frac{\pi i k}{m} + \tilde{R}_m \cos \pi k \right], k = 0,1,...,m \tag{3.42}$$

3.5.6 Exact Lag Product Method

In the discretized lag product method, the values of the individual time intervals between successive samples are not used in the estimation of spectrum. The exact lag product method [58] uses the time information between samples. Instead of lumping the lag products into uniformly distributed slots as in the previous method, the exact lag values are used here in the computation.

Consider a record of length T containing N samples, $x(t_1)$, $x(t_2)$, ..., $x(t_n)$, where t_i are Poisson distributed. The products $x(t_i)\,x(t_j)$, $j > i$ can be regarded as estimates of the true autocorrelation function for lag $(t_j - t_i)$. Since the autocorrelation function is the expected or average value of the individual lag products, the individual lag products will scatter around the true autocorrelation function. The method estimates the spectrum from these individual autocorrelation estimates by a cosine transform (Eq. 3.6).

The two-sided spectral estimate can be written as,

$$S(f) = 2 \int_0^{\infty} R(\tau) \cos(2\pi f\tau) \, d\tau \tag{3.43}$$

where $R(\tau)$ is the autocorrelation function.

Introducing a window function, $w(\tau)$, which is non-zero in the interval $-\tau_m \leq \tau \leq \tau_m$, the spectral estimate becomes,

$$\hat{S}(f) = 2 \int_0^{\tau_m} \hat{R}(\tau) \, w(\tau) \cos(2\pi f\tau) \, d\tau \tag{3.44}$$

The limits of integration are 0 to τ_m because $w(\tau)$ is zero outside the maximum lag τ_m.

The estimate for the autocorrelation function for positive lag values can be written as,

$$\hat{R}(\tau) = \frac{1}{T-\tau} \int_0^{T-\tau} x(t) \, x(t+\tau) \, dt \tag{3.45}$$

where $x(t)$ is the continous process from which the samples $x(t_i)$ has been obtained.

Now substituting Eq. 3.45 into Eq. 3.44 gives a double integral in terms of the time t and the lag τ .

$$\hat{S}(f) = \frac{2}{T-\tau} \int_0^{\tau_m} \int_0^{T-\tau} x(t) \, x(t+\tau) \, w(t) \cos(2\pi f\tau) \, dt \, d\tau \tag{3.46}$$

The lagged products $x(t) \, x(t+\tau)$ can be replaced by the products $x(t_i) \, x(t_j)$ for a lag of $\tau = t_j - t_i$. Gaster and Roberts [63] have shown that the individual correlation estimates have

a uniform distribution along the lag axis when samples are Poisson distributed. Hence, they argued that the integral can be replaced by a summation multiplied by the mean spacing of the autocorrelation estimates. On the basis of the preceding arguments, Eq. 3.46 is directly extended for discrete data (without any rigorous basis) to give the exact lag product estimator as,

$$\hat{S}(f) = \frac{2}{\lambda^2 T} \sum_{i=1}^{N} \sum_{j=1}^{N} x(t_i)\, x(t_j)\, w(t_j - t_i)\, \cos[2\pi f (t_j - t_i)], \quad j > i \tag{3.47}$$

where λ is the mean sample rate and T is the total record length. The summation is carried out over all possible lag products with $j > i$.

Equation 3.47 differs from the form given by Gaster and Roberts [63] by a factor of 2π because of the use of cyclic frequency rather than angular frequency.

The factor $1/\lambda^2 T$ in Eq. 3.47 is equivalent to the mean spacing of the autocorrelation estimates, i.e., the mean value of $d\tau$. This can be seen from the fact that the average number of data points in T is given by λT . Also for each data point, $\lambda \tau_m$ lag products can be formed on the average. Hence, the total number of lag products (on the average) in T with a maximum lag τ_m is $\lambda^2 T \tau_m$. So the mean spacing of the autocorrelation estimates is given by $1/\lambda^2 T$.

An advantage of this method is that because 'zero lag' products are not used in the computation, spectral estimates generated by this method are insensitive to any white noise which may be added to the signal.

The major disadvantage of this method is that it is very slow because of the necessity of computing a cosine function for each lag product.

3.5.7 Direct Transform Method

The previous methods of spectral estimation were based on the cosine transformation of the estimated autocorrelation function. Here an estimator is given based on direct Fourier transform of the sampled data, or rather short blocks of the data. It is analogous to the periodogram approach for periodically sampled data.

In the periodogram approach, a spectral estimate is given by,

$$\hat{S}(f) = \frac{1}{T} \left| \int_0^T x(t)\, w(t)\, \exp(-j2\pi ft)\, dt \right|^2 \tag{3.48}$$

For discrete instants of time, not necessarily uniformly distributed, one can write,

$$\hat{S}(f) = \frac{1}{T} \left| \sum_{i=1}^{N} x(t_i)\, w(t_i)\, \exp(-j2\pi ft_i)\, \Delta t_i \right|^2 \tag{3.49}$$

where $\Delta t_i = t_{i+1} - t_i$.

This equation is equivalent to Eq. 3.18 for uniformly sampled data when the sample times are equally spaced and same windows are used.

For random sample times with a Poisson distribution, Gastor and Roberts [58] suggest a spectral estimate by replacing Δt_i by the mean time interval $\Delta t = \frac{1}{\lambda}$ where λ is the average sampling rate. This spectral estimate is then given by,

$$\hat{S}(f) = \frac{1}{\lambda^2 T} \left| \sum_{i=1}^{N} x(t_i)\, w(t_i)\, \exp(-j2\pi ft_i) \right|^2 \tag{3.50}$$

Gaster and Roberts [58] show that this estimator is biased by a constant amount (asymptotic value). A true estimate is given by, subtracting the bias term from Eq. 3.50 as,

$$\hat{S}(f) = \frac{1}{\lambda^2 T}\left[\left|\sum_{i=1}^{N} x(t_i)\, w(t_i)\, \exp(-j2\pi f t_i)\right|^2 - \sum_{i=1}^{N} x^2(t_i)\, w^2(t_i)\right] \tag{3.51}$$

This method has the disadvantage of having a high variance. To reduce the variability, the authors suggested the use of ensemble averaging over short blocks of data. This is a common practice for uniformly sampled data, and it is applicable here also.

In a later paper [59], Gastor and Roberts examined ways to reduce the variability of this method. They found that subtracting the mean of the data block from each data point in the block prior to computing the transform reduces the variability.

3.5.8 Statistics of the Estimators

The exact lag product method is considered first. Gaster and Roberts [63] have assumed that $x(t)$ is normally distributed and the record length T is large to calculate the mean and variance of this estimator. Their results show that the estimator is unbiased and alias-free. The version of the estimator used by Gaster and Roberts used a Hanning window function with maximum lag $\tau_m = t_k - t_j$. They evaluated the variance of the exact lag product estimator with the Hanning window function for the asymptotic case where the maximum lag time, τ_m , is much larger than the integral scale of the autocorrelation function. The variance is given approximately by,

$$var\left[\hat{S}(f)\right] = \frac{3\tau_m}{4T}\left[S(f) + \frac{R(0)}{\lambda}\right]^2 \tag{3.52}$$

where $R(0)$ is the autocorrelation value at zero lag and λ is the mean sample rate.

A factor of 2π has been deleted in the denominator of the second term inside the brackets in Eq. 3.52 to make the result compatible with the definition of the spectrum used here. The factor $3\tau_m/4$ arises from the Hanning window and is the inverse of the bandwidth of the Hanning window (calculated by the second method in Section 3.4.5).

Masry and Lui [66,67] also have derived a formula similar to Eq. 3.52 for the variance of the exact lag product estimator.

The variance of $\hat{S}(f)$ obtained by the correlogram method for uniformly sampled data with a Hanning window is given by Blackman and Tukey [46] as,

$$var\left[\hat{S}(f)\right] = \frac{3\tau_m}{4T}\left[S(f)\right]^2 \tag{3.53}$$

Thus the effect of random sampling is an increase in the variance of the spectral estimates. A comparison of Eqs. 3.52 and 3.53 shows that the second term of Eq. 3.52 inside the brackets can be interpreted as arising from the random sampling and approaches zero for high data rates. It should also be noted that the this term will dominate when spectral levels are low.

For the special case when the spectral level is small, the variance approaches,

$$var\left[\hat{S}(f)\right] = \frac{3\tau_m R(0)^2}{4T\lambda^2} \tag{3.54}$$

The direct transform estimator was analyzed by Gaster and Roberts [58]. They show that the estimator is asymptotically unbiased. The variance of the direct transform estimator for large data collection time was derived by Gaster and Roberts and is given by,

$$var\left[\hat{S}(f)\right] = \left[S(f) + \frac{R(0)}{\lambda}\right]^2 \tag{3.55}$$

The corresponding result for uniformly sampled data using the periodogram method is derived in Jenkins and Watts [42] as,

$$var\,[\hat{S}(f)] = [S(f)]^2 \tag{3.56}$$

Thus it is seen that the variance is increased by the random sampling in this method as well. The extra term due to random sampling is the same as that obtained for the exact lag product estimator.

The variance given by Eq. 3.55 is very high. As in the periodogram method, this estimator is also inconsistent. That is, the variance does not decrease as the record length is increased. To reduce the variability, some sort of averaging procedure must be used with this method. Usually the total record is divided into short blocks and the estimates from each block are ensemble averaged.

Unlike the two earlier estimators, the discretized lag product method produces an estimate of the autocorrelation function. The properties of the autocorrelation estimate have been studied by Scott [62]. He showed that the autocorrelation estimates are asymptotically (vanishing slot width) unbiased and consistent.

By applying the slotting technique to simulated data, it has been shown by Gaster and Roberts [63] that the slotting procedure does not significantly influence the validity of the variance formula given by Eq. 3.52.

Mayo, et al. [65] used the low data rate assumption to derive an expression for the variance of the discretized lag product method. This result is presented in reference 65 for a Bartlett window for the case when spectral level is small as,

$$var\left[\hat{S}(f)\right] = \frac{2\tau_m}{3\lambda^2 T}\,[R(0)]^2 \tag{3.57}$$

Noting that the bandwidth of the Bartlett window is $3/2\tau_m$ as opposed to the bandwidth of the Hanning window, $4/3\tau_m$, it is clear that the variances for the exact lag product estmator (Eq. 3.52) and the discretized lag product estimator (Eq. 3.57) are the same when spectral level is very small (approaches zero).

The variance formula (Eq. 3.57) was verified for simulated data by Mayo, et al. [65] and Gaster and Roberts [63] for regions of the spectrum where the spectral level is close to zero.

4.0 Experimental Methods

4.1 Scattering Volume Location

Accurate positioning of the scattering volume is essential in reducing experimental uncertainty. It is even more important in the case of a complex flow field like the junction vortex flow, where large velocity gradients are present. Inaccuracies in locating the scattering volume can lead to poor repeatability of data and large uncertanties in the measured data and the results.

The technique used in the present experiments for positioning the scattering volume utilized a small pinhole drilled into a square positioning block. Two edges of the square block were used as reference edges. The pinhole was located at a distance of 38.10 mm (1.5 in.) from the two reference edges and was 0.20 mm in diameter. Since the nominal diameter of the scattering volume is 0.15 mm, all the laser beams would easily pass through the pinhole if the scattering volume coincides with the pinhole location. A small error in positioning would result if one of the beams was being blocked.

To position the scattering volume, the positioning block was placed at the corner formed by the body leading edge and the wind tunnel floor, i.e., at the origin of the coordinate system in Fig. 2.1. The scattering volume was then positioned until all the laser beams entered the pinhole and exited from the other side unobstructed. This position (-38.1 mm, 38.1 mm) was used as a reference in locating all other measurement positions.

The traverse system for positioning the scattering volume used two dial indicators, with a least count of 0.025 mm. With this technique, an accuracy of ± 0.1 mm in locating the scattering volume was achieved.

4.2 Non-Dimensionalization

All the velocity and turbulence data presented in this report was non-dimensionalized with the speed at the throat of the wind tunnel used as the reference velocity.

4.3 Throat Speed Measurement

The speed at the throat of the wind tunnel was used both as a reference velocity in non-dimensionalizing and to set the tunnel speed in order to maintain dynamic similarity.

The air speed at the throat was measured using a 1.6 mm diameter pitot-static tube positioned at the center of the throat. The dynamic pressure obtained from the pitot-static tube was read off a Datametrics digital manometer. The air speed was then computed using Bernoulli's equation,

$$V_* = \left(\frac{2Q_*}{\rho_\infty} \right)^{1/2} \tag{4.1}$$

where Q_* is the dynamic pressure, V_* is the speed at the throat of the wind tunnel, and ρ_∞ is the density of air at room temperature and pressure.

4.4 Determination of the Half-Angle for LDV

The half-angle between the laser beams needs to be measured for the calculation of the velocity from the Doppler frequency from Eq. 2.4. The half-angle was computed by directing the

laser beams onto a wall of the laboratory approximately 2.5 m away from the scattering volume. From the separation of the beams on the wall, the half-angle was then computed.

4.5 Spectral Analysis

The data acquisition from the LDV was performed by a DEC PDP11 microcomputer running a program called DRP3. DRP3 is a commercially available software package marketed by TSI Inc. Besides collection of data, this program can also perform statistical analysis of data and display results graphically. The software needed for the subsequent spectral analysis of the data were developed by the author.

The spectrum at each measurement point was calculated using 512,000 data points. The data was collected in fifty sets of 10,240 points each and stored on the system disk. The raw data stored by DRP3 consisted of the Doppler frequency and the time between data points. The raw data were further processed to calculate the velocity. The velocity and the time information was ultimately stored in a binary format to save disk space and subsequent file transfer time. These data files were then transferred to the IBM mainframe computer for spectral analysis.

Before any spectral analysis, the data was preprocessed to remove the mean and flag any data point with erroneous time information. A point with an erroneous time information results from the following reason. The time between data points was counted with an internal clock in the data collection unit (TSI 1998A perepheral interface), and had a maximum count of 4095. The least count corresponding to each tick of the clock was user selectable, and had a value of 2^N, where N could be selected from a range of 0 to 12. If the true time between two data points was larger than the maximum time that the clock could count, the counter stopped at 4095 and this value may not be the true time between data points. The least count of the clock was carefully selected during the experiments so that the number of data points with such erroneous time between data points was kept to a minimum. Typically about 5-10 bad

points were found in a set of 10,240 data points. Whenever a bad data point was found, appropriate actions were taken (discussed later) in the spectral computations.

The least count of the time between data points was usually selected to be 8 microseconds. This was determined by the data rate (which was usually in the range of 250-800 Hz) and the maximum count of the clock (4095). Because of the least count, a few data points would be found in each data set with time between data points equal to zero. Such data points were discarded, as if they were never measured.

Spectra were calculated by using both the discretized lag product method and the direct transform method. The exact lag product method is known to be computationally very slow but had the advantage of being unbiased and theoretically more accurate than the discretized lag product method. The exact lag product method was tried in two cases and the resulting spectra compared with the spectra obtained by the other two methods. It was found (see Chap. 5.8) that the exact lag product method did not offer significant improvements in the spectral estimates to justify its use.

4.5.1 Discretized Lag Product Method

A few parameters needed to be chosen before any spectral analysis could be conducted. The maximum lag time up to which autocorrelation estimates are to be computed was selected depending on the resolution of the spectrum required. A value of τ_m corresponding to an approximate resolution of 5 Hz was decided to be sufficient. Using Eq. 3.25, this required a value of τ_m equal to 0.2 seconds.

The value of the slot width, Δt, has important effects on the estimated spectrum. Scott [62] has shown that the estimates of the autocorrelation functions are biased for finite values of the slot width and vanishes as the slot width tends to zero. This biasing effect is a direct consequence of the fact that the errors in the time domain in estimating the autocorrelation function were

of the order of $\pm \Delta t/2$. This bias error due to the excessive slot width results in aliasing of the spectra (similar to the periodic sampling case) and uncertainties in the high frequency end of the computed spectrum.

In order to keep the bias error small, the slot width should be kept much smaller than the mean time interval between the data points. But the slot width cannot be made as small as possible and a lower limit is enforced by the requirement that there must be enough lag products in each slot in order to get a meaningful average. Thus the slot width has to be much larger than the minimum time observed (least count) between the data points.

After some preliminary experimentation, it was found that a value of the slot width of 128 or 256 microsecond gave the best results.This conclusion was based on a qualitative comparison of the spectra. It should be noted that this value is dependent on the data rate and corresponded to a data rate of about 250-800 Hz.

The computation of the autocorrelation estimates using the discretized lag product method proceeded as follows. Starting with the first data point, a buffer of data points up to the maximum lag time, τ_m, was read in. All possible lag products with the first data point were then calculated. The first data point was then removed from the buffer and the next data point in time became the first data point in the buffer. Additional data points were read to the buffer as needed to maintain a series up to the maximum lag time. All possible lag products were again computed with the current first data point. This process was continued for all the points in the data set. If a bad data point with erroneous time between data was found, all lag products calculated from the data points for a time lag of τ_m before the bad data were discarded. The estimation process started again with the next data point following the bad data.

Once the autocorrelation estimates were formed, a Hanning window was applied to the autocorrelation estimates and the spectra was computed using Eq. 3.42.

Zero lag products have special effects in spectral estimation from randomly sampled data. It has been shown in George, et al. [68] that as a consequence of the random sampling of the data, the autocorrelation function has a spike at the origin, and consequently the estimated spectrum has a white noise term added to it. George, et al. [68] suggested that this problem can be avoided by simply ignoring the zero lag terms in the spectral computations.

Srikantaiah and Coleman [69] have also shown the presence of the white noise term. Their results also show that better estimates are obtained by omiting the zero lag terms. To avoid the increased white noise, the zero lag terms were always omitted from the spectral computations reported here.

For the discretized lag product method, the total amount of data (512,000 points) was divided into 5 subsets of 102,400 points each. The spectrum was calculated from each subset separately and the average of the five subsets was taken to yield the final spectrum. This procedure was arrived at after comparing results from averages of subsets of different lengths.

4.5.2 Direct Transform Method

To generate spectral estimates using the direct transform method, the total data set was divided into short blocks, and the resulting spectral estimates from each block were then ensemble averaged. The length of the blocks, T, was determined to correspond to an approximate resolution of 5 Hz using Eq. 3.26.

A block of data points having a length of T was first read in. All the data points in the block were then checked for any bad data, i.e., a data point with erroneous time information. If any bad data was present, the entire block was discarded. Once an error-free block of data was found, the mean value for the block was computed and the block mean was subtracted from each data point. This procedure reduces the variability of the spectral estimates as shown by Roberts and Gaster [59]. A Hanning window was then applied to the data and spectral es-

timates were generated for this block using Eq. 3.51. This procedure was repeated for all the blocks and the resulting estimates were ensemble averaged.

4.5.3 Normalizing of the Spectra

In order to be able to compare spectra obtained from different methods or different data sets, the spectra needs to be normalized. Three methods of normalizing the spectra were considered,

1. Set area under the spectrum, that is, the total energy equal to one.

2. Normalize by dividing by the maximum value of the spectrum.

3. Normalize by dividing by the total energy in the spectrum.

The second method of normalization was used throughout this report as it was found to be the most convenient to use.

4.5.4 Octave Averaging

Averaging of the adjacent spectral estimates is often done to improve the appearance of the spectra at the cost of the resolution. For logarithmic plots, the averaged estimates should be logarithmically placed to avoid crowding in the higher frequency regions. Averaging over frequency octaves is used in such a case. In lower frequencies, fewer estimates are averaged whereas in higher frequencies larger number of estimates are averaged.

An one-third octave spacing of averaged estimates is often used. According to one-third octave spacing, the frequency limits of the n^{th} interval can be written as,

$$f_1\, 2^{(n-1)/3} \;\leq\; f_n \;\leq\; f_1\, 2^{n/3} \tag{4.2}$$

where f_1 is the lowest frequency and f_n is the frequency of the n^{th} interval.

The estimates which fall inside this interval are averaged and are assumed to correspond to the midpoint of the interval.

4.6 Vortex Shedding Flow

In order to gain confidence in the spectral estimation methods, it was decided to test their ability to resolve dominant frequencies in a spectrum of velocity fluctuations. The classic example of such a flow field is the vortex shedding flow behind a cylinder. This flow was investigated for its spectral content by using both LDV and a hot wire system.

The experimental arrangement consisted of a wooden cylinder, 7.62 mm (0.3 in.) in diameter, supported horizontally between two stands 203.2 mm (8 in.) apart. The height of the cylinder axis above the wind tunnel floor was 133.5 mm (5.25 in.). This placed the cylinder well outside the boundary layer on the floor. Measurements were taken downstream of the cylinder at a point located 44.5 mm (1.75 in.) behind the cylinder axis and at a height of 133.5 mm (5.25 in.) from the wind tunnel floor. The experimental arrangement for the vortex shedding flow is shown in Fig. 4.1. The selection of the measurement point was arbitrary.

The LDV and the hot wire systems were set up to measure only the u-component of the velocity. So the computed spectrum reflects the fluctuation characteristics of the u-component of the velocity. It should be noted here that the hot wire is sensitive to the velocities in the other directions also and probably measures a combination of all the velocity components.

4.7 Calibration of the Hot Wire

A single tungsten 1.5 micron dia. hot wire (TSI probe 1210-T1.5) was used for the present experiments. The hot wire was carefully calibrated in the free jet of the calibration wind tunnel

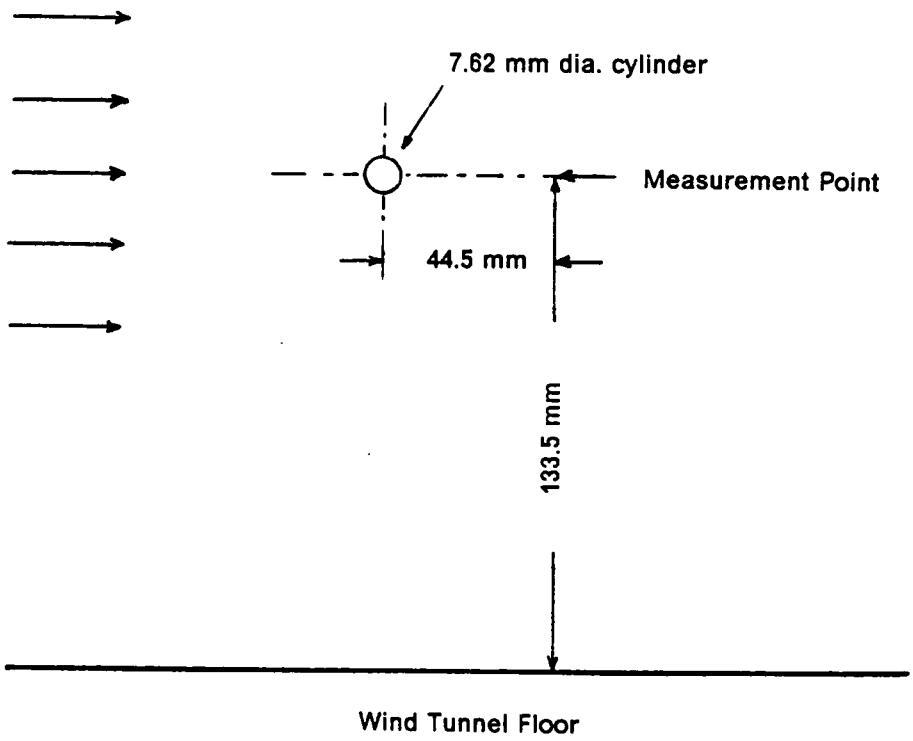

Figure 4.1. Experimental Arrangement for Vortex Shedding Flow

using a 3.18 mm United Sensor Kiel probe to measure the dynamic pressure. The Kiel probe was positioned near, but not too near, the hot wire to be calibrated. The speed was given by,

$$V = \sqrt{\frac{2RT_\infty Q}{P_\infty}} \tag{4.3}$$

where $Q = P_k - P_\infty$, and P_k is the Kiel probe pressure. The dynamic pressure in Eq. 4.3 was measured by a Datametrics model 1400-9AX digital manometer.

The output voltage from the DISA 55M10 constant temperature anemometer bridge was measured by a DISA 55D31 digital voltmeter. The calibration function used for the calibration method was given by,

$$E^2 = A + Bu^n \tag{4.4}$$

where E is the output voltage from the anemometer and u is the velocity. A, B, and n were taken as constants.

The exponent n obtained from the calibration process was used to set the parameters of a DISA 55M25 linearizer which was connected at the output of the bridge. Figure 4.2 shows the final calibration curve for the linearized voltage versus the velocity.

The output from the hot wire system was low-pass filtered at 2 kHz to prevent aliasing effects by a DISA 55D26 signal conditioner before spectral analysis. The filters in the signal conditioner had a rolloff of 18 db/octave. The sampling rate was set at 5 kHz and the spectral analysis was performed by a DATA 6000 signal analyser.

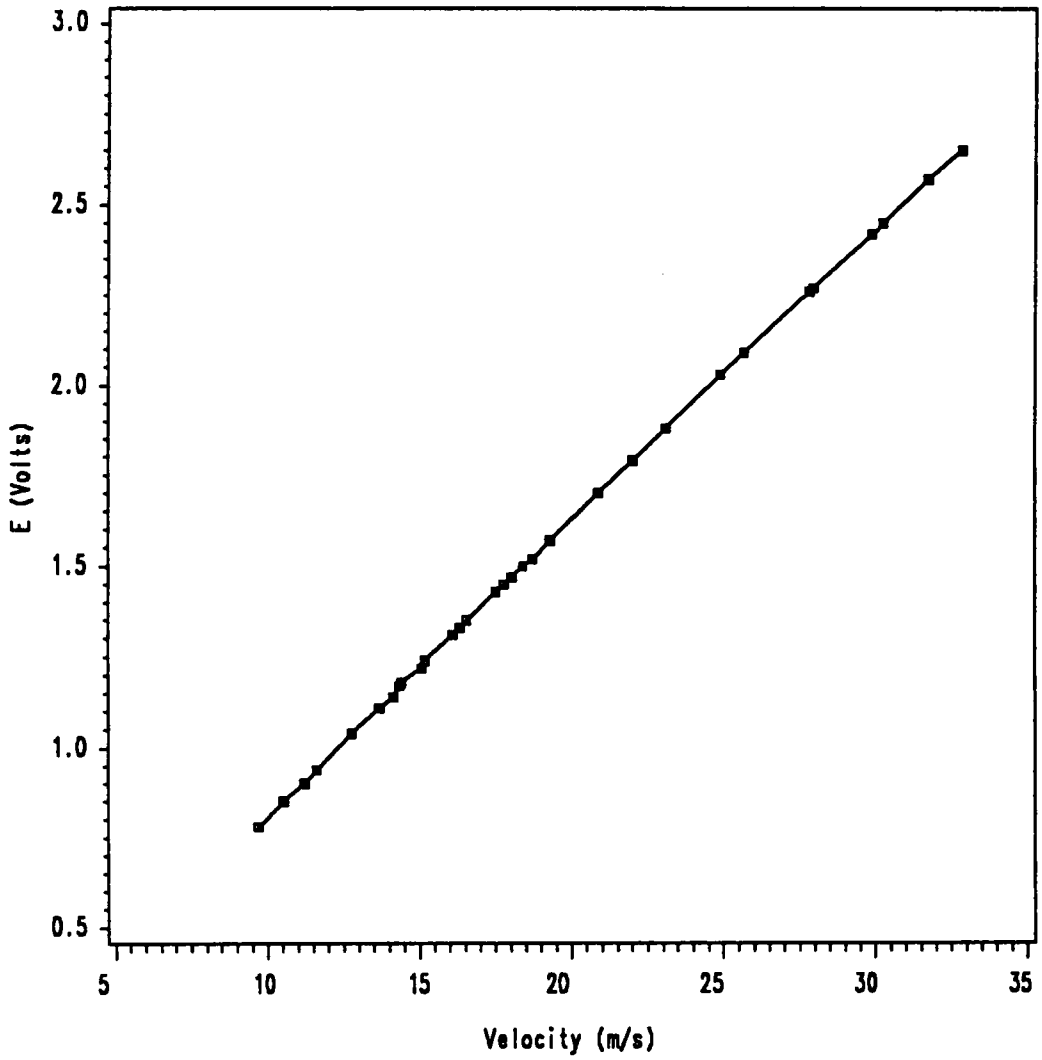

Figure 4.2. Calibration Curve of Hot Wire

5.0 Performance of Spectral Analysis Methods

5.1 Review

The spectral analysis methods for randomly sampled data have been applied on simulated data by several investigators [51-52,58-63]. Applications of these methods for real LDV data have been limited. Roberts, et al. [51] used the direct transform method to obtain spectra on the centerline of an air jet of diameter 25.4 mm, at one diameter downstream from the mouth of the jet. Two LDV data sets of 24,000 points each with average sampling rates of 147 and 1115 samples per second were used. The computed spectrum from LDV data was compared with spectra obtained from hot wire signal and good agreement was found. It was noted that their spectral estimates were given up to a maximum frequency of about 60 Hz for the data set with the average sampling rate of 147 samples/sec and up to a maximum frequency of about 600 Hz for the data set with average sampling rate of 1115 samples/sec. Spectral estimates were presented only at a few discrete points in these two cases.

Smith and Meadows [61] used the discretized lag product method to obtain spectra from LDV data for a jet excited by a loudspeaker at frequencies of 850 and 4400 Hz. They show computed spectral estimates up to a maximum frequency of 50 kHz. The spectra show the peak expected corresponding to the exciting frequencies but had significant levels of noise elsewhere. An additional spectrum was presented on the centerline of an unexcited jet using the discretized lag product method. Comparisons were made in this case with spectra obtained from a hot wire and good agreement was found. The spectrum was computed up to a maximum fre-

of 20 kHz and had relatively small variances everywhere. The amount of data used and the average sampling rates were not mentioned.

Scott [62] obtained spectra from LDV data for a free jet, six diameters downstream from the mouth of the jet, using the discretized lag product method. Comparisons were made with spectra computed from hot wire data and good agrrement was found. The presented spectrum was smooth, with little variance. His data sets contained 45,000 points and the spectrum was shown up to 9 kHz. He does not mention the average sampling rate for the data set.

Srikantaiah and Coleman [69] also obtained LDV spectra for MHD flow, using both the discretized lag product and the direct transform methods. He analyzed two data sets of 100,000 points each with average sampling rates of 107 and 796 samples/sec to obtain the spectra. He reported spectral estimates up to 1000 Hz and mentions that non-negative estimates only up to the mean sampling frequency were found for both the methods.

Reis, et al. [70] used the discretized lag product method to obtain spectra from LDV data in an MHD flow. They show spectra computed from two data sets with average sampling rates of 8 kHz and 1.8 kHz. Each data set contained 90,000 points. They show spectral estimates up to 16 kHz for the data set with average sampling rate of 8 kHz but after about 2 kHz mostly noise-like spectra were obtained. Similarly spectral estimates were shown up to 4 kHz for the data set with average sampling rate of 1.8 kHz, but after about 1 kHz mostly noise-like spectra were obtained.

Saxena [71] shows spectra computed from LDV data using the discretized lag product method for the swirling flow in a cylinder and the flow near the spark plugs of an engine during intake. For the swirling flow, the spectrum was shown up to 300 Hz and showed noisy spectra away from the peak corresponding to the swirling frequency. For the other case, spectra were shown up to 5 kHz, but were noisy after about 1.5 kHz. He does not report any details about the parameters used in the spectral estimation.

5.2 Tests of the Spectral Estimation Methods

It was felt that there was a need for a comprehensive study of the performance of the spectral estimation methods, when applied to real data. The results obtained from the different methods of spectral analysis for randomly sampled data are compared in this chapter. The performance of the various methods are investigated in detail to compare their performance. The methods have been tested under both simulated and real flow situations. Tests have been performed under the following situations:

1. Only simulated data.

2. Simulated sine wave, but the time between data points taken from real LDV data.

3. Vortex shedding flow behind a cylinder.

4. Two-dimensional turbulent boundary layer.

Spectra were computed using all the three methods discussed in Chapter Three. However, in the following sections, spectra computed by the discretized lag product method and the direct transform method will be discussed in detail. The exact lag product method has the disadvantage of being extremely slow computationally. However, at least one spectra for each test case was computed using the exact lag product method. The spectra calculated using the exact lag product method are presented in a separate section.

Unless otherwise mentioned, it should be assumed that all data sets contained 512,000 points. For the discretized lag product method, a slot width of 128 microseconds was always used. A resolution of 10 Hz was used for the first three cases. For the 2DTBL, a resolution of 5 Hz was utilized. Spectral estimates were calculated upto 3900 Hz, which is the maximum value consistent with the slot width. For the direct transform method, the whole data set was divided into short blocks of length 0.2 seconds each, giving an approximate resolution of about 5 Hz

for the 2DTBL, while a resolution of 10 Hz was used for the other cases. The estimates resulting from each block were then ensemble averaged. Spectral estimates were calculated up to an arbitrary maximum limit of 2000 Hz. A Hanning window was used in all cases.

5.3 Poisson Distribution Assumption

In theoretical analysis of spectra from randomly sampled data, it is usually assumed that the sampling follows a Poisson distribution. Shapiro and Silverman [47] showed from theoretical considerations that for Poisson distributed sampling, alias free spectral estimates can be obtained for any sampling rate.

Thus the assumption that the sampling follows a Poisson distribution plays an important role in spectral analysis of randomly sampled data. For real LDV data, the validity of this assumption needs to be experimentally demonstrated for data sets arising from various flow fields and experimental situations. The only attempts at verifying the Poisson distribution were reported by Roberts, et al. [51] and Srikantaiah [52]. These authors show that the sampling follows a Poisson distribution for their data sets.

5.3.1 Poisson Distribution

A sequence of random events occuring in time are considered, where each event is represented by a point on the time axis. The probability of finding exactly k points within a fixed interval of length t is given according to the Poisson distribution as

$$p(k) = e^{-\lambda t} \frac{(\lambda t)^k}{k!} \tag{5.1}$$

where λ is the Poisson parameter and is equal to the mean number of points per unit time.

It can be also shown that [72] the time between successive events in such a case follows a negative exponential distribution. Thus the probability distribution function for the time between events is given by

$$F(t) = 1 - e^{-\lambda t} \tag{5.2}$$

The corresponding probability density function is given by

$$f(t) = \lambda e^{-\lambda t} \tag{5.3}$$

In the case of the data from LDV, the events correspond to the arrival of a particle in the measurement volume and subsequent validation of the doppler burst. To determine whether an observed sequence of points can be reasonably identified as a Poisson process, the exponential distribution of the time intervals is used as a criterion [73].

If consecutive intervals $t_1, t_2, \ldots, t_n$, occuring from a Poisson distribution are considered, the probability distribution function is given by Eq. 5.2. It follows that the probability of an interval τ being greater than t is given by

$$Pr[\tau > t] = e^{-\lambda t} \tag{5.4}$$

Equation 5.4 can also be written as

$$\frac{N}{N_0} = e^{-\lambda t} \tag{5.5}$$

where N is the number of intervals of size larger than t and N_0 is the total number of intervals. It follows that if the intervals are ranked by order of magnitude and $\log N$ is plotted versus t, a straight line should be obtained.

5.3.2 Verification of a Poisson Distribution

Histograms of the time between data points were computed for two LDV data sets used later in the spectral analysis of the two-dimensional boundary layer. Each data set contained 102,400 points. The time intervals between data points had a range from zero to 32,760 microseconds in these cases. To compute the histogram, this range of possible time intervals was subdivided into 40 slots of equal length. The time between data points were checked for each data point and the slots in which it fell was determined. This procedure gave a histogram containing the number of data points in each slot. From the histogram data, the number of data points, N, having the time between data points larger than *t* was computed for each slot. A plot of log N vs. t was then made, and this should be a straight line if the sampling followed a Poisson distribution.

Figures 5.1 and 5.2 show histograms obtained from the LDV data sets 1 and 2 respectively. The discontinuity of the y-axis for the first histogram bar should be noted, with the value of the first bar displayed at the top. From the histograms, it can be seen that distributions follow an exponential law. In Figs. 5.1 and 5.2, slots around 4800 microseconds seems to have fewer data points than expected. This feature was present in many of the data sets analyzed. The reason for this was not clear.

As discussed earlier, the Poisson distribution can also be verified by a plot of log N vs. t where N is the number of intervals of size larger than t. These data should fall on a straight line if it follows a Poisson distribution.

Figures 5.3-5.4 shows plots of log N vs. t for the two data sets. The solid line in each of these plots is the computed best fit line through the data points. It is seen from the plots that the Poisson distribution was followed closely with possibly minor deviations, as observed by the dips in the histograms.

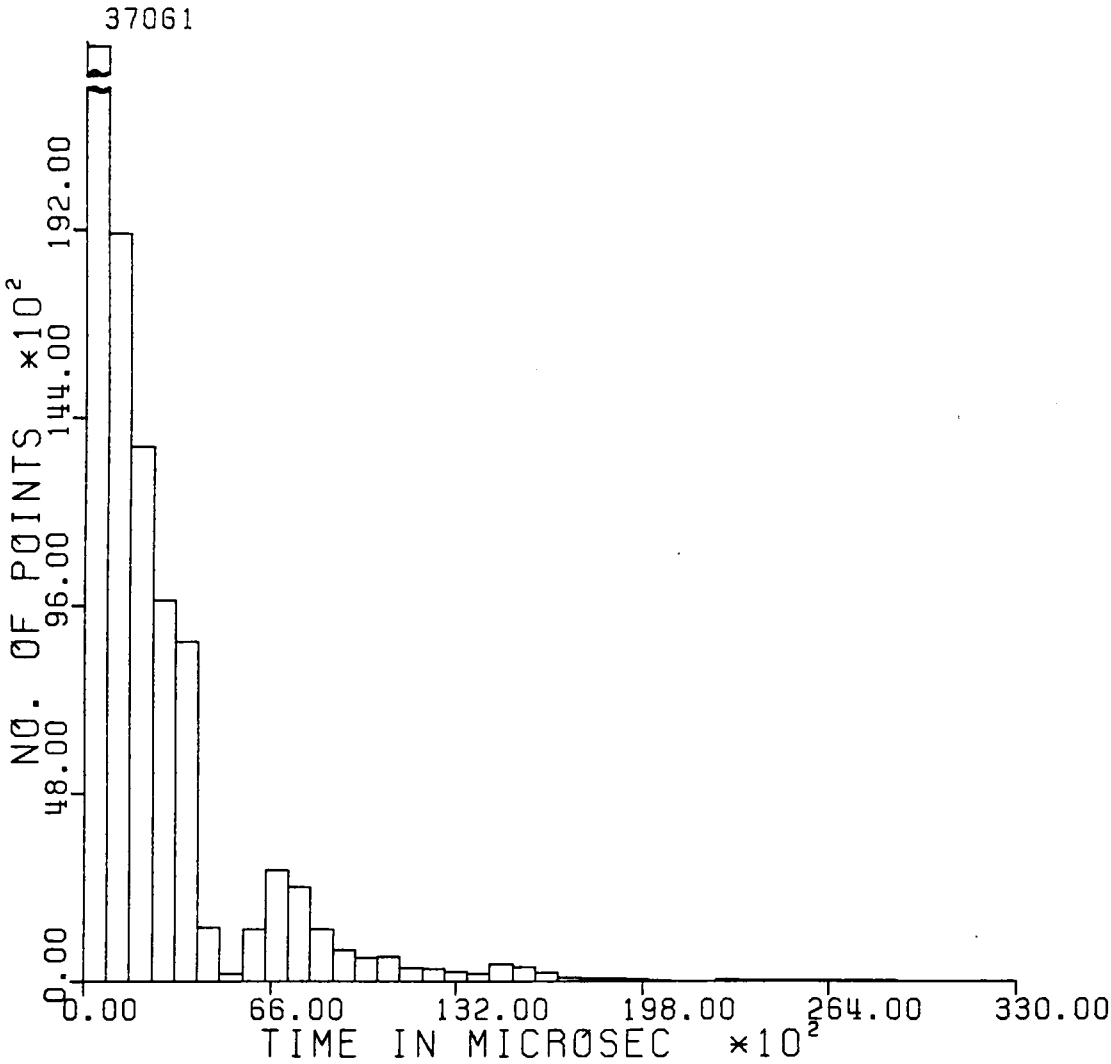

Figure 5.1. Histogram of Time Between Data for LDV Data Set 1, 102,400 Data Points

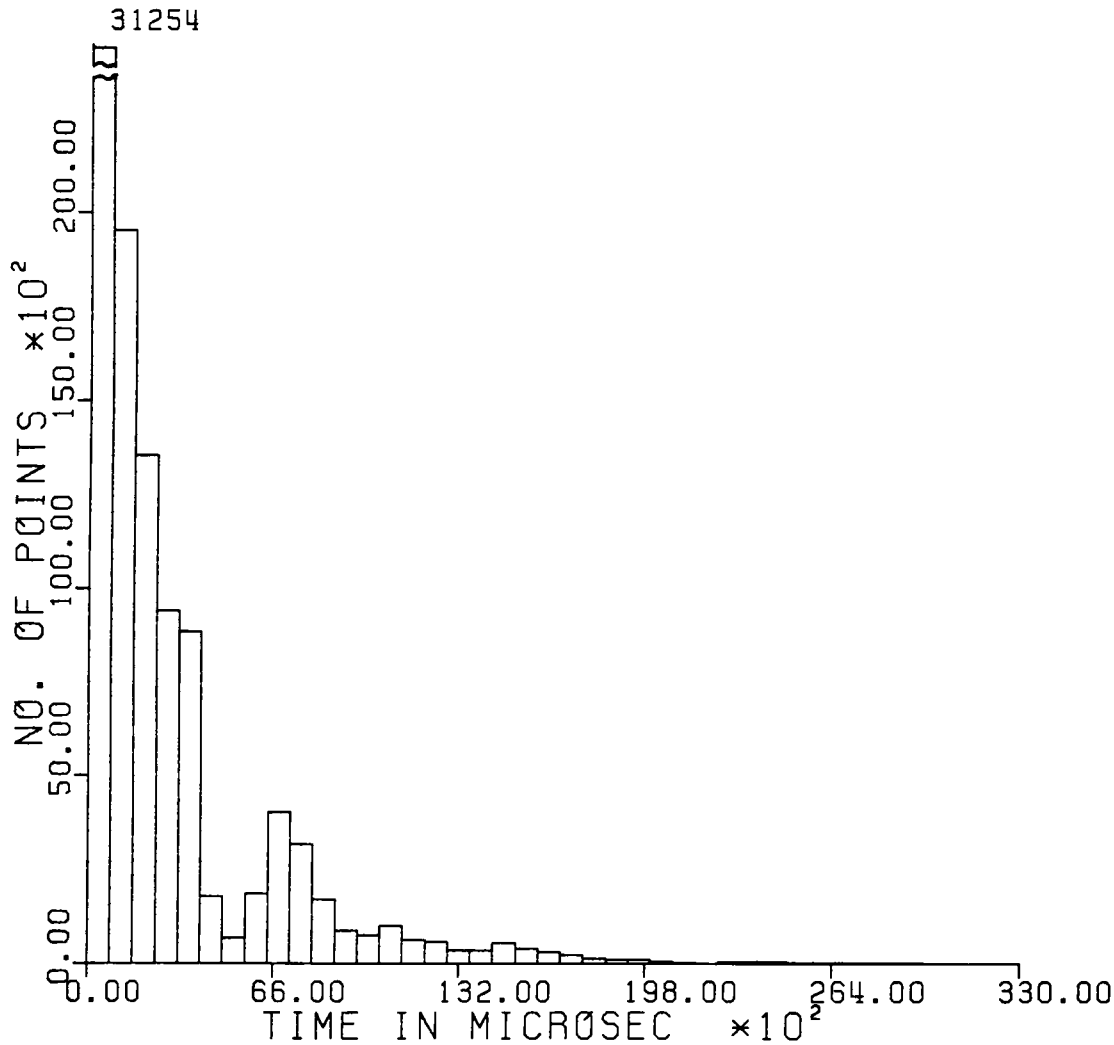

Figure 5.2. Histogram of Time Between Data for LDV Data Set 2, 102,400 Data Points

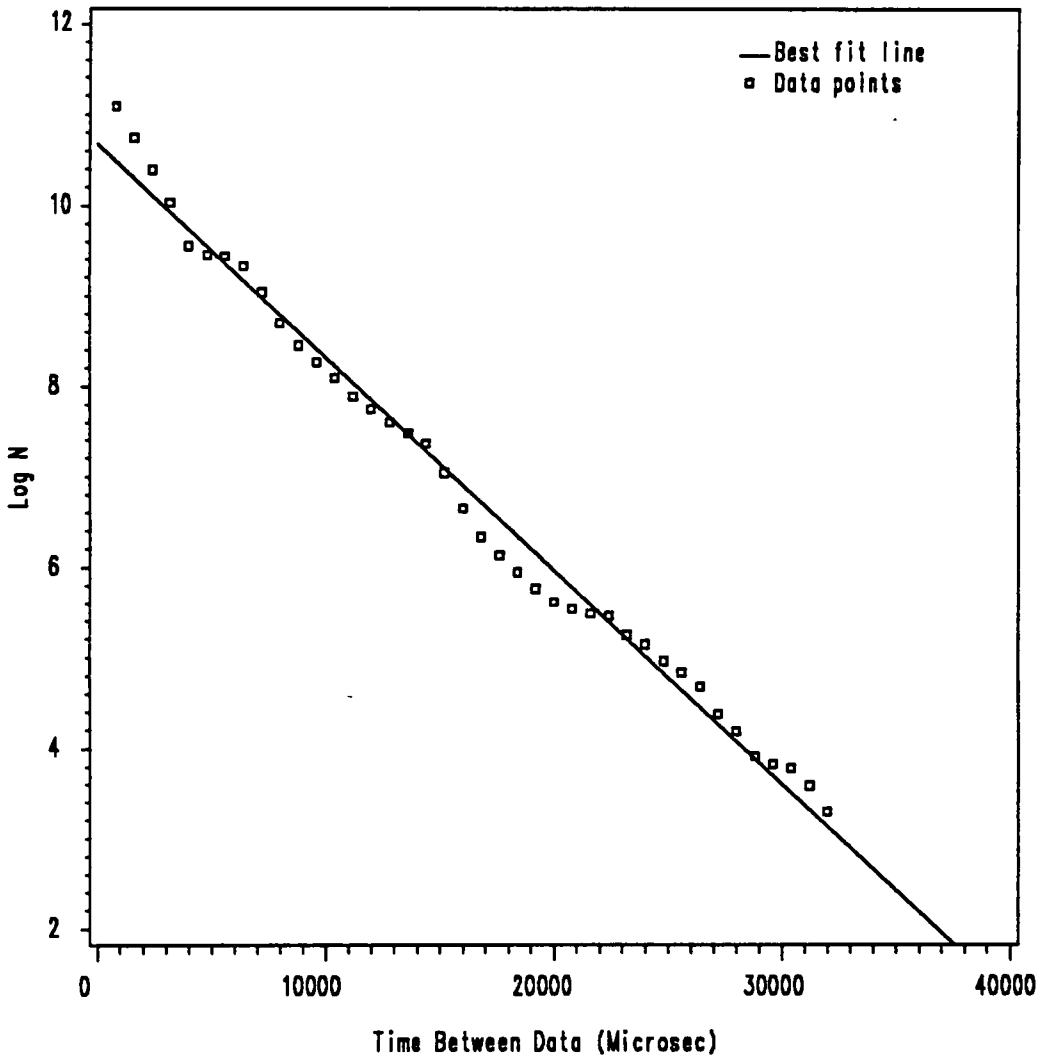

Figure 5.3. Verification of Poisson Distribution for LDV Data Set 1

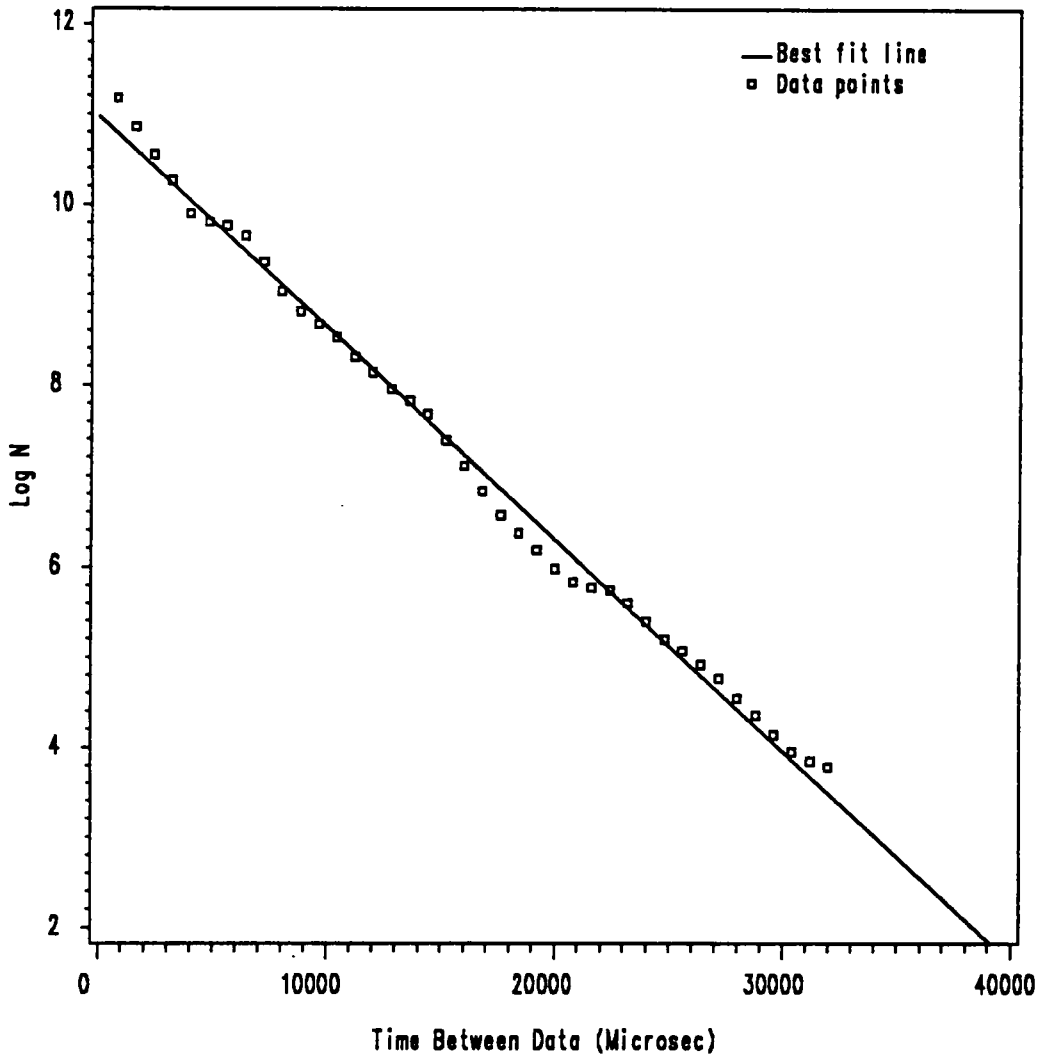

Figure 5.4. Verification of Poisson Distribution for LDV Data Set 2

5.4 Simulation Study

The methods for the spectral analysis for randomly sampled data sets were first studied using a simulated data set. A first order spectrum, which represents the output of a first order linear system excited by white noise, was chosen for the simulation study. This spectrum was given by,

$$S(f) = \frac{A}{1 + B(2\pi f)^2} \tag{5.6}$$

with constants $A = 1$ and $B = 10^{-4}$. This spectrum was chosen because of its similarity with a typical turbulence spectrum. Similar spectra were also simulated and studied by Gaster and Roberts [58,59] and Srikantaiah and Coleman [69].

Data sets corresponding to the spectrum given by Eq. 5.6 can be generated by a method described by Franklin [74]. Franklin described the method for uniformly sampled data, but the method is easily adapted to compute randomly sampled data sets.

A data set containing randomly sampled data was generated using Franklin's method and the spectra were computed. The data set contained 100,000 data points. The time between data points in the data set were generated using an IMSL routine such that the sampling followed a Poisson distribution. The mean sampling rate was set to 500 Hz. This value was chosen as it is in the range of the actual LDV sample rates obtained in later experiments. Spectra were calculated by using both the discretized lag product method and the direct transform method.

Figure 5.5 compares the spectrum calculated by the discretized lag product method with the theoretical spectrum. The figure shows an excellent agreement with the theoretical spectrum. After about 150 Hz, where the spectral level is close to zero, spectral estimates became negative. Because of the presence of these negative spectral estimates, the spectrum here is shown in a semilog scale rather than the usual log-log scale.

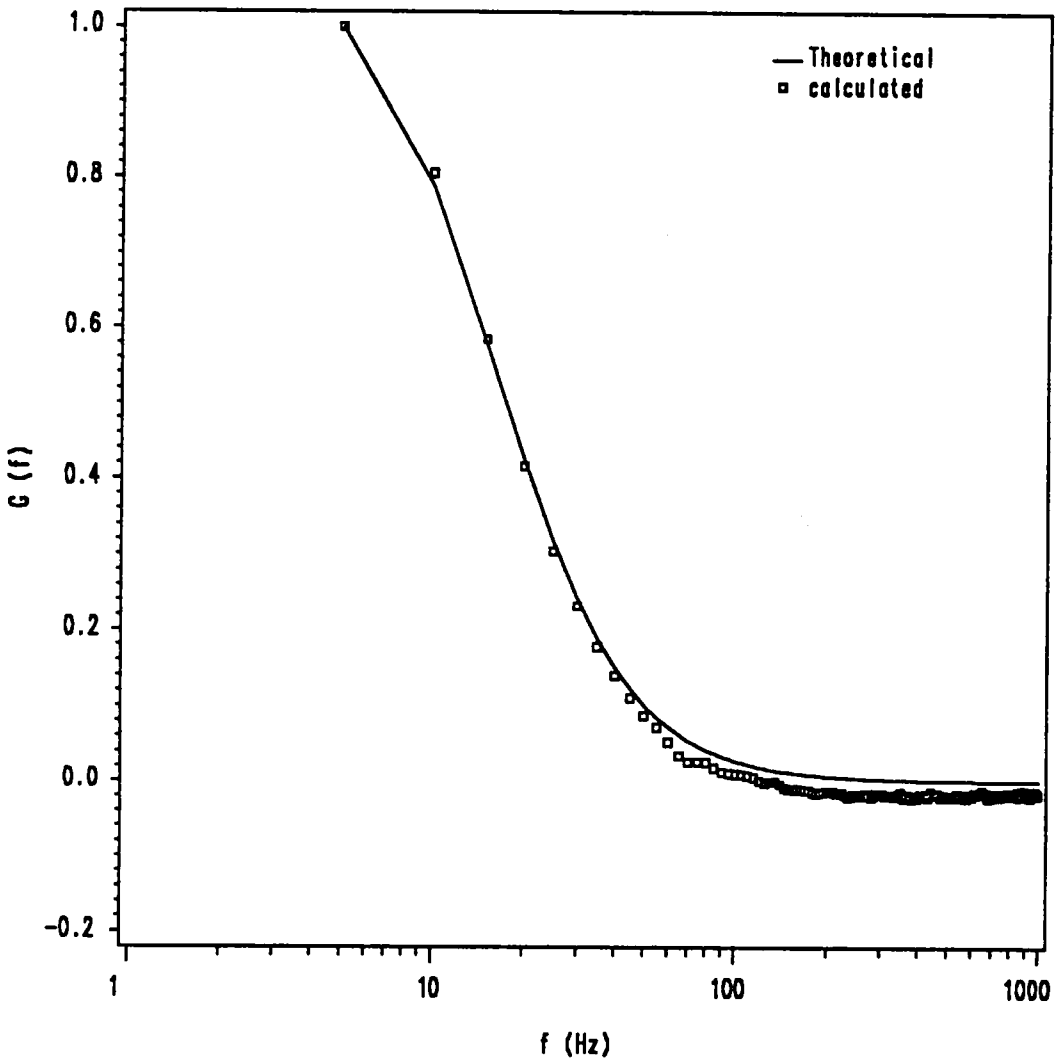

Figure 5.5. Spectrum from Simulated Data Using DLPM

Figure 5.6 shows the spectrum computed by the direct transform method. The total data set was divided into blocks of length 0.1 seconds each and the estimates from all the blocks were ensemble averaged to yield the final spectrum. The direct transform method is also seen to perform very well for the simulated data set. Negative spectral estimates were found in this case also, but were relatively fewer.

5.5 Simulated Sine Wave

In this exercise the performance of the methods of spectral estimation were investigated for a simulated sine wave. This was not a pure simulation, however, because the time between data points were taken from an actual LDV data set. Thus this exercise was one step closer to the real situation.

To generate the simulated sine wave, the velocity information in a LDV data set was replaced by the value corresponding to a sine wave or a mixture of sine waves. The time between the data points in the LDV data set was left undisturbed. Two situations were examined:

1. A pure sine wave.

2. A mixture of two sine waves, with closely spaced frequencies.

The LDV data set from which the simulated sine waves were constructed contained approximately 20,000 points and had an average sample rate of 230 samples/sec. The simulated sine waves had frequencies of 200 Hz or 400 Hz for the single frequency case. A mixture of sine waves with frequencies 200 Hz and 220 Hz in equal amplitude was used for the second case.

Figure 5.7 shows the spectrum computed by using the discretized lag product method. As expected, the calculated spectrum has a peak at the sine wave frequency and is close to zero elsewhere. It is also interesting to note that the average sample rate was 230 samples/sec,

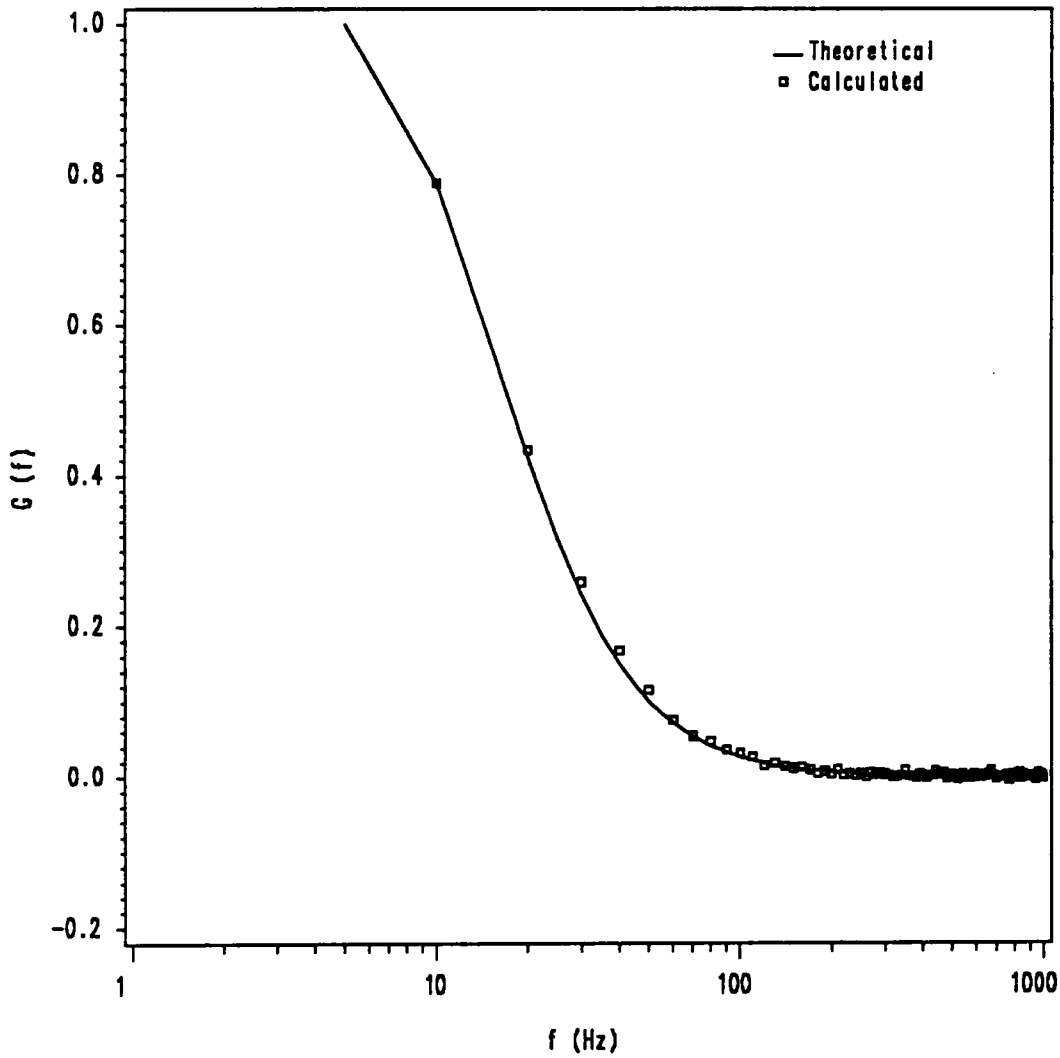

Figure 5.6. Spectrum from Simulated Data Using DTM

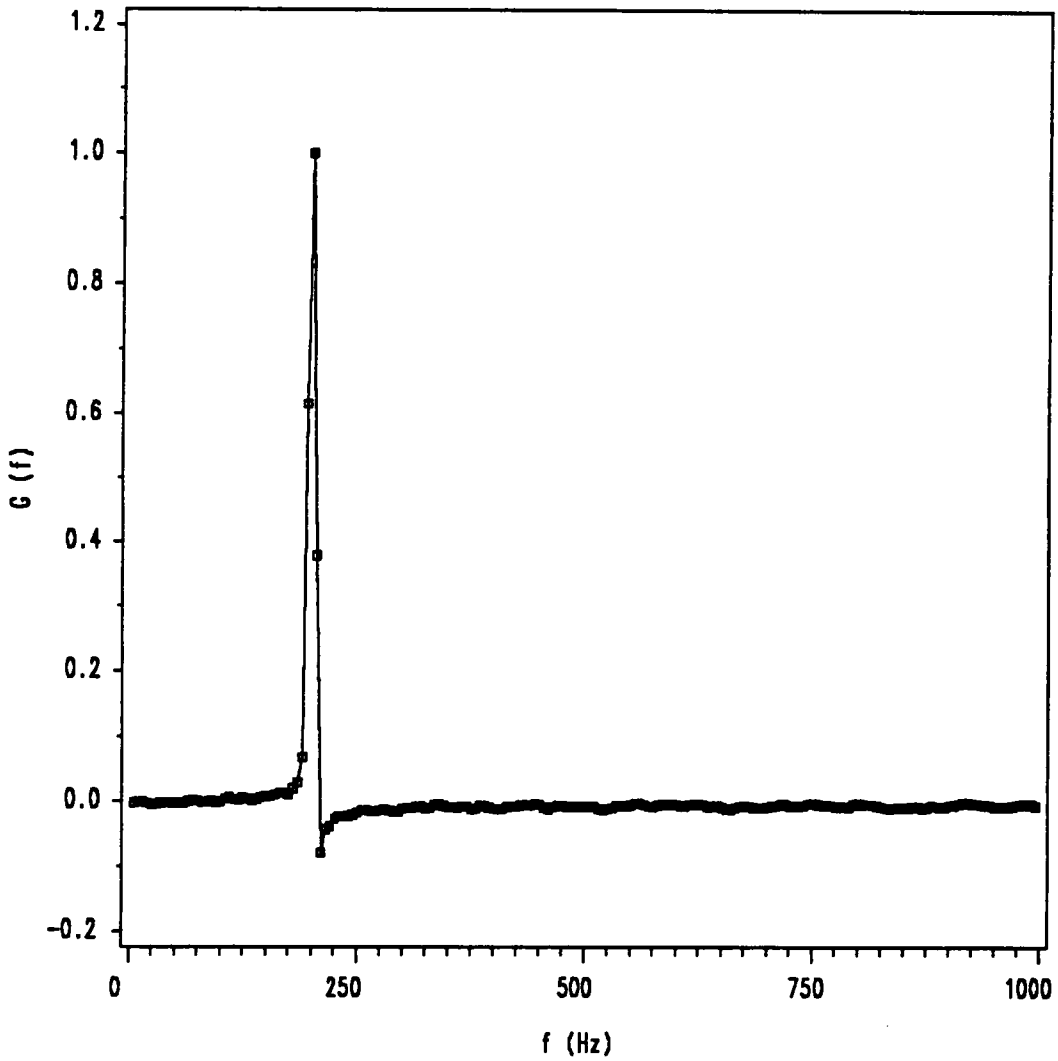

Figure 5.7. Spectrum for Simulated Sine Wave (f=200 Hz) Using DLPM

which corresponds to a Nyquist frequency of 115 Hz for uniformly sample data. The figure shows spectra calculated up to a maximum of 1000 Hz, without any noticeable aliasing effects, thus demonstrating the lack of aliasing for randomly sampled data.

Figure 5.8 shows the spectrum for the same data set obtained with the direct transform method. Excellent agreement is obtained again.

A second data set containing simulated sine wave of frequency 400 Hz was studied in the same manner as before and the results are shown in Figs. 5.9 and 5.10.

The preceding experiments with simulated sine waves with actual time between data clearly demonstrate the feasibility of resolving a spectral peak with sampling rates much lower in the case of randomly sampled data than what would be needed if the data were uniformly sampled. For example, to detect a frequency of 400 Hz with uniformly sampled data, a minimum sampling rate of 800 Hz is required. For the randomly sampled data, an average sampling rate of 230 Hz was used and this rate was demonstrated as adequate to detect the frequency component correctly, with no detectable aliasing.

Resolution of two closely spaced sine waves was also studied for these two spectral estimation method. Figures 5.11 and 5.12 show the spectra computed by the discretized lag product method and the direct transform method respectively. Both methods are seen to produce good results. The peaks corresponding to the sine wave frequencies were detected correctly and the spectral levels were close to zero elsewhere.

5.6 Vortex Shedding Flow

It was seen from real time smoke flow visualizations of the junction vortex flow field that the flow is strongly time variant. It was also suspected that there might be periodic components in the fluctuations of the velocity. In order to be confident that the spectral analysis methods

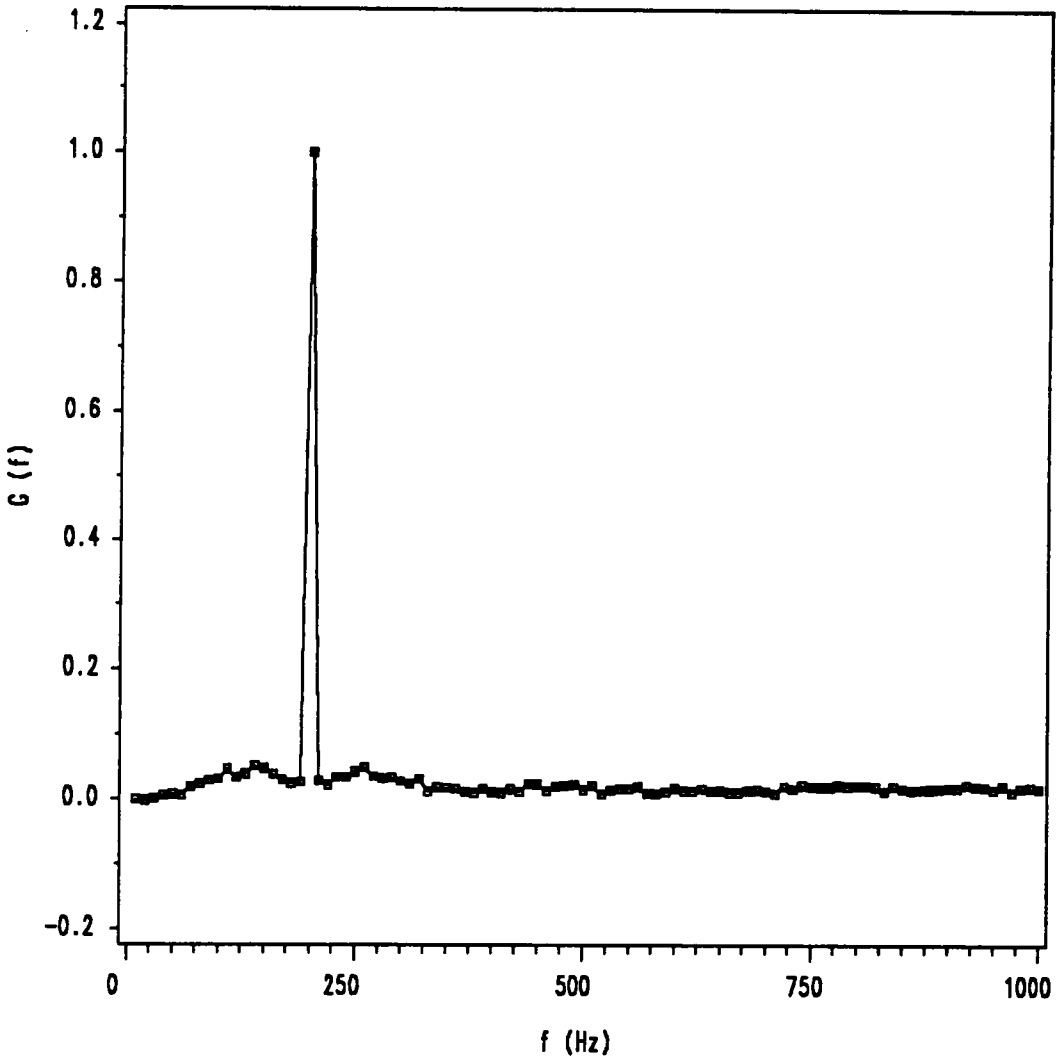

Figure 5.8. Spectrum for Simulated Sine Wave (f=200 Hz) Using DTM

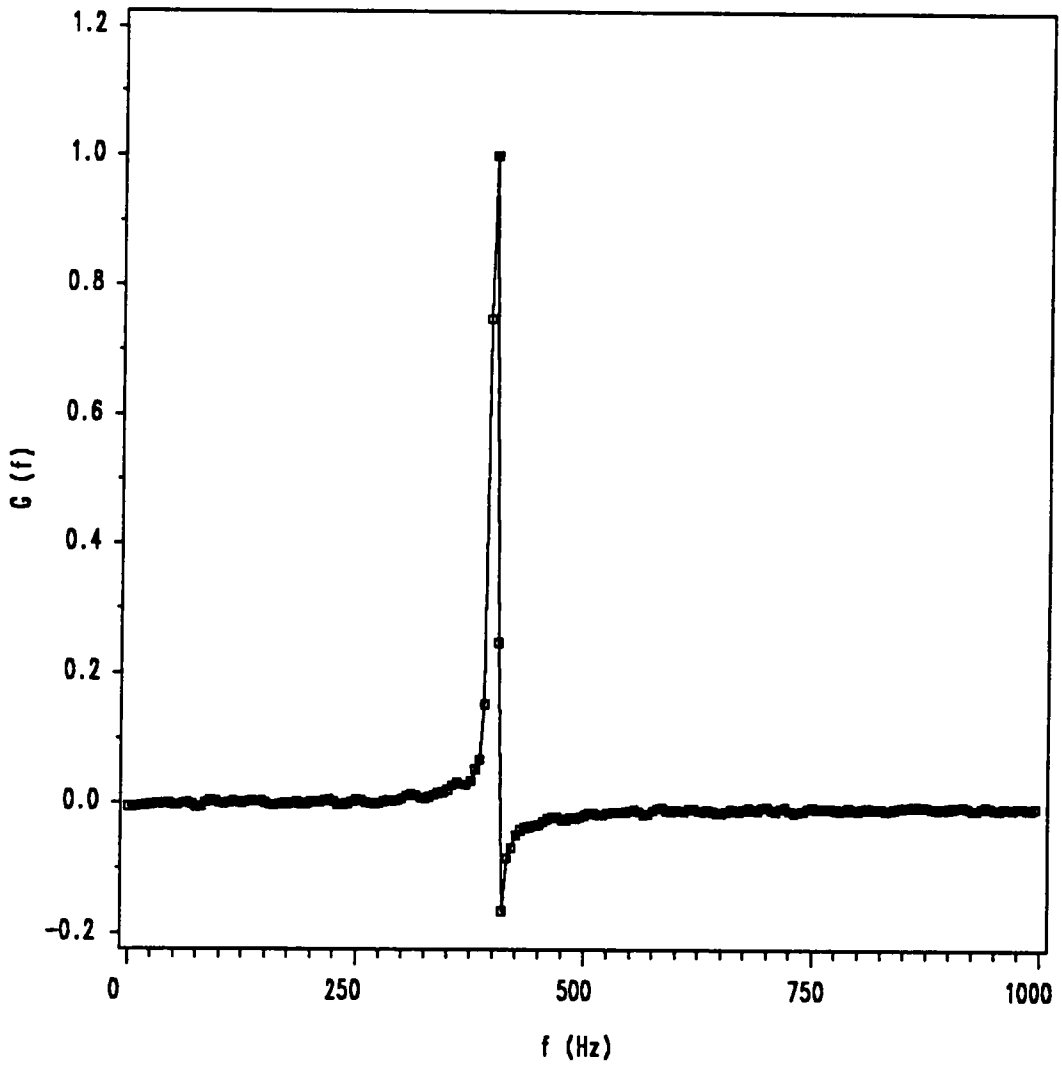

Figure 5.9. Spectrum for Simulated Sine Wave (f=400 Hz) Using DLPM

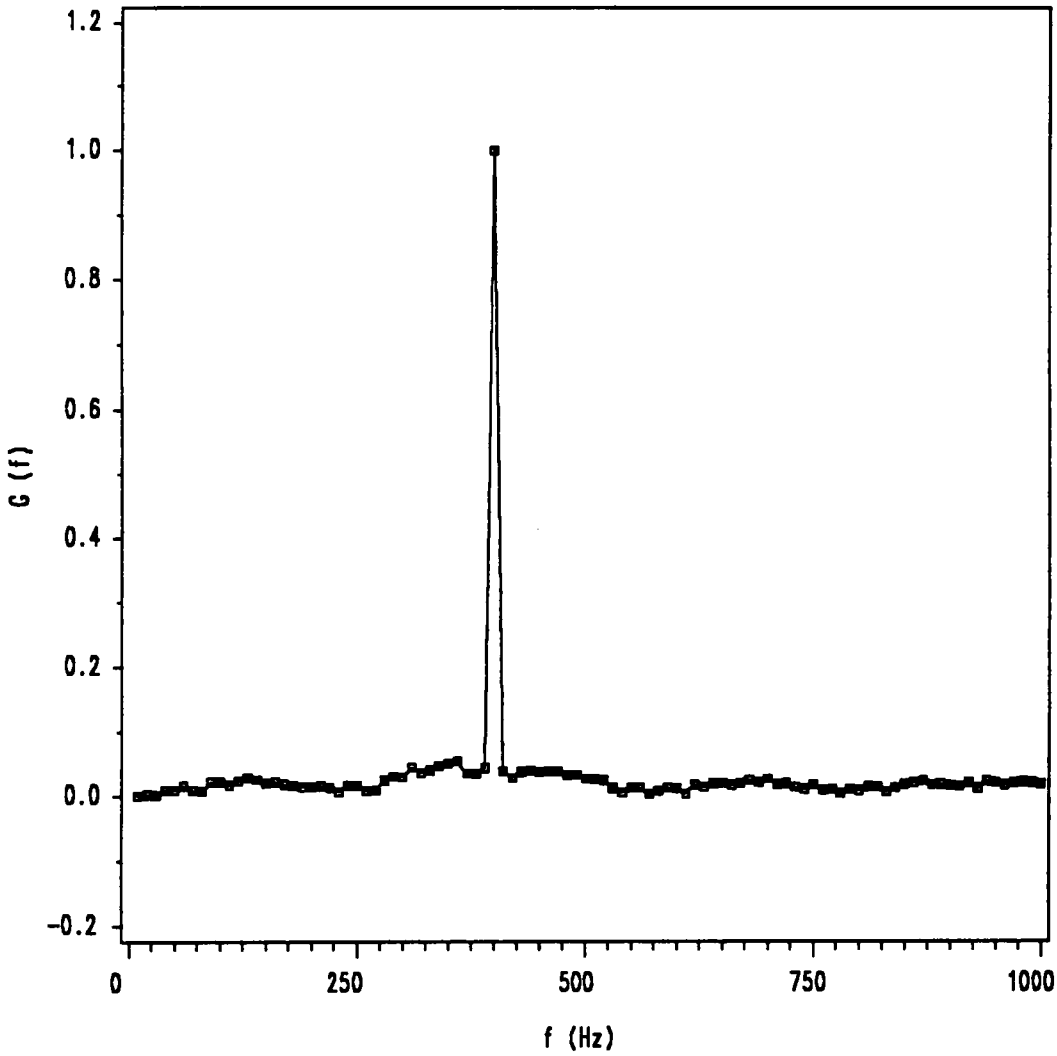

Figure 5.10. Spectrum for Simulated Sine Wave (f=400 Hz) Using DTM

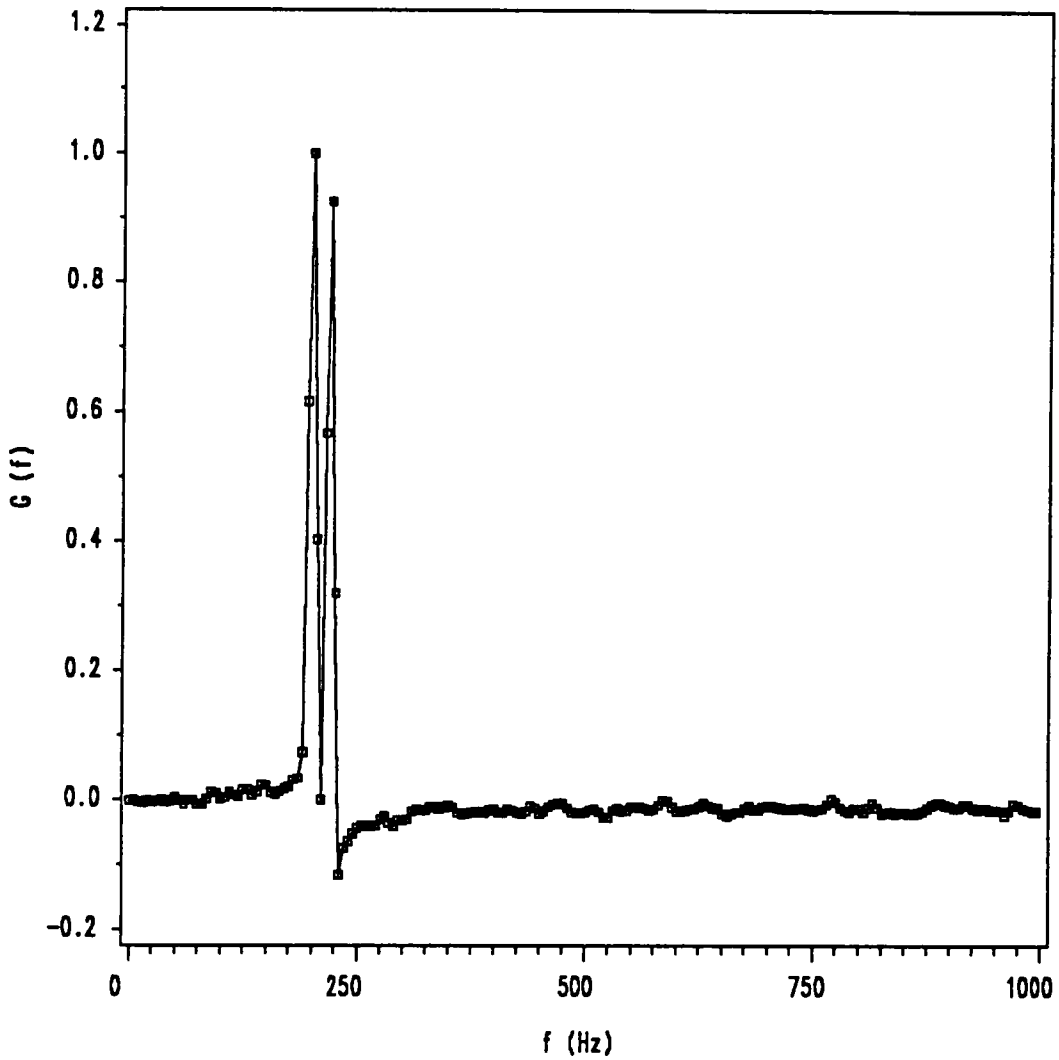

Figure 5.11. Spectrum for a Simulated Mixture of Sine Waves Using DLPM

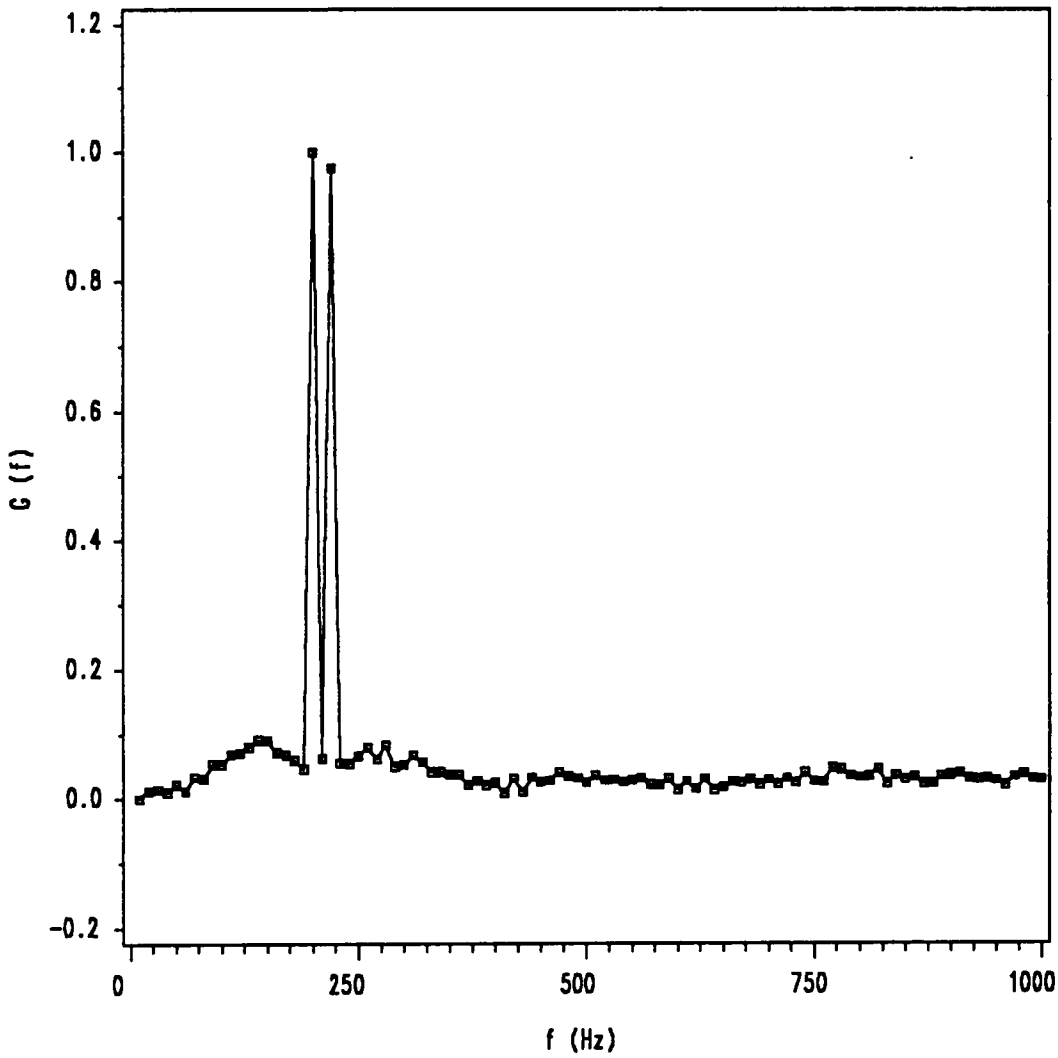

Figure 5.12. Spectrum for a Simulated Mixture of Sine Waves Using DTM

used in investigating the junction vortex flow are capable of reproducing a spectra with a dominant frequency, it was decided to test the spectral analysis methods for a real flow with a dominant frequency. A convenient and well documented example of such a flow is the vortex shedding flow behind a circular cylinder, and so it was chosen for the test.

The flow configuration and the experimental location were discussed in Section 4.6. The spectra were computed from the data obtained by both a single hot wire and LDV and the results were compared.

Assuming a Strouhal number of 0.21 (Schlichting [75]),the vortex shedding frequency for the cylinder under the experimental conditions was expected to be about 615 Hz.

Figure 5.13 shows the spectrum of the vortex shedding flow as computed from uniformly sampled data from a hot wire using the DATA 6000 (periodogram method). The output from the linearized hot wire was filtered at 2.5 kHz. The sampling interval was 200 microseconds and 100 ensembles were averaged to produce the final spectrum. Each ensemble consisted of 1024 points. The spectrum shows a peak at 565 Hz and is close to zero elsewhere. A very weak peak at the frequency corresponding to the second harmonic can also be observed.

A set of LDV data consisting of 102,400 points were also taken at the same point in the flow field. The average sample rate was about 230 samples/sec. The entire data set was then analyzed using the two different methods of spectral estimation for randomly sampled data.

Figure 5.14 shows the spectrum computed by using the discretized lag product method. The spectrum shows a peak at 565 Hz. It should be noted again that the average sample rate is well below the minimum suggested by the Nyquist criterion.

Away from the peak, the spectral level should be close to zero, as seen from the hot wire spectrum. Figure 5.14 shows the calculated spectral points scattered about the zero value, with a high variability. The higher variability has been predicted by the analyses of spectral

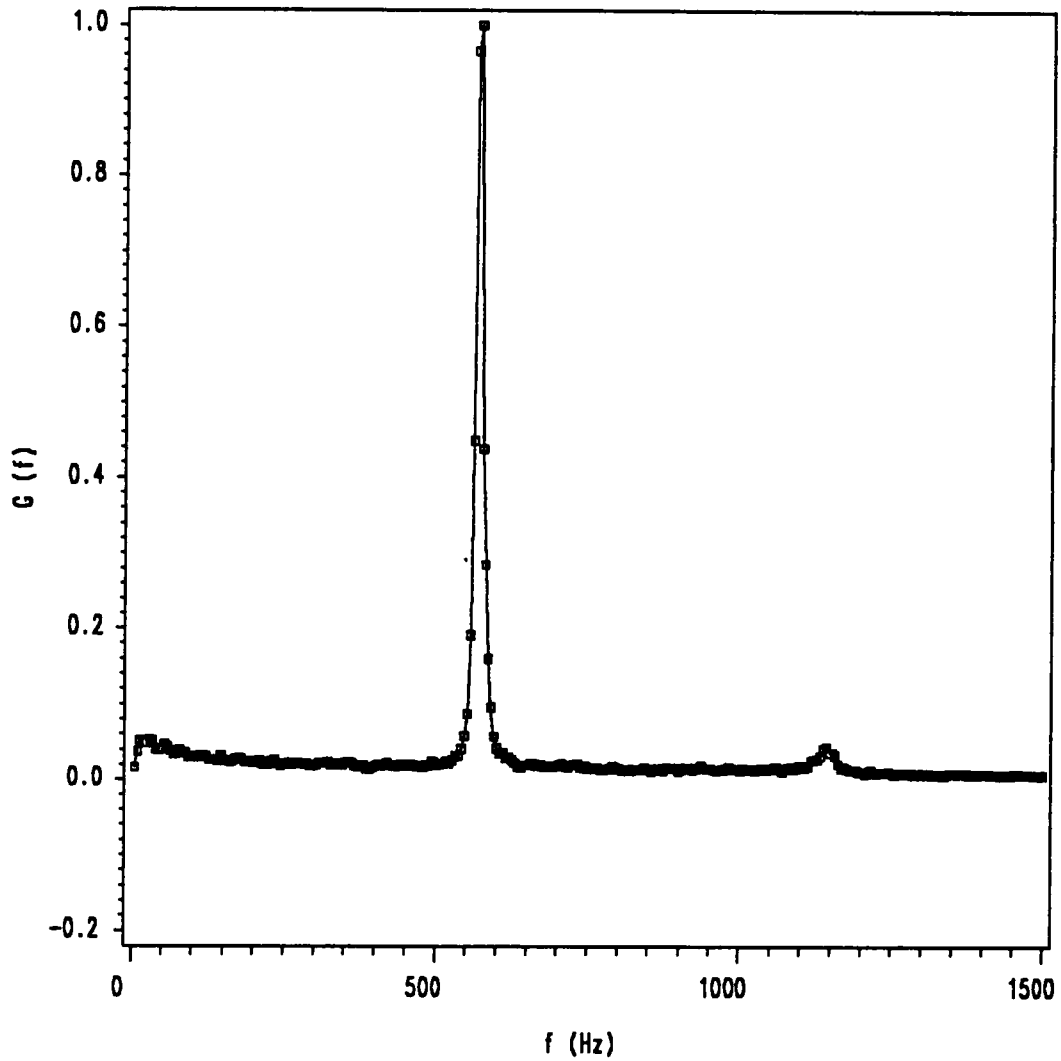

Figure 5.13. Spectrum for Vortex Shedding Flow from Hot Wire Using Data 6000

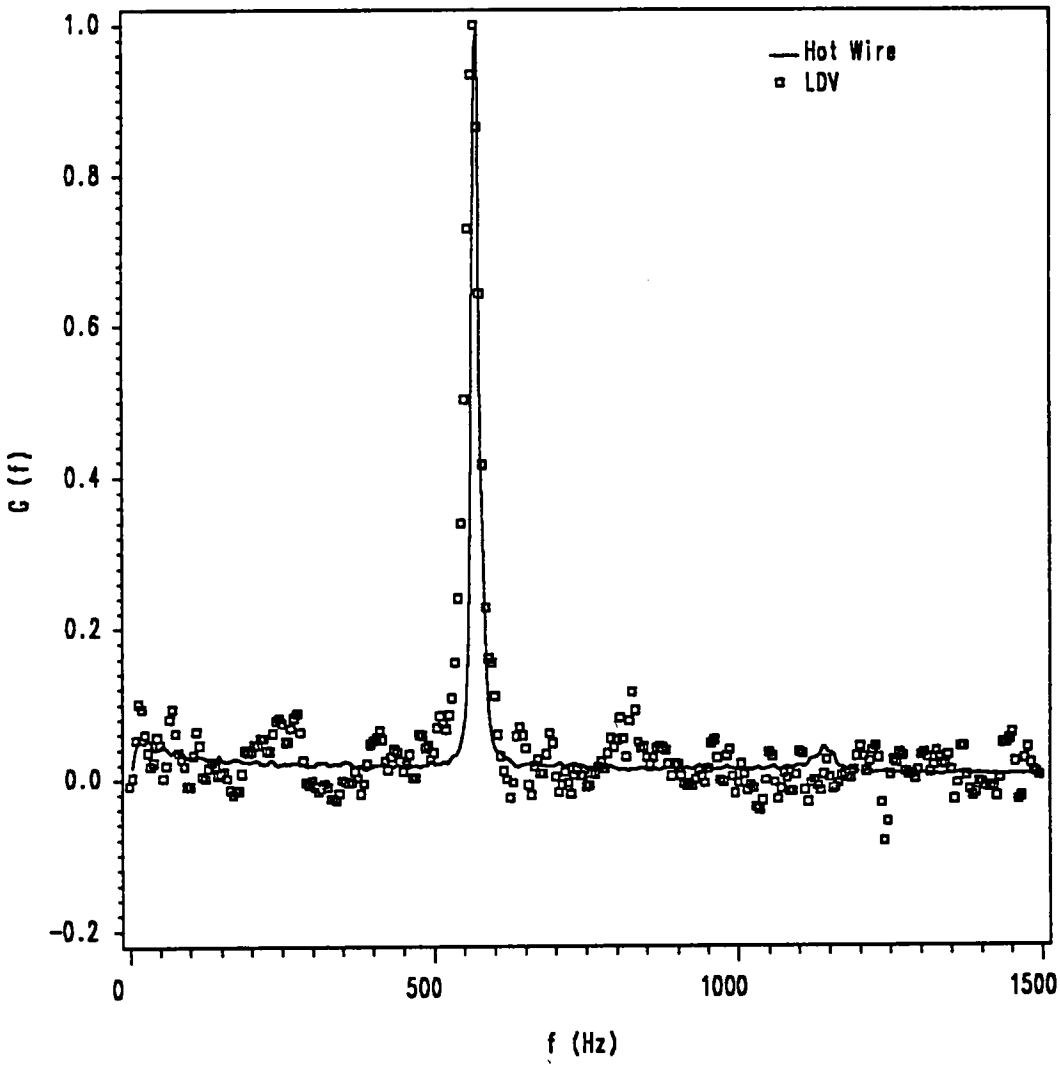

Figure 5.14. Spectrum for the Vortex Shedding Flow Using DLPM

estimation methods (see Section 3.5.8) and arises due to the random sampling of the data. For spectral levels close to zero, the variability of the discretized lag product method is given by Eq. 3.54. The standard deviation of the spectral estimates computed from Eq. 3.54 and 3.55 for this case was of the order of 0.01. The extent of variability found here is much larger than that predicted by Eq. 3.54. It should be also noted that due to the higher variability, the second very weak peak as seen in the hot wire spectrum is impossible to resolve with this method.

Figure 5.15 shows the spectrum computed using the direct transform method. The peak is again reproduced correctly at 565 Hz. Away from the peak, an added white noise is present in the spectrum, in the regions where expected spectral levels were close to zero. This added white noise will be found in most other spectra computed by the direct transform method, and is a serious disadvantage of the method. There is also a large scatter of the computed spectral points around the added white noise level. The scatter is much larger than the predicted theoretical limits as given by Eq. 3.55.

For the vortex shedding flow studied here, it was seen that both the discretized lag product and the direct transform methods performed very well in reproducing the dominant spectral peak exactly. The tests also demonstrated the lack of alising for average sampling rates much below the Nyquist value. Away from the peak, where the spectral levels were close to zero, the discretized lag product method showed high variance and yielded negative estimates. In the same regions, the direct transform method also showed high variance, but around an added white noise level.

5.7 Two-Dimensional Turbulent Boundary Layer

The two-dimensional turbulent boundary layer is the most common and most investigated flow field. Hence the methods of spectral estimation were applied for this type of flow. The spectrum of a two-dimensional turbulent boundary layer has been discussed in Klebanoff's classic work [76]. Klebanoff computed his spectra from measurements obtained with a hot wire

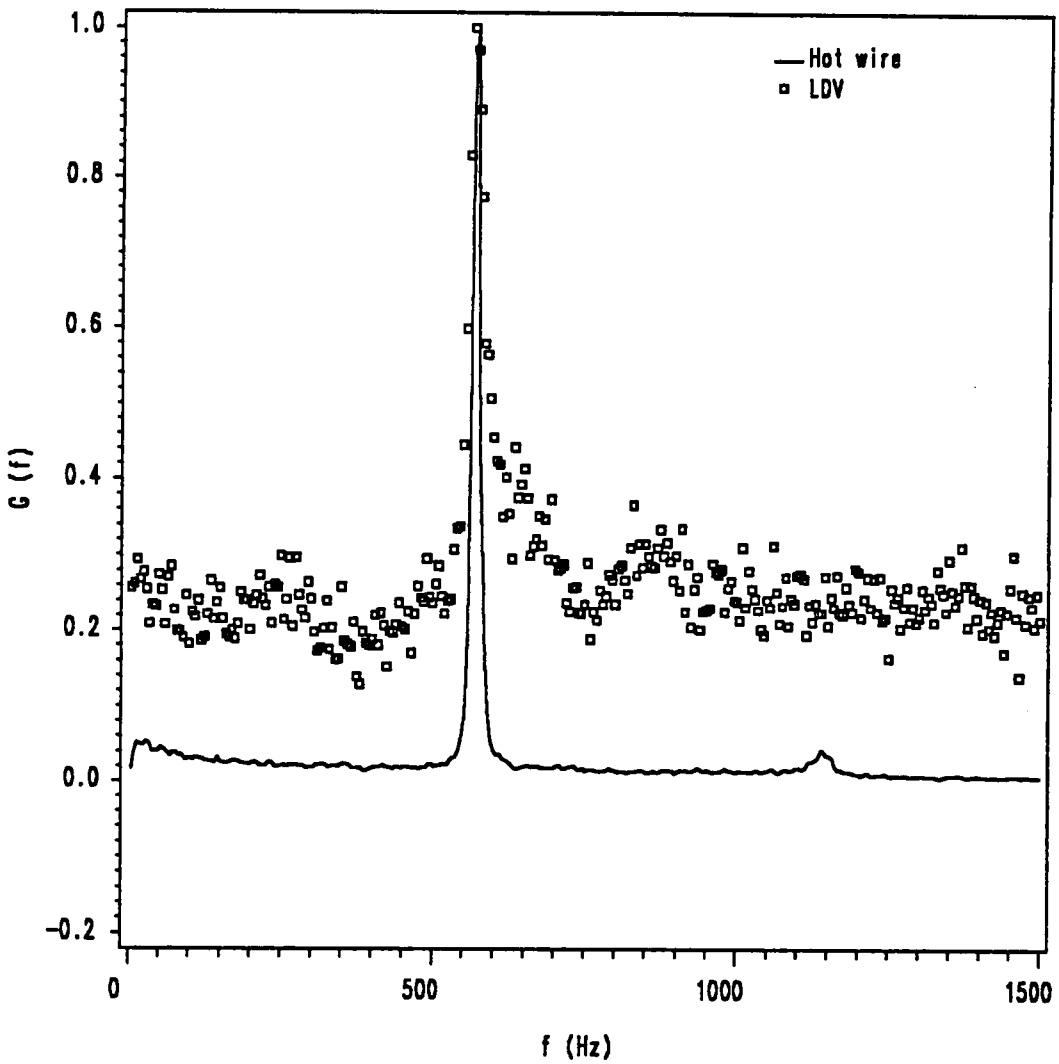

Figure 5.15. Spectrum for the Vortex Shedding Flow Using DTM

anemometer. Klebannoff's results will be used here as a basis for comparison in the spectral results presented below.

The two-dimensional turbulent boundary layer used in the present investigation was the boundary layer growing on the flat floor of the wind tunnel. The relevant parameters for this boundary layer were listed in Table 2.1. The data was taken at a height of 16.3 mm above the floor. This was chosen to give a value of y/δ of 0.2, which corresponds to one of the stations reported by Klebanoff.

To begin the investigation, the spectrum for the u-component of the two-dimensional turbulent boundary layer was investigated using a single hot wire anemometer. The output from the hot wire was filtered at 2 kHz and sampled at a rate of 5 kHz. Two thousand forty-eight points were used for each ensemble in the periodogram method and 256 ensembles were averaged. Figure 5.16 shows a comparison of the hot wire spectrum with Klebannoff's data. Excellent agreement is obtained.

Because of the presence of negative values in the spectral estimates, computed spectra are shown later in a semilog scale rather than the usual log-log scale. For ease of comparison with Klebanoff's data, Fig. 5.16 is shown again in Fig. 5.17, but in a semilog scale.

Five LDV data sets containing 102,400 points each were then collected at the same point where hot wire spectra was obtained. The average sample rates for these data sets were about 250 samples/sec. Initially it was thought that a set of 102,400 points would be enough to produce good spectra. Figures 5.18 and 5.19 show the spectra computed from two of the five data sets using the discretized lag product method. The spectrum shown in Figs. 5.18 and 5.19 was plotted in a semilog scale rather than the usual log-log scale because of the presence of negative spectral estimates towards the high frequency end. This arises due to the variability of the spectral estimates in regions where the spectral levels were close to zero.

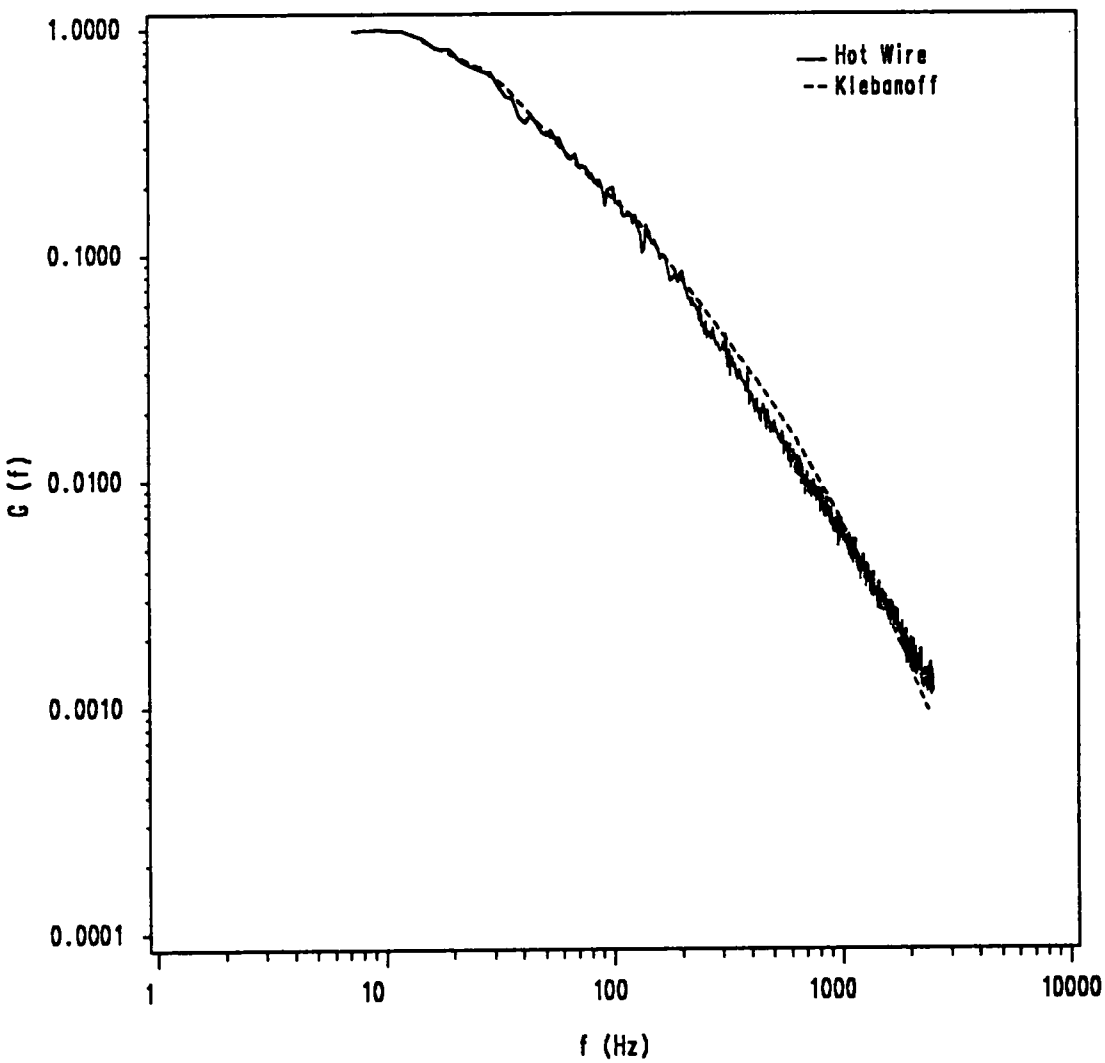

Figure 5.16. Comparison of Klebanoff's Results with Hot Wire Spectra: Uniformly Sampled Data, Using Data 6000

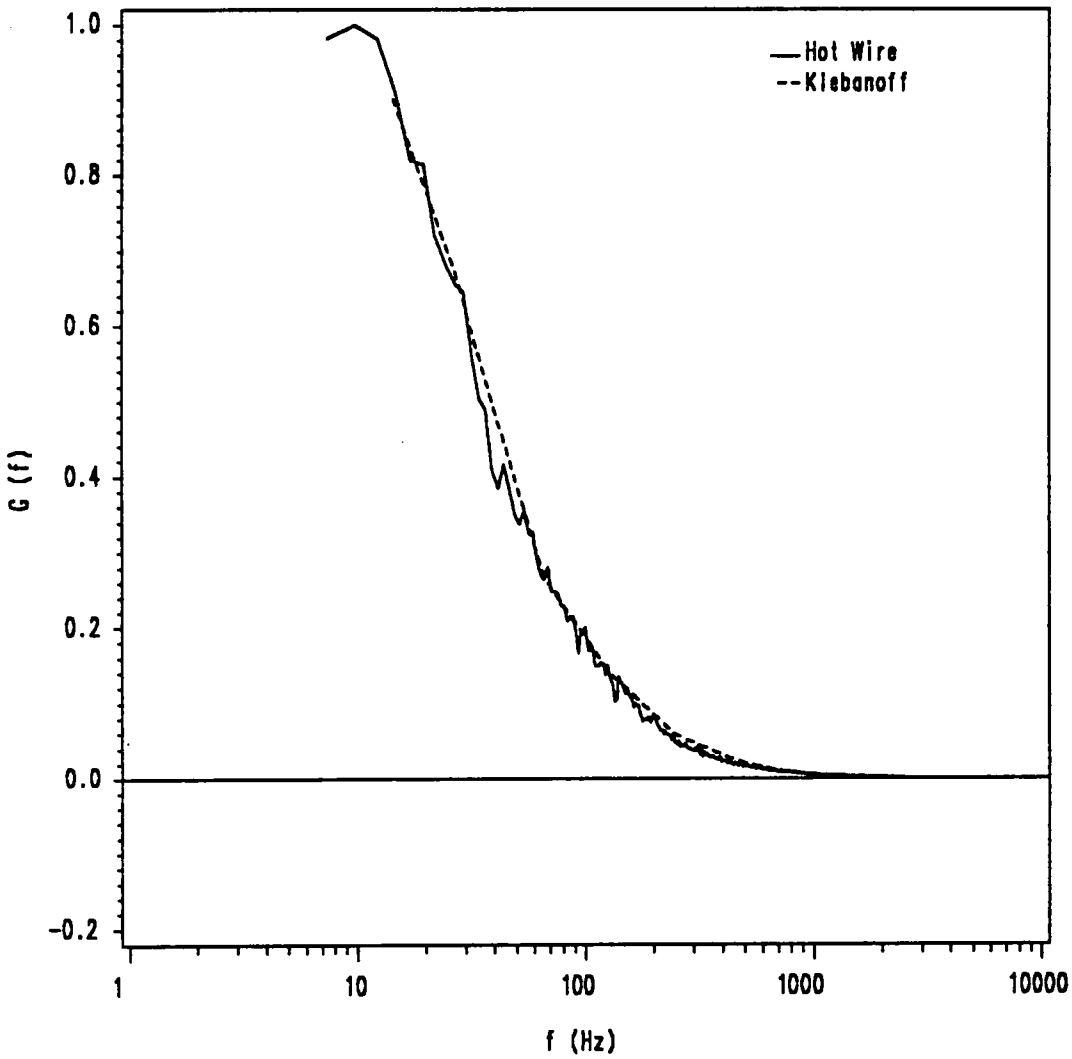

Figure 5.17. Comparison of Klebanoff's Spectra with Hot Wire Spectra: Uniformly Sampled Data, Using Data 6000

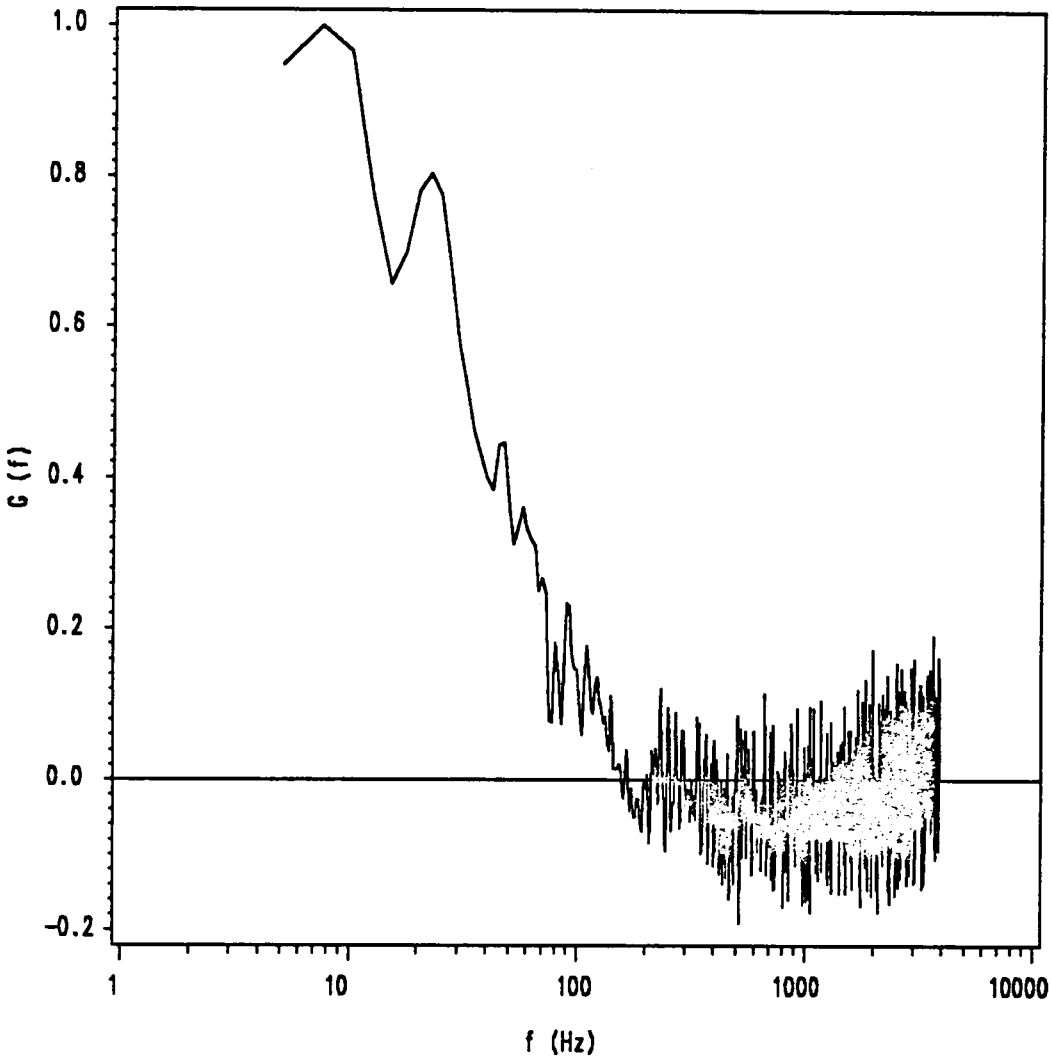

Figure 5.18. LDV Spectrum From Data Set 1 (102,400 points) Using DLPM

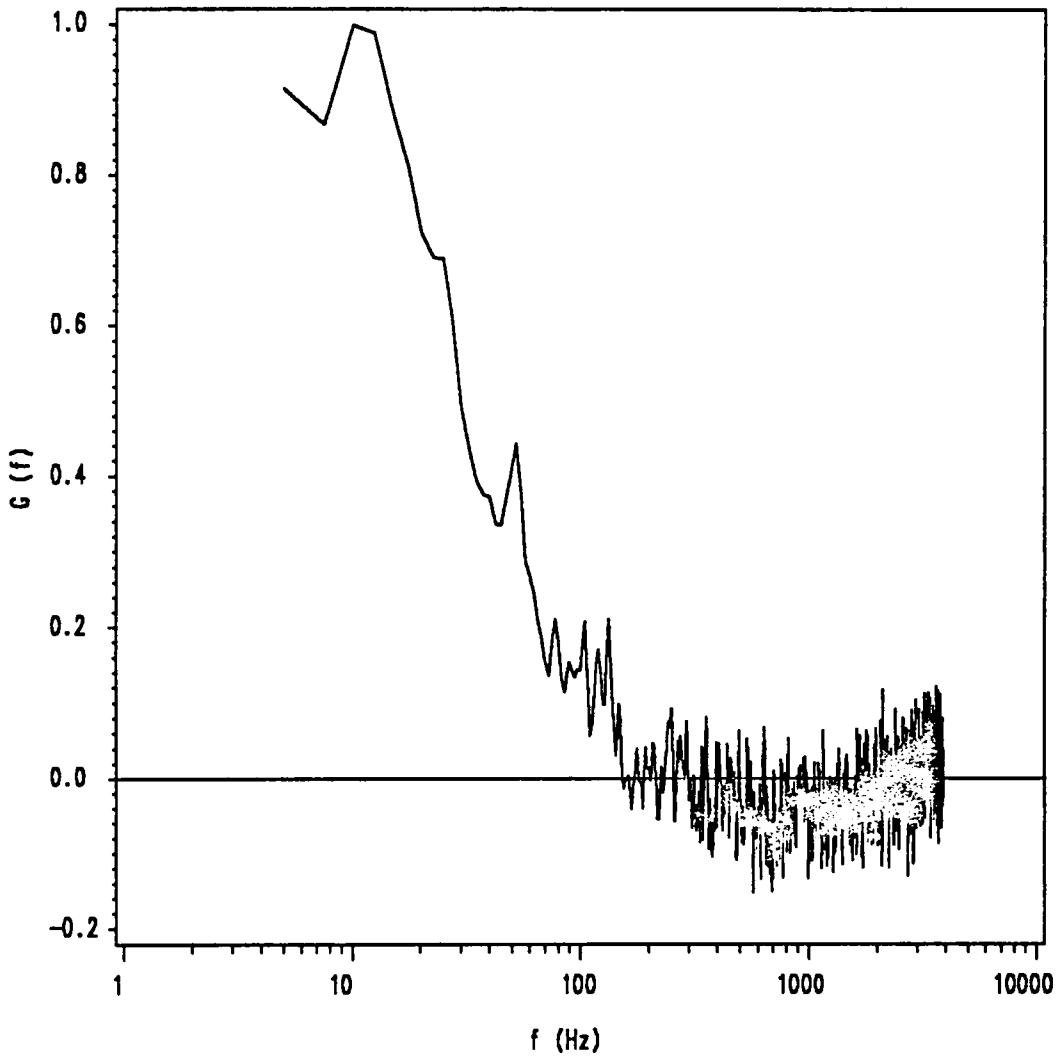

Figure 5.19. LDV Spectrum From Data Set 2 (102,400 points) Using DLPM

It was seen that there was still substantial amount of variability present in these spectra. After experimenting with averages of subsets of different lenghts, it was decided that averaging spectral results computed from five subsets of 102,400 points each gave the best spectra. Figure 5.20 shows the averaged spectra in comparison with Klebanoff's data.

In order to improve the appearance of the spectra, and possibly to eliminate some of the negative estimates, it was decided to average the spectral estimates according to an one-third octave averaging scheme (discussed in Section 4.5.4). Figure 5.21 shows the averaged spectrum from the five data sets using the discretized lag product method after octave averaging. The negative spectral estimates are still present, although the appearance of the spectrum is improved, as seen by comparing with Fig. 5.20. All the spectra presented henceforth will be presented after octave averaging, unless otherwise stated.

For frequencies below about 200 Hz, the spectral estimates from the LDV data sets were found to agree well with Klebanoff's data, with some amount of scatter. Beyond 200 Hz, when the spectral levels were small, negative estimates were found. Spectral estimates became positive again at frequencies above approximately 2500 Hz.

Figure 5.22 shows the spectral estimates using the discretized lag product method for the five data sets in the more usual log-log scale. To plot the spectral estimates in this way, all negative estimates found after octave averaging were discarded.

The averaged spectrum computed using the direct transform method from all the five data sets is shown in Fig. 5.23. The direct transform method is seen to have lesser variance but appears to have an added white noise level in the regions where spectral levels are close to zero. A trend to overestimate the spectral levels can also be observed for the direct transform method. The spectrum after octave averaging is shown in Fig. 5.24.

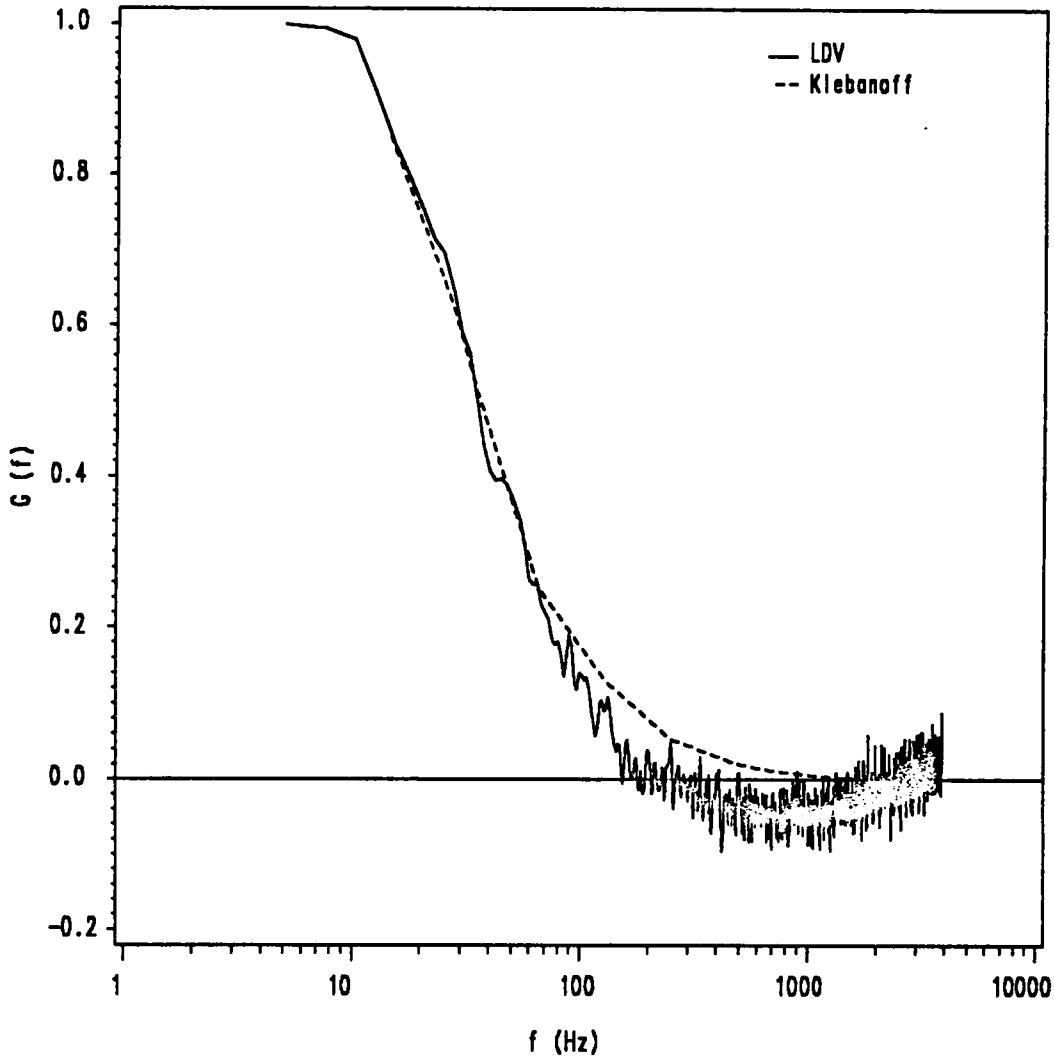

Figure 5.20. Average LDV Spectrum from 512,000 data points Using DLPM

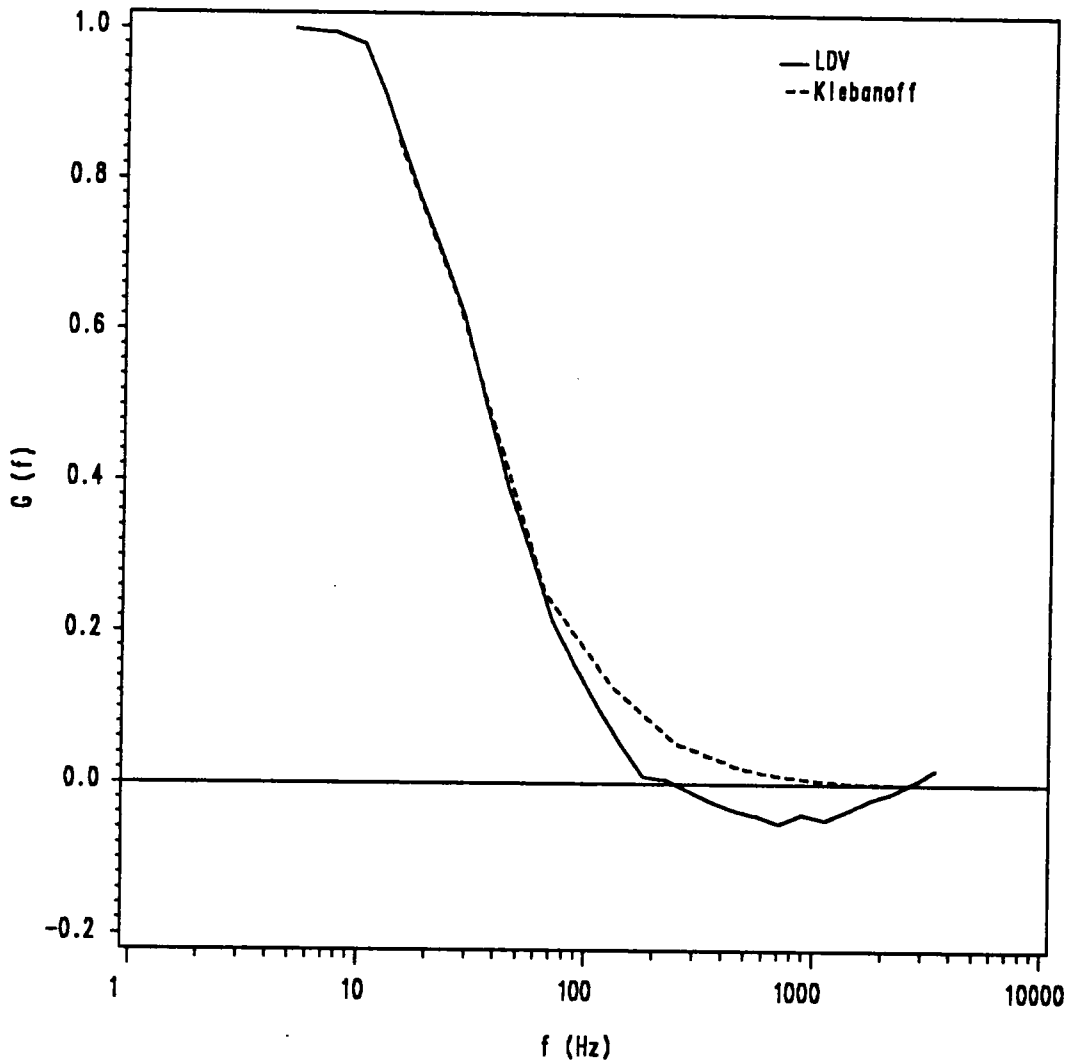

Figure 5.21. Average LDV Spectrum After Octave Averaging

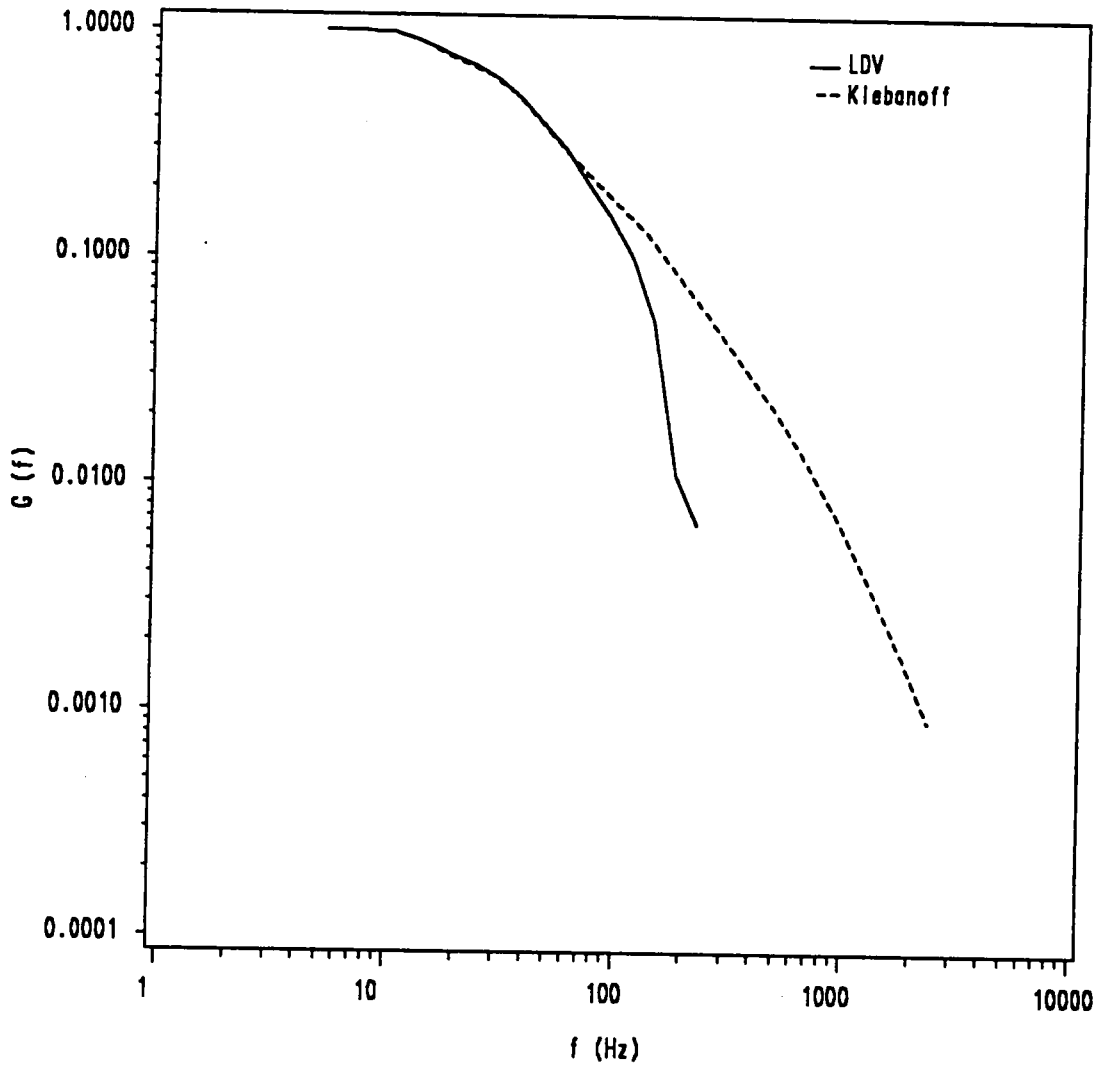

Figure 5.22. Average LDV Spectrum for 2DTBL Using DLPM in Log-Log Scale

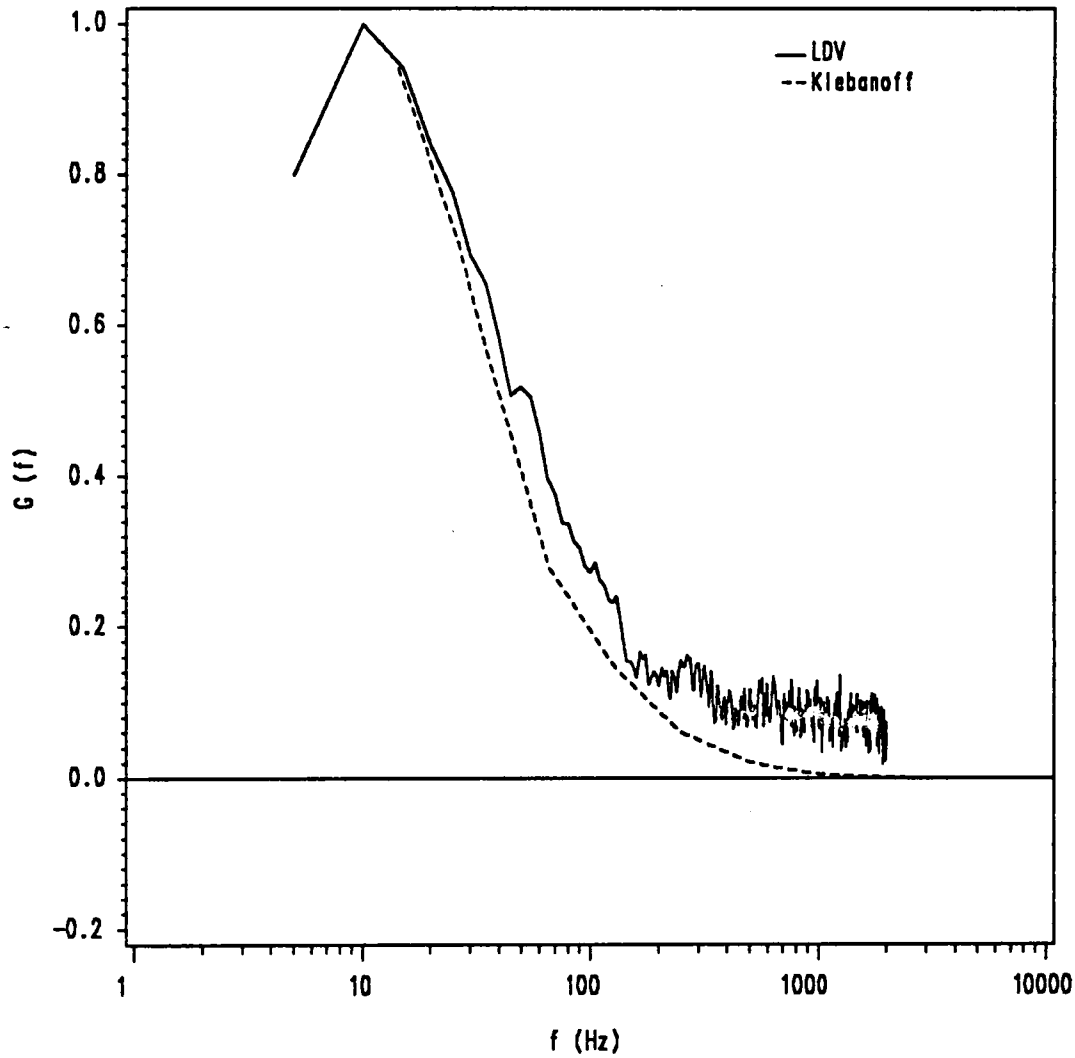

Figure 5.23. LDV Spectrum for 2DTBL Using DTM, 512,000 Data Points

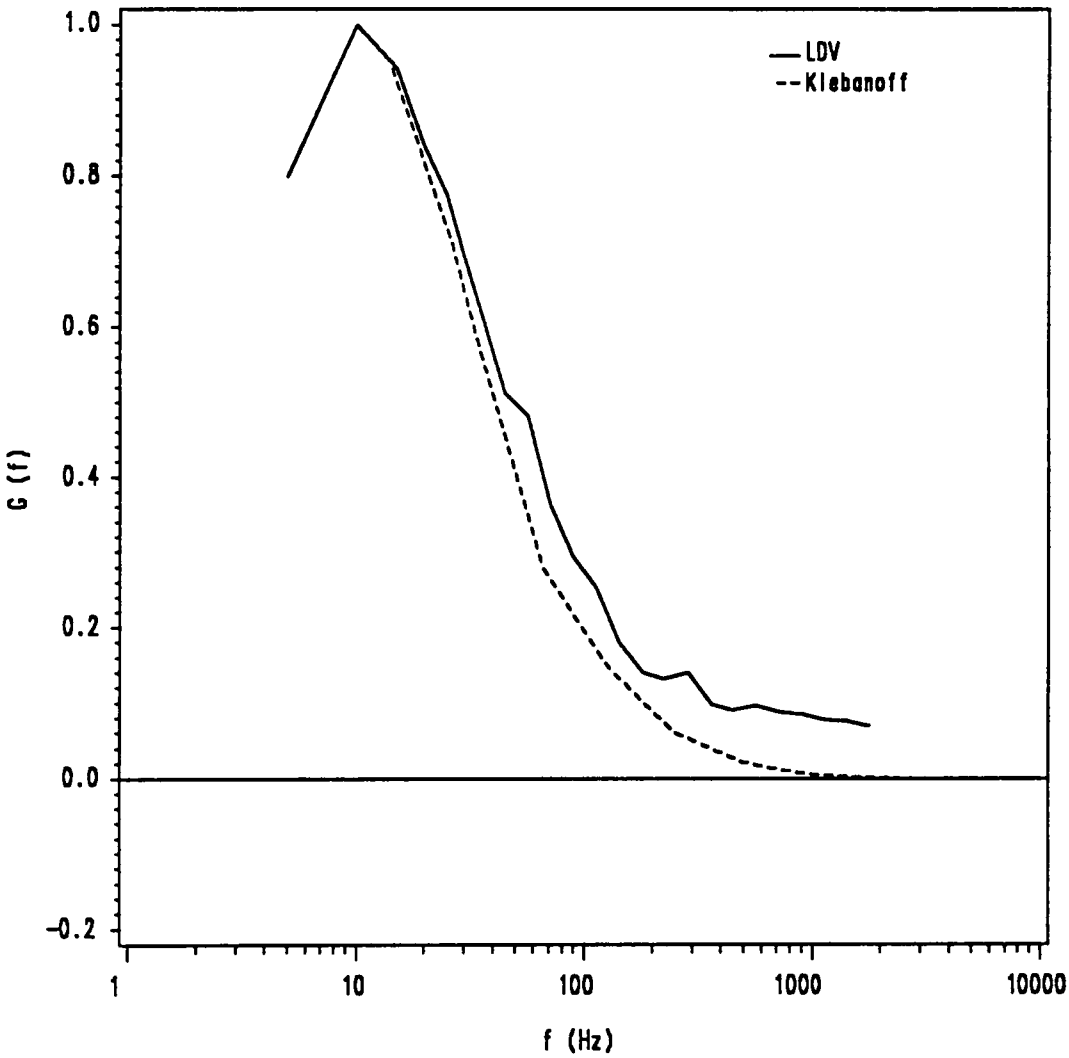

Figure 5.24. LDV Spectrum for 2DTBL Using DTM, After Octave Averaging

For the two-dimensional turbulent boundary layer, good spectral estimates were obtained only up to a maximum limit of about 300 Hz. At higher frequencies, the spectral level for the two-dimensional turbulent boundary layer was close to zero, and the discretized lag product method yielded negative estimates whereas the direct transform method had a significant amount of white noise.

It is recalled from the review earlier in this chapter that the spectra obtained from LDV data were all limited to lower frequencies, except for the experiments with jet flows. It should be noted that for jets, the spectral level did not fall close to zero up to frequencies of the order of 10-20 kHz.

Comparing the performance of the two methods, it was observed that at lower frequencies, the estimates from the discretized lag product method were relatively better. The direct transform method had a tendency to overestimate the spectral levels at lower frequencies. At higher frequencies with near zero spectral values, both methods performed poorly.

5.8 The Exact Lag Product Method

All the spectra presented so far have been calculated by the discretized lag product method or the direct transform method. The third method, the exact lag product nethod, has the disadvantage of being extremely slow computationally. On the other hand, it does not suffer from inaccuracies due to the slotting. Perhaps due to the slowness of this method, no reports of spectra computed using this method were found except for one simulation study by Gaster and Roberts [63].

It was decided to investigate whether this method offers any improvements in the spectral estimates to offset its computational disadvantage. Spectra were calculated for all the cases already discussed and the results are presented in the following.

Figure 5.25 shows the spectra computed for the simulated data set using the exact lag product method. Execellent results were obtained. However, the improvement over the results of the other two methods of Fig. 5.5 and 5.6 were found to be only modest.

Figure 5.26 shows the spectrum for the simulated sine wave at 200 Hz with real LDV time between data using the exact lag product method. Again the results were comaparable to the other two methods as seen by comparing with Figs. 5.7 and 5.8.

Figure 5.27 shows the spectra obtained by the exact lag product method for the vortex shedding flow. It is seen that the spectrum is similar to that obtained by the direct transform method shown in Fig. 5.15. That is, an added white noise level occurs where the spectral levels are small, with high variability in the estimates. The results for the discretized lag product method in Fig. 5.14 show a similar variability but around a spectral level close to zero. It should be noted that octave averaging was not performed for the spectra presented in Figs. 5.31-5.33. This is consistent with the results in the comparable figures, Figs 5.5-5.8.

Figure 5.28 shows the spectrum computed by the exact lag product method for the two-dimensional turbulent boundary layer. Averages of the spectra computed from the five individual data sets of 102,400 points each were used to yield the final spectrum. This method is again seen to have a higher noise level when spectral levels are close to zero, similar to the results in Fig. 5.23 for the direct transform method.

It was concluded that for these selected data sets studied, the exact lag product method did not perform significantly or consistently better than the other two methods. Hence it was concluded that the use of this method was not justified as it did not lead to any significant improvements to offset its computational slowness.

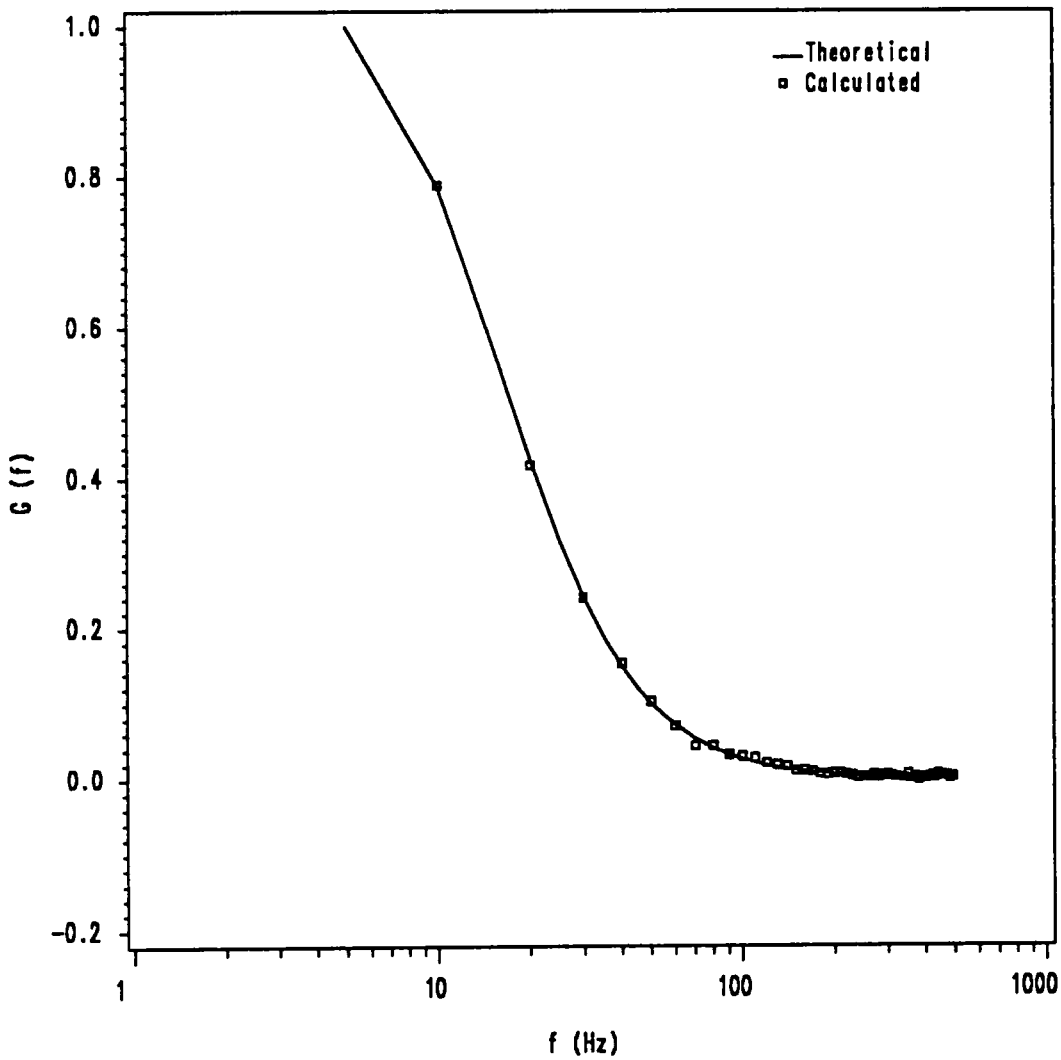

Figure 5.25. Spectrum from Simulated Data Using ELPM

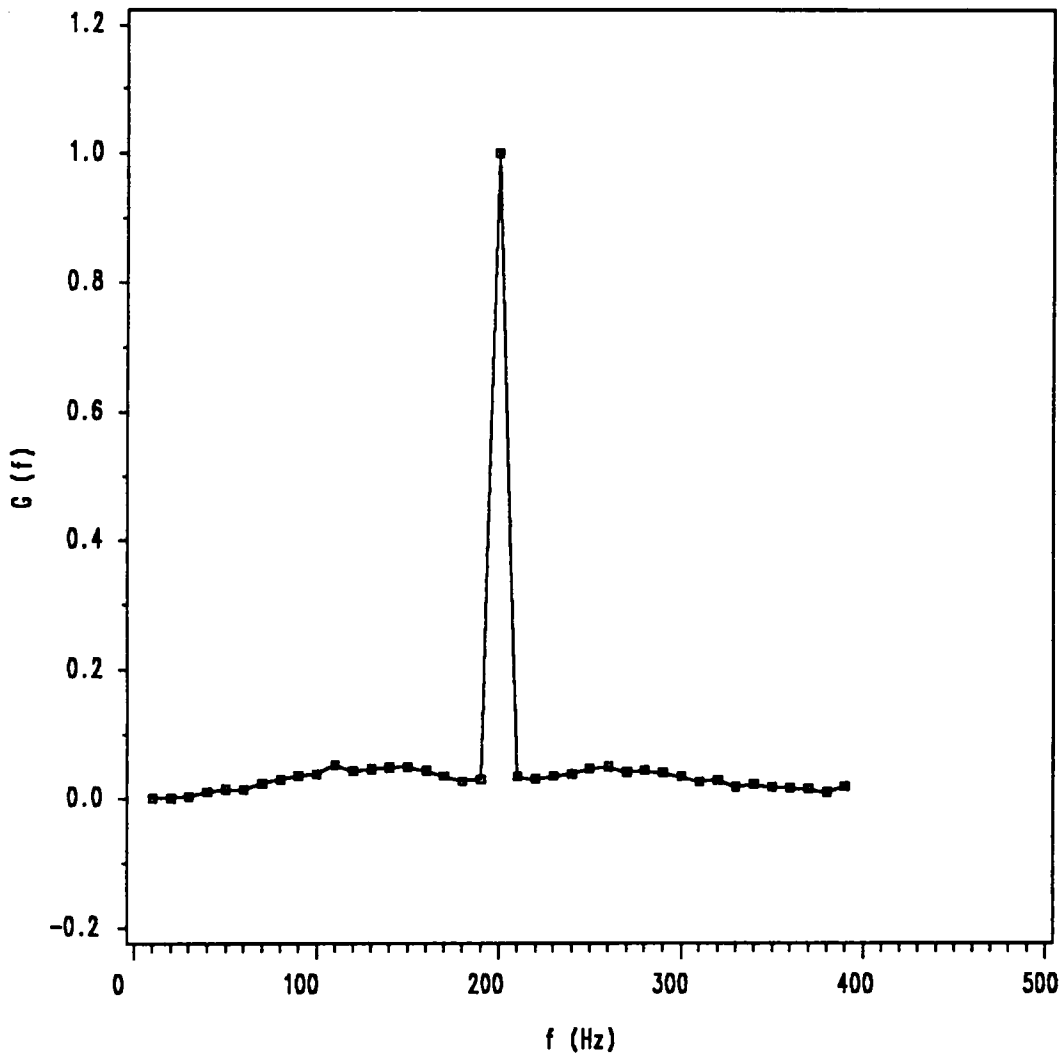

Figure 5.26. Spectrum for Simulated Sine Wave (f=200 Hz) using ELPM

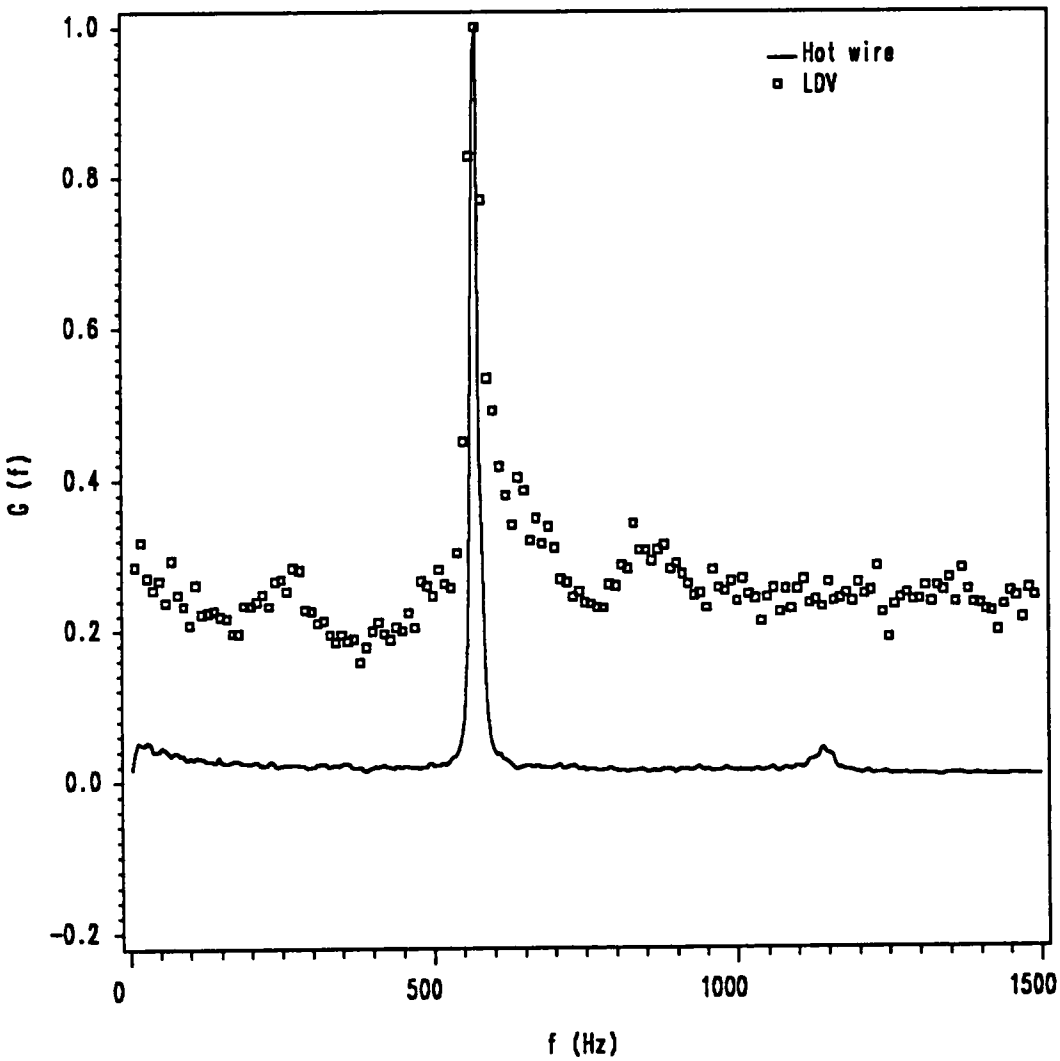

Figure 5.27. Spectrum for Vortex Shedding Flow Using ELPM

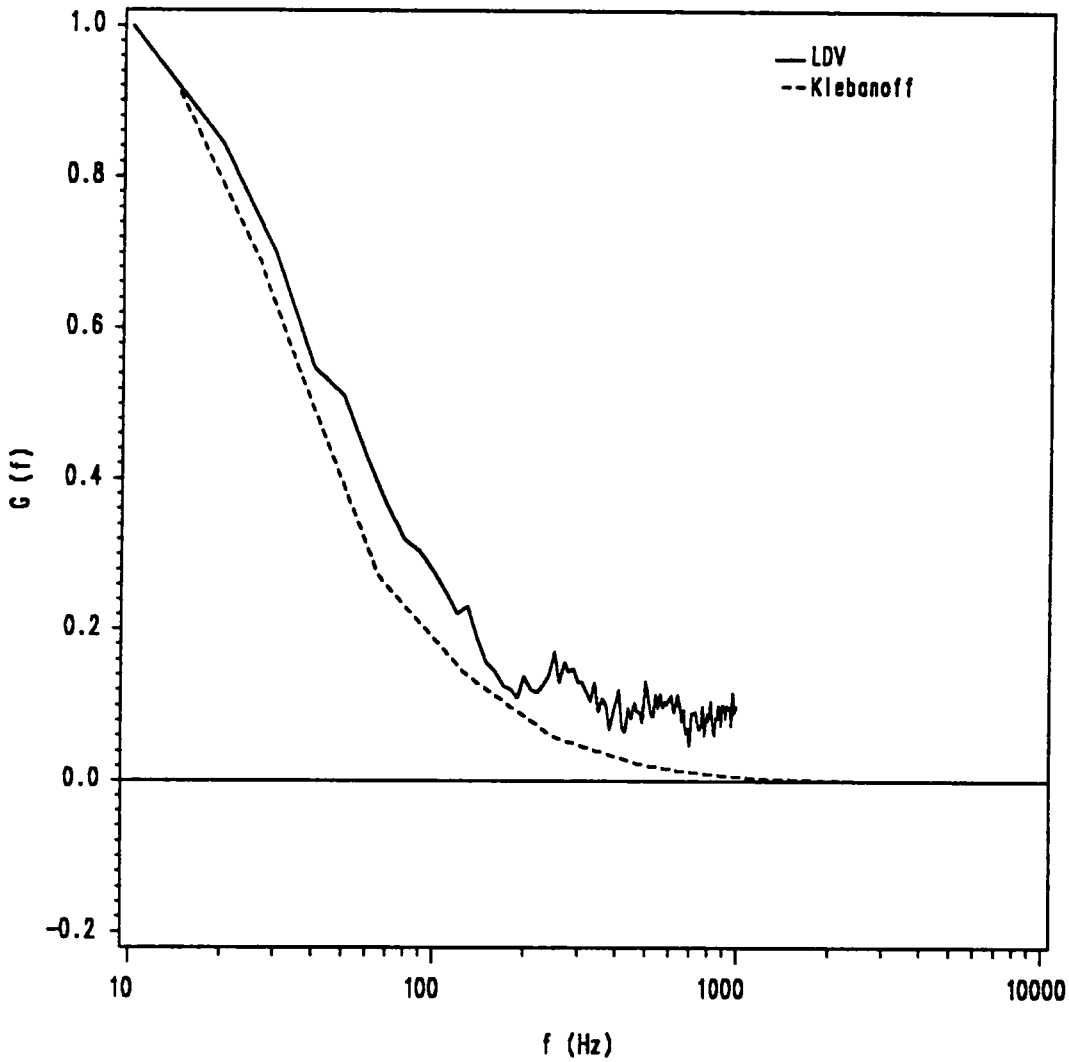

Figure 5.28. LDV Spectrum for 2DTBL Using ELPM

5.9 Conclusions

Three methods of spectral estimation for randomly sampled data, the discretized lag product method, the direct transform method and the exact lag product method, were tested for their performance under various simulated and real flow situations.

The discretized lag product method and the direct transform method both resulted in good spectral estimates for simulated data. In real flow situations, however, the direct transform method was seen to have an added white noise level where the spectral level was close to zero. On the other hand, the discretized lag product method gave rise to negative estimates where the spectral levels were close to zero. In the regions where the spectral levels were not small, both methods produced good spectral estimates. For spectra with a dominant frequency, accurate resolution of the spectral peak was possible using both the methods. For the two-dimensional boundary layer, reasonable prediction was possible only up to a maximum frequency of about 300 Hz. This upper limit appears to be determined by the near zero spectral levels after this frequency. In general, it was found that the spectral estimates were poor when spectral levels fell close to zero.

The absence of aliasing effects for randomly sampled data was demonstrated for the simulated sine waves with real time between data and for the vortex shedding flow. In both cases the average sampling rates were significantly below the classical Nyquist rate.

The spectral estimates obtained from the discretized lag product method were generally considered to be better than the those obtained from the direct transform method. This was evident in the cases of the vortex shedding flow and the boundary layer flow. For this reason, the discretized lag product method was used in all further spectral computations.

The exact lag product method was found to yield spectral estimates which were not significantly better than the other two methods, and also had high noise levels in the regions where

the spectral level was close to zero, similar to the direct transform method. Hence it was concluded that the use of the exact lag product method was not justified as it did not lead to any improvements in the spectral estimates to offset its computational slowness.

The assumption that the sampling follows the Poisson distribution was verified for two data sets. These data sets were found to follow a Poisson distribution closely.

6.0 Results for the Junction Vortex

6.1 Introduction

The characteristics of the strongly time variant flow in the junction vortex are discussed in this chapter. Evidence of this strongly time variant flow was first observed in real time smoke visualizations and subsequently confirmed in the real time measurements of Tree [23]. Several mechanisms for the strongly time variant flow in the junction vortex can be hypothesized. Possible mechanisms are:

1. The time variant flow in the junction vortex is associated with an inherent instability or natural frequency of the particular flow geometry. The spectrum of velocity fluctuations in such a flow could be characterized by a signature such as the dominant peak for a vortex shedding behind a cylinder.

2. The time variance in the junction vortex flow may be associated with the random flow fluctuations present in the upstream boundary layer.

3. The time variant flow may be generated by the random oscillations of the three-dimensional separation line.

6.2 Overview of the Junction Vortex Flow

The flow in the junction vortex has been investigated in great detail by Pierce, et al., [2] and Tree [23]. Some prominent features of the flow field obtained from these investigations are discussed in the following.

Figure 6.1 shows the picture of a surface flow visualization conducted by Pierce, et al. [2]. The separation point where the streamwise flow from upstream meets the reverse flow in the junction vortex was located from the surface flow visualization to be between x=-60 mm and x=-57 mm. From the separation point, two lines emanate, one to each side of the centerline, corresponding to the loci of ordinary separation points. Downstream of the ordinary separation line at x=-38 mm, is a distinct line under the vortex and corresponds to a relative minimum in the surface pressure distribution.

Figure 6.2 shows the mean flow field from LDV measurements made by Tree [23]. The mean flow field shows a single well defined vortex, the center of which was estimated by Tree at x=-35.7 mm, y=6.6 mm. The separation point is also shown upstream from the vortex and was estimated by Tree from the LDV velocity data closest to the floor to be at x=-50.8 mm. The differences in the location of the separation point indicated by the surface flow visualizations and the near wall velocity data suggested possible large gradients in a thin fluid layer. Figure 6.3 shows a summary of the features of the junction vortex flow obtained from different measurements.

6.3 Time Resolved Measurements in the Junction Vortex

In order to study the characteristics of time variant flow, a detailed set of time resolved LDV measurements were taken in the junction vortex flow region. From these data, various parameters which help in characterizing the time variant flow were computed.

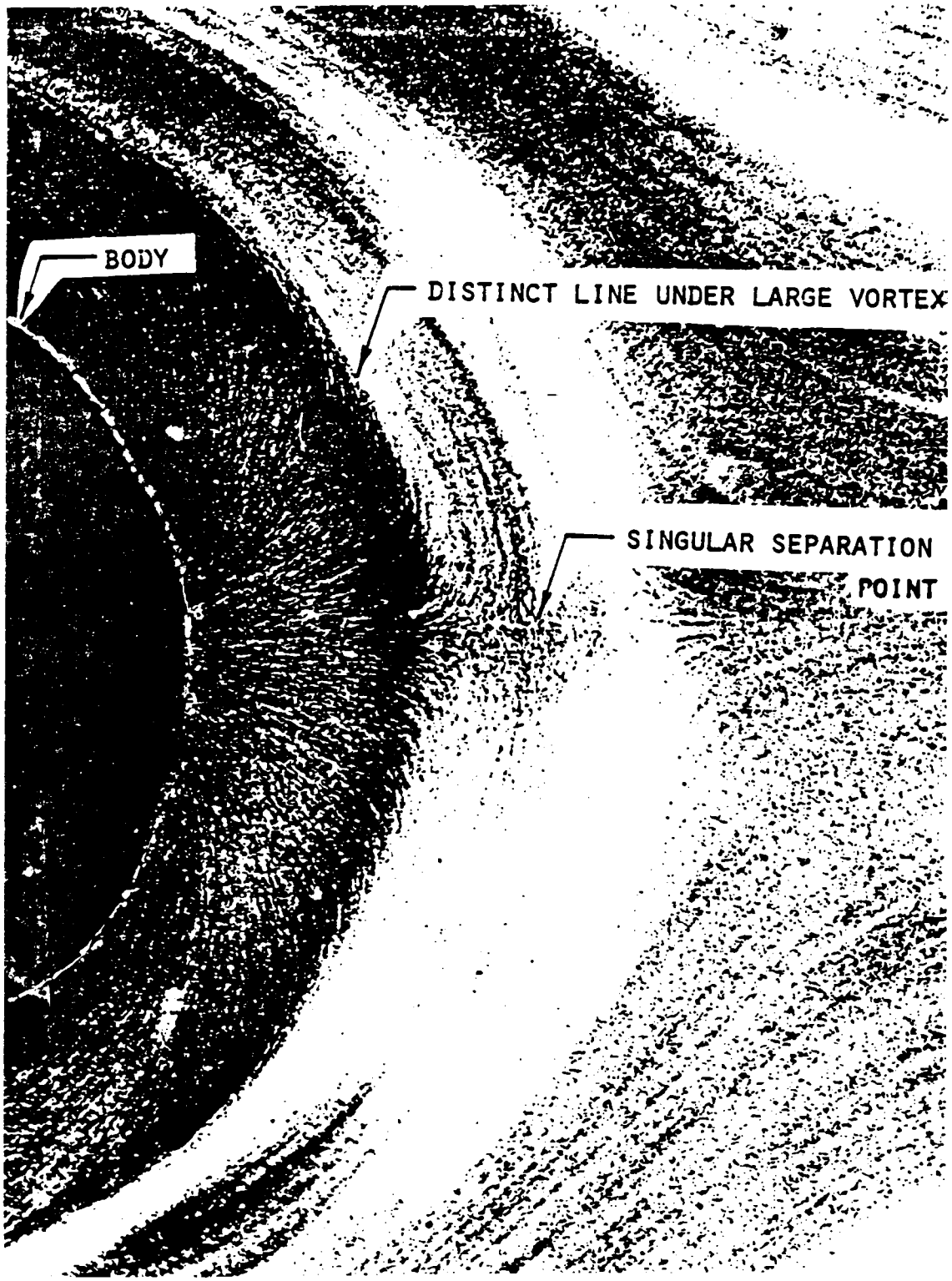

Figure 6.1. Surface Flow Visualization

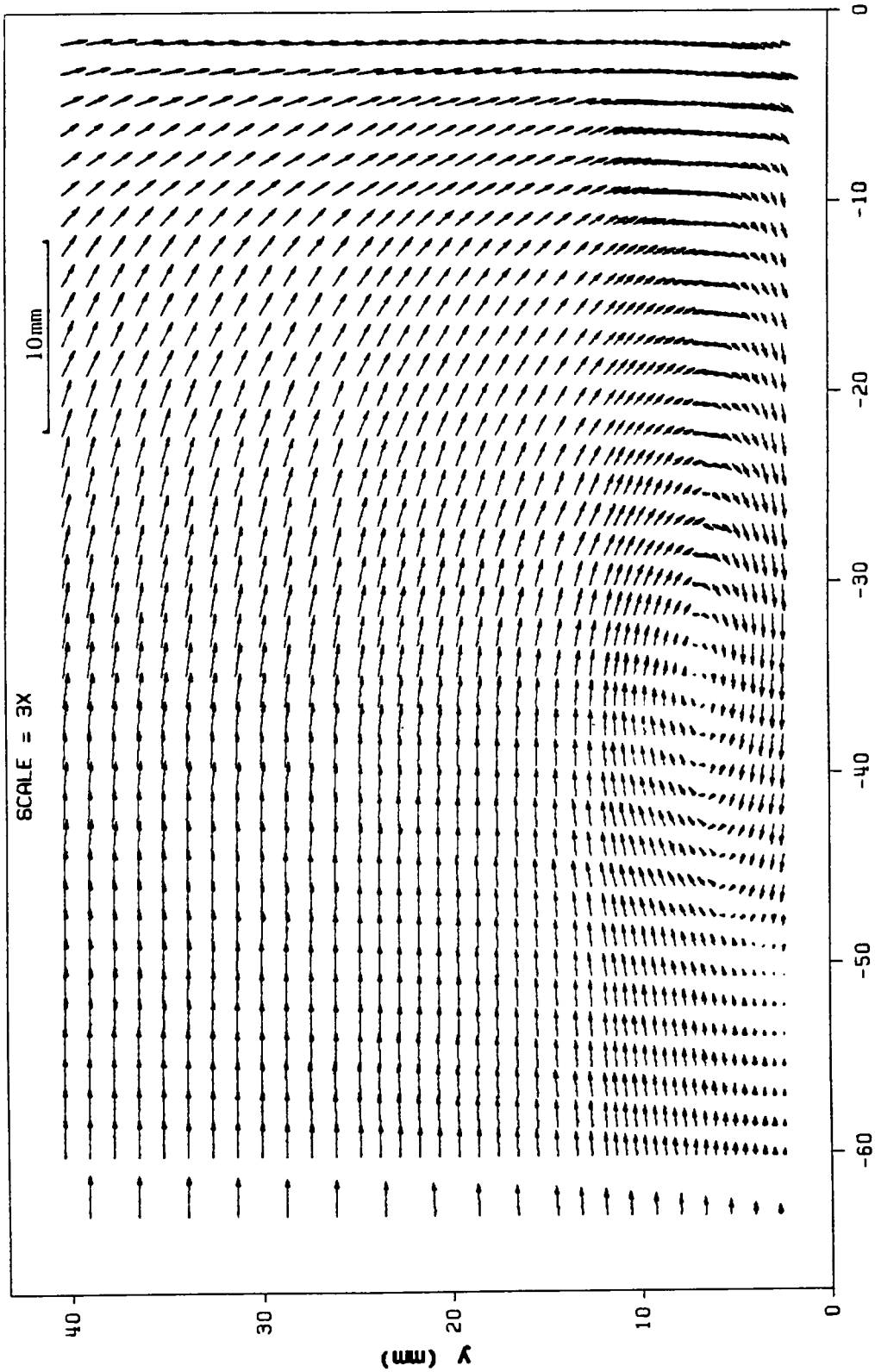

Figure 6.2. Mean Flow Field in the Junction Vortex from Tree [23]

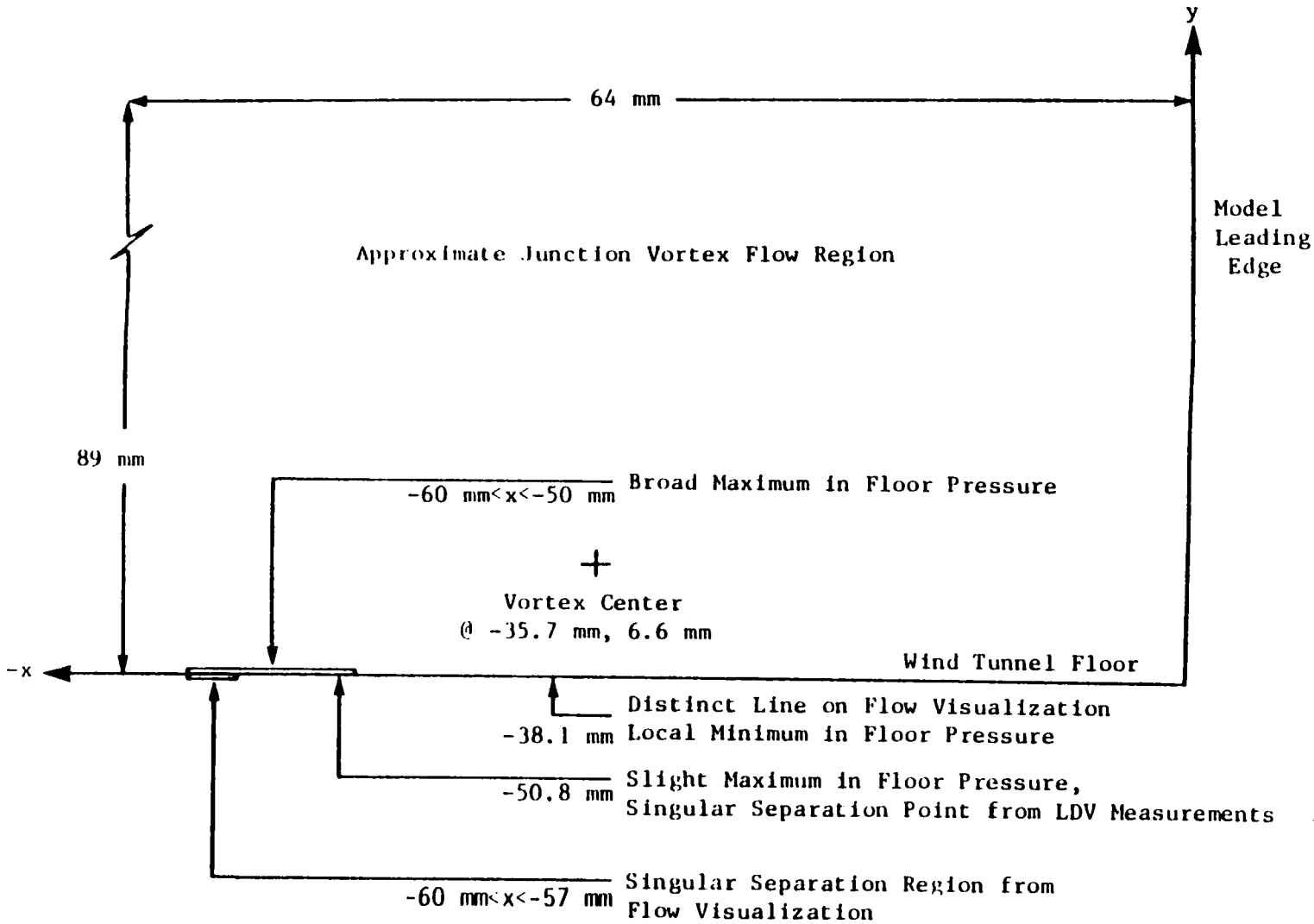

Figure 6.3. Some Features of the Junction Vortex Flow

The measurement region and the points where LDV data were taken in the present investigation is shown in Fig. 6.4. Data were taken in a total of five hundred and four points. The measurement region extended 66.7 mm upstream from the leading edge of the body and 50.8 mm in the vertical direction. The closest data points from the body leading edge were at a distance of 3.2 mm. The data points closest to the floor were at a distance of 2 mm. Additional data were collected around the separation region at y=2 mm up to x=-82.6 mm and are not shown in Fig. 6.4. At each measurement point, 10,240 individual LDV realizations with a nominal data rate of about 250 Hz were collected. The various parameters characterizing the time variant flow are presented in the following.

6.3.1 Mean Flow Field

The mean velocity vectors of the junction vortex flow are shown in Fig. 6.5. The LDV measurements show a single, well defined vortex, and a separation point in the region between the vortex induced reverse flow and the incoming flow from upstream. These features are essentially identical to those obtained from the more detailed LDV measurements made by Tree [23], and summarized in Fig. 6.3. From a linear interpolation of the velocity vectors, the center of the time mean vortex was located at x=-38.8 mm, y=6.9 mm. This position differs only slightly from the position given by Tree (x=-35.7 mm, y=6.6 mm).

If the separation point is defined as a point bounded by positive and negative velocities on opposite sides, then this point can be approximately located from the velocity data closest to the floor. Using linear interpolation between the velocity values closest to the floor, the singular separation point was located at x=-60 mm. This value differs significantly from the position estimated by Tree (-50.8 mm) but is consistent with surface flow visualizations. It should be noted that in the present investigation velocity data were obtained closer to the floor (2 mm) than those obtained by Tree [23] (2.3 mm).

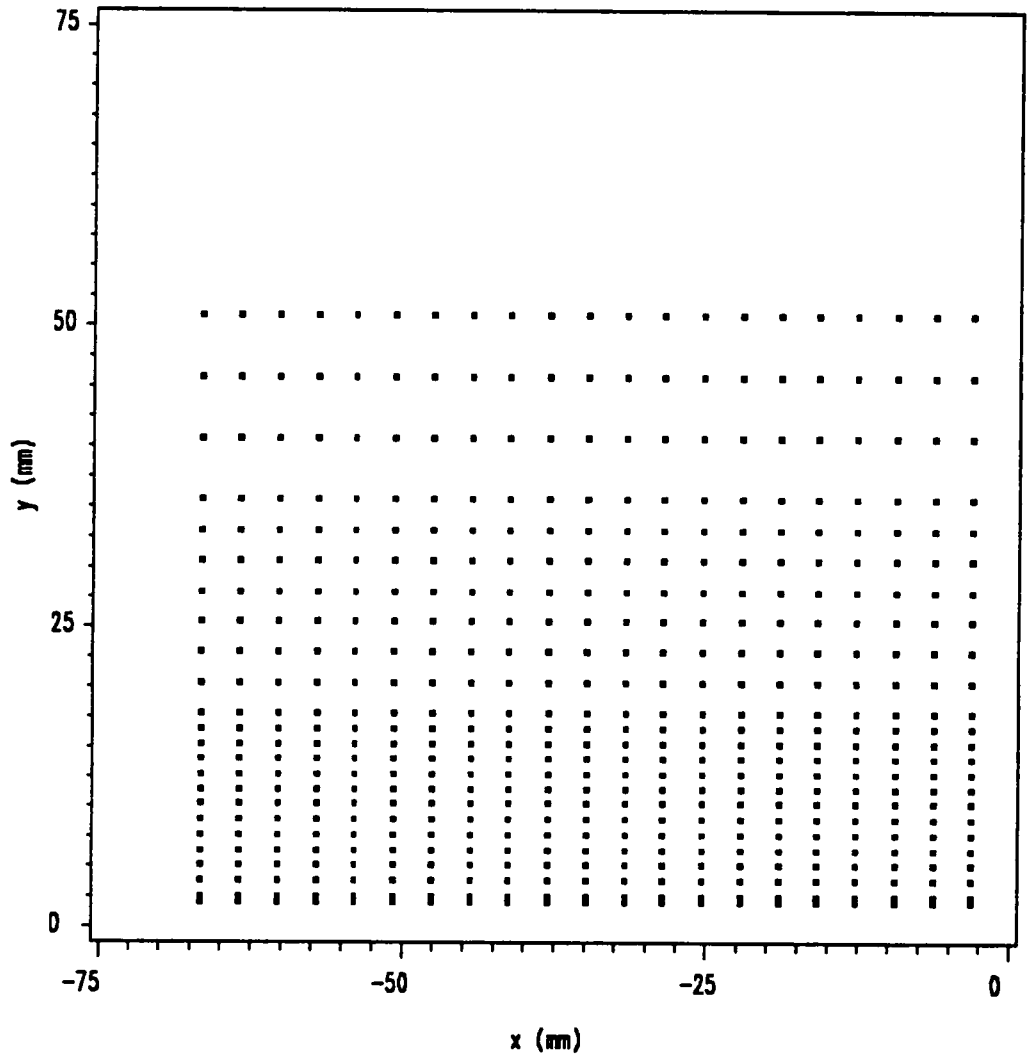

Figure 6.4. Time Resolved LDV Measurement Points

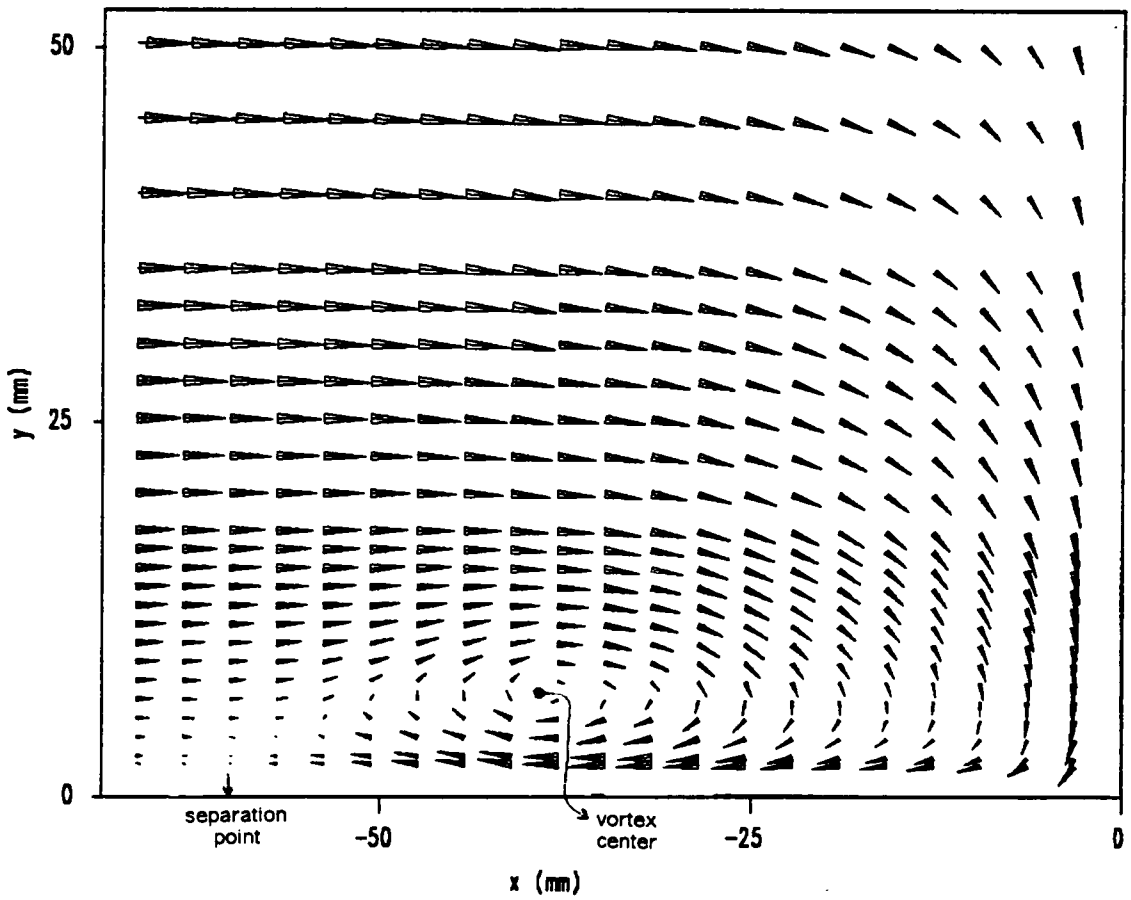

Figure 6.5. Mean Flow Field in the Junction Vortex

The nominal center of the mean vortex is indicated by the dot in Fig. 6.5. The arrow in the x-axis indicates the location of the separation point as calculated from the mean velocity vectors. In some of the figures which follow, the dot and the arrow will be used to show the locations of the vortex center and the separation point respectively.

Figure 6.6 shows the distribution of the vorticity values computed from the velocity data. The vorticity values were computed by using a second order accurate central difference formula for the interior points and forward or backward difference formula for the boundary points. From the 504 vorticity values computed from the measured velocity field, the contour generating software interpolated and estimated the vorticity values on a 100 x 100 grid. The vorticity distribution is consistent with the mean flow field. The core of the large vortex as seen from the vorticity plot and the mean flow field were coincident, and the highest values of vorticity of about negative 500 rad/sec were found in the approximate region of the center of the vortex. From the vorticity contours, the presence of two other vortices located close to the floor may also be inferred. The vortex located around x=-50 mm is physically the more prominent and has positive values of vorticity of up to about 200 rad/sec. While the other smaller vortex close to the body leading edge is less prominent, it has peak values of vorticities of up to about negative 700 rad/sec.

6.3.2 Turbulence Intensities

Turbulence intensities were calculated for both the u and v component of the velocities from the LDV data. The turbulence intensity, $\hat{u}$, of the u component was calculated from

$$\hat{u} = \frac{\sqrt{\overline{u'^2}}}{V_*} \tag{6.1}$$

where u' is the fluctuating component of the velocity and V_* is the reference velocity at the throat of the wind tunnel. For a two-dimensional boundary layer usually the freestream velocity or the local velocity is used to normalize the turbulence intensities. Normalizing by the

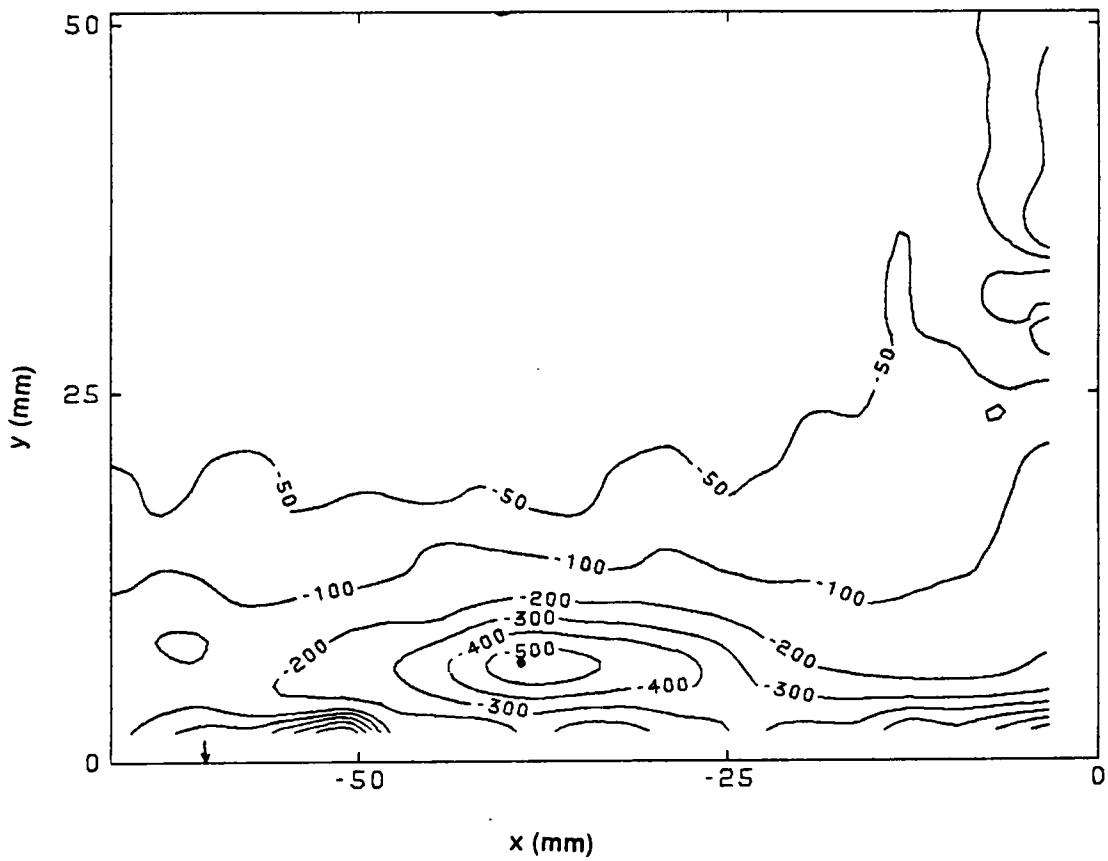

Figure 6.6. Computed Distribution of Vorticities (rad/sec)

local velocity is not convenient for the junction vortex flow as there are locations with velocities near zero. In such locations the turbulence intensity would tend to infinity if normalization with the local velocity were used. A residence time weighting was used in the calculation of the numerator in Eq. 6.1 to remove velocity bias as discussed in Chapter two.

Figure 6.7 shows the distribution of turbulence intensities of the u component for the entire flow field. The maximum turbulence intensities were found in the region between the time mean center of the vortex and the time mean separation point. Typical maximum values of turbulence intensity found in boundary layer flows is of the order of 0.1, when non-dimensionalized with the freestream velocity. The turbulence intensities found in the junction vortex were very high, being two to three times higher than typical boundary layer values. Relatively lower turbulence intensities were found near the leading edge of the body.

Figure 6.8 shows the distribution of turbulence intensities for the v component of the velocities. Again very high values of the turbulence intensities were obtained. Peak values of turbulence intensities of the v component were found in the vicinity of the time mean center of the vortex.

Relatively smaller turbulence intensities were found above approximately $y = 15$ mm, indicating that most of the energetic fluctuations in the junction vortex are confined within a distance of approximately 15 mm from the wall. This is about twice the distance from the floor of the position of the time mean center of the large vortex.

Thus the time variant flow in the junction vortex is found to be characterized by very energetic fluctuations, confirming the observation from smoke flow visualizations. Fluctuations of velocities at least two to three times stronger than the usual boundary layer intensities are observed in the junction vortex.

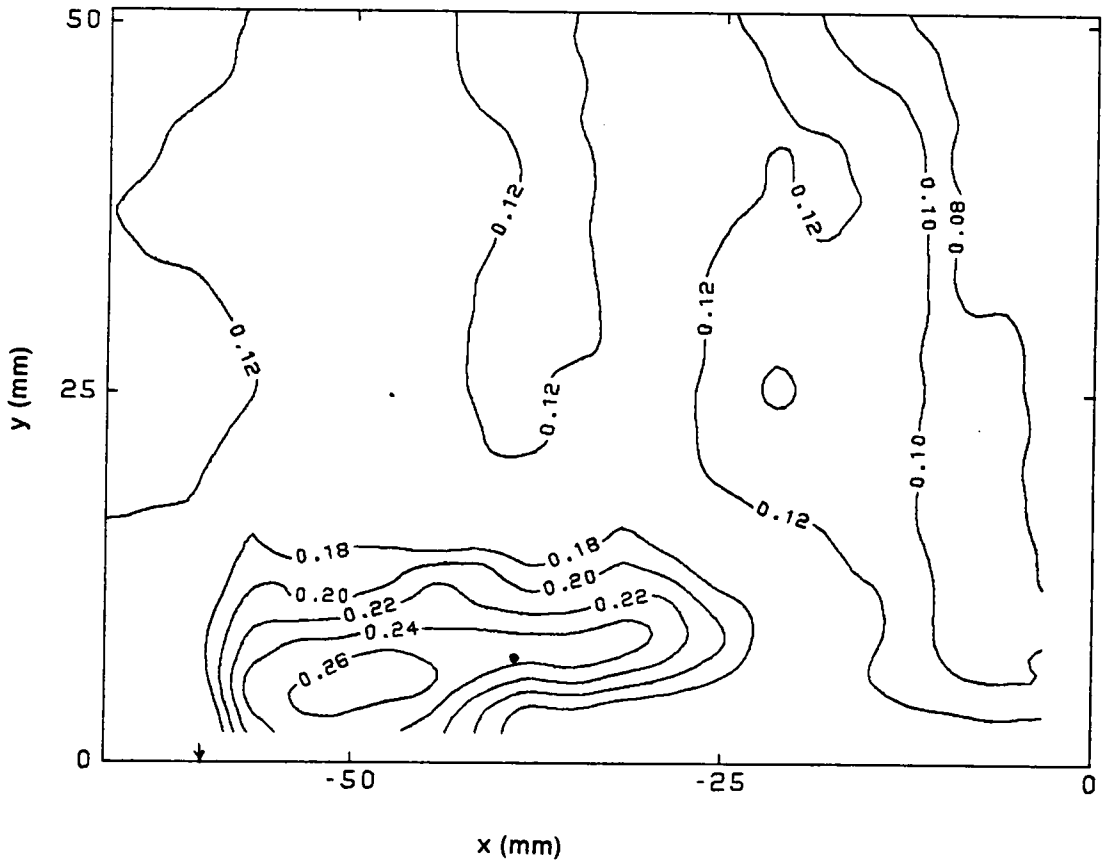

Figure 6.7. Distribution of u Component Turbulence Intensities., $\hat{u}$

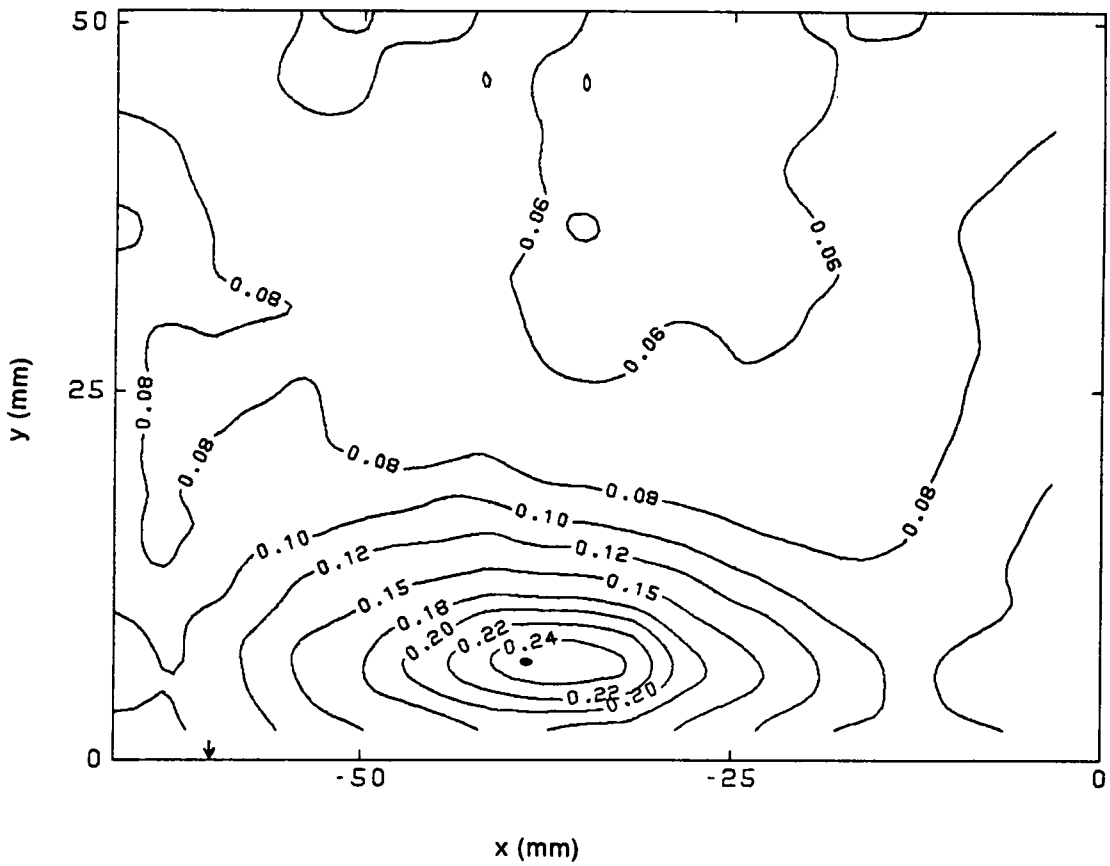

Figure 6.8. Distribution of v Component Turbulence Intensities, $\hat{v}$

6.3.3 Histograms of the Instantaneous Velocities

It is usually assumed that the turbulence is Gaussian, i.e., the instantaneous velocities follow a normal distribution. Regions of flow were found in the junction vortex flow, where marked deviations from the normal distribution were observed.

An approximate boundary where such histograms were found, is given by Fig. 6.9. In particular, histograms with multiple peaks were found for all points below the solid line. This region encompasses the whole junction vortex flow, including the mean separation point. This similarity in characteristics for the three-dimensional separation flow and the junction vortex flow may be speculated as an evidence that these two flow structures are interdependent.

Eighteen most prominent histograms for the u and v components of the velocities are shown in Figs. 6.10 and 6.11. The locations of the u histograms were denoted by the points marked with plus signs and the locations of the v histograms were marked with crosses in Fig. 6.9. Although the outer envelope of the histograms are similar to a normal distribution, there are two or more prominent peaks in the histograms. Tree [23] and subsequently Devenport and Simpson [22] also reported two peaks in the histograms of the velocities in the junction vortex. Histograms with multiple peaks were less frequent for the v component. Most of the histograms for the v component were close to the shape of a normal distribution.

Initially it was thought that the peaks in the histograms were occuring because of an inadequate number of data points used in the histogram construction. It was thought that as larger data sets were used, the gaps in the histograms would fill in, with the histograms more closely resembling the normal distribution. The histograms in Figs. 6.10 and 6.11 were computed from 10,240 LDV realizations. To test whether this amount of data was adequate, u histograms with ten times the usual number, i.e., with 102,400 LDV realizations were constructed at $x=-38.1$ mm, $y=5.1$ mm. No differences in the histograms were found with the increased number of data as seen from Fig. 6.12. It is believed that the peaked shapes of the histograms occur

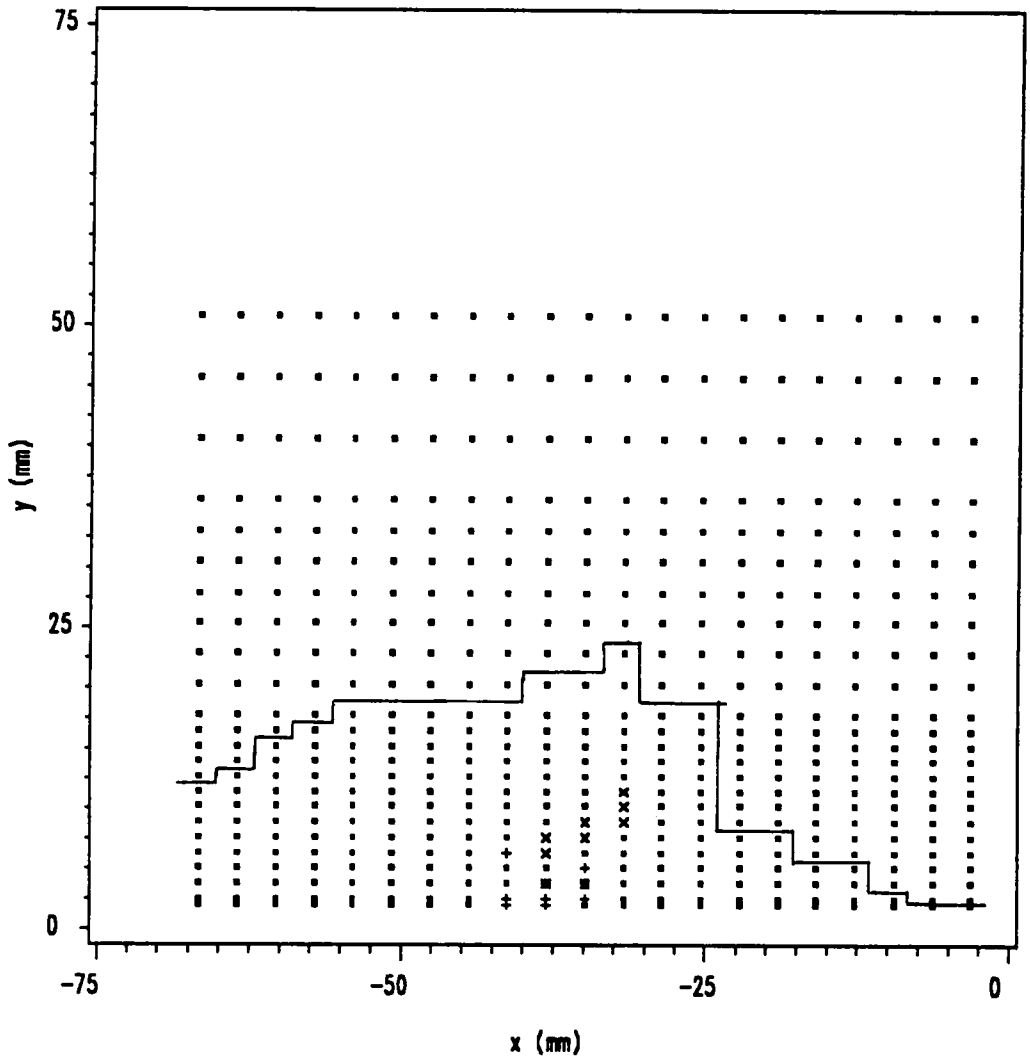

Figure 6.9. Locations of Histograms with Multiple Peaks

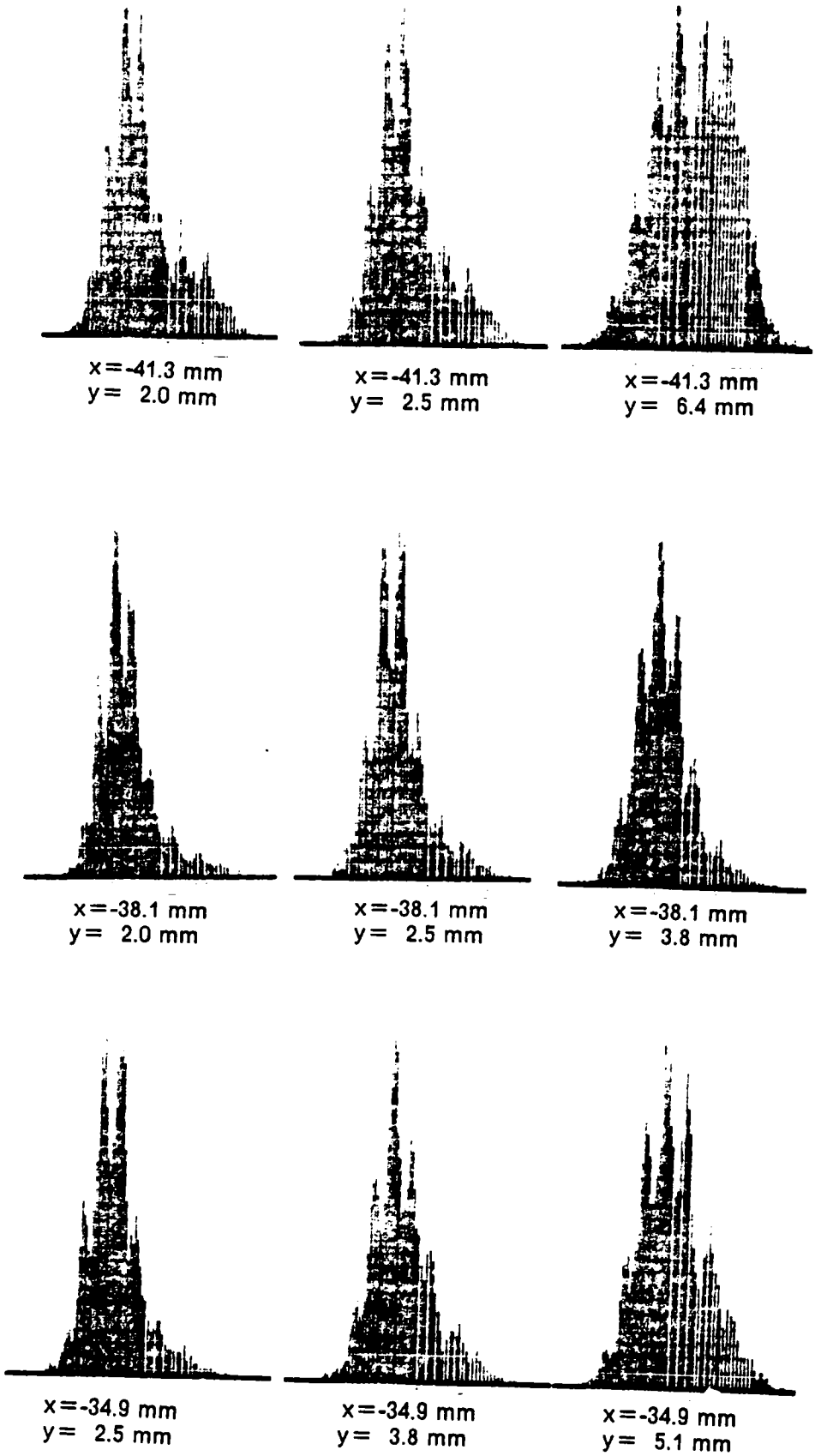

Figure 6.10. Selected Histograms of the u Component

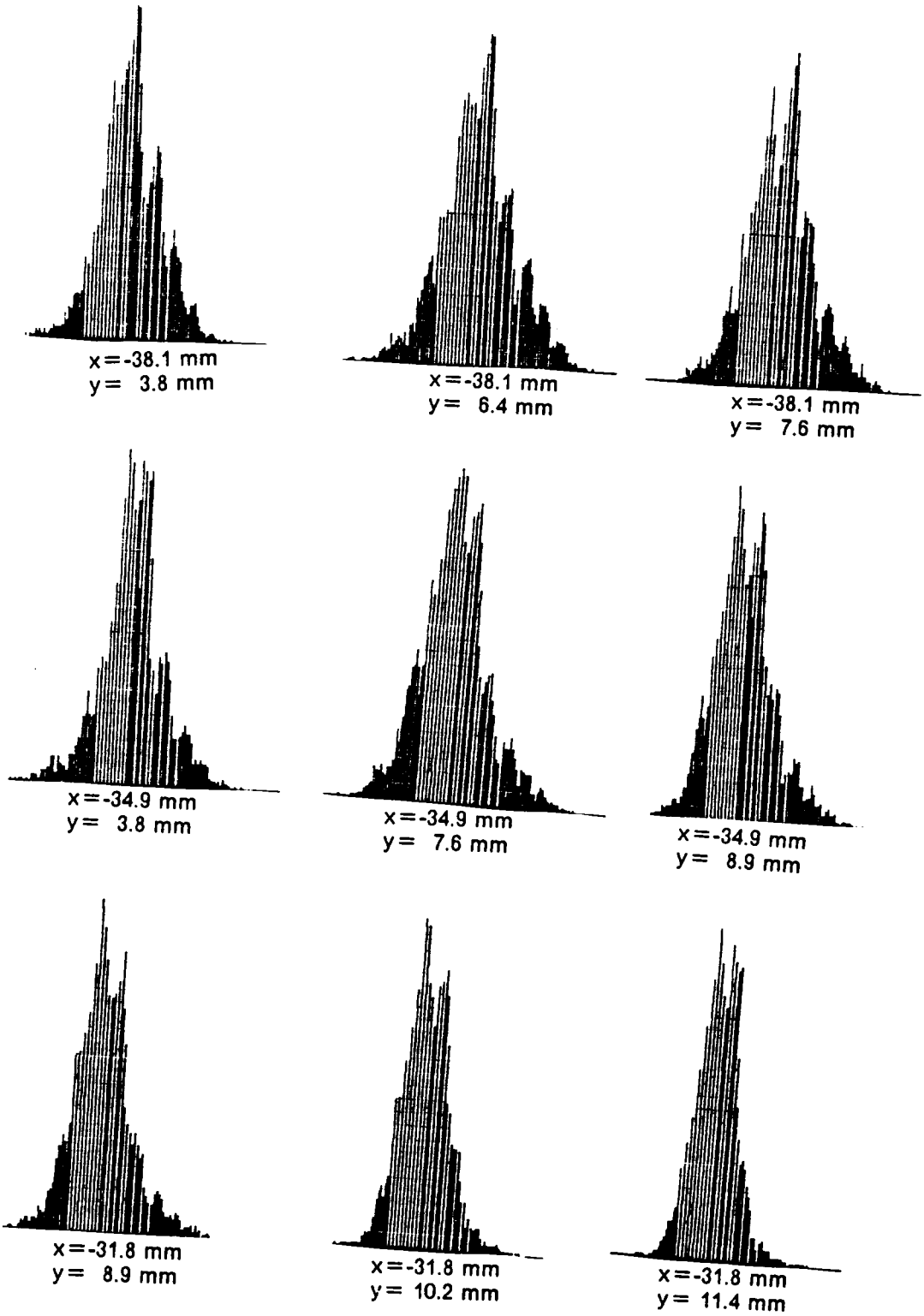

Figure 6.11. Selected Histograms of the v Component

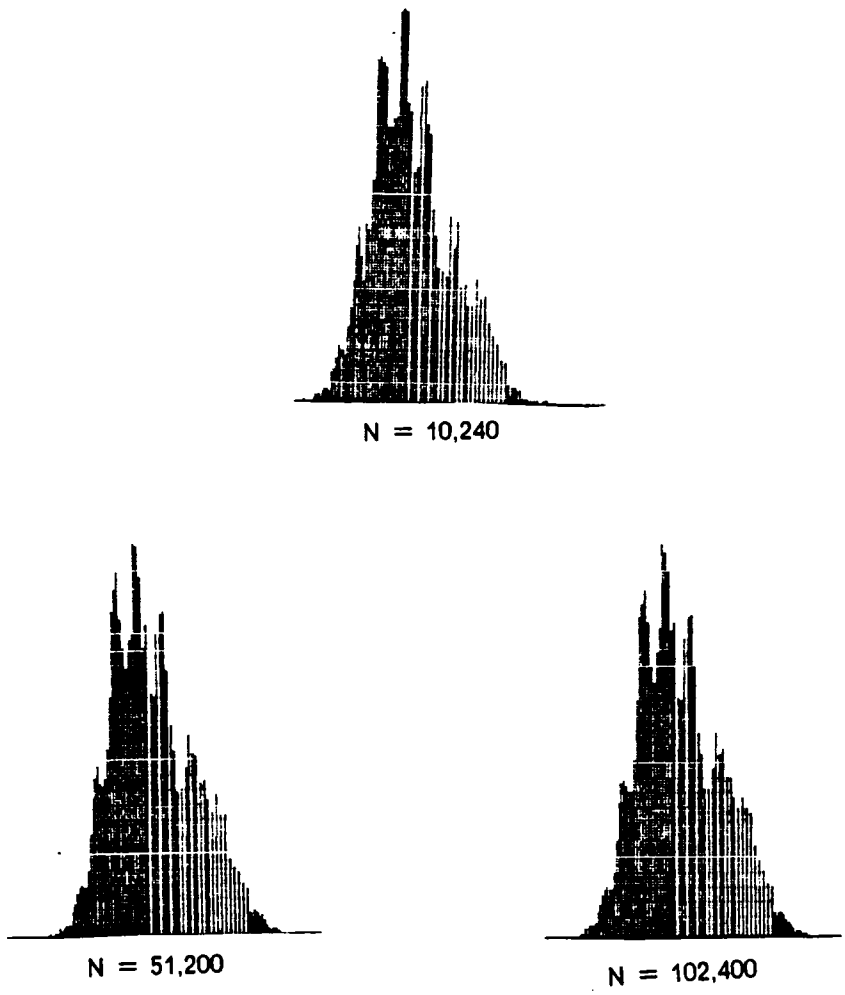

Figure 6.12. Effect of Amount of Data for Histograms

because of some yet to be determined characteristics of the junction vortex flow. It is also interesting to note that there were always at least a few empty slots in the histograms, in spite of the large number of data analyzed. These are very interesting phenomena, whose study may lead to new physical insights for the junction vortex flow.

6.3.4 Reverse Flow Intermittency

The reverse flow intermittency is defined here as the probability that the instantaneous velocity is in the reverse direction. The positive directions of the coordinate axes were taken as the forward directions. The reverse flow intermittency was computed for both the u and the v components of the velocity. Histograms of the instantaneous velocity values were first constructed for each measurement point, a few of which were shown in Figs. 6.10 and 6.11. From the histogram data, the reverse flow intermittency was calculated as follows.

If $h_1, h_2, \ldots, h_n$ are the histogram ordinates for velocity values $u_1, u_2, \ldots, u_n$, then the reverse flow intermittency was given by,

$$I = \frac{\sum_{i=1}^{m} h_i}{\sum_{i=1}^{n} h_i} \tag{6.2}$$

where m is the maximum histogram ordinate up to which the velocity is negative.

The distributions of the reverse flow intermittency for the u component of the velocity are shown in Fig. 6.13 for the entire flow field. From the contour line corresponding to 0.1 in Fig. 6.13 it can be seen that for an approximate value of y greater than 10 mm, the flow is primarily in the forward direction. In a similar way, mostly reverse flow (contour line = 0.9) is present in a region approximately bounded by y = 4.3 mm and -44.7 mm $\leq x \leq$ 0 mm. Between these two

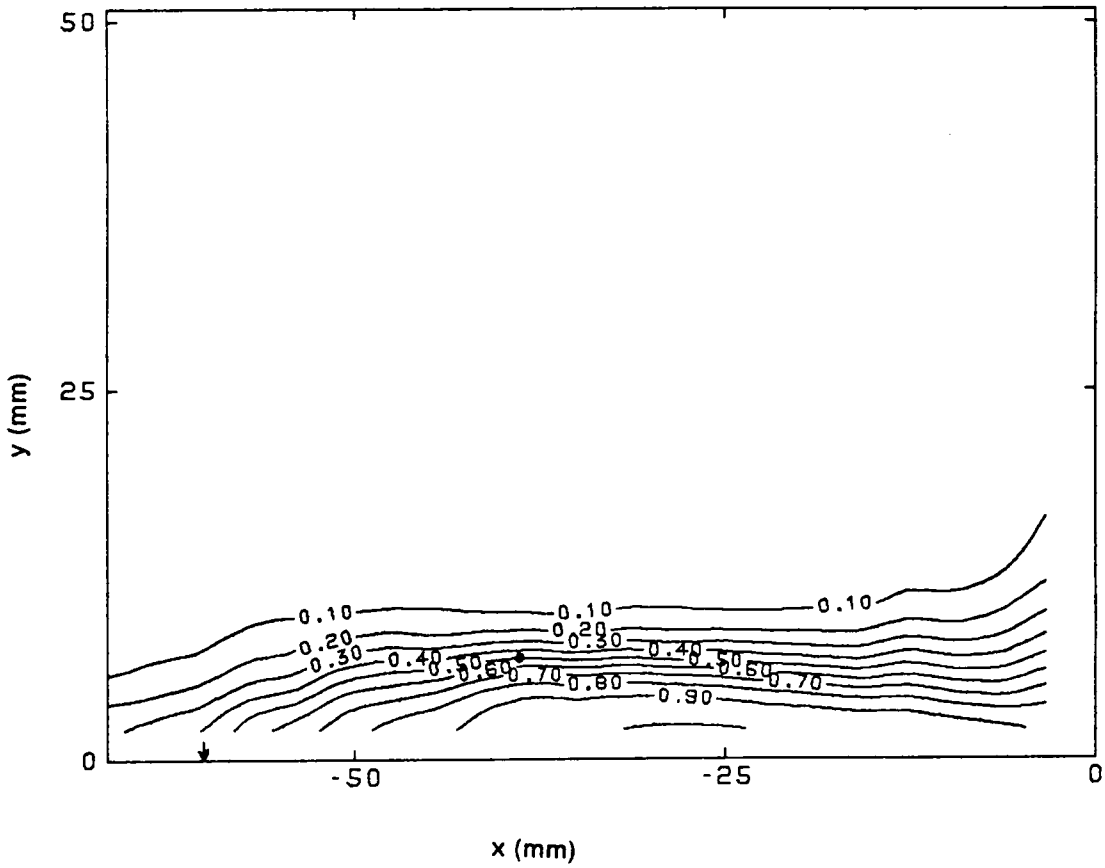

Figure 6.13. Reverse Flow Intermittency Distribution for the u Component

extremes, the flow is partly in the forward and partly in the reverse direction. These results are consistent with the location of the time mean center of the vortex and the singular separation point.

Figure 6.14 shows the reverse flow intermittency distribution for the v component of the velocity. Here a region in the range -38.1 mm $\leq x \leq$ 0 mm is seen to have mostly reverse velocities, corresponding to the contour line of 0.9.

The center of the time mean vortex can be defined as a location where the reverse flow intermittencies for both the u and v component of the velocities have a value equal to 0.5. This point was computed from the reverse flow intermittency data and was located at x=-39 mm and y=6.9 mm. This value agrees very closely with the position of the center of the vortex obtained from the mean velocities.

6.3.5 Fluctuations in the Neighborhood of the Separation Point

From the mean flow information, the time mean separation point was computed to be at approximately 60 mm. In real time, the separation point for turbulent flows is not a single point well defined in space, but fluctuates with time. This was demonstrated by Simpson, et al. [77] for a two-dimensional turbulent boundary layer under adverse pressure gradient.

Figure 6.15 shows the reverse flow intermittencies calculated at the measurement point closest to the wall (y=2 mm) plotted as a function of distance from the leading edge of the body. The intermittent reverse flow starts appearing at around x=-80 mm to -70 mm and increases continually until a region around x=-38 mm to -30 mm is reached where the flow is in the reverse direction most of the time. This is consistent with the mean flow results as under the vortex the velocity is in the reverse direction most of the time. It should be noted that these results are obtained from velocity data very close to the floor, but not on the floor.

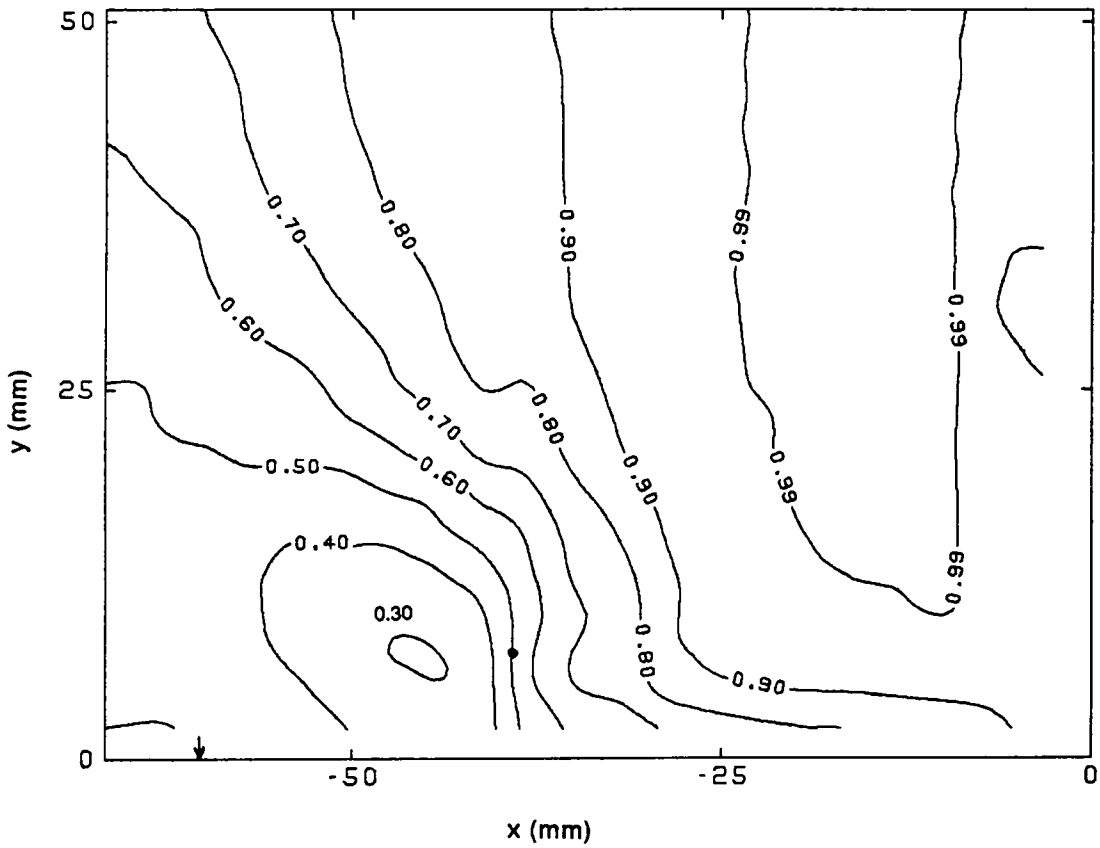

Figure 6.14. Reverse Flow Intermittency Distribution for the v Component

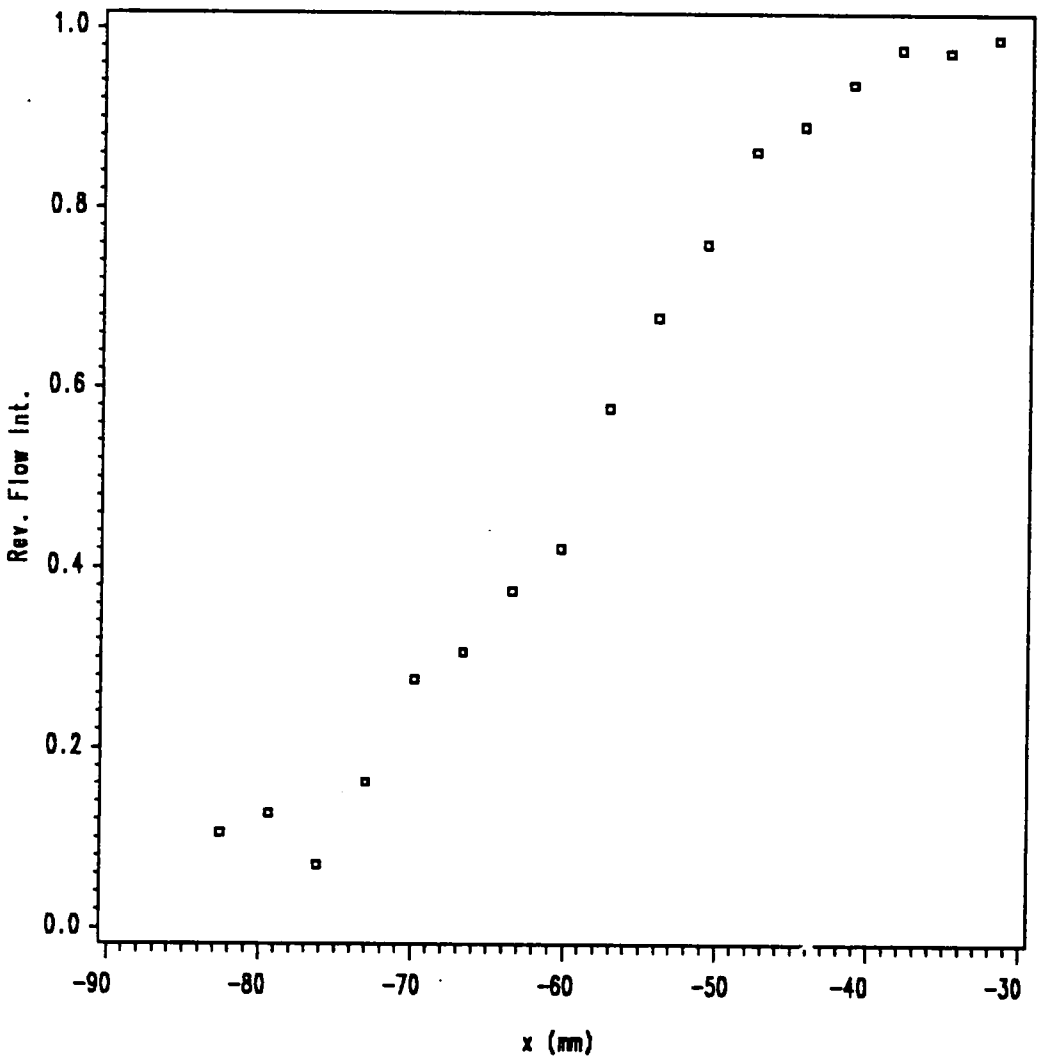

Figure 6.15. Reverse Flow Intermittencies Near the Separation Point

It is also interesting to note that the location corresponding to a value of reverse flow of intermittency of 0.5 from Fig. 6.15 is given as x=-58.8mm. This location of the singular separation point agrees within 1.2 mm with the location obtained from the mean flow results.

The instantaneous singular separation point can be defined as a location of zero instantaneous velocity. Also, positive values of velocity are expected before separation and negative values of velocity after separation. From the reverse flow intermittency data, then it can be concluded that the instantaneous position of the separation point fluctuates between the approximate limits -80 mm $\leq x \leq$ -30 mm. The position of the junction vortex is bounded by the separation point and the leading edge of the body. Hence the size of the junction vortex can be envisioned to fluctuate between these two limits.

6.3.6 Maximum and Minimum Positions of the Junction Vortex

From the instantaneous velocity data collected at each point, average values of maximum and minimum velocities were calculated. The maximum and the minimum values of the fluctuating velocities were defined here as the maximum or the minimum value between two zero crossings, where the mean value was subtracted from the instantaneous velocities before processing. For a given sequence of instantaneous velocities, there will be many such maxima and minima. All the maxima and minima found were averaged to give an average value of the maximum or minimum velocity at the measurement point.

Figures 6.16 and 6.17 show vector plots of the maximum and the minimum velocities respectively. Since the separation point in the plane of symmetry bounds the junction vortex on one side, it is reasonable to assume that the size of the junction vortex flow region changes with the location of the instantaneous separation point. If it is further hypothesized that the fluctuating velocities at all points attain the maximum and minimum at the same time, so that the vortex moves as a rigid body, then Figs. 6.16 and 6.17 can be viewed as the extreme positions and shapes of the junction vortex. In any case, the limits seen in these figures are the maxi-

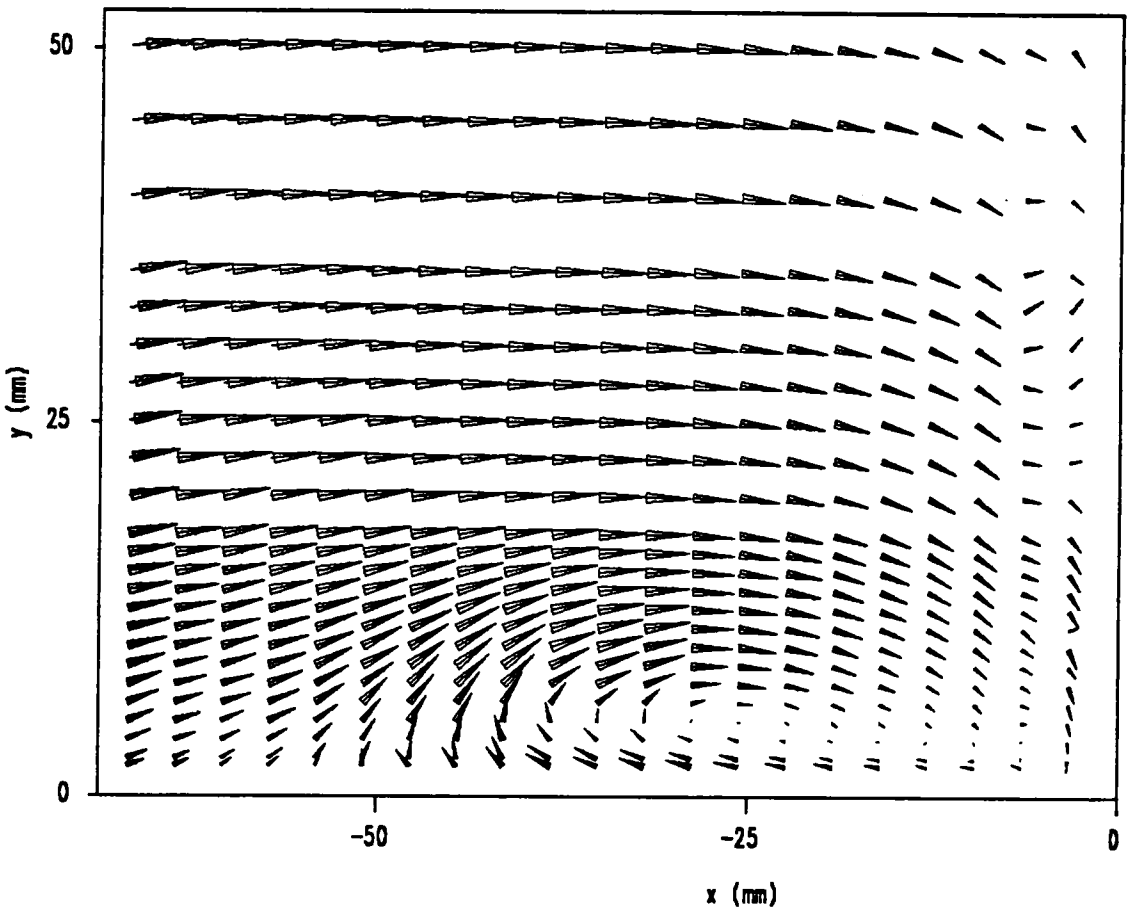

Figure 6.16. Maximum Velocities in the Junction Vortex

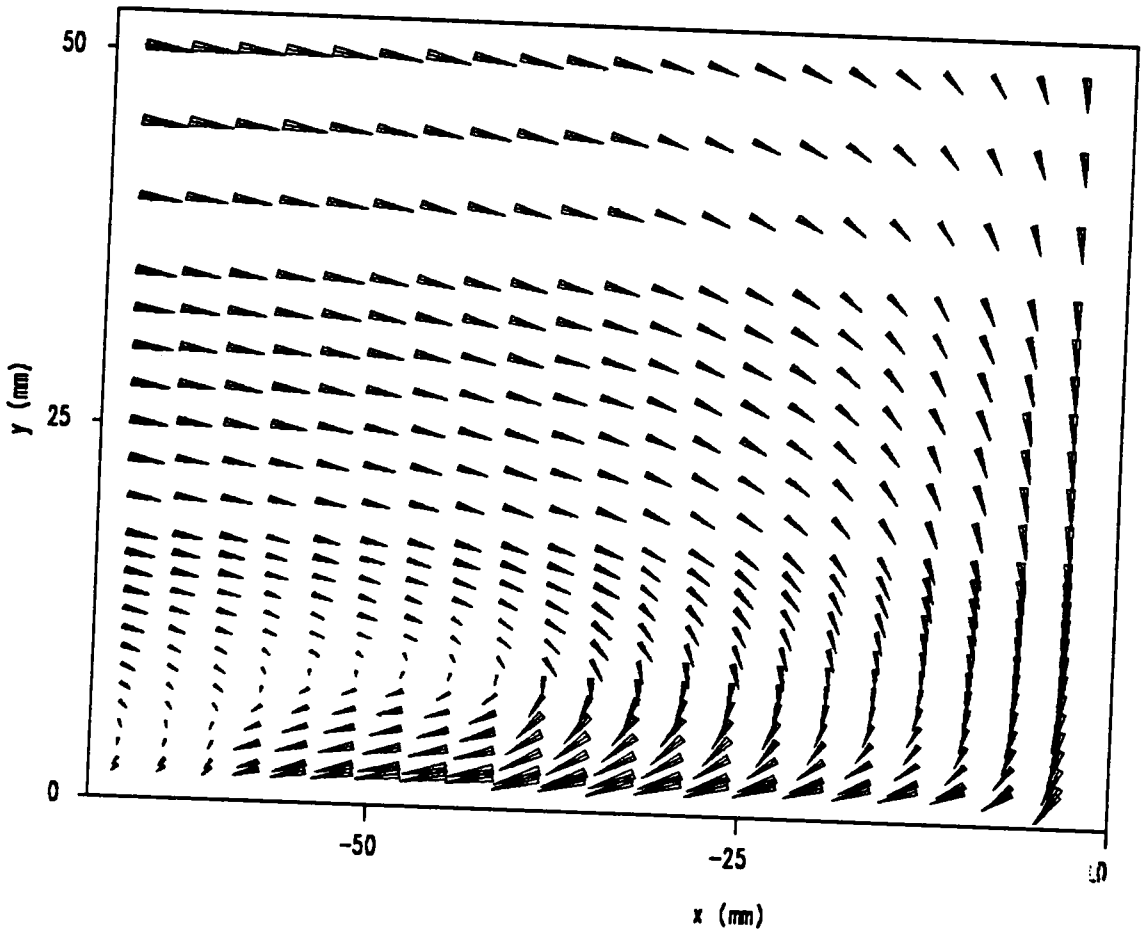

Figure 6.17. Minimum Velocities in the Junction Vortex

mum possible excursions of the junction vortex in a mean sense. The reader is cautioned that other than the preceding description, no other physical meaning should be attached to these plots.

6.4 Spectra of the Junction Vortex Flow

The strongly time variant character of the junction vortex flow was investigated using the time resolved LDV measurements as described in the previous sections. In addition to the very strong fluctuations, it was found that the histograms of the instantaneous velocity fluctuations had multiple peaks. This, along with the very dynamic nature of the junction vortex fluctuations observed in the real time smoke flow visualizations raised questions about the presence of a single characteristic frequency or a band of dominant frequencies in the junction vortex flow. The results of the investigation of the spectral content of the junction vortex flow are presented in this section.

The junction vortex flow was studied for its spectral content using the discretized lag product method. Both the u and v components of the velocity were analyzed for their spectral content. The locations where the spectra were computed are shown in Fig. 6.18. The spectra for the u and v components were computed at nine locations in and around the core of the time mean junction vortex. At each point where spectrum was computed, 512,000 LDV realizations were collected for computing the spectra. The average sample rate was kept around 250 samples per second. In all cases, a slot width of 128 microseconds was used. Fifteen hundred sixty-two autocorrelation estimates were computed, giving an approximate resolution of 5 Hz. Spectral estimates were computed up to a maximum frequency of 3900 Hz. The total data set of 512,000 points at each point was divided into five subsets of 102,400 points each. The spectral estimates from the five subsets were then averaged to yield the final spectrum. The spectrum was further smoothed by octave averaging before plotting. In each case, spectra are shown in

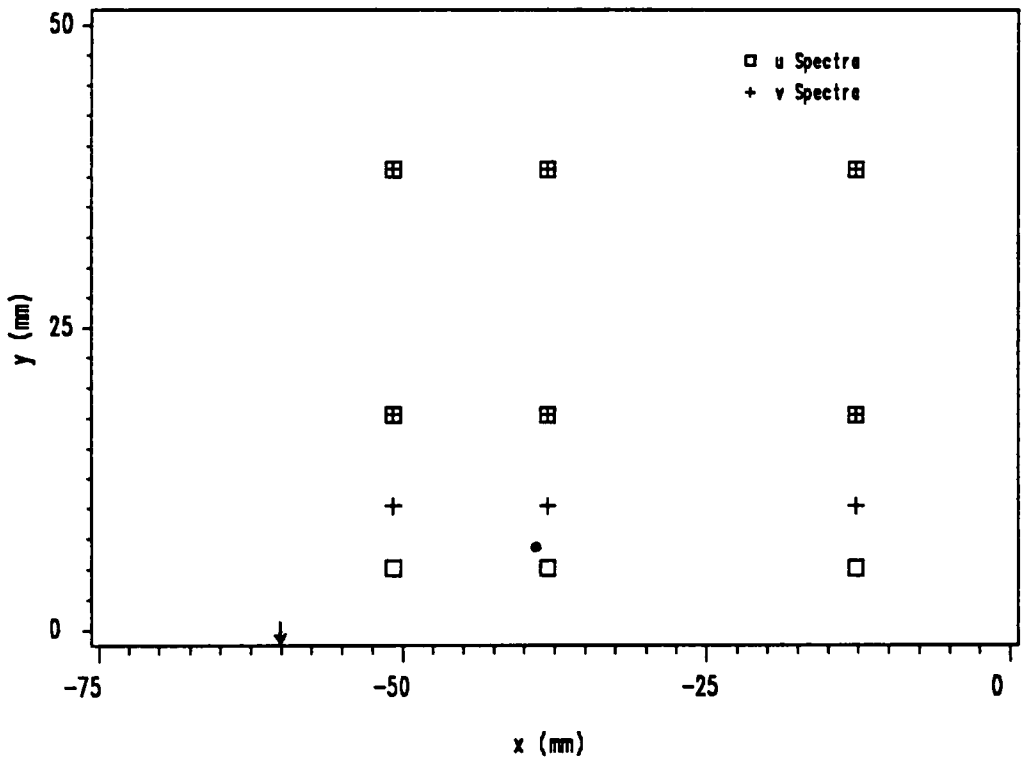

Figure 6.18. Locations for Spectral Computations

both semilog and the more usual log-log scale. To plot the spectra in the log-log scale, all negative estimates found after octave averaging were discarded.

All the spectra presented for the u component were superimposed with Klebanoff's data for a two-dimensional turbulent boundary layer [76]. The two-dimensional boundary layer results presented from Klebanoff here were for a value of $y/\delta = 0.2$. Since the spectra presented in Klebanoff did not vary substantially with y/δ, the results at 0.2 was chosen as a representative spectrum. It should be noted that the nature of the junction vortex flow is very much different from a two-dimensional turbulent boundary layer and agreement with Klebanoff's results were not sought. The purpose of superimposing Klebanoff's results was merely to give a reference, deviations from which can be more clearly observed.

Figures 6.19-6.27 show the spectra obtained for the u component of the velocity fluctuations in the junction vortex flow. Figures 6.19-6.21 show the spectra at x=-12.7 mm, and y=5.1 mm, 17.8 mm and 38.1 mm respectively. Figures 6.22-6.24 show the spectra at x=-38.1 mm for the same y locations. Figures 6.25-6.27 show the spectra at x=-50.8 mm, also for the same three y locations.

Reasonable spectral estimates were obtained up to a maximum frequency of approximately 200-300 Hz. After 300 Hz, the spectral levels became close to zero, and the discretized lag product method typically yielded negative spectral estimates. Thus the effective range of spectral measurements were confined up to a maximum frequency of about 300 Hz. It is noted here that most of spectral energy is concentrated in this band and hence this range may be adequate for practical spectral estimations where the intention is to detect dominant spectral components. It should be also noted that this cutoff frequency of approximately 300 Hz appears specific for this and similar cases where spectral levels fall close to zero after 300 Hz.

A few positive spectral estimates were found again in higher frequencies around 2000-3000 Hz. These estimates were rather erratic, although close to zero. The differences appear rather

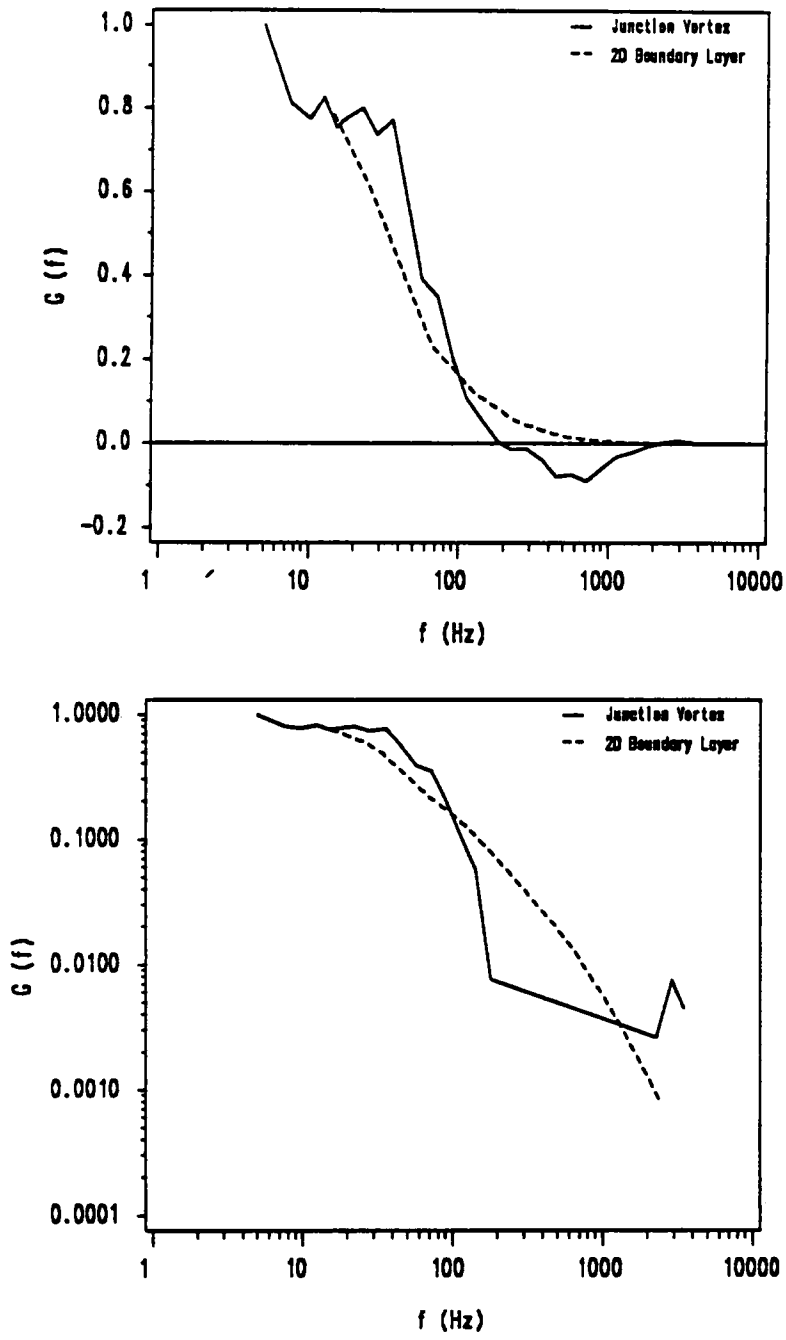

Figure 6.19. Spectrum of u Component at x=-12.7 mm, y=5.1 mm

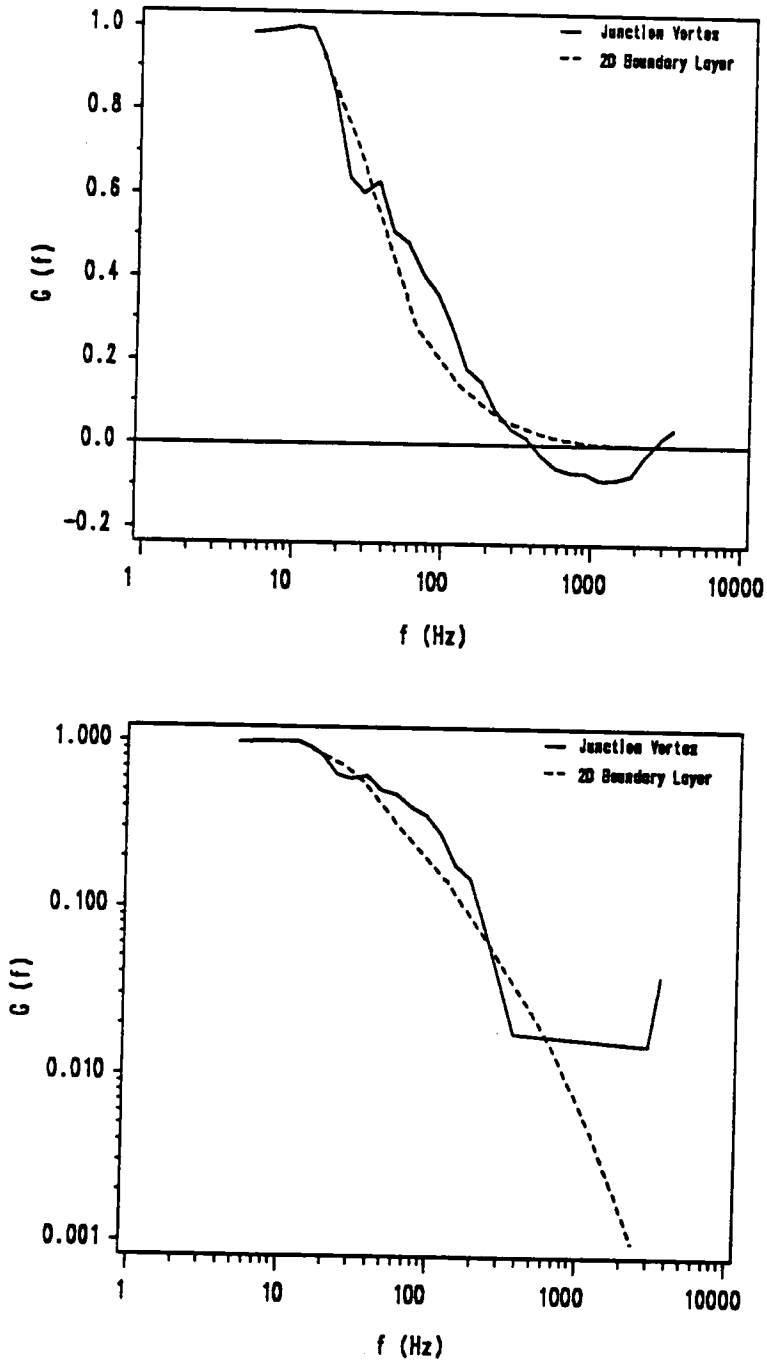

Figure 6.20. Spectrum of u component at x=-12.7 mm, y=17.8 mm

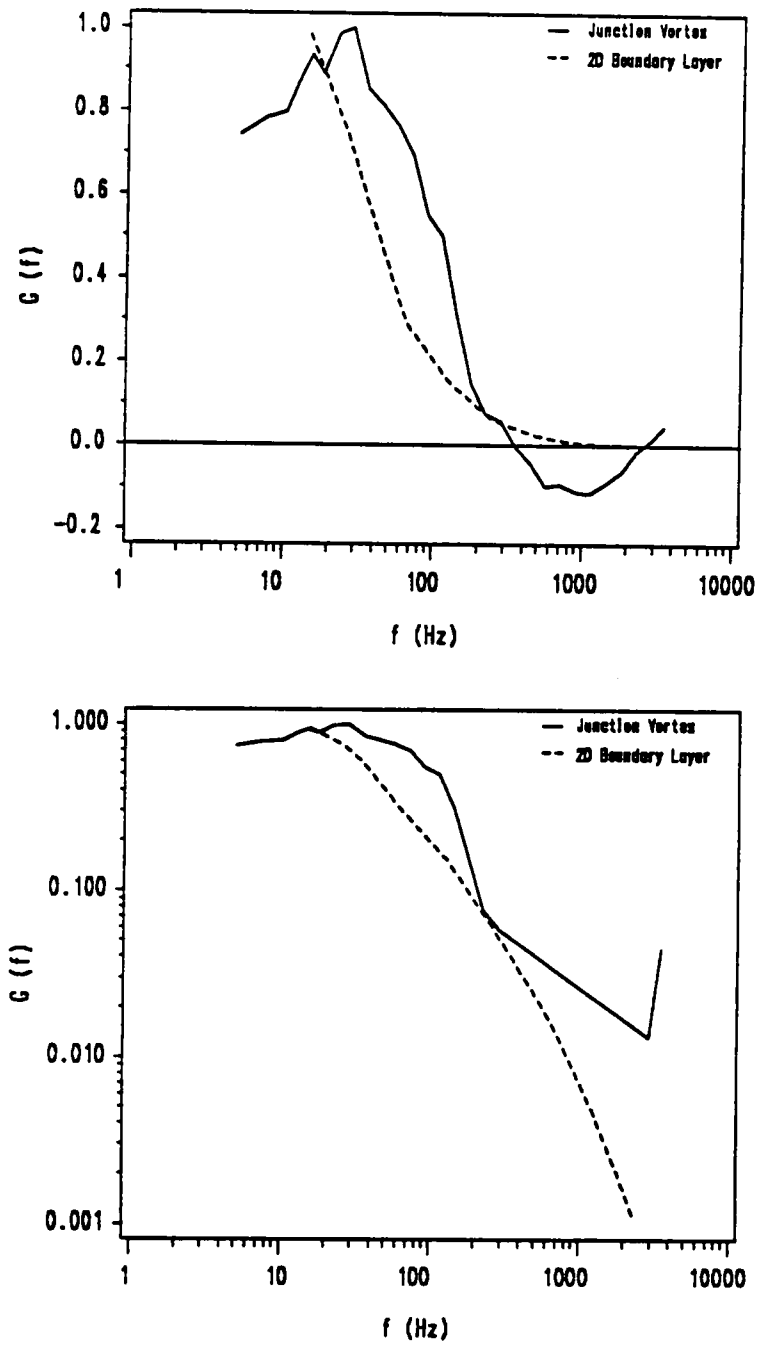

Figure 6.21. Spectrum of u Component at x=-12.7 mm, y=38.1 mm

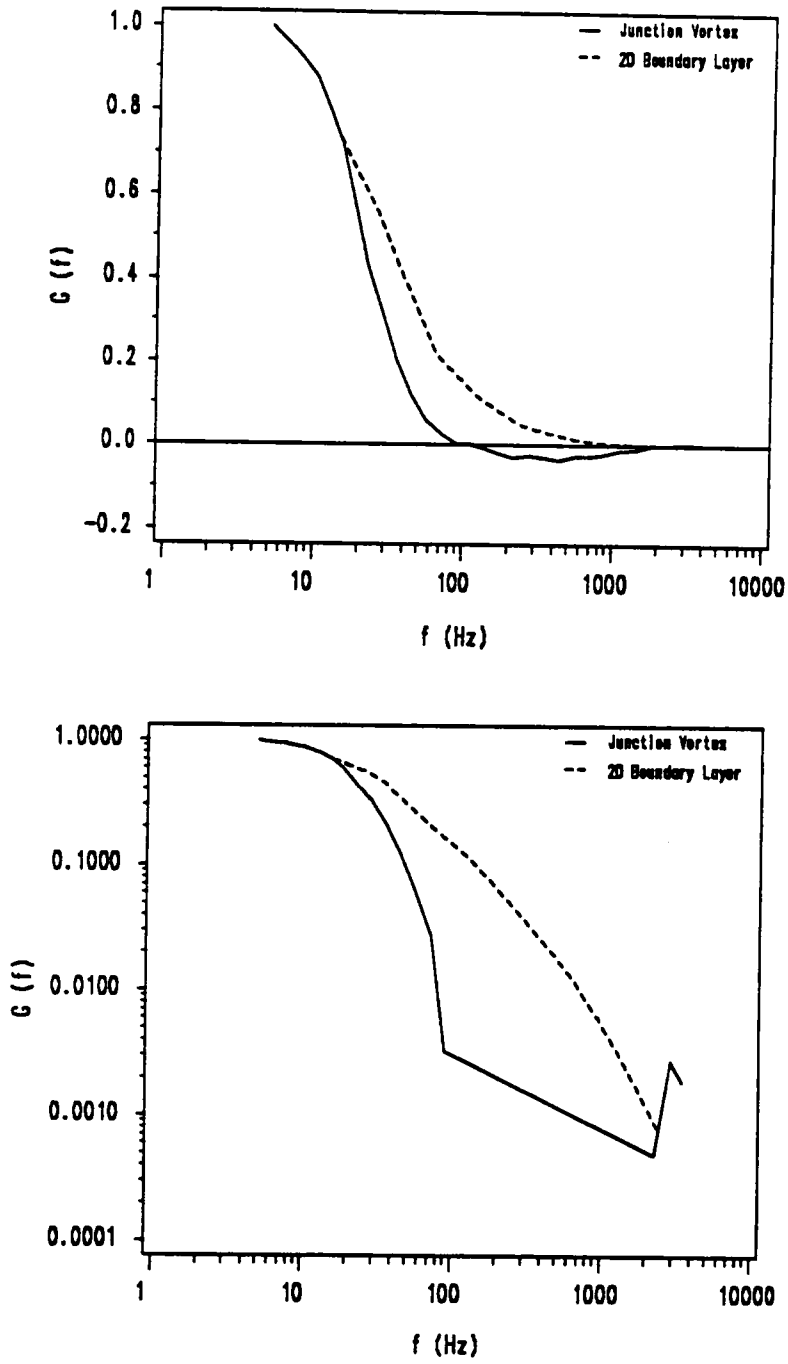

Figure 6.22. Spectrum of u Component at x=-38.1 mm, y=5.1 mm

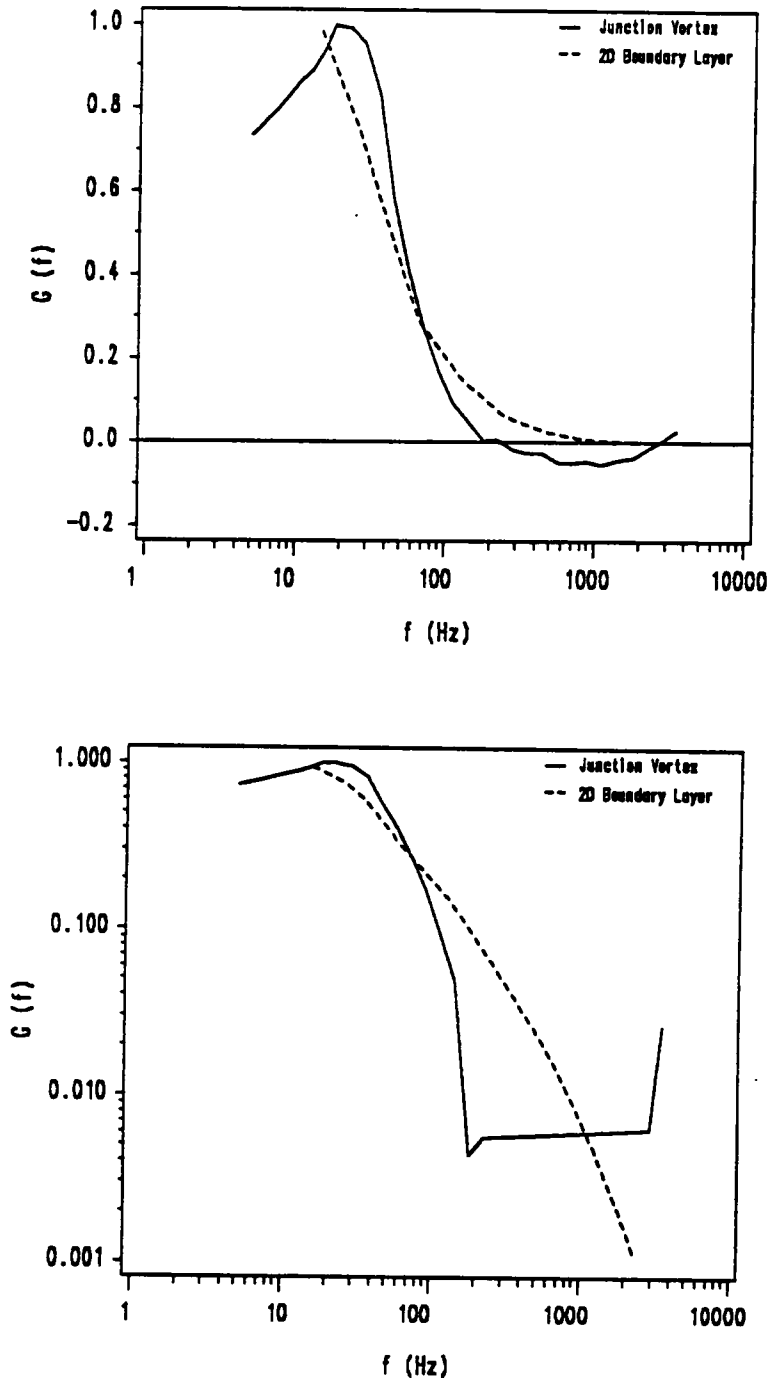

Figure 6.23. Spectrum of u Component at x=-38.1 mm, y=17.8 mm

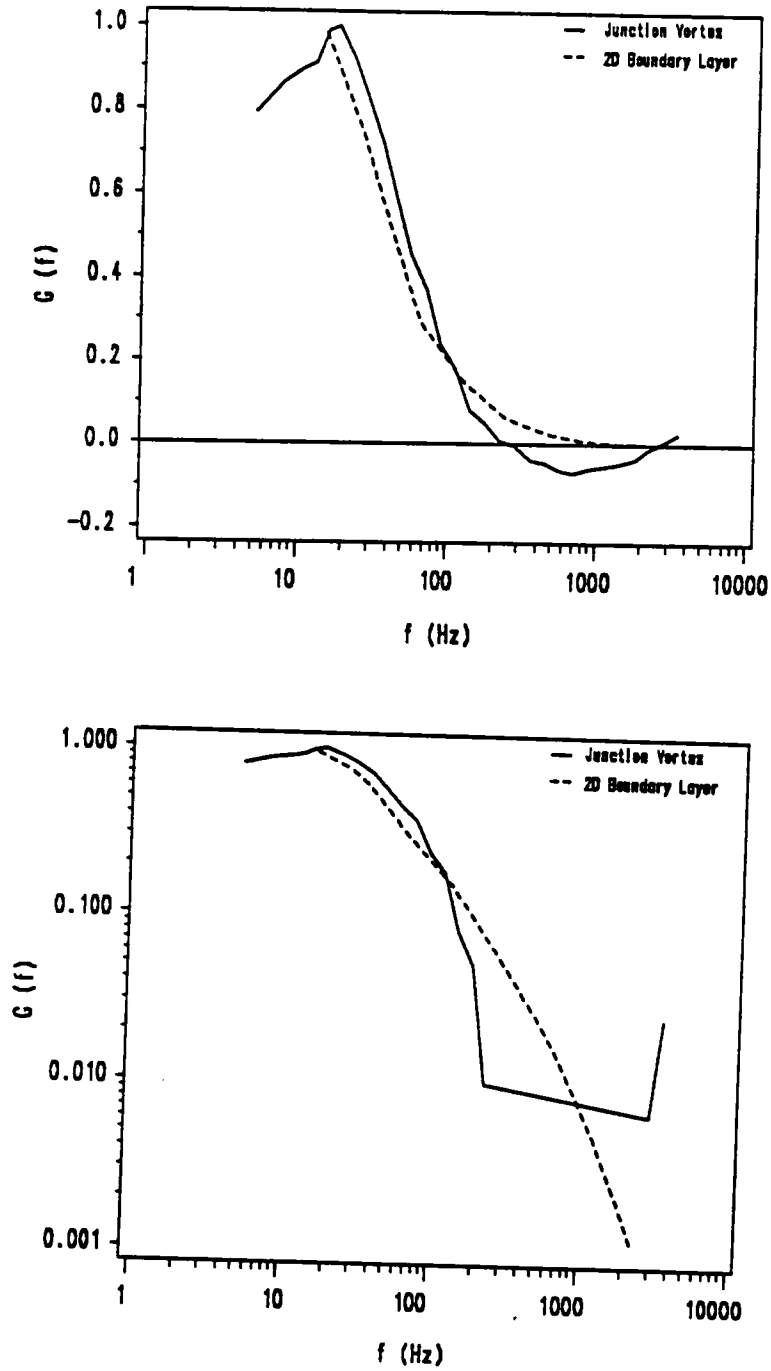

Figure 6.24. Spectrum of u Component at x=-38.1 mm, y=38.1 mm

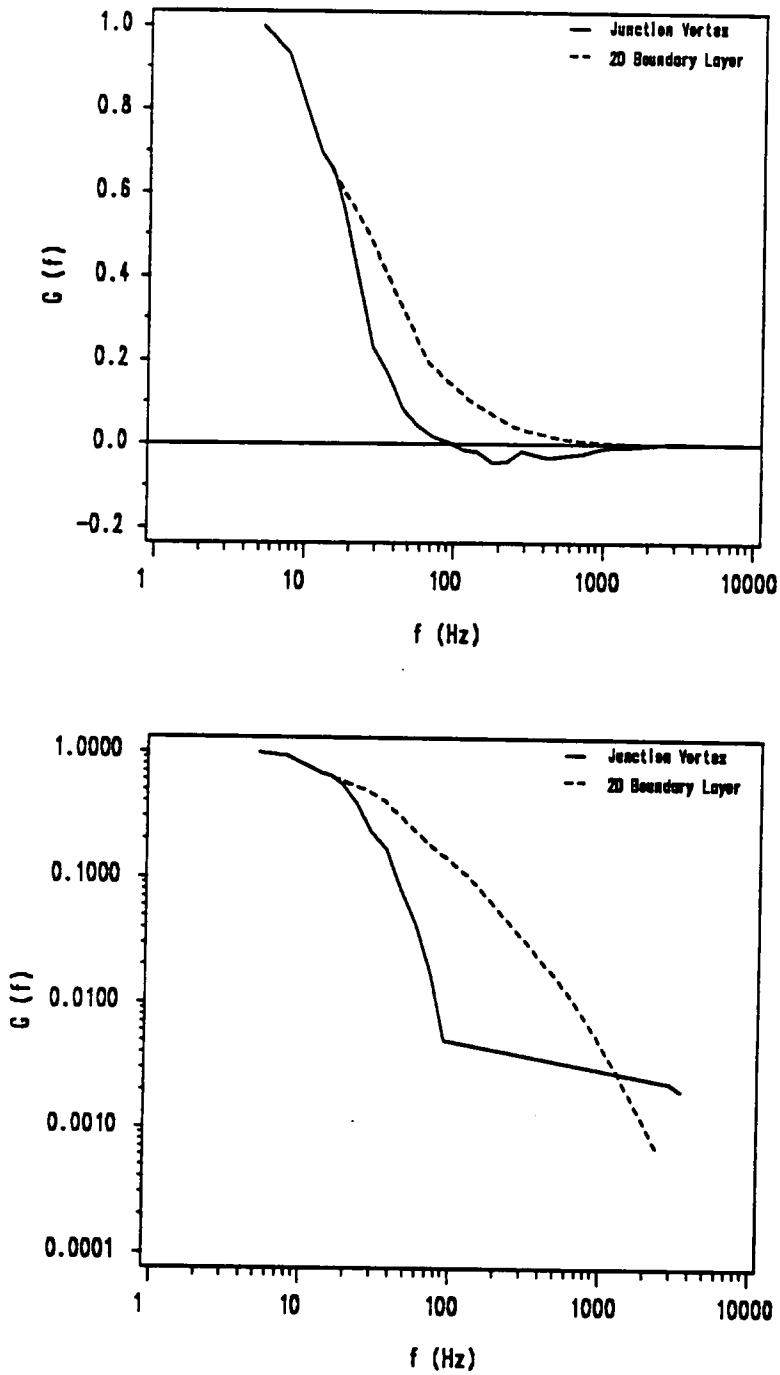

Figure 6.25. Spectrum of u Component at x=-50.8 mm, y=5.1 mm

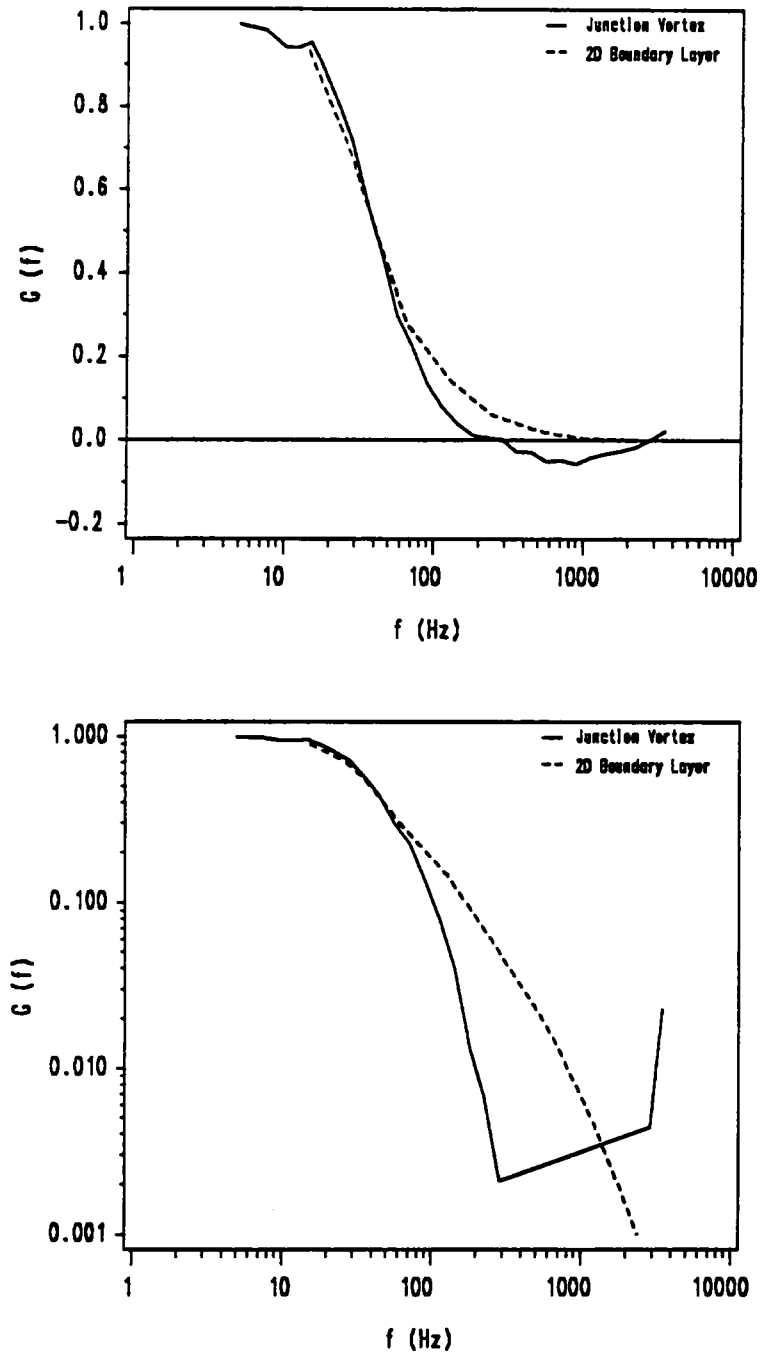

Figure 6.26. Spectrum of u Component at x=-50.8 mm, y=17.8 mm

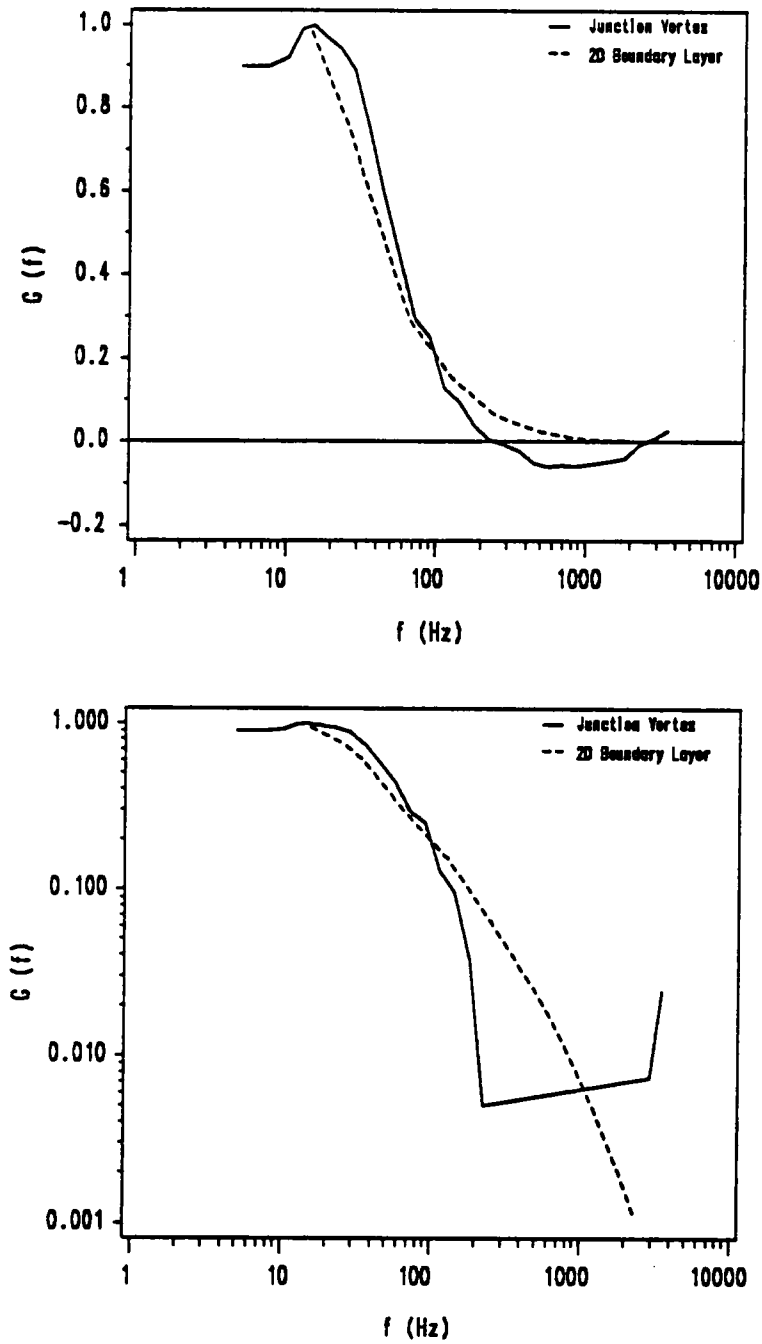

Figure 6.27. Spectrum of u Component at x=-50.8 mm, y=38.1 mm

magnified in the log-log plots. Not much confidence should be placed on these higher frequency spectral estimates, and these were included merely for completeness. It should be noted here that that the sample rates for the data sets were in the range of 250 Hz. Although theoretical results show that spectral estimates can be obtained up to any frequency for randomly sampled data, the limited results shown here demonstrate that the spectral estimates are very noisy in regions where the spectral level is close to zero.

Although the general nature of the spectra shown in Figs. 6.19-6.27 were similar to a two-dimensional boundary layer flow, some of the individual spectra showed marked and systematic deviations. The spectra shown in Figs. 6.20 and 6.26 were found to agree with a 2DTBL most closely. The spectra in the two locations around the separation region as shown in Figs. 6.22 and 6.25 were also essentially similar to a 2DTBL, with the difference being that the spectral levels fell close to zero at around 100 Hz, in contrast with around 200-300 Hz for a 2DTBL. This behavior may be connected to the separation phenomena, with most of the fluctuating energy of the turbulent flow around the separation point being concentrated in frequencies less than 100 Hz.

The spectra shown in Figs. 6.21, 6.23, 6.24 and 6.27 showed clear evidence of a peak at around 20-30 Hz. It should be noted that all the locations with spectral peaks were in the upper portions of the measurement region. It appears that the outer boundary of the junction vortex flow region fluctuates with a frequency of about 20-30 Hz.

To summarize, the overall character of the junction vortex flow appears to have similar characteristics to a two-dimensional boundary layer, with relatively greater energies in the lower frequencies. Based on the spectra at the individual locations, it can be speculated that there is an evidence of different flow regimes in the junction vortex flow. The approximate region below the time mean center of the junction vortex appears to behave similar to a two-dimensional turbulent boundary layer, while the upper region showed a peak around 20-30 Hz, and had increased spectral energies in the lower frequencies.

In the case of the v component of the velocity, the junction vortex flow is drastically different from a two-dimensional turbulent boundary layer. The magnitude of the v component of velocity is comparable to the u component of velocity in the junction vortex, as opposed to the dominant u component in a two-dimensional turbulent boundary layer. In addition, both positive and negative values of the v component are found in the junction vortex. For these reasons, a comparison with the spectra of a two-dimensional turbulent boundary layer were not considered to be very meaningful. However, the spectra for the v component in a two-dimensional turbulent boundary layer obtained by Klebanoff [76] at $y/\delta = 0.05$ is shown for comparisons. Figures 6.28-6.36 show the spectra obtained from the v component of the fluctuations in the junction vortex. The spectral computations for the v component were performed in exactly the same manner as the u component. The spectrum at each location is shown in both semilog and log-log scale.

The spectra for the v component of the velocity fluctuations show very much the same features as the u component. The spectral level decreased in a continuous fashion up to about 200-300 Hz. After about 300 Hz, spectral levels became close to zero, and negative spectral estimates were found. Evidence of a peak can be found in Figs. 6.32 and 6.33. The spectra of v component at x=-50.8 mm, y=38.1 mm as shown in Fig. 6.36 exhibited noise-like behavior. This behavior persisted after repeated experiments and was concluded to be due to some feature of the flow and not due to any mistake in data acquisition or computations. The reason for this noise-like behavior could not be explained.

6.5 Uncertainty Estimates

Techniques for estimating uncertainties of experimental results in engineering have been treated in detail by Kline and McClintock [78]. These methods were followed to report the uncertainties in the mean velocities in the present experiments. The reader should be cautioned, however, that there are various types of bias errors that can occur in the measurement

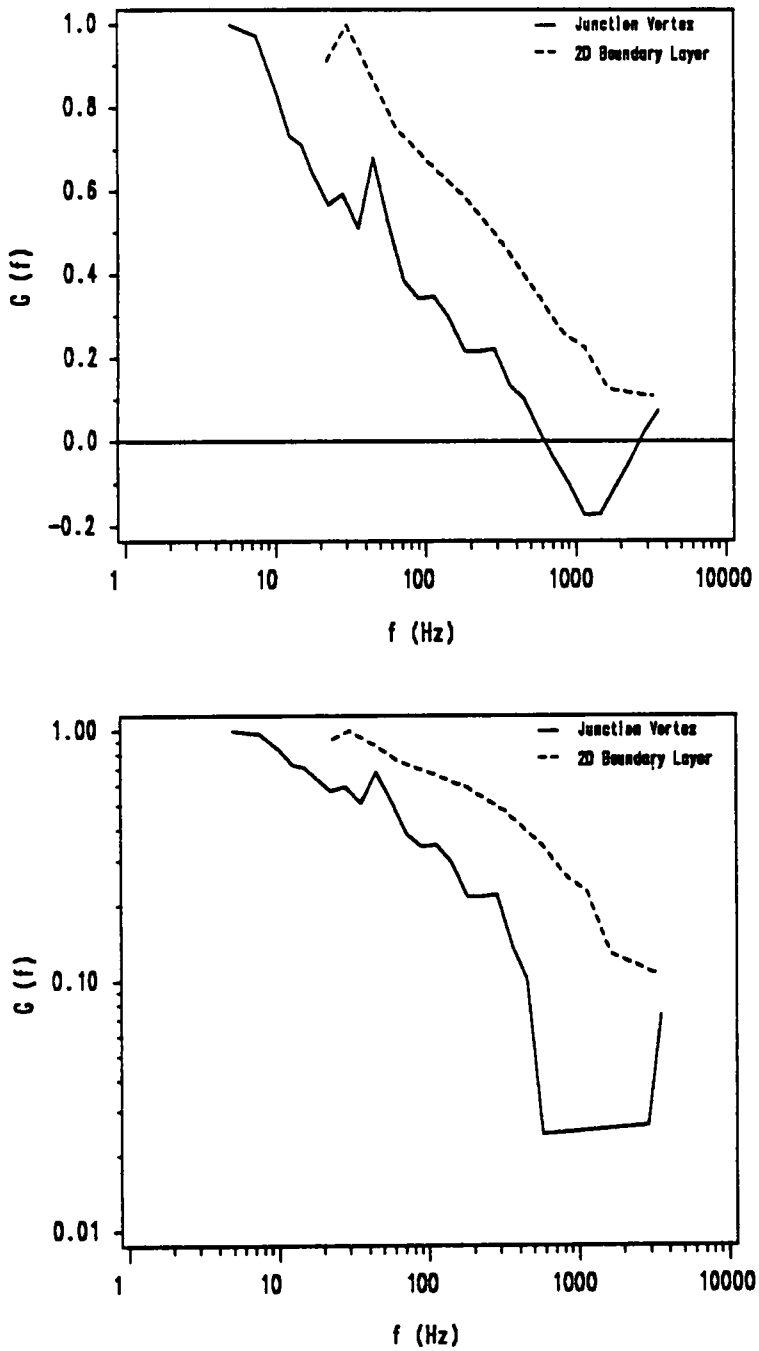

Figure 6.28. Spectrum of v Component at x=-12.7 mm, y=10.2 mm

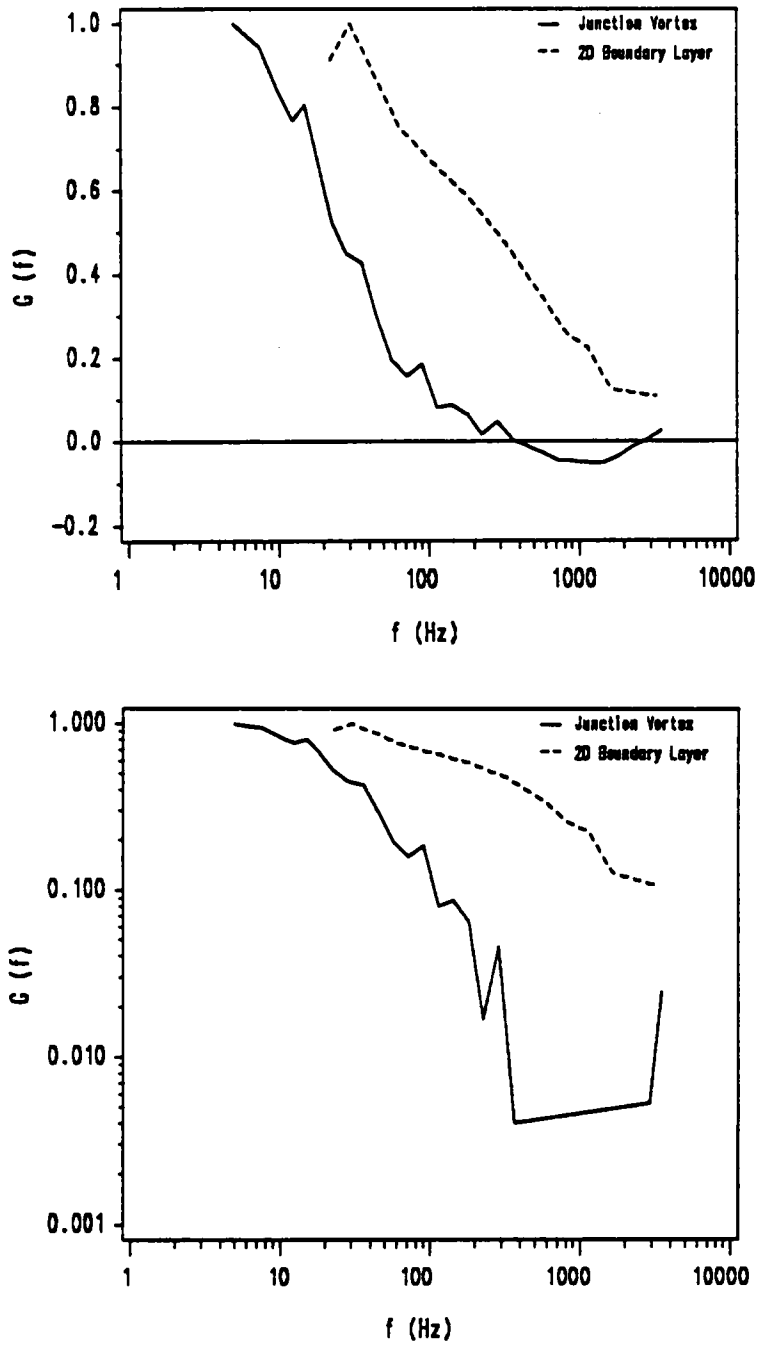

Figure 6.29. Spectrum of v component at x=-12.7 mm, y=17.8 mm

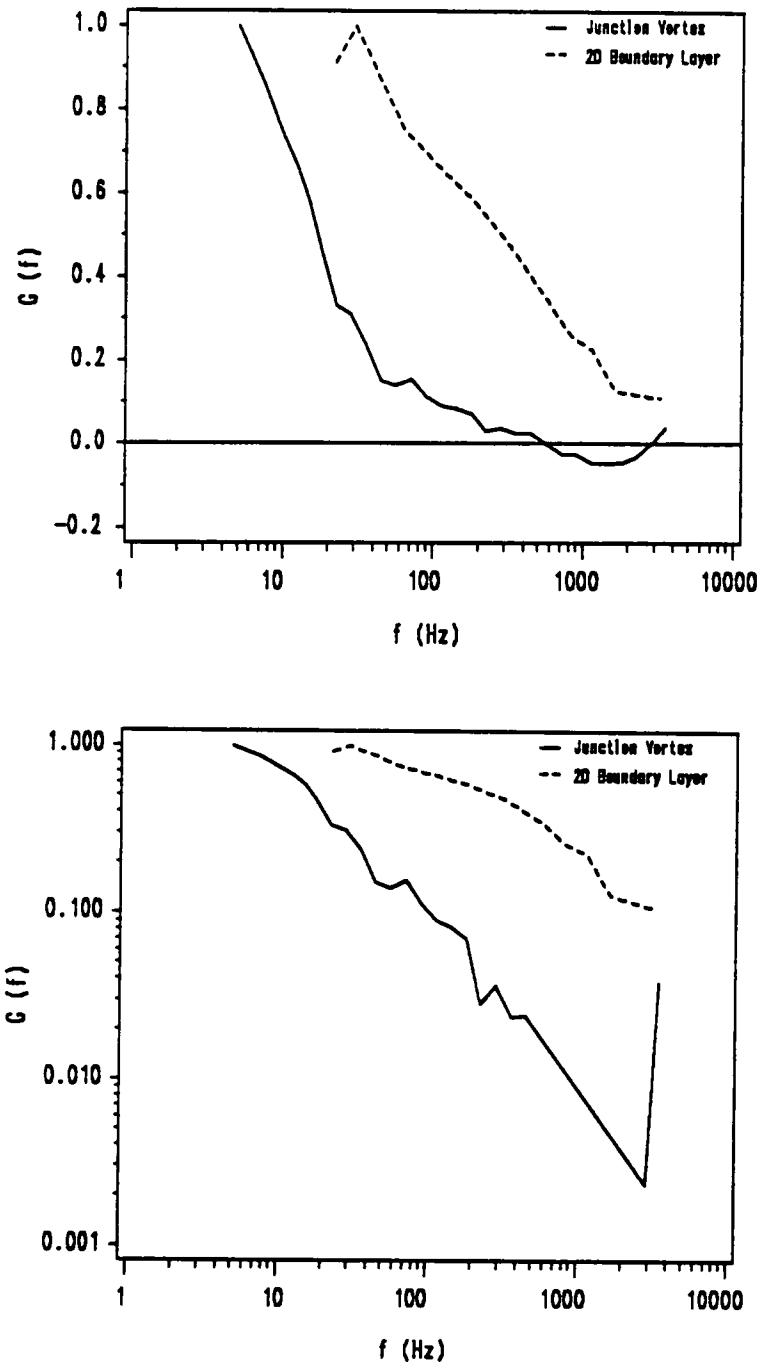

Figure 6.30. Spectrum of v Component at x=-12.7 mm, y=38.1 mm

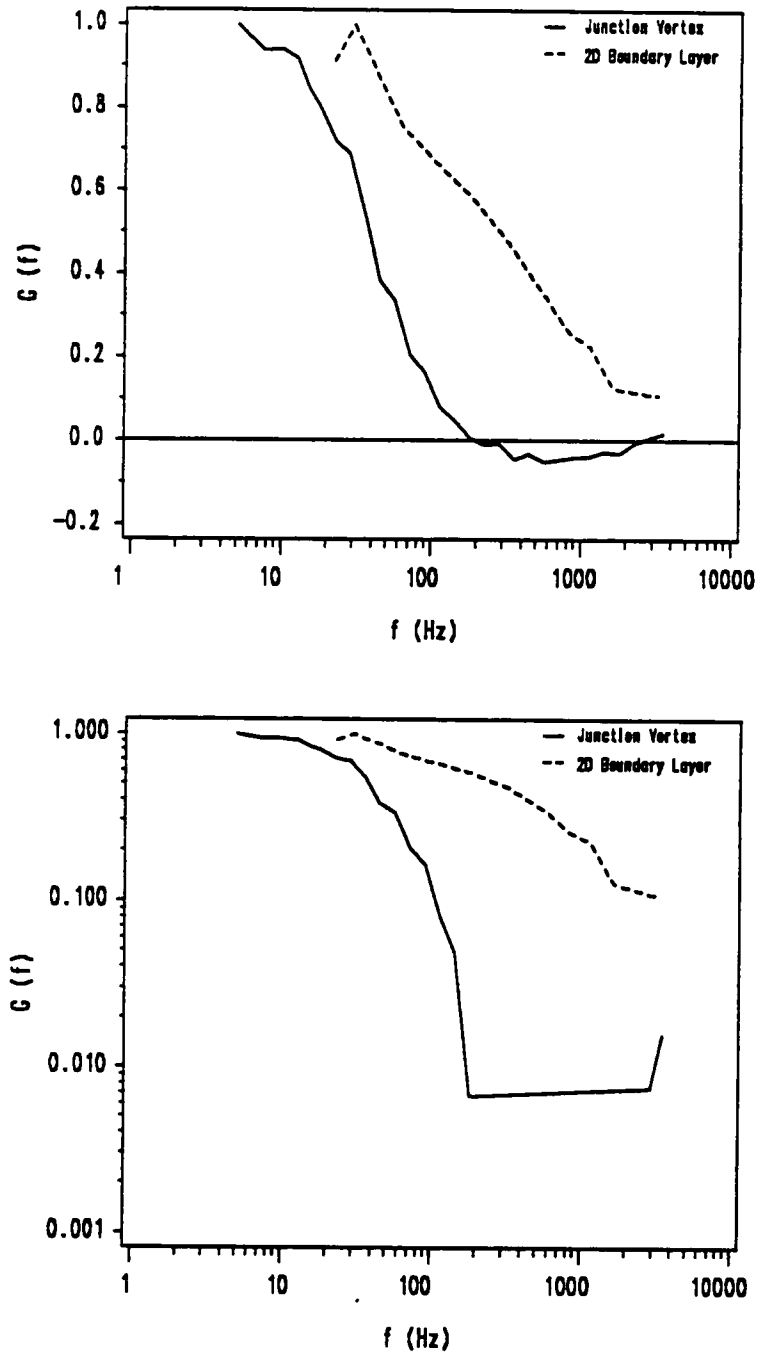

Figure 6.31. Spectrum of v Component at x=-38.1 mm, y=10.2 mm

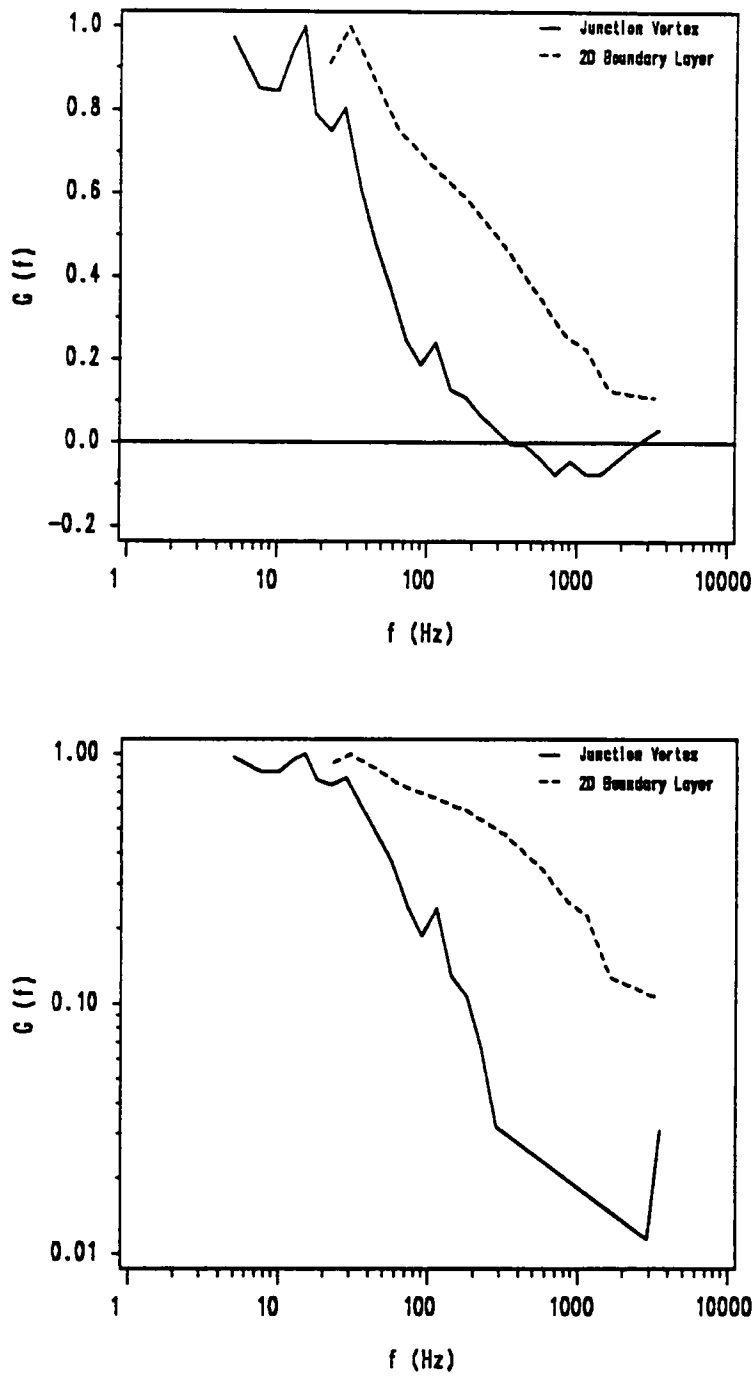

Figure 6.32. Spectrum of v Component at x=-38.1 mm, y=17.8 mm

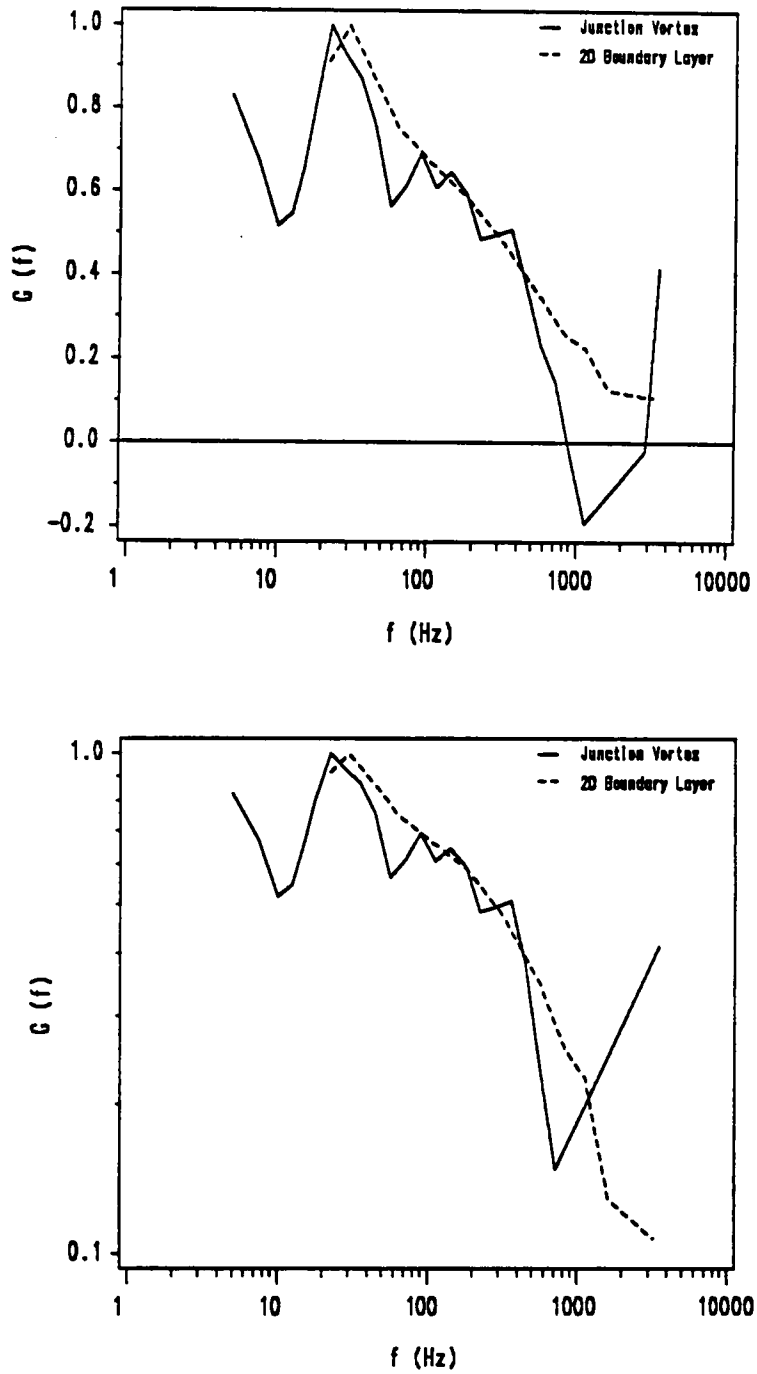

Figure 6.33. Spectrum of v Component at x=-38.1 mm, y=38.1 mm

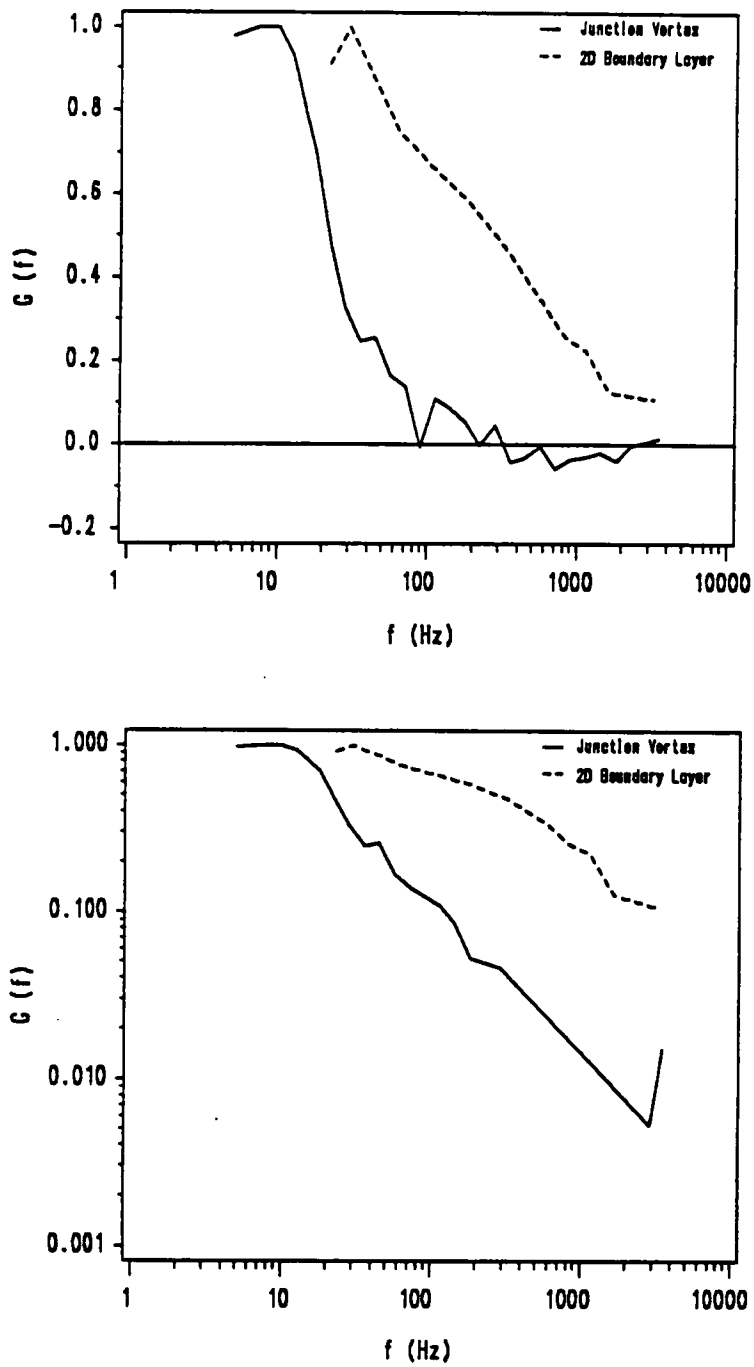

Figure 6.34. Spectrum of v Component at x=-50.8 mm, y=10.2 mm

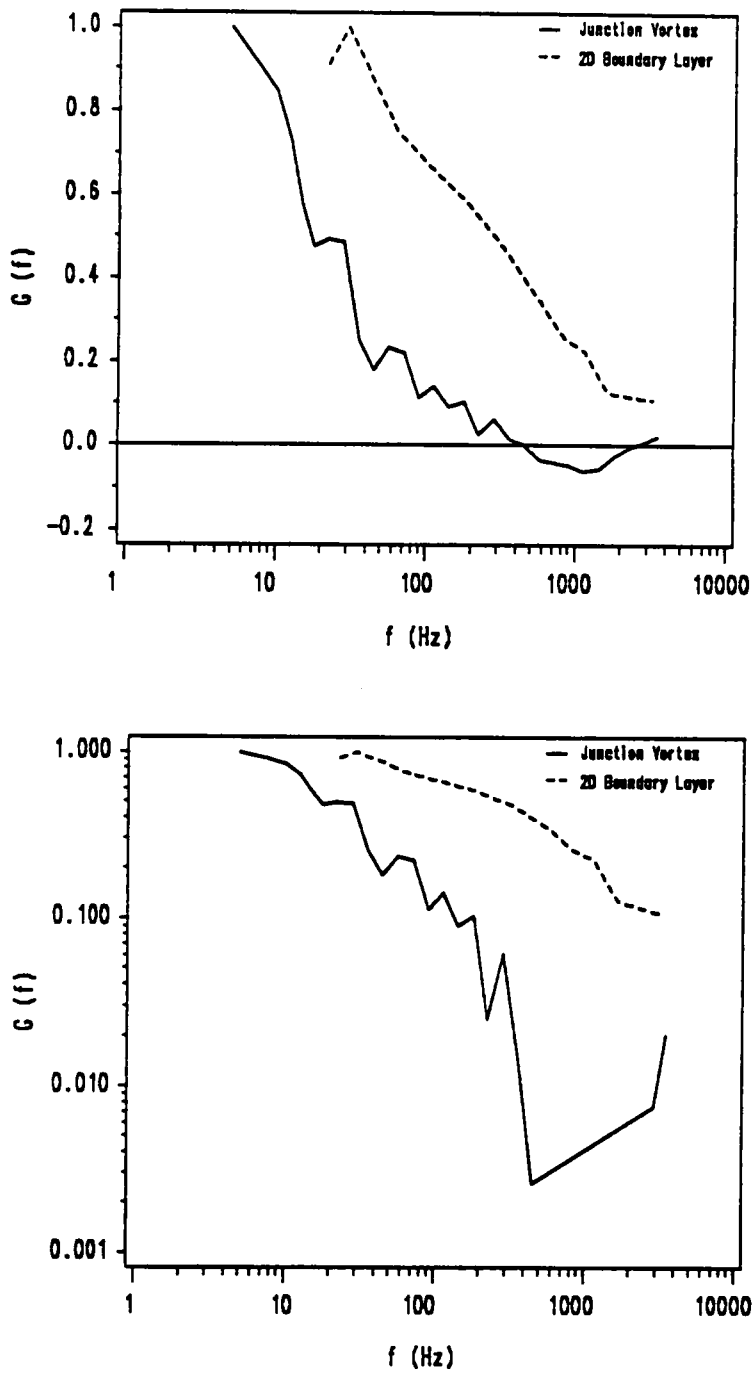

Figure 6.35. Spectrum of v Component at x=-50.8 mm, y=17.8 mm

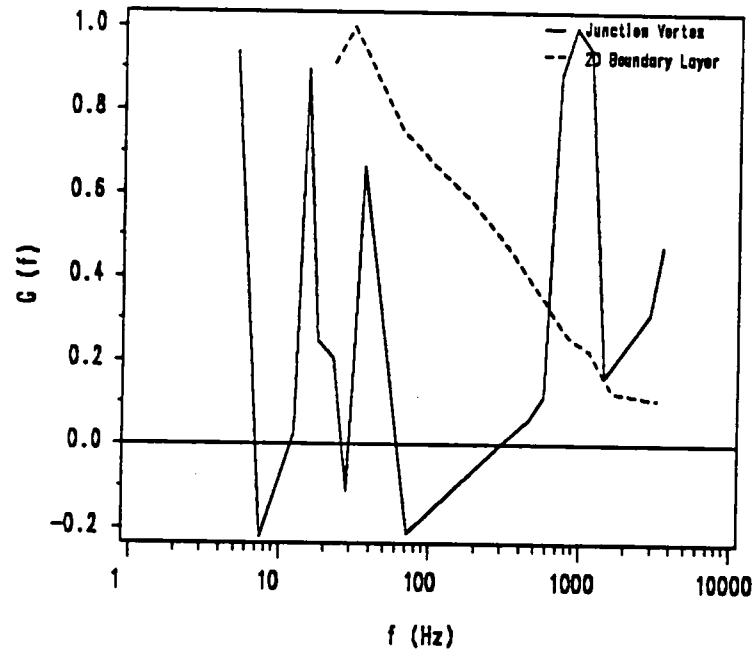

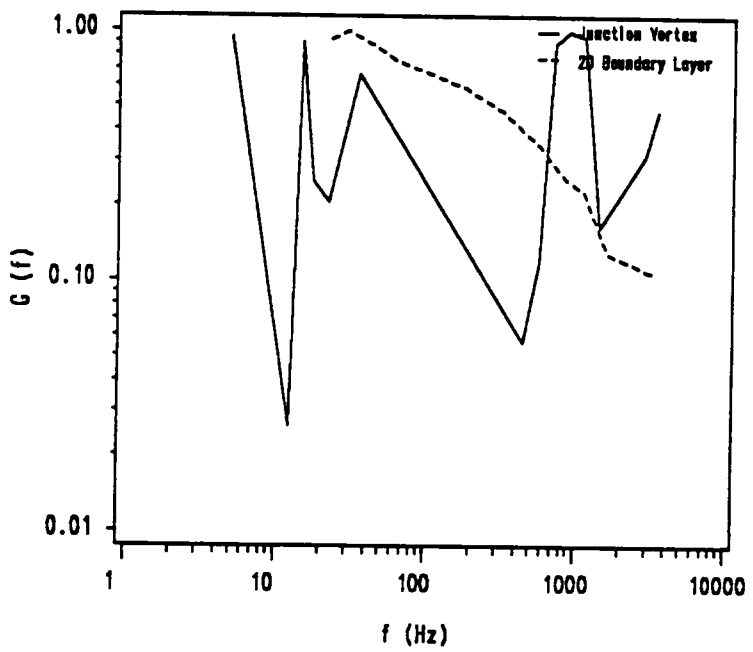

Figure 6.36. Spectrum of v Component at x=-50.8 mm, y=38.1 mm

with a LDV. Some of these have been experimentally demonstrated, while the existence of others have only been speculated on. But in all cases, the present uncertainty estimates do not account for possible errors which might be attributed to such LDV bias errors. For the mean velocities, the maximum uncertainty was estimated to be about ± 0.009 on the non-dimensional velocity values. This uncertainty estimate is based on a 95 percent confidence level. Because this estimate is based on single sample data, it only reflects the author's best estimate at the specified odds. The computed maximum and minimum velocities were also estimated to have an uncertainty of the same order as the mean velocities.

For the turbulence data, a rigorous analysis of the uncertainties were not carried out. However, based on differences with previous independent measurements by Tree [23] and repeated observations at the same point, the uncertainty was estimated to be not more than ten percent.

Uncertainties in the reverse flow intermittency data were estimated to be about ± 0.05. Again this value reflects the author's best estimate and was arrived at from experimental experiences rather than a rigorous analysis.

Uncertainties in the spectral estimates are very difficult to estimate for randomly sampled data. The relative error in a spectral estimate from uniformly sampled data is primarily dependent on the number of averages made for the periodogram method and the ratio τ_m/T for the correlogram method. From this consideration alone, the uncertainty in the spectral estimates would not have exceeded three percent if the data were uniformly sampled. For the non-uniformly sampled data used here, the uncertainties in spectral estimates may be much larger. These uncertainties were difficult to quantify accurately but the author's best estimate is that they would not exceed ten per cent.

7.0 Summary

The spectral content and the characteristics of the strongly time variant flow in the junction vortex were investigated using time resolved velocity data. Time resolved mesurements in the junction vortex were taken with a laser Doppler velocimeter.

The randomly sampled data from a LDV with a counter processor posed special problems for spectral analysis of the velocity fluctuations. Three different methods for spectral analysis from randomly sampled data were examined. The three methods were, 1) exact lag product method, 2) discretized lag product method, and 3) direct transform method. The performance of these methods were compared for various simulated and real flow situations.

Simulation studies were carried out with simulated data corresponding to a first order spectrum and a sine wave or a mixture of sine waves. In the case of simulated sine waves, the sampling times were taken from an actual LDV data set, so this simulation was one step closer to the real situation. All three methods of spectral estimation performed very well for simulated data.

The three methods of spectral estimation for randomly sampled data were then further tested for two real flow situations. The first flow to be tested was the vortex shedding flow behind a cylinder. The spectrum for this flow has a dominant peak at the vortex shedding frequency. The results from the spectral analysis methods for the LDV data agreed well with the spectra

computed from hot wire data (uniformly sampled). The spectral peak at the vortex shedding frequency was reproduced exactly by all three methods.

The spectral analysis methods were also applied to a two-dimensional turbulent boundary layer. The results from the spectral analysis of the LDV data were compared with hot wire spectra and Klebanoff's data.

In regions of relatively small spectral magnitudes, the discretized lag product method tended to produce negative spectral estimates, whereas the spectrum from the direct transform method usually had a significant white noise. In the regions where the spectral levels were not close to zero, both methods performed well. The estimates from the discretized lag product method were found to be consistently better than the estimates from the direct transform method. The discretized lag product method was used for computing spectra for the junction vortex flow.

The assumption that the sampling times follow a Poisson distribution was verified for several representative LDV data sets. The tests also demonstrated the lack of aliasing effects in the case of Poisson sampled data. No aliasing was found for sampling rates much lower than that necessary for uniformly sampled data, as given by the Nyquist criterion.

From a comparison of the performances of the three methods of spectral analysis for randomly sampled data, it was found that the exact lag product method produced spectral estimates which were not significantly better than the other two methods. Hence it was concluded that the use of this method is not justified because it does not offer any improvements in the spectral estimates to offset its computational slowness.

The characteristics of the time variant flow were studied from a detailed set of time resolved LDV measurements. The mean velocity vectors showed a single well defined vortex and a

singular separation point in the region between the vortex induced reverse flow and the flow coming from upstream.

The turbulence intensities found for the junction vortex flow confirmed the observation from smoke flow visualizations that the flow is strongly time variant. In the junction vortex, turbulence intensities normalized by the free stream velocity were at least two to three times greater than the typical two-dimensional boundary layer values.

The histograms computed from the u component of the velocity fluctuations deviated markedly from the normal distribution, and exhibited multiple peaks. Such histograms were found all around the core of the junction vortex and near the mean singular separation point.

The reverse flow intermittency data shed some light on the separation point on the plane of symmetry. It was found that the instantaneous separation point oscillates in a random fashion between two extreme limits. The extreme positions of the junction vortex was also identified approximately from the time resolved measurements.

The spectral content of the junction vortex flow was studied using the discretized lag product method. The overall character of the junction vortex flow appeared to have similar characteristics as a two-dimensional turbulent boundary layer, with relatively greater energies in the lower frequencies than in the higher frequencies. Based on the individual spectra, it is possible that there exists two different flow regimes in the junction vortex. The spectra in the upper region showed peaks around 20-30 Hz in contrast with the spectra in the regions below the time mean vortex center, which resembled boundary layer spectra and showed no peaks.

8.0 References

1. Harsh, M. D., and Pierce, F. J., "An Experimental Investigation of a Turbulent Junction Vortex," Report No. VPI-E-85-4, Mechanical Engineering, Virginia Polytechnic Institute and State University, Blacksburg, Virginia, February, 1985.

2. Pierce, F. J., Kim, C. M., and Harsh, M. D., "The Mean Flow Structure of a Turbulent Junction Vortex," Report No. VPI-E-87-6, Mechanical Engineering, Virginia Polytechnic and State University, Blacksburg, Virginia, April, 1987.

3. Pierce, F. J., Kim, C. M., Nath, S. K., and Shin, J., "The Mean Flow Structure in the Near Wake of a Turbulent Junction Vortex," Report No. VPI-E-87-26, Mechanical Engineering, Virginia Polytechnic and State University, Blacksburg, Virginia, December, 1987.

4. Peak, D. J., and Galway, R. D., "The Three-Dimensional Separation of a Plane Incompressible Laminar Boundary Layer Produced by a Circular Cylinder Mounted Normal to a Flat Plate," *Recent Developments in Boundary layer Research,* Part II, NATO Agardograph No. 97, May, 1965, pp. 1049-1080.

5. Belik, L., "The Secondary Flow About Circular Cylinders Mounted Normal to a Flat Plate," Aeronautical Quarterly, Vol. 26, February, 1973, pp. 47-54.

6. Mojola, O. O., "Measurements in a Turbulent Horseshoe Vortex and the Problem of Probe Interference," Report No. 73-08, Department of Aeronautics, Imperial College of Science and Technology, December, 1973.

7. Barber, T. J., "An Investigation of Strut-Wall Intersection Losses," Journal of Aircraft, Vol. 15, No. 10, october, 1978, pp. 676- 681.

8. Baker, C. J., "The Laminar Horseshoe Vortex," Journal of Fluid Mechanics, Vol. 95, Part 2, November, 1979, pp. 347-368.

9. Baker, C. J., "The Turbulent Horseshoe Vortex," Journal of Wind Engineering and Industrial Aerodynamics, Vol. 6, No. 1-2, July, 1980, pp. 9-23.

10. Dickinson, S. C., "Flow Visualizations and Velocity Measurements in the Separated Region of an Appendage-Flat Plate Junction," *Proceedings of the Ninth Biennial Symposium on Turbulence,* held at University of Missouri-Rolla, October 1-3, 1984.

11. Moore, J., and Forlini, T. J., "A Horseshoe Vortex in a Duct," ASME paper No. 84-GT-202, presented at the ASME 29th International Gas Turbine Conference and Exhibit, Amsterdam, The Netherlands, June 4-7, 1984.

12. Ishii, J., and Honami, S., "A Three-Dimensional Turbulent Detached Flow with a Horseshoe Vortex," Transactions of the ASME, Journal of Engineering for Gas Turbines and Power, Vol. 108, January, 1986, pp. 125-130.

13. Eckerle, W. A., and Langston, L. S., "Horseshoe Vortex Formation Around a Cylinder," Transactions of the ASME, Journal of Turbomachinery, Vol. 109, April, 1987, pp. 278-285.

14. Mehta, R. D., "Effect of Wing Nose Shape on the Flow in a Wing/Body Junction," Aeronautical Journal, Vol. 88, December, 1988, pp. 456-460.

15. Dechow, R., and Felsch, K. O., "Measurements of the Mean Velocity and of the Reynolds Stress Tensor in a Three-Dimensional Turbulent Boundary Layer Induced by a Cylinder Standing on a Flat Wall," *Symposium on Turbulent Shear Flows,* Vol. 1, at University Park, Pennsylvania, April 18-20, 1977, pp. 9.11-9.20.

16. Shabaka, I. M. M. A., and Bradshaw, P., "Turbulent Flow Measurements in an Idealized Wing/Body Junction," AIAA Journal, Vol. 19, No. 2, February, 1981, pp. 131-132.

17. McMahon, H., Hubbartt, J., and Kubendran, L., "Mean Velocities and Reynolds Stresses in a Juncture Flow," NASA CR 3605, National Aeronautics and Space Administration, Langley Research Center, Hampton, Virginia, 1982.

18. McMahon, H., Hubbartt, J., and Kubendran, L., "Mean Velocities and Reynold Stresses Upstream of a Simulated Wing Fuselage Juncture," NASA CR 3695, National Aeronautics and Space Administration, Langley Research Center, Hampton, Virginia, 1984.

19. Hsing, T. D., and Teng, H. Y., "Experimental Study of the Behavior of 3D-Turbulent Boundary Layer in a Simplified Wing/Body Junction," AIAA Paper No. 84-1529, presented at the AIAA 17th Fluid Dynamics, Plasma Dynamics, and Lasers conference, Snowmass, Colorado, June 25-27, 1984.

20. Kubendran, L. R., McMahon, H. M., and Hubbartt, J. E., "Turbulent Flow Around a Wing/Fuselage Type Junction," AIAA Journal, Vol. 24, No. 9, September, 1986, pp. 1447-1452.

21. Abid, R., and Schmitt, R., "Experimental Study of a Turbulent Horseshoe Vortex Using a Three Component Laser Velocimeter," AIAA-86-1069, presented at the AIAA/ASME 4th Fluid Dynamics, Plasma Dynamics, and Lasers Conference, Atlanta, Georgia, May 12-14, 1986.

22. Devenport, W. J., and Simpson, R. L., "Turbulence Structure near the Nose of a Wing-Body Junction," AIAA-87-1310, presented at the AIAA 19th Fluid Dynamics, Plasma Dynamics and Lasers Conference, Honolulu, Hawaii, June 8-10, 1987.

23. Tree, I. K., "Laser Doppler Velocimeter Measurements in a Turbulent Junction Vortex," Ph.D. Dissertation, Mechanical Engineering, Virginia Polytechnic Institute and State University, Blacksburg, Virginia, June, 1986.

24. Hunt, J. C., Abell, C. J., Peterka, J. A., and Woo, H., "Kinematical Studies of the Flows Around Free and Surface-Mounted Obstacles; Applying Topology to Flow Visualizations," Journal of Fluid Mechanics, Vol. 86, Part 1, 1978, pp. 179-200.

25. Pierce, F. J., and Tree, I. K., "The Mean Flow Structure on the Symmetry Plane of a Turbulent Junction Vortex," to be published in Trans. ASME, Journal of Fluids Engineering.

26. Gorski, J. J., Govindan, T. R., and Laksminarayana, B., "Computation of Three-Dimensional Turbulent Shear Flows in Corners," AIAA Journal, Vol. 23, No. 5, May, 1985, pp. 685-692.

27. Smith, F. T., and Gajjar, J., "Flow Past Wing-Body Junctions," Journal of Fluid Mechanics, Vol. 144, 1984, pp. 191-215.

28. Kaul, U. K., Kwak, D., and Wagner, C., "A Computational Study of Saddle Point Separation and Horseshoe Vortex System using the Three-Dimensional Incompressible Navier-Stokes Code," AIAA-85-0182, presented in the AIAA 23rd Aerospace Sciences Meeting, Reno, Nevada, January 14-17, 1985.

29. Briley, W. R., and McDonald, H., "Computation of Three-Dimensional Horseshoe Vortex Flow using Navier Stokes Equations," *Seventh International Conference in Numerical Methods in Fluid Mechanics*, Springer Verlag, 1980.

30. Moore, J., and Moore, J. G., "Performance Evaluation of Linear Turbine Cascades Using Three-Dimensional Viscous Flow Calculations," Transactions of the ASME, Journal of Enginnering for Gas Turbine and Power, Vol. 107, October, 1985, pp. 969-975.

31. Ilegbusi, J. O., "Numerical Calculation of Turbulent Corner Flows," Applied Math. Modelling, Vol. 9, August, 1985, pp. 263-270.

32. Rood, E. P., "Experimental Investigation of the Turbulent Large Scale Temporal Flow in the Wing-Body Junction," Ph.D. Dissertation, The Catholic University of America, Washington, D. C., 1984.

33. Rood, E. P., and Keller, J. E. C., "Evidence of Large Scale Time Dependent Flow in the Wing-Wall Interaction Wake," *Unsteady Turbulent Boundary Layers and Friction,* ASME Publication, FED Vol. 12, 1984, pp. 39-44.

34. Rood, E. P., "The Governing Influence of the Nose Radius on the Unsteady Effects of Large Scale Flow Structure in the Turbulent Wing and Plate Junction Flow," *Forum on Unsteady Flow,* ASME Publication, FED Vol. 15, December, 1984, pp. 30-32.

35. Rood, E. P., and Anthony, D. G., "Tail Profile Effects on Unsteady Large Scale Flow Structure in the Wing and Plate Junction," *Forum on Unsteady Flow,* ASME Publication, FED Vol. 27, 1985, pp. 30-32.

36. Hasan, M. A. Z., Casarella, M. J., and Rood, E. P., "An Experimental Study of the Flow and Wall Pressure Field Around a Wing-Body Junction," Transactions of the ASME, Journal of Vibration, Accoustics, Stress, and Reliability in Design, Vol. 108, July, 1986, pp. 308-314.

37. Thomas, A. S. W., "The Unsteady Characteristics of Laminar Juncture Flow," Physics of Fluids, Vol. 30, No. 2, 1987, pp. 283-285.

38. Duranni, T. S., and Greated, C. A., *Laser Systems in Flow Measurent,* Plenum Press, New York, New York, 1977.

39. Drain, L. E., *The Laser Doppler Technique,* John Wiley & Sons, 1980.

40. Durst, F., Melling, A., and Whitelaw, J., *Principles and Practice of Laser Doppler Anemometry,* 2nd edition, Academic Press Inc., New York, New York, 1981.

41. Edwards, R. V., "Report of the Special Panel on Statistical Particle Bias Problems in Laser Anemometry," Transactions of the ASME, Journal of Fluids Engineering, Vol. 109, June 1987, pp. 89-93.

42. Jenkins, G. M., and Watts, D. G., *Spectral Analysis and Its Applications,* Holden-Day Inc., San Francisco, 1968.

43. Newland, D. E., *An Introduction to Random Vibrations and Spectral Analysis,* Longman Group Limited , New York, 1975.

44. Marple, S. L. Jr., *Digital spectral Analysis with Applications,* Prentice-Hall Inc., New Jersey, 1987.

45. Otnes, R. K., and Enochson, L., *Digital Time Series Analysis* John Wiley and Sons, New York, 1972.

46. Blackman, R. B., and Tukey, J. W., *The Measurement of Power Spectra from the Point of View of Communication Engineering,* Dover Publications Inc., New York, 1958.

47. Shapiro, H. S., and Silverman, R. A., "Alias-Free Sampling of Random Noise," J. Soc. Indust. Appl. Math., Vol. 8, No. 2, June, 1960, pp. 225-248.

48. Beutler, F. J., "Alias-Free Randomly Timed Sampling of Stochastic Processes," IEEE Transactions on Information Theory, Vol. IT-16, No. 2, March, 1970, pp. 147-152.

49. Thompson, R. O. R. Y., "Spectral Estimation from Irregularly Spaced Data," IEEE Transactions on Geoscience Electronics, Vol. GE-9, No. 2, April, 1971, pp. 107-110.

50. Masry, E., "Random Sampling and Reconstruction of Spectra", Information and Control, Vol. 19, 1971, pp. 275-288.

51. Roberts, J. B., Downie J., and Gaster, M., "Spectral Analysis of Signals from a Laser Doppler Anemometer Operating in the Burst Mode," Journal of Physics E: Scientific Instruments, Vol. 13, 1980, pp. 977-981.

52. Srikantaiah, D. V., "An Analytical and Experimental Study of Spectral Analysis Techniques for Turbulence Data Obtained Using Laser Velocimetry," Ph.D. Dissertation, Mechanical and Nuclear Engineering Department, Mississippi State University, December, 1982.

53. Leneman, O. A. Z., and Lewis, J. B., "Random Sampling of Random Processes: Mean-Square Comparison of Various Interpolators," IEEE Transactions on Automatic Control, Vol. AC-11, No. 3, July 1966, pp. 396-403.

54. Adrian, R. J., and Yao, C. S., "Power Spectra of Fluid Velocities by Laser Doppler Velocimetry," *International Symposium on Laser Anemometry,* Winter Annual Meeting of the ASME, Miami Beach, Florida, November 17-22, 1985, pp. 197-208.

55. Jones, R. H., "Spectrum Estimation with Unequally Spaced Observations," Proceedings of the Kyoto International Conference on Circuit and System Theory, September 9-11, 1970, AFOSR-70-2747TR.

56. Jones, R. H., "Spectrum Estimation with Missing Observations," Annals of the Institute of Statistical Mathematics, Vol. 23, 1971, pp. 387-398.

57. Jones, R. H., "Aliasing with Unequally Spaced Observations," Journal of Applied Meteorology, Vol. 11, No. 2, March, 1972, pp. 245-254.

58. Gaster, M., and Roberts, J. B., "The Spectral Analysis of Randomly Sampled Records by a Direct Transform," Proceedings of the Royal Society, London, Vol. A-354, 1977, pp. 27-58.

59. Roberts, J. B., and Gaster, M., "On the Estimation of Spectra from Randomly Sampled Signals: a Method of Reducing Variability," Proceedings of the Royal Society, London, Vol. A-371, 1980, pp. 235-258.

60. Mayo, W. T. Jr., Shay, M. T., and Riter, S., "Digital Estimation of Turbulence Power Spectra from Burst Counter LDV Data," *Proceedings of the Second International Workshop on Laser Velocimetry,* Purdue University, March 27-29, 1974, pp. 16-24.

61. Smith, D. M., and Meadows, D. M., "Power Spectra from Random-Time Samples for Turbulence Measurements with a Laser Velocimeter," *Proceedings of the Second International Workshop on Laser Velocimetry,* Purdue University, March 27-29, 1974, pp. 27-44.

62. Scott, P. F., "Theory and Implementation of Laser Velocimeter Turbulence Spectrum Measurements," *Proceedings of the Second International Workshop on Laser Velocimetry,* Purdue University, March 27-29, 1974, pp. 47-66.

63. Gaster, M., and Roberts, J. B., "Spectral Analysis of Randomly Timed Signals," J. Inst. Maths. Applics., Vol. 15, 1975, pp. 195-216.

64. Marquardt, D. W., and Acuff, S. K., "Direct Quadratic Spectrum Estimation with Irregularly Spaced Data," in *Time Series Analysis of Irregularly Observed Data,* Springer Verlag, New York, 1984, pp. 211-223.

65. Mayo, W. T. Jr., "Error Prediction for LV Turbulence Power Spectra," Final Reort for NASA Langley Reasearch Center, Contract No. NAS1-15353, Spectron Development Laboratories Inc., SDL Report No. 78-6378, February, 1979.

66. Masry, E., and Lui, M. C., "A Consistent Estimate of the Spectrum by Random Sampling of the Time Series," SIAM Journal of Applied Mathematics, Vol. 28, No. 4, June, 1975, pp. 793-810.

67. Masry, E., and Lui, M. C., "Discrete-Time Spectral Estimation of Continuous-Parameter Processes-A New Consistent Estimate," IEEE Transactions in Information Theory, Vol. IT-24, No. 2, May, 1976, pp. 298-312.

68. George, W. K. Jr., P. D. Beuther and J. L. Lumley, "Processing of Random Signals," *Proc. of the Dynamic Flow Conference,* Skovlunde, Denmark, 1978, pp. 757-799.

69. Srikantaiah, D. V. and H. W. Coleman, "Turbulence Spectra from Individual Realization Laser Velocimetry Data," Experiments in Fluids, Vol. 3, 1985, pp. 35-44.

70. Reis, J. C., C. H. Kruger and S. A. Self, "Laser Doppler Velocimetry Measurements of Turbulence Suppression in a Combustion-Driven MHD Generator," *Engineering Applications of Laser Velocimetry,* Papers presented at the Winter Annual Meeting of the ASME, Phoenix, Arizona, November 14-19, 1982, pp. 49-55.

71. Saxena, V., "Power Spectrum Estimation from Randomly Sampled Velocity Data," *International Symposium on Laser Anemometry,* Winter Annual Meeting of the ASME, Miami Beach, Florida, November 17-22, 1985, pp. 209-219.

72. Parzen, E., *Stochastic Processes,* Holden-Day Inc., 1962.

73. Blanc-Lapierre, A., and Fortet, R., *Theory of Random Functions,* Gordon and Breach Science Publishers, New York, 1967.

74. Franklin, J. N., "Numerical Simulation of Stationary and Nonstationary Gaussian random Processes," SIAM Review, Vol. 7, No. 1, January, 1965, pp. 68-80.

75. Schlichting, H., *Boundary Layer Theory,* Fourth Edition, McGraw Hill, New York, 1960.

76. Klebanoff, P. S., "Characteristics of Turbulence in a Boundary Layer with Zero Pressure Gradient," NACA TN 3178, July, 1954.

77. Simpson, R. L., Chew, Y. T., and Shivaprasad, B. G., "The Structure of a Separating Turbulent Boundary Layer. Part 1. Mean Flow and Reynolds Stresses," Journal of Fluid Mechanics, Vol. 113, 1981, pp. 23-51.

78. Kline, S. J., and McClintock, F. A., "Describing Uncertainties in Single-Sample Experiments," Mechanical Engineering, January, 1953, pp. 3-8.

Appendix A. LDV Data for the Junction Vortex

The data computed from the time resolved measurements using a LDV in the junction vortex is presented in the following tables. In the following tables,

x,y,z	Coordinates
U,V	Non-dimensional mean velocities
$\hat{u}$, $\hat{v}$	Turbulence intensities
I_u, I_v	Reverse flow intermittencies
Umax, Vmax	Average maximum velocities
Umin, Vmin	Average minimum velocities

Table A.1. LDV Data at (x,z)=(-3.2 mm, 0 mm)

y	U	$\hat{u}$	I_u	Umax	Umin	V	$\hat{v}$	I_v	Vmax	Vmin
2.0	-0.1997	0.1407	0.923	-0.0127	-0.3269	-0.2493	0.1520	0.954	-0.0436	-0.4111
2.5	-0.1140	0.1242	0.844	-0.0046	-0.2515	-0.2726	0.1522	0.964	-0.0965	-0.4397
3.8	-0.0944	0.1113	0.817	0.0067	-0.2156	-0.3189	0.1567	0.974	-0.1405	-0.4778
5.1	-0.0525	0.1011	0.698	0.0365	-0.1491	-0.3327	0.1575	0.979	-0.1546	-0.4888
6.3	-0.0233	0.0949	0.579	0.0649	-0.1166	-0.3532	0.1494	0.984	-0.1853	-0.5001
7.6	-0.0096	0.1143	0.477	0.0837	-0.1103	-0.3723	0.1456	0.984	-0.2166	-0.5166
8.9	0.0173	0.0874	0.370	0.0957	-0.0694	-0.3544	0.1888	0.956	-0.1308	-0.5091
10.2	0.0302	0.0868	0.299	0.1086	-0.0527	-0.4009	0.1304	0.993	-0.2503	-0.5304
11.4	0.0466	0.0796	0.212	0.1211	-0.0293	-0.3226	0.2703	0.882	0.0450	-0.5182
12.7	0.0551	0.0771	0.178	0.1283	-0.0192	-0.4086	0.1527	0.982	-0.1887	-0.5410
14.0	0.0658	0.0795	0.137	0.1397	-0.0065	-0.4224	0.1429	0.986	-0.2151	-0.5502
15.2	0.0701	0.0768	0.122	0.1419	-0.0009	-0.4259	0.1451	0.986	-0.2126	-0.5503
16.5	0.0756	0.0719	0.102	0.1442	0.0024	-0.4260	0.1595	0.974	-0.2249	-0.5587
17.8	0.0791	0.0750	0.093	0.1497	0.0093	-0.4236	0.1721	0.966	-0.1877	-0.5572
20.3	0.0841	0.0691	0.077	0.1520	0.0188	-0.4148	0.1885	0.955	-0.1485	-0.5517
22.9	0.0884	0.0709	0.063	0.1534	0.0200	-0.3513	0.2733	0.889	0.0248	-0.5370
25.4	0.0878	0.0682	0.058	0.1502	0.0237	-0.3718	0.2478	0.913	0.0350	-0.5246
27.9	0.0912	0.0679	0.048	0.1527	0.0245	-0.3246	0.2912	0.868	0.1218	-0.5080
30.5	0.0891	0.0707	0.048	0.1496	0.0243	-0.2518	0.3245	0.801	0.1753	-0.4773
33.0	0.0904	0.0699	0.049	0.1483	0.0242	-0.2455	0.3271	0.798	0.1846	-0.4741
35.6	0.0896	0.0647	0.045	0.1470	0.0282	-0.3799	0.1514	0.973	-0.1106	-0.4918
40.6	0.0908	0.0623	0.040	0.1438	0.0320	-0.3520	0.1828	0.954	-0.1351	-0.4803
45.7	0.0925	0.0571	0.024	0.1443	0.0359	-0.3455	0.1373	0.978	-0.1945	-0.4519
50.8	0.0896	0.0688	0.000	0.1394	0.0305	-0.3368	0.1288	0.982	-0.2028	-0.4471

Table A.2. LDV Data at (x,z)=(-6.4 mm, 0 mm)

y	U	$\hat{u}$	I_u	Umax	Umin	V	$\hat{v}$	I_v	Vmax	Vmin
2.0	-0.2486	0.1274	0.970	-0.1182	-0.3795	-0.1267	0.1209	0.875	0.0484	-0.2310
2.5	-0.1597	0.1301	0.900	-0.0012	-0.2837	-0.1532	0.1395	0.892	0.0343	-0.2739
3.8	-0.0671	0.1071	0.738	0.0139	-0.2322	-0.1822	0.1528	0.915	0.0089	-0.2949
5.1	-0.0273	0.1024	0.601	0.0723	-0.1359	-0.2177	0.1535	0.932	-0.0020	-0.3335
6.3	0.0039	0.0959	0.460	0.1026	-0.0961	-0.2375	0.1517	0.951	-0.0371	-0.3585
7.6	0.0266	0.0941	0.352	0.1114	-0.0668	-0.2646	0.1437	0.962	-0.0713	-0.3779
8.9	0.0493	0.0982	0.244	0.1380	-0.0474	-0.2788	0.1509	0.960	-0.0793	-0.3985
10.2	0.0671	0.0934	0.181	0.1510	-0.0233	-0.2925	0.1481	0.967	-0.1016	-0.4097
11.4	0.0842	0.0891	0.122	0.1637	-0.0032	-0.3159	0.1409	0.971	-0.1448	-0.4254
12.7	0.0995	0.0855	0.089	0.1795	0.0108	-0.3120	0.1551	0.964	-0.1115	-0.4340
14.0	0.1117	0.0914	0.067	0.1916	0.0206	-0.3143	0.1650	0.957	-0.0804	-0.4315
15.2	0.1215	0.0871	0.056	0.2018	0.0375	-0.3218	0.1713	0.952	-0.0754	-0.4343
16.5	0.1291	0.0881	0.049	0.2130	0.0476	-0.3248	0.1637	0.955	-0.0851	-0.4433
17.8	0.1356	0.0868	0.038	0.2199	0.0574	-0.3289	0.1623	0.959	-0.0967	-0.4469
20.3	0.1462	0.0865	0.025	0.2253	0.0645	-0.3174	0.1854	0.937	-0.0404	-0.4445
22.9	0.1528	0.0953	0.024	0.2296	0.0603	-0.3182	0.1889	0.936	-0.0368	-0.4391
25.4	0.1602	0.0877	0.018	0.2354	0.0771	-0.3183	0.1844	0.938	-0.0421	-0.4417
27.9	0.1602	0.0898	0.018	0.2404	0.0808	-0.3245	0.1804	0.944	-0.0519	-0.4387
30.5	0.1645	0.0815	0.013	0.2348	0.0875	-0.2516	0.2476	0.895	0.0540	-0.4030
33.0	0.1701	0.0769	0.009	0.2426	0.0986	-0.2689	0.2048	0.929	0.1540	-0.3892
35.6	0.1681	0.0786	0.008	0.2383	0.1006	-0.2664	0.2175	0.916	0.0664	-0.3932
40.6	0.1681	0.0802	0.007	0.2335	0.1017	-0.2793	0.1871	0.943	-0.0057	-0.3867
45.7	0.1754	0.0744	0.006	0.2394	0.1094	-0.2641	0.1671	0.951	-0.0500	-0.3580
50.8	0.1757	0.0677	0.005	0.2334	0.1102	-0.2662	0.1405	0.969	-0.1173	-0.3493

Table A.3. LDV Data at (x,z)=(-9.5 mm, 0 mm)

y	U	$\hat{u}$	I_u	Umax	Umin	V	$\hat{v}$	I_v	Vmax	Vmin
2.0	-0.3005	0.1324	0.982	-0.1646	-0.4360	-0.0688	0.0948	0.814	0.0283	-0.1664
2.5	-0.2148	0.1313	0.948	-0.0644	-0.3580	-0.0907	0.0989	0.859	0.0057	-0.1920
3.8	-0.0949	0.1149	0.785	0.0083	-0.2562	-0.1297	0.1022	0.910	-0.0357	-0.2467
5.1	-0.0362	0.1030	0.619	0.0678	-0.1425	-0.1648	0.1049	0.954	-0.0661	-0.2793
6.3	0.0058	0.1014	0.453	0.0985	-0.0872	-0.1846	0.1055	0.961	-0.0984	-0.3100
7.6	0.0409	0.0965	0.314	0.1262	-0.0544	-0.2063	0.1021	0.973	-0.1165	-0.3200
8.9	0.0742	0.0902	0.190	0.1567	-0.0228	-0.2241	0.0964	0.987	-0.1433	-0.3313
10.2	0.0939	0.0946	0.138	0.1878	0.0041	-0.2349	0.0939	0.992	-0.1557	-0.3459
11.4	0.1193	0.0919	0.079	0.2086	0.0306	-0.2526	0.0934	0.996	-0.1664	-0.3540
12.7	0.1329	0.0917	0.055	0.2281	0.0461	-0.2623	0.0945	0.995	-0.1815	-0.3675
14.0	0.1513	0.0885	0.034	0.2356	0.0594	-0.2752	0.0919	0.997	-0.1879	-0.3686
15.2	0.1662	0.0890	0.024	0.2539	0.0792	-0.2741	0.0903	0.997	-0.1966	-0.3746
16.5	0.1718	0.0887	0.022	0.2691	0.0917	-0.2793	0.0871	0.997	-0.1957	-0.3712
17.8	0.1806	0.0880	0.018	0.2648	0.0982	-0.2867	0.0881	0.997	-0.1958	-0.3739
20.3	0.1954	0.0869	0.014	0.2751	0.1055	-0.2902	0.0834	0.999	-0.2149	-0.3799
22.9	0.2073	0.0835	0.007	0.2905	0.1243	-0.2867	0.0805	0.998	-0.2151	-0.3716
25.4	0.2151	0.0845	0.006	0.2962	0.1296	-0.2843	0.0798	0.997	-0.2134	-0.3697
27.9	0.2203	0.0810	0.005	0.3019	0.1469	-0.2786	0.0778	0.998	-0.2108	-0.3692
30.5	0.2255	0.0811	0.005	0.3044	0.1489	-0.2828	0.0784	0.998	-0.2033	-0.3629
33.0	0.2319	0.0741	0.003	0.3029	0.1592	-0.2719	0.0785	0.998	-0.1991	-0.3536
35.6	0.2292	0.0774	0.003	0.3017	0.1553	-0.2689	0.0817	0.997	-0.1960	-0.3526
40.6	0.2351	0.0716	0.002	0.3007	0.1629	-0.2548	0.0736	0.998	-0.1916	-0.3424
45.7	0.2422	0.0732	0.003	0.3042	0.1633	-0.2462	0.0668	0.999	-0.1881	-0.3219
50.8	0.2420	0.0699	0.003	0.3070	0.1782	-0.2250	0.0661	0.999	-0.1663	-0.2972

Table A.4. LDV Data at (x,z)=(-12.7 mm, 0 mm)

y	U	$\hat{u}$	I_u	Umax	Umin	V	$\hat{v}$	I_v	Vmax	Vmin
2.0	-0.3491	0.1302	0.991	-0.1362	-0.5002	-0.0591	0.0970	0.796	0.0402	-0.1600
2.5	-0.2500	0.1299	0.963	-0.1202	-0.3858	-0.0723	0.0985	0.825	0.0217	-0.1769
3.8	-0.1436	0.1224	0.862	-0.0293	-0.3030	-0.1122	0.0960	0.911	-0.0225	-0.2135
5.1	-0.0676	0.1143	0.696	0.0637	-0.1891	-0.1385	0.0968	0.941	-0.0503	-0.2458
6.3	-0.0129	0.1133	0.510	0.1018	-0.1452	-0.1618	0.0972	0.962	-0.0727	-0.2675
7.6	0.0229	0.1118	0.371	0.1634	-0.0863	-0.1824	0.0963	0.975	-0.0953	-0.2895
8.9	0.0646	0.1174	0.227	0.1950	-0.0487	-0.1943	0.0925	0.981	-0.1222	-0.2930
10.2	0.0958	0.1119	0.141	0.2379	-0.0070	-0.2060	0.0907	0.987	-0.1278	-0.3084
11.4	0.1292	0.1138	0.085	0.2570	0.0269	-0.2147	0.0872	0.990	-0.1402	-0.3174
12.7	0.1418	0.1157	0.062	0.2705	0.0381	-0.2237	0.0891	0.991	-0.1439	-0.3231
14.0	0.1743	0.1122	0.034	0.2858	0.0537	-0.2317	0.0831	0.995	-0.1517	-0.3205
15.2	0.1884	0.1057	0.026	0.3058	0.0899	-0.2364	0.0795	0.998	-0.1692	-0.3315
16.5	0.2000	0.1025	0.020	0.3132	0.1024	-0.2425	0.0794	0.998	-0.1701	-0.3329
17.8	0.2134	0.1058	0.000	0.3274	0.1166	-0.2428	0.0780	0.999	-0.1722	-0.3304
20.3	0.2362	0.1057	0.000	0.3382	0.1285	-0.2491	0.0759	0.999	-0.1761	-0.3352
22.9	0.2500	0.1062	0.000	0.3514	0.1457	-0.2454	0.0743	0.998	-0.1777	-0.3282
25.4	0.2621	0.1119	0.000	0.3597	0.1425	-0.2360	0.0710	0.999	-0.1705	-0.3224
27.9	0.2699	0.1069	0.000	0.3678	0.1691	-0.2347	0.0749	0.998	-0.1603	-0.3161
30.5	0.2728	0.1158	0.000	0.3677	0.1636	-0.2341	0.0702	0.999	-0.1651	-0.3127
33.0	0.2782	0.1179	0.000	0.3726	0.1616	-0.2271	0.0727	0.998	-0.1604	-0.3062
35.6	0.2828	0.1146	0.000	0.3706	0.1677	-0.2271	0.0727	0.998	-0.1604	-0.3062
40.6	0.2932	0.1139	0.000	0.3769	0.1858	-0.2119	0.0705	0.998	-0.1455	-0.2840
45.7	0.3084	0.0988	0.000	0.3822	0.2080	-0.2027	0.0619	0.999	-0.1476	-0.2701
50.8	0.3173	0.0786	0.000	0.3798	0.2297	-0.1892	0.0582	0.998	-0.1367	-0.2573

Table A.5. LDV Data at (x,z)=(-15.9 mm, 0 mm)

y	U	$\hat{u}$	I_u	Umax	Umin	V	$\hat{v}$	I_v	Vmax	Vmin
2.0	-0.3480	0.1339	0.993	-0.1924	-0.4836	-0.0533	0.0943	0.770	0.0393	-0.1566
2.5	-0.2718	0.1355	0.968	-0.1471	-0.4169	-0.0672	0.1001	0.811	0.0280	-0.1811
3.8	-0.1546	0.1283	0.873	-0.0361	-0.3195	-0.1011	0.1048	0.886	-0.0014	-0.2034
5.1	-0.0542	0.1249	0.639	0.0713	-0.1971	-0.1343	0.1022	0.932	-0.0453	-0.2497
6.3	0.0095	0.1191	0.443	0.1400	-0.1125	-0.1525	0.1055	0.946	-0.0643	-0.2760
7.6	0.0620	0.1269	0.262	0.1999	-0.0555	-0.1793	0.1005	0.977	-0.0807	-0.2882
8.9	0.1004	0.1267	0.167	0.2411	-0.0127	-0.1903	0.0956	0.983	-0.1112	-0.3066
10.2	0.1377	0.1294	0.063	0.2732	0.0128	-0.1903	0.0948	0.982	-0.1145	-0.3042
11.4	0.1739	0.1252	0.047	0.3068	0.0525	-0.2018	0.0868	0.989	-0.1242	-0.3001
12.7	0.1931	0.1196	0.044	0.3205	0.0780	-0.2073	0.0833	0.991	-0.1283	-0.3009
14.0	0.2201	0.1128	0.023	0.3436	0.1144	-0.2094	0.0790	0.996	-0.1334	-0.2960
15.2	0.2404	0.1107	0.024	0.3592	0.1413	-0.2078	0.0761	0.995	-0.1315	-0.2905
16.5	0.2598	0.1088	0.000	0.3687	0.1497	-0.2121	0.0761	0.997	-0.1433	-0.3033
17.8	0.2682	0.1086	0.000	0.3773	0.1668	-0.2142	0.0744	0.997	-0.1376	-0.2915
20.3	0.2929	0.1030	0.000	0.3953	0.1964	-0.2116	0.0707	0.998	-0.1472	-0.2961
22.9	0.3064	0.1021	0.000	0.3985	0.2045	-0.2085	0.0691	0.998	-0.1396	-0.2825
25.4	0.3108	0.1113	0.000	0.4114	0.2118	-0.2035	0.0679	0.999	-0.1394	-0.2750
27.9	0.3244	0.1044	0.000	0.4137	0.2199	-0.2012	0.0762	0.998	-0.1364	-0.2782
30.5	0.3278	0.1102	0.000	0.4168	0.2225	-0.1969	0.0658	0.998	-0.1368	-0.2741
33.0	0.3356	0.1160	0.000	0.4246	0.2241	-0.1891	0.0632	0.998	-0.1320	-0.2631
35.6	0.3391	0.1144	0.000	0.4279	0.2328	-0.1845	0.0663	0.997	-0.1221	-0.2535
40.6	0.3452	0.1168	0.000	0.4275	0.2357	-0.1800	0.0646	0.997	-0.1209	-0.2480
45.7	0.3550	0.1016	0.000	0.4301	0.2635	-0.1701	0.0682	0.995	-0.1134	-0.2406
50.8	0.3612	0.0845	0.000	0.4257	0.2815	-0.1603	0.0554	0.997	-0.1035	-0.2155

Table A.6. LDV Data at (x,z)=(-19.1 mm, 0 mm)

y	U	$\hat{u}$	I_u	Umax	Umin	V	$\hat{v}$	I_v	Vmax	Vmin
2.0	-0.3663	0.1374	0.992	-0.2336	-0.5146	-0.0555	0.0994	0.775	0.0497	-0.1536
2.5	-0.2896	0.1317	0.982	-0.1653	-0.4303	-0.0696	0.1020	0.810	0.0342	-0.1765
3.8	-0.1824	0.1369	0.898	-0.0556	-0.3348	-0.1110	0.1170	0.876	0.0071	-0.2471
5.1	-0.0850	0.1357	0.723	0.0657	-0.2175	-0.1415	0.1173	0.935	-0.0497	-0.2834
6.3	0.0068	0.1356	0.464	0.1571	-0.1294	-0.1715	0.1211	0.953	-0.0717	-0.3097
7.6	0.0707	0.1439	0.278	0.2672	-0.0477	-0.1757	0.1129	0.972	-0.0882	-0.3268
8.9	0.1217	0.1532	0.156	0.2946	-0.0176	-0.1892	0.1045	0.978	-0.0946	-0.3096
10.2	0.1582	0.1406	0.089	0.3197	0.0204	-0.1893	0.0963	0.980	-0.1104	-0.3047
11.4	0.2092	0.1437	0.041	0.3730	0.0768	-0.1916	0.0919	0.977	-0.1130	-0.2980
12.7	0.2393	0.1423	0.040	0.3881	0.1027	-0.1951	0.0852	0.987	-0.1172	-0.2905
14.0	0.2578	0.1344	0.035	0.3934	0.1203	-0.1932	0.0811	0.990	-0.1200	-0.2838
15.2	0.2779	0.1258	0.030	0.4034	0.1538	-0.1906	0.0768	0.990	-0.1216	-0.2777
16.5	0.2991	0.1199	0.000	0.4185	0.1817	-0.1869	0.0732	0.994	-0.1188	-0.2727
17.8	0.3078	0.1145	0.000	0.4197	0.1910	-0.1865	0.0726	0.992	-0.1129	-0.2630
20.3	0.3251	0.1155	0.000	0.4341	0.2139	-0.1813	0.0681	0.995	-0.1129	-0.2536
22.9	0.3451	0.1021	0.000	0.4422	0.2398	-0.1800	0.0647	0.996	-0.1146	-0.2470
25.4	0.3554	0.1020	0.000	0.4543	0.2585	-0.1769	0.0651	0.996	-0.1148	-0.2460
27.9	0.3623	0.1040	0.000	0.4578	0.2717	-0.1741	0.0621	0.997	-0.1138	-0.2414
30.5	0.3676	0.1034	0.000	0.4655	0.2806	-0.1693	0.0626	0.996	-0.1022	-0.2319
33.0	0.3769	0.1015	0.000	0.4713	0.2878	-0.1632	0.0574	0.996	-0.1024	-0.2218
35.6	0.3795	0.1248	0.000	0.4749	0.2646	-0.1610	0.0602	0.996	-0.1002	-0.2235
40.6	0.3825	0.1251	0.000	0.4760	0.2716	-0.1557	0.0628	0.995	-0.0975	-0.2191
45.7	0.3974	0.1102	0.000	0.4775	0.2977	-0.1483	0.0575	0.995	-0.0919	-0.2110
50.8	0.4069	0.1018	0.000	0.4844	0.3216	-0.1366	0.0642	0.995	-0.0863	-0.2069

Table A.7. LDV Data at (x,z)=(-21.8 mm, 0 mm)

y	U	$\hat{u}$	I_u	Umax	Umin	V	$\hat{v}$	I_v	Vmax	Vmin
2.0	-0.4065	0.1396	0.996	-0.2539	-0.5483	-0.0537	0.1065	0.753	0.0505	-0.1579
2.5	-0.3311	0.1406	0.987	-0.2007	-0.4930	-0.0700	0.1148	0.795	0.0404	-0.1884
3.8	-0.2132	0.1469	0.922	-0.0632	-0.3694	-0.1212	0.1314	0.880	0.0126	-0.2659
5.1	-0.1119	0.1530	0.759	0.0528	-0.2665	-0.1561	0.1493	0.916	-0.0221	-0.3454
6.3	-0.0034	0.1597	0.495	0.1734	-0.1886	-0.1800	0.1443	0.943	-0.0545	-0.3588
7.6	0.0754	0.1702	0.305	0.2955	-0.0714	-0.1906	0.1351	0.957	-0.0640	-0.3448
8.9	0.1560	0.1725	0.144	0.3632	0.0049	-0.1943	0.1255	0.955	-0.0854	-0.3413
10.2	0.1970	0.1739	0.073	0.4111	0.0443	-0.1931	0.1136	0.969	-0.0896	-0.3216
11.4	0.2539	0.1645	0.036	0.4319	0.0888	-0.1842	0.1002	0.974	-0.0951	-0.3021
12.7	0.2666	0.1565	0.041	0.4396	0.1239	-0.1760	0.0938	0.972	-0.0832	-0.2755
14.0	0.3004	0.1412	0.041	0.4437	0.1578	-0.1658	0.0874	0.970	-0.0732	-0.2539
15.2	0.3302	0.1240	0.030	0.4582	0.2117	-0.1655	0.0788	0.981	-0.0806	-0.2459
16.5	0.3334	0.1245	0.000	0.4554	0.2082	-0.1625	0.0749	0.984	-0.0838	-0.2390
17.8	0.3483	0.1131	0.000	0.4658	0.2470	-0.1579	0.0726	0.984	-0.0820	-0.2318
20.3	0.3733	0.1029	0.000	0.4808	0.2771	-0.1546	0.0683	0.988	-0.0858	-0.2236
22.9	0.3796	0.1026	0.000	0.4910	0.2919	-0.1483	0.0647	0.987	-0.0837	-0.2173
25.4	0.3947	0.0992	0.000	0.4900	0.2990	-0.1472	0.0614	0.992	-0.0872	-0.2133
27.9	0.4013	0.1011	0.000	0.5044	0.3125	-0.1448	0.0605	0.992	-0.0857	-0.2101
30.5	0.4115	0.1069	0.000	0.5091	0.3163	-0.1440	0.0565	0.993	-0.0791	-0.2013
33.0	0.4147	0.1104	0.000	0.5152	0.3223	-0.1399	0.0565	0.993	-0.0795	-0.1967
35.6	0.4209	0.1057	0.000	0.5172	0.3255	-0.1378	0.0582	0.992	-0.0757	-0.1950
40.6	0.4289	0.1147	0.000	0.5214	0.3262	-0.1326	0.0597	0.992	-0.0756	-0.1922
45.7	0.4411	0.1206	0.000	0.5359	0.3323	-0.1266	0.0538	0.993	-0.0758	-0.1819
50.8	0.4522	0.1027	0.000	0.5349	0.3623	-0.1204	0.0572	0.992	-0.0654	-0.1744

Table A.8. LDV Data at (x,z)=(-25.4 mm, 0 mm)

y	U	$\hat{u}$	I_u	Umax	Umin	V	$\hat{v}$	I_v	Vmax	Vmin
2.0	-0.4477	0.1276	0.997	-0.3067	-0.5746	-0.0535	0.1251	0.732	0.0642	-0.1845
2.5	-0.3939	0.1389	0.994	-0.2371	-0.5360	-0.0682	0.1320	0.769	0.0568	-0.2156
3.8	-0.2874	0.1569	0.962	-0.1289	-0.4604	-0.1169	0.1518	0.850	0.0411	-0.2842
5.1	-0.1564	0.1755	0.800	0.0303	-0.3511	-0.1659	0.1726	0.900	0.0057	-0.3639
6.3	-0.0346	0.1870	0.561	0.1830	-0.2210	-0.1813	0.1703	0.919	-0.0149	-0.3800
7.6	0.0817	0.2079	0.327	0.3610	-0.0991	-0.1880	0.1578	0.924	-0.0331	-0.3684
8.9	0.1899	0.2133	0.141	0.4260	-0.0473	-0.1869	0.1486	0.933	-0.0401	-0.3484
10.2	0.2430	0.1950	0.077	0.4851	0.0826	-0.1847	0.1248	0.946	-0.0593	-0.3187
11.4	0.2964	0.1843	0.036	0.4949	0.1197	-0.1713	0.1153	0.944	-0.0608	-0.2958
12.7	0.3159	0.1677	0.040	0.4948	0.1525	-0.1614	0.1030	0.949	-0.0524	-0.2677
14.0	0.3556	0.1509	0.035	0.5037	0.2021	-0.1584	0.0919	0.963	-0.0612	-0.2548
15.2	0.3608	0.1467	0.026	0.5035	0.2255	-0.1518	0.0850	0.965	-0.0669	-0.2395
16.5	0.3757	0.1433	0.000	0.5084	0.2441	-0.1416	0.0795	0.965	-0.0653	-0.2280
17.8	0.3858	0.1292	0.000	0.5120	0.2708	-0.1393	0.0750	0.970	-0.0573	-0.2146
20.3	0.3979	0.1087	0.000	0.5077	0.2968	-0.1365	0.0676	0.979	-0.0655	-0.2040
22.9	0.4152	0.1139	0.000	0.5221	0.3073	-0.1297	0.0648	0.978	-0.0632	-0.1985
25.4	0.4249	0.1104	0.000	0.5300	0.3193	-0.1267	0.0607	0.984	-0.0663	-0.1907
27.9	0.4358	0.1115	0.000	0.5418	0.3330	-0.1269	0.0599	0.985	-0.0670	-0.1885
30.5	0.4456	0.1098	0.000	0.5497	0.3440	-0.1153	0.0541	0.985	-0.0640	-0.1771
33.0	0.4495	0.1165	0.000	0.5557	0.3473	-0.1187	0.0541	0.987	-0.0610	-0.1732
35.6	0.4547	0.1214	0.000	0.5581	0.3428	-0.1179	0.0535	0.985	-0.0612	-0.1712
40.6	0.4593	0.1473	0.000	0.5645	0.3202	-0.1119	0.0573	0.984	-0.0573	-0.1701
45.7	0.4782	0.1389	0.000	0.5753	0.3459	-0.1075	0.0551	0.983	-0.0564	-0.1632
50.8	0.4944	0.1241	0.000	0.5794	0.3761	-0.1050	0.0541	0.985	-0.0563	-0.1603

Table A.9. LDV Data at (x,z)=(-28.6 mm, 0 mm)

y	U	$\hat{u}$	I_u	Umax	Umin	V	$\hat{v}$	I_v	Vmax	Vmin
2.0	-0.4682	0.1315	0.997	-0.3250	-0.6010	-0.0436	0.1372	0.688	0.0911	-0.1799
2.5	-0.4203	0.1370	0.995	-0.2796	-0.5619	-0.0566	0.1477	0.726	0.0859	-0.1983
3.8	-0.3310	0.1621	0.963	-0.1662	-0.5082	-0.1234	0.1747	0.831	0.0631	-0.3017
5.1	-0.2058	0.1874	0.857	0.0065	-0.3985	-0.1507	0.1876	0.854	0.0381	-0.3620
6.3	-0.0427	0.2150	0.568	0.1923	-0.2865	-0.1637	0.2020	0.871	0.0455	-0.3811
7.6	0.1178	0.2316	0.290	0.3919	-0.1204	-0.1832	0.1902	0.893	0.0230	-0.3922
8.9	0.2143	0.2342	0.148	0.4778	-0.0538	-0.1732	0.1725	0.899	-0.0011	-0.3609
10.2	0.2716	0.2321	0.087	0.5314	0.0452	-0.1612	0.1510	0.888	-0.0173	-0.3235
11.4	0.3141	0.2228	0.053	0.5471	0.1014	-0.1421	0.1389	0.884	0.0004	-0.2836
12.7	0.3422	0.1963	0.037	0.5400	0.1540	-0.1353	0.1197	0.891	-0.0085	-0.2545
14.0	0.3713	0.1840	0.038	0.5515	0.1966	-0.1269	0.1054	0.905	-0.0193	-0.2334
15.2	0.3909	0.1634	0.032	0.5479	0.2380	-0.1226	0.0919	0.919	-0.0231	-0.2139
16.5	0.4034	0.1533	0.000	0.5440	0.2579	-0.1161	0.0857	0.922	-0.0253	-0.2020
17.8	0.4145	0.1341	0.000	0.5510	0.2969	-0.1135	0.0774	0.934	-0.0324	-0.1910
20.3	0.4287	0.1413	0.000	0.5594	0.3054	-0.1107	0.0701	0.951	-0.0401	-0.1855
22.9	0.4464	0.1276	0.000	0.5655	0.3268	-0.1079	0.0651	0.955	-0.0433	-0.1765
25.4	0.4542	0.1285	0.000	0.5731	0.3385	-0.1060	0.0613	0.963	-0.0452	-0.1725
27.9	0.4627	0.1400	0.000	0.5793	0.3342	-0.1054	0.0721	0.966	-0.0457	-0.1697
30.5	0.4684	0.1327	0.000	0.5803	0.3504	-0.1040	0.0566	0.969	-0.0479	-0.1654
33.0	0.4806	0.1269	0.000	0.5842	0.3538	-0.1024	0.0576	0.970	-0.0467	-0.1638
35.6	0.4869	0.1300	0.000	0.5900	0.3634	-0.1031	0.0575	0.968	-0.0467	-0.1642
40.6	0.4952	0.1461	0.000	0.5952	0.3505	-0.0990	0.0547	0.971	-0.0485	-0.1606
45.7	0.5110	0.1608	0.000	0.6082	0.3438	-0.0943	0.0505	0.974	-0.0427	-0.1462
50.8	0.5215	0.1450	0.000	0.6096	0.3761	-0.0875	0.0515	0.965	-0.0379	-0.1419

Table A.10. LDV Data at (x,z)=(-31.8 mm, 0 mm)

y	U	$\hat{u}$	I_u	Umax	Umin	V	$\hat{v}$	I_v	Vmax	Vmin
2.0	-0.4773	0.1409	0.989	-0.3262	-0.6116	-0.0353	0.1665	0.624	0.1117	-0.2150
2.5	-0.4446	0.1389	0.989	-0.3023	-0.5819	-0.0343	0.1687	0.642	0.1192	-0.2152
3.8	-0.3567	0.1667	0.967	-0.1680	-0.5192	-0.0763	0.2059	0.719	0.1484	-0.2880
5.1	-0.2268	0.1997	0.858	0.0153	-0.4251	-0.0903	0.2375	0.733	0.1807	-0.3477
6.3	-0.0804	0.2279	0.637	0.1985	-0.3006	-0.1072	0.2517	0.747	0.1892	-0.3812
7.6	0.0960	0.2553	0.324	0.4008	-0.1476	-0.1152	0.2343	0.747	0.1441	-0.3708
8.9	0.2310	0.2464	0.150	0.5284	0.0190	-0.0960	0.2210	0.732	0.1508	-0.3300
10.2	0.2888	0.2389	0.095	0.5550	0.0666	-0.0909	0.1830	0.738	0.1079	-0.2903
11.4	0.3508	0.2146	0.043	0.5818	0.1733	-0.0833	0.1574	0.752	0.0844	-0.2426
12.7	0.3694	0.2110	0.040	0.5767	0.1731	-0.0811	0.1356	0.772	0.0621	-0.2199
14.0	0.3865	0.1988	0.037	0.5710	0.1931	-0.0771	0.1121	0.788	0.0350	-0.1936
15.2	0.4112	0.1882	0.033	0.5712	0.2178	-0.0769	0.1005	0.814	0.0289	-0.1722
16.5	0.4305	0.1812	0.000	0.5779	0.2297	-0.0750	0.0881	0.831	0.0175	-0.1600
17.8	0.4454	0.1578	0.000	0.5852	0.2933	-0.0757	0.0804	0.850	0.0098	-0.1539
20.3	0.4588	0.1372	0.000	0.5858	0.3242	-0.0795	0.0677	0.895	-0.0080	-0.1457
22.9	0.4786	0.1343	0.000	0.5934	0.3384	-0.0779	0.0606	0.909	-0.0206	-0.1465
25.4	0.4820	0.1229	0.000	0.5974	0.3651	-0.0812	0.0625	0.922	-0.0236	-0.1463
27.9	0.4899	0.1263	0.000	0.5980	0.3622	-0.0826	0.0564	0.935	-0.0268	-0.1442
30.5	0.5057	0.1283	0.000	0.6055	0.3798	-0.0792	0.0540	0.938	-0.0283	-0.1399
33.0	0.5122	0.1290	0.000	0.6135	0.3853	-0.0794	0.0537	0.933	-0.0266	-0.1388
35.6	0.5236	0.1282	0.000	0.6177	0.3920	-0.0814	0.0527	0.944	-0.0311	-0.1405
40.6	0.5280	0.1391	0.000	0.6230	0.3893	-0.0803	0.0527	0.946	-0.0304	-0.1384
45.7	0.5405	0.1552	0.000	0.6314	0.3752	-0.0761	0.0503	0.947	-0.0287	-0.1343
50.8	0.5600	0.1379	0.000	0.6402	0.4168	-0.0783	0.0508	0.949	-0.0247	-0.1291

Table A.11. LDV Data at (x,z)=(-34.9 mm, 0 mm)

y	U	$\hat{u}$	I_u	Umax	Umin	V	$\hat{v}$	I_v	Vmax	Vmin
2.0	-0.4781	0.1617	0.974	-0.2972	-0.6268	-0.0384	0.1529	0.646	0.1255	-0.1776
2.5	-0.4501	0.1582	0.976	-0.2920	-0.5999	-0.0186	0.1758	0.589	0.1467	-0.2164
3.8	-0.3674	0.1796	0.943	-0.1590	-0.5332	-0.0695	0.2252	0.691	0.1635	-0.3007
5.1	-0.2476	0.2123	0.846	0.0162	-0.4391	-0.0889	0.2433	0.717	0.1771	-0.3333
6.3	-0.0512	0.2521	0.575	0.2610	-0.3136	-0.1061	0.2539	0.732	0.1992	-0.3784
7.6	0.1328	0.2566	0.283	0.4387	-0.1351	-0.0922	0.2512	0.709	0.1930	-0.3635
8.9	0.2709	0.2387	0.120	0.5360	0.0196	-0.0678	0.2289	0.674	0.1909	-0.3153
10.2	0.3549	0.2220	0.055	0.5829	0.1514	-0.0688	0.1986	0.689	0.1548	-0.2760
11.4	0.3983	0.2003	0.043	0.5880	0.2098	-0.0653	0.1698	0.704	0.1255	-0.2402
12.7	0.4239	0.1914	0.032	0.5978	0.2413	-0.0685	0.1457	0.730	0.0890	-0.2119
14.0	0.4378	0.1872	0.030	0.6013	0.2547	-0.0620	0.1269	0.730	0.0686	-0.1901
15.2	0.4659	0.1505	0.022	0.6083	0.3200	-0.0574	0.1067	0.739	0.0503	-0.1679
16.5	0.4721	0.1466	0.000	0.6060	0.3277	-0.0577	0.0952	0.764	0.0470	-0.1478
17.8	0.4775	0.1415	0.000	0.6104	0.3460	-0.0598	0.0828	0.787	0.0299	-0.1390
20.3	0.4911	0.1286	0.000	0.6135	0.3724	-0.0616	0.0730	0.828	0.0103	-0.1369
22.9	0.5115	0.1270	0.000	0.6239	0.3907	-0.0615	0.0642	0.853	0.0017	-0.1290
25.4	0.5191	0.1472	0.000	0.6289	0.3746	-0.0630	0.0610	0.867	-0.0033	-0.1276
27.9	0.5328	0.1121	0.000	0.6274	0.4160	-0.0664	0.0575	0.890	-0.0098	-0.1270
30.5	0.5412	0.1131	0.000	0.6331	0.4285	-0.0677	0.0546	0.912	-0.0135	-0.1235
33.0	0.5555	0.1155	0.000	0.6426	0.4323	-0.0686	0.0516	0.915	-0.0163	-0.1221
35.6	0.5552	0.1180	0.000	0.6427	0.4382	-0.0697	0.0645	0.910	-0.0136	-0.1266
40.6	0.5709	0.1120	0.000	0.6496	0.4661	-0.0667	0.0525	0.916	-0.0148	-0.1206
45.7	0.5907	0.1126	0.000	0.6607	0.4775	-0.0645	0.0630	0.915	-0.0150	-0.1282
50.8	0.5942	0.1205	0.000	0.6619	0.4902	-0.0625	0.0612	0.918	-0.0148	-0.1229

Table A.12. LDV Data at (x,z)=(-38.1 mm, 0 mm)

y	U	$\hat{u}$	I_u	Umax	Umin	V	$\hat{v}$	I_v	Vmax	Vmin
2.0	-0.4787	0.1572	0.977	-0.3137	-0.6233	-0.0040	0.1703	0.539	0.1634	-0.1787
2.5	-0.4443	0.1597	0.974	-0.2890	-0.5961	-0.0005	0.1824	0.535	0.1691	-0.2035
3.8	-0.3800	0.1694	0.960	-0.1619	-0.5358	-0.0014	0.2145	0.557	0.2140	-0.2589
5.1	-0.2727	0.2021	0.877	-0.0598	-0.4665	-0.0255	0.2449	0.600	0.2440	-0.2982
6.3	-0.0831	0.2402	0.623	0.2005	-0.3280	-0.0232	0.2624	0.591	0.2783	-0.3311
7.6	0.0937	0.2563	0.332	0.3890	-0.1781	-0.0275	0.2493	0.592	0.2503	-0.2855
8.9	0.2277	0.2419	0.153	0.5027	-0.0156	-0.0194	0.2351	0.567	0.2317	-0.2791
10.2	0.3188	0.2110	0.060	0.5732	0.1603	-0.0146	0.1991	0.560	0.1949	-0.2232
11.4	0.3577	0.2079	0.029	0.5852	0.1857	-0.0103	0.1702	0.558	0.1758	-0.1711
12.7	0.4029	0.1778	0.035	0.5840	0.2484	-0.0172	0.1477	0.586	0.1419	-0.1553
14.0	0.4194	0.1772	0.027	0.5986	0.2707	-0.0198	0.1279	0.594	0.1203	-0.1392
15.2	0.4430	0.1550	0.033	0.5950	0.2949	-0.0203	0.1057	0.607	0.0972	-0.1194
16.5	0.4627	0.1434	0.000	0.6066	0.3274	-0.0245	0.0958	0.630	0.0823	-0.1083
17.8	0.4702	0.1455	0.000	0.6098	0.3335	-0.0293	0.0855	0.663	0.0701	-0.1080
20.3	0.4912	0.1233	0.000	0.6085	0.3657	-0.0377	0.0723	0.722	0.0539	-0.1055
22.9	0.5043	0.1141	0.000	0.6162	0.3937	-0.0443	0.0686	0.771	0.0239	-0.1134
25.4	0.5192	0.1107	0.000	0.6255	0.4059	-0.0445	0.0629	0.788	0.0178	-0.1103
27.9	0.5353	0.1069	0.000	0.6330	0.4250	-0.0474	0.0587	0.810	0.0127	-0.1075
30.5	0.5469	0.1087	0.000	0.6399	0.4355	-0.0500	0.0539	0.837	0.0046	-0.1040
33.0	0.5546	0.1084	0.000	0.6455	0.4511	-0.0502	0.0543	0.845	0.0044	-0.1049
35.6	0.5680	0.1081	0.000	0.6512	0.4554	-0.0544	0.0563	0.863	0.0033	-0.1099
40.6	0.5786	0.1179	0.000	0.6617	0.4642	-0.0539	0.0578	0.863	0.0022	-0.1103
45.7	0.6014	0.1214	0.000	0.6782	0.4957	-0.0493	0.0517	0.870	-0.0016	-0.1001
50.8	0.6134	0.1070	0.000	0.6810	0.5193	-0.0527	0.0625	0.884	-0.0026	-0.1098

Table A.13. LDV Data at (x,z)=(-41.3 mm, 0 mm)

y	U	$\hat{u}$	I_u	Umax	Umin	V	$\hat{v}$	I_v	Vmax	Vmin
2.0	-0.4383	0.1995	0.938	-0.2165	-0.6209	0.0591	0.1725	0.334	0.2493	-0.0958
2.5	-0.4165	0.1929	0.940	-0.1408	-0.5924	0.0687	0.1879	0.327	0.2828	-0.1131
3.8	-0.3437	0.2024	0.905	-0.1084	-0.5300	0.0918	0.2054	0.325	0.3329	-0.1281
5.1	-0.2303	0.2298	0.804	0.0602	-0.4442	0.1070	0.2299	0.322	0.3864	-0.1429
6.3	-0.0611	0.2562	0.566	0.2401	-0.3325	0.1197	0.2462	0.315	0.4160	-0.1512
7.6	0.1009	0.2546	0.314	0.4005	-0.1770	0.1000	0.2406	0.333	0.3942	-0.1406
8.9	0.2348	0.2433	0.136	0.4856	-0.0305	0.0781	0.2229	0.354	0.3671	-0.1235
10.2	0.3081	0.2262	0.075	0.5399	0.0850	0.0502	0.2043	0.392	0.3034	-0.1330
11.4	0.3646	0.2026	0.036	0.5578	0.1610	0.0379	0.1759	0.403	0.2418	-0.1227
12.7	0.3801	0.2267	0.057	0.5773	0.1702	0.0116	0.1528	0.460	0.1978	-0.1207
14.0	0.4193	0.1901	0.038	0.5862	0.2254	0.0019	0.1378	0.496	0.1620	-0.1135
15.2	0.4551	0.1596	0.029	0.6010	0.2898	-0.0079	0.1205	0.532	0.1291	-0.1091
16.5	0.4662	0.1598	0.000	0.6090	0.3187	-0.0212	0.1093	0.586	0.1018	-0.1170
17.8	0.4863	0.1394	0.000	0.6163	0.3435	-0.0309	0.0943	0.632	0.0735	-0.1150
20.3	0.5133	0.1220	0.000	0.6249	0.3889	-0.0478	0.0815	0.722	0.0424	-0.1222
22.9	0.5325	0.1188	0.000	0.6386	0.4137	-0.0542	0.0726	0.769	0.0208	-0.1240
25.4	0.5402	0.1131	0.000	0.6427	0.4271	-0.0632	0.0706	0.812	0.0133	-0.1293
27.9	0.5551	0.1124	0.000	0.6502	0.4372	-0.0649	0.0697	0.825	0.0120	-0.1285
30.5	0.5656	0.1170	0.000	0.6593	0.4562	-0.0689	0.0685	0.856	-0.0009	-0.1256
33.0	0.5778	0.1167	0.000	0.6657	0.4618	-0.0688	0.0610	0.862	-0.0056	-0.1268
35.6	0.5814	0.1251	0.000	0.6713	0.4663	-0.0703	0.0735	0.880	0.0130	-0.1257
40.6	0.5960	0.1295	0.000	0.6802	0.4719	-0.0697	0.0782	0.890	0.0171	-0.1245
45.7	0.6223	0.1102	0.000	0.6953	0.5196	-0.0674	0.0840	0.885	0.0259	-0.1226
50.8	0.6309	0.1066	0.000	0.7006	0.5520	-0.0704	0.0780	0.901	0.0182	-0.1220

Table A.14. LDV Data at (x,z)=(-44.5 mm, 0 mm)

y	U	$\hat{u}$	I_u	Umax	Umin	V	$\hat{v}$	I_v	Vmax	Vmin
2.0	-0.3772	0.2276	0.891	-0.1724	-0.6038	0.0540	0.1600	0.335	0.2345	-0.0960
2.5	-0.3484	0.2317	0.869	-0.0335	-0.5694	0.0610	0.1693	0.335	0.2664	-0.0979
3.8	-0.2766	0.2445	0.802	0.0784	-0.5058	0.0865	0.1967	0.324	0.3287	-0.1111
5.1	-0.1455	0.2663	0.653	0.1946	-0.4048	0.1192	0.2137	0.294	0.3787	-0.1089
6.3	-0.0122	0.2645	0.472	0.3001	-0.3099	0.1260	0.2181	0.295	0.4089	-0.0915
7.6	0.1407	0.2482	0.251	0.4225	-0.1610	0.1144	0.2179	0.299	0.4036	-0.0981
8.9	0.2434	0.2377	0.126	0.4631	-0.0290	0.0919	0.1972	0.321	0.3658	-0.0901
10.2	0.2869	0.2402	0.094	0.5148	0.0513	0.0724	0.1808	0.330	0.3070	-0.0890
11.4	0.3540	0.2202	0.059	0.5469	0.1142	0.0572	0.1687	0.356	0.2937	-0.0860
12.7	0.3704	0.2341	0.069	0.5634	0.1291	0.0335	0.1395	0.392	0.2222	-0.0866
14.0	0.4268	0.1732	0.026	0.5823	0.2528	0.0234	0.1296	0.419	0.1689	-0.0852
15.2	0.4516	0.1599	0.029	0.5941	0.2907	0.0057	0.1119	0.474	0.1225	-0.0943
16.5	0.4799	0.1524	0.000	0.6135	0.3241	-0.0002	0.1052	0.500	0.1117	-0.0900
17.8	0.4858	0.1575	0.000	0.6213	0.3320	-0.0044	0.1045	0.510	0.1018	-0.1022
20.3	0.5155	0.1432	0.000	0.6340	0.3561	-0.0263	0.0766	0.631	0.0512	-0.0955
22.9	0.5352	0.1448	0.000	0.6502	0.3870	-0.0365	0.0778	0.682	0.0493	-0.1057
25.4	0.5532	0.1301	0.000	0.6551	0.4223	-0.0448	0.0695	0.740	0.0297	-0.1093
27.9	0.5615	0.1337	0.000	0.6612	0.4272	-0.0520	0.0650	0.777	0.0138	-0.1176
30.5	0.5735	0.1309	0.000	0.6687	0.4369	-0.0496	0.0663	0.785	0.0184	-0.1113
33.0	0.5881	0.1294	0.000	0.6799	0.4549	-0.0529	0.0610	0.806	0.0105	-0.1109
35.6	0.6005	0.1527	0.000	0.6950	0.4588	-0.0576	0.0600	0.833	0.0039	-0.1132
40.6	0.6112	0.1421	0.000	0.6999	0.4846	-0.0597	0.0676	0.853	0.0098	-0.1140
45.7	0.6388	0.1298	0.000	0.7166	0.5282	-0.0619	0.0715	0.870	0.0112	-0.1152
50.8	0.6530	0.1267	0.000	0.7296	0.5592	-0.0572	0.0854	0.868	0.0262	-0.1139

Table A.15. LDV Data at (x,z)=(-47.6 mm, 0 mm)

y	U	$\hat{u}$	I_u	Umax	Umin	V	$\hat{v}$	I_v	Vmax	Vmin
2.0	-0.3384	0.2368	0.863	-0.1614	-0.5827	0.0371	0.1517	0.370	0.2050	-0.0921
2.5	-0.3057	0.2449	0.816	0.0194	-0.5498	0.0494	0.1560	0.354	0.2425	-0.0896
3.8	-0.2305	0.2596	0.728	0.1003	-0.4937	0.0706	0.1808	0.361	0.3076	-0.1033
5.1	-0.1156	0.2669	0.598	0.2118	-0.4018	0.0889	0.1946	0.348	0.3435	-0.0965
6.3	-0.0042	0.2790	0.466	0.3097	-0.3237	0.1144	0.1991	0.295	0.3762	-0.0804
7.6	0.1165	0.2674	0.288	0.3746	-0.2090	0.1060	0.1943	0.300	0.3820	-0.0759
8.9	0.2241	0.2317	0.152	0.4502	-0.0402	0.0942	0.1858	0.305	0.3306	-0.0804
10.2	0.2797	0.2347	0.095	0.4955	0.0391	0.0708	0.1676	0.326	0.3050	-0.0749
11.4	0.3557	0.1970	0.045	0.5342	0.1576	0.0579	0.1515	0.339	0.2314	-0.0717
12.7	0.3871	0.1883	0.036	0.5531	0.2127	0.0414	0.1375	0.365	0.2084	-0.0741
14.0	0.4089	0.2016	0.044	0.5681	0.2029	0.0296	0.1246	0.385	0.1685	-0.0765
15.2	0.4492	0.1562	0.027	0.5826	0.2736	0.0206	0.1123	0.408	0.1460	-0.0749
16.5	0.4666	0.1592	0.000	0.5981	0.3024	0.0118	0.1042	0.445	0.1202	-0.0833
17.8	0.4826	0.1540	0.000	0.6121	0.3283	-0.0051	0.0862	0.512	0.0839	-0.0819
20.3	0.5125	0.1325	0.000	0.6243	0.3721	-0.0159	0.0786	0.575	0.0634	-0.0910
22.9	0.5395	0.1327	0.000	0.6461	0.4045	-0.0246	0.0657	0.629	0.0387	-0.0966
25.4	0.5569	0.1292	0.000	0.6552	0.4230	-0.0344	0.0648	0.691	0.0284	-0.1002
27.9	0.5708	0.1293	0.000	0.6683	0.4348	-0.0360	0.0725	0.702	0.0356	-0.1021
30.5	0.5850	0.1312	0.000	0.6772	0.4587	-0.0369	0.0671	0.732	0.0290	-0.0991
33.0	0.6005	0.1377	0.000	0.6914	0.4680	-0.0434	0.0610	0.765	0.0200	-0.1004
35.6	0.6026	0.1544	0.000	0.6962	0.4699	-0.0463	0.0661	0.783	0.0169	-0.1090
40.6	0.6103	0.1795	0.000	0.7126	0.4598	-0.0484	0.0705	0.815	0.0193	-0.1073
45.7	0.6463	0.1447	0.000	0.7301	0.5132	-0.0487	0.0723	0.831	0.0194	-0.1050
50.8	0.6619	0.1235	0.000	0.7407	0.5726	-0.0496	0.0841	0.841	0.0293	-0.1084

Table A.16. LDV Data at (x,z)=(-50.8 mm, 0 mm)

y	U	$\hat{u}$	I_u	Umax	Umin	V	$\hat{v}$	I_v	Vmax	Vmin
2.0	-0.2326	0.2481	0.760	0.0006	-0.5382	0.0275	0.1433	0.397	0.2151	-0.1024
2.5	-0.2485	0.2576	0.751	0.0993	-0.4927	0.0245	0.1397	0.416	0.2148	-0.1087
3.8	-0.1930	0.2654	0.682	0.1587	-0.4465	0.0522	0.1741	0.379	0.2785	-0.1048
5.1	-0.0889	0.2702	0.553	0.2370	-0.3892	0.0697	0.1703	0.357	0.3020	-0.0842
6.3	0.0429	0.2657	0.381	0.3180	-0.2857	0.0686	0.1730	0.367	0.3295	-0.0864
7.6	0.1489	0.2550	0.242	0.3955	-0.1764	0.0716	0.1674	0.348	0.2872	-0.0812
8.9	0.2409	0.2291	0.137	0.4649	0.0059	0.0631	0.1556	0.352	0.2557	-0.0712
10.2	0.3017	0.2168	0.084	0.5053	0.0766	0.0601	0.1498	0.333	0.2570	-0.0671
11.4	0.3622	0.1787	0.032	0.5251	0.1789	0.0461	0.1343	0.356	0.2310	-0.0679
12.7	0.3937	0.1836	0.033	0.5552	0.2322	0.0356	0.1211	0.369	0.1809	-0.0643
14.0	0.4051	0.2012	0.038	0.5670	0.2137	0.0268	0.1154	0.395	0.1489	-0.0703
15.2	0.4465	0.1609	0.030	0.5810	0.2687	0.0188	0.1117	0.424	0.1408	-0.0731
16.5	0.4665	0.1554	0.000	0.6004	0.3109	0.0107	0.0926	0.439	0.1141	-0.0679
17.8	0.4851	0.1575	0.000	0.6111	0.3353	0.0085	0.0885	0.448	0.0979	-0.0727
20.3	0.5101	0.1542	0.000	0.6315	0.3493	-0.0052	0.0829	0.520	0.0820	-0.0770
22.9	0.5397	0.1266	0.000	0.6435	0.3984	-0.0185	0.0732	0.592	0.0557	-0.0883
25.4	0.5659	0.1309	0.000	0.6703	0.4215	-0.0226	0.0706	0.626	0.0500	-0.0885
27.9	0.5828	0.1362	0.000	0.6812	0.4462	-0.0290	0.0670	0.669	0.0405	-0.0902
30.5	0.5925	0.1379	0.000	0.6880	0.4612	-0.0323	0.0584	0.693	0.0257	-0.0936
33.0	0.6068	0.1413	0.000	0.7005	0.4764	-0.0349	0.0701	0.725	0.0350	-0.0952
35.6	0.6192	0.1446	0.000	0.7126	0.4933	-0.0382	0.0642	0.755	0.0252	-0.0942
40.6	0.6388	0.1450	0.000	0.7274	0.5136	-0.0397	0.0707	0.778	0.0277	-0.0946
45.7	0.6544	0.1692	0.000	0.7450	0.5238	-0.0410	0.0852	0.799	0.0374	-0.0962
50.8	0.6750	0.1406	0.000	0.7581	0.5607	-0.0446	0.0767	0.816	0.0336	-0.0977

Table A.17. LDV Data at (x,z)=(-54.0 mm, 0 mm)

y	U	$\hat{u}$	I_u	Umax	Umin	V	$\hat{v}$	I_v	Vmax	Vmin
2.0	-0.1645	0.2437	0.678	0.0807	-0.4546	0.0082	0.1271	0.449	0.1584	-0.1006
2.5	-0.1584	0.2530	0.648	0.1381	-0.4189	0.0161	0.1396	0.438	0.1911	-0.1202
3.8	-0.0668	0.2675	0.495	0.2156	-0.3953	0.0277	0.1470	0.431	0.2129	-0.1043
5.1	0.0310	0.2590	0.355	0.2814	-0.3096	0.0397	0.1486	0.412	0.2139	-0.0974
6.3	0.1216	0.2528	0.241	0.3694	-0.1996	0.0486	0.1577	0.394	0.2542	-0.0857
7.6	0.1808	0.2496	0.181	0.4274	-0.1128	0.0526	0.1561	0.381	0.2413	-0.0780
8.9	0.2430	0.2376	0.127	0.4669	-0.0029	0.0524	0.1474	0.356	0.2219	-0.0770
10.2	0.3145	0.1992	0.064	0.4910	0.1120	0.0391	0.1286	0.371	0.1896	-0.0685
11.4	0.3587	0.1895	0.040	0.5206	0.1756	0.0355	0.1250	0.371	0.1863	-0.0690
12.7	0.3772	0.2102	0.056	0.5481	0.1610	0.0308	0.1203	0.372	0.1555	-0.0701
14.0	0.4269	0.1603	0.036	0.5643	0.2589	0.0236	0.1104	0.394	0.1458	-0.0688
15.2	0.4492	0.1532	0.023	0.5847	0.2925	0.0163	0.0956	0.403	0.1216	-0.0652
16.5	0.4719	0.1468	0.000	0.6005	0.3227	0.0103	0.0881	0.425	0.0967	-0.0742
17.8	0.4881	0.1516	0.000	0.6146	0.3387	0.0067	0.0881	0.439	0.0932	-0.0738
20.3	0.5246	0.1297	0.000	0.6341	0.3841	-0.0056	0.0794	0.519	0.0784	-0.0754
22.9	0.5520	0.1271	0.000	0.6551	0.4098	-0.0099	0.0851	0.552	0.0734	-0.0859
25.4	0.5671	0.1336	0.000	0.6673	0.4322	-0.0101	0.0850	0.555	0.0730	-0.0837
27.9	0.5903	0.1356	0.000	0.6876	0.4473	-0.0216	0.0708	0.614	0.0500	-0.0870
30.5	0.6103	0.1168	0.000	0.6997	0.5010	-0.0216	0.0809	0.646	0.0597	-0.0834
33.0	0.6217	0.1266	0.000	0.7132	0.5054	-0.0234	0.0781	0.661	0.0541	-0.0829
35.6	0.6341	0.1331	0.000	0.7261	0.5211	-0.0283	0.0787	0.694	0.0522	-0.0866
40.6	0.6484	0.1442	0.000	0.7417	0.5313	-0.0328	0.0764	0.741	0.0405	-0.0917
45.7	0.6680	0.1555	0.000	0.7586	0.5484	-0.0317	0.0830	0.740	0.0462	-0.0921
50.8	0.6890	0.1348	0.000	0.7701	0.5800	-0.0326	0.0807	0.755	0.0391	-0.0901

Table A.18. LDV Data at (x,z)=(-57.2 mm, 0 mm)

y	U	$\hat{u}$	I_u	Umax	Umin	V	$\hat{v}$	I_v	Vmax	Vmin
2.0	-0.0815	0.2147	0.577	0.1319	-0.3292	-0.0038	0.1062	0.489	0.1160	-0.0879
2.5	-0.0698	0.2287	0.547	0.1840	-0.2736	-0.0010	0.1115	0.480	0.1291	-0.0817
3.8	-0.0298	0.2524	0.443	0.2521	-0.3297	0.0127	0.1225	0.452	0.1400	-0.0956
5.1	0.0752	0.2538	0.292	0.3490	-0.1990	0.0173	0.1212	0.436	0.1577	-0.0875
6.3	0.1350	0.2447	0.224	0.3975	-0.1111	0.0238	0.1274	0.431	0.1633	-0.0852
7.6	0.2099	0.2271	0.146	0.4428	-0.0174	0.0240	0.1267	0.434	0.1584	-0.0810
8.9	0.2728	0.2195	0.092	0.4733	0.0398	0.0265	0.1200	0.415	0.1559	-0.0735
10.2	0.3298	0.2091	0.081	0.5083	0.0870	0.0194	0.1086	0.427	0.1396	-0.0698
11.4	0.3587	0.2003	0.061	0.5272	0.1578	0.0245	0.1099	0.406	0.1424	-0.0667
12.7	0.3958	0.1946	0.046	0.5552	0.1833	0.0186	0.1034	0.419	0.1285	-0.0693
14.0	0.4133	0.1946	0.047	0.5654	0.2033	0.0157	0.0994	0.428	0.1269	-0.0641
15.2	0.4505	0.1722	0.031	0.5899	0.2842	0.0164	0.0981	0.420	0.1252	-0.0652
16.5	0.4542	0.1987	0.000	0.6073	0.2589	0.0086	0.0921	0.452	0.1166	-0.0670
17.8	0.4785	0.1769	0.000	0.6189	0.2864	0.0034	0.0871	0.468	0.1031	-0.0700
20.3	0.5270	0.1421	0.000	0.6398	0.3549	-0.0051	0.0772	0.513	0.0759	-0.0732
22.9	0.5536	0.1276	0.000	0.6599	0.4312	-0.0017	0.0862	0.501	0.0801	-0.0702
25.4	0.5806	0.1156	0.000	0.6770	0.4654	-0.0114	0.0732	0.552	0.0681	-0.0759
27.9	0.5922	0.1205	0.000	0.6892	0.4887	-0.0175	0.0655	0.590	0.0471	-0.0812
30.5	0.6087	0.1331	0.000	0.7017	0.4865	-0.0149	0.0862	0.610	0.0659	-0.0798
33.0	0.6214	0.1525	0.000	0.7192	0.4885	-0.0189	0.0694	0.636	0.0490	-0.0758
35.6	0.6324	0.1544	0.000	0.7318	0.5009	-0.0233	0.0718	0.667	0.0632	-0.0786
40.6	0.6566	0.1528	0.000	0.7503	0.5084	-0.0265	0.0664	0.693	0.0419	-0.0801
45.7	0.6855	0.1249	0.000	0.7668	0.5799	-0.0265	0.0781	0.707	0.0508	-0.0813
50.8	0.7032	0.1201	0.000	0.7822	0.6055	-0.0281	0.0776	0.737	0.0499	-0.0786

Table A.19. LDV Data at (x,z)=(-60.3 mm, 0 mm)

y	U	$\hat{u}$	I_u	Umax	Umin	V	$\hat{v}$	I_v	Vmax	Vmin
2.0	0.0085	0.1182	0.421	0.1376	-0.1151	-0.0051	0.1046	0.484	0.1019	-0.0972
2.5	0.0201	0.1260	0.395	0.1736	-0.0926	-0.0035	0.1095	0.495	0.1040	-0.1076
3.8	0.0627	0.1399	0.269	0.2374	-0.0472	0.0000	0.1048	0.481	0.1089	-0.1053
5.1	0.1028	0.1574	0.201	0.2864	-0.0329	0.0037	0.1100	0.469	0.1240	-0.0972
6.3	0.1685	0.1693	0.118	0.3752	0.0486	0.0074	0.1057	0.463	0.1109	-0.0863
7.6	0.1959	0.1686	0.086	0.4147	0.1068	0.0096	0.1049	0.455	0.1134	-0.0827
8.9	0.2252	0.1719	0.060	0.4338	0.1210	0.0169	0.1194	0.435	0.1366	-0.0857
10.2	0.2837	0.1598	0.034	0.4614	0.1406	0.0140	0.1033	0.437	0.1280	-0.0739
11.4	0.3171	0.1597	0.019	0.4928	0.2048	0.0095	0.0885	0.443	0.1098	-0.0658
12.7	0.3636	0.1475	0.028	0.5158	0.2370	0.0155	0.0965	0.416	0.1232	-0.0671
14.0	0.3957	0.1415	0.031	0.5429	0.2880	0.0138	0.0949	0.425	0.1193	-0.0657
15.2	0.4141	0.1336	0.028	0.5578	0.3132	0.0090	0.0881	0.435	0.1062	-0.0679
16.5	0.4437	0.1264	0.000	0.5701	0.3310	0.0067	0.0780	0.448	0.0953	-0.0627
17.8	0.4627	0.1193	0.000	0.5850	0.3551	0.0097	0.0988	0.449	0.1132	-0.0724
20.3	0.5018	0.1118	0.000	0.6182	0.3981	0.0015	0.0906	0.485	0.0949	-0.0738
22.9	0.5315	0.1055	0.000	0.6381	0.4283	-0.0069	0.0743	0.527	0.0695	-0.0729
25.4	0.5532	0.1009	0.000	0.6567	0.4515	-0.0095	0.0742	0.540	0.0616	-0.0797
27.9	0.5753	0.1019	0.000	0.6789	0.4734	-0.0125	0.0772	0.563	0.0623	-0.0814
30.5	0.5923	0.1044	0.000	0.6951	0.4927	-0.0104	0.0915	0.582	0.0771	-0.0792
33.0	0.6068	0.1189	0.000	0.7161	0.4945	-0.0126	0.0795	0.594	0.0640	-0.0763
35.6	0.6168	0.1357	0.000	0.7284	0.4880	-0.0139	0.0806	0.598	0.0631	-0.0770
40.6	0.6479	0.1356	0.000	0.7510	0.5145	-0.0222	0.0673	0.661	0.0458	-0.0761
45.7	0.6813	0.1166	0.000	0.7692	0.5607	-0.0242	0.0641	0.676	0.0393	-0.0763
50.8	0.7062	0.1078	0.000	0.7860	0.6085	-0.0257	0.0600	0.701	0.0347	-0.0746

Table A.20. LDV Data at (x,z)=(-63.5 mm, 0 mm)

y	U	$\hat{u}$	I_u	Umax	Umin	V	$\hat{v}$	I_v	Vmax	Vmin
2.0	0.0275	0.1221	0.374	0.1897	-0.0849	-0.0088	0.0948	0.514	0.0874	-0.0809
2.5	0.0447	0.1317	0.333	0.2008	-0.0775	-0.0062	0.0941	0.493	0.0889	-0.0924
3.8	0.0947	0.1423	0.207	0.2702	-0.0262	-0.0045	0.1005	0.493	0.0936	-0.0863
5.1	0.1343	0.1546	0.149	0.3345	0.0179	0.0015	0.0977	0.479	0.1054	-0.0856
6.3	0.1725	0.1593	0.110	0.3677	0.0611	0.0057	0.1024	0.475	0.1101	-0.0836
7.6	0.2237	0.1647	0.067	0.4157	0.0750	0.0041	0.0926	0.464	0.0959	-0.0800
8.9	0.2382	0.1641	0.051	0.4311	0.1251	0.0071	0.0930	0.456	0.0981	-0.0798
10.2	0.2933	0.1624	0.030	0.4690	0.1478	0.0091	0.0878	0.443	0.0964	-0.0730
11.4	0.3319	0.1534	0.018	0.4957	0.1987	0.0111	0.0871	0.436	0.0934	-0.0698
12.7	0.3720	0.1477	0.009	0.5222	0.2402	0.0077	0.0798	0.442	0.0835	-0.0676
14.0	0.4138	0.1359	0.000	0.5570	0.3021	0.0064	0.0752	0.447	0.0802	-0.0667
15.2	0.4368	0.1267	0.000	0.5744	0.3383	0.0067	0.0764	0.449	0.0820	-0.0644
16.5	0.4555	0.1227	0.000	0.5811	0.3476	0.0043	0.0723	0.452	0.0763	-0.0655
17.8	0.4717	0.1188	0.000	0.5966	0.3691	0.0036	0.0776	0.463	0.0774	-0.0665
20.3	0.5078	0.1070	0.000	0.6214	0.4083	-0.0006	0.0653	0.483	0.0678	-0.0629
22.9	0.5346	0.1062	0.000	0.6419	0.4281	-0.0026	0.0667	0.500	0.0664	-0.0653
25.4	0.5546	0.1065	0.000	0.6673	0.4557	-0.0024	0.0688	0.498	0.0674	-0.0648
27.9	0.5725	0.1066	0.000	0.6808	0.4704	-0.0064	0.0646	0.519	0.0614	-0.0661
30.5	0.5969	0.1075	0.000	0.6978	0.4921	-0.0068	0.0865	0.557	0.0813	-0.0695
33.0	0.6119	0.1181	0.000	0.7198	0.5032	-0.0063	0.0912	0.552	0.0800	-0.0773
35.6	0.6163	0.1264	0.000	0.7245	0.4932	-0.0061	0.0950	0.575	0.0814	-0.0753
40.6	0.6634	0.1188	0.000	0.7597	0.5514	-0.0127	0.0912	0.617	0.0784	-0.0769
45.7	0.6933	0.1095	0.000	0.7761	0.5856	-0.0195	0.0721	0.637	0.0498	-0.0775
50.8	0.7137	0.1074	0.000	0.7908	0.6158	-0.0191	0.0761	0.649	0.0526	-0.0766

Table A.21. LDV Data at (x,z)=(-66.7 mm, 0 mm)

y	U	$\hat{u}$	I_u	Umax	Umin	V	$\hat{v}$	I_v	Vmax	Vmin
2.0	0.0510	0.1265	0.306	0.2277	-0.0789	-0.0075	0.0869	0.508	0.0744	-0.0747
2.5	0.0729	0.1312	0.254	0.2646	-0.0593	-0.0060	0.0928	0.486	0.0946	-0.0892
3.8	0.1017	0.1401	0.194	0.3009	-0.0118	0.0039	0.1153	0.475	0.1276	-0.0887
5.1	0.1667	0.1516	0.103	0.3425	0.0328	0.0032	0.1127	0.475	0.1328	-0.0948
6.3	0.2162	0.1580	0.066	0.4029	0.0925	0.0080	0.1213	0.471	0.1555	-0.0910
7.6	0.2545	0.1627	0.047	0.4386	0.1193	0.0098	0.1279	0.457	0.1490	-0.0915
8.9	0.3028	0.1558	0.025	0.4701	0.1688	0.0087	0.1129	0.462	0.1384	-0.0854
10.2	0.3448	0.1507	0.027	0.5007	0.2197	0.0083	0.0994	0.447	0.1130	-0.0795
11.4	0.3928	0.1423	0.000	0.5409	0.2715	0.0083	0.0958	0.448	0.1068	-0.0757
12.7	0.4162	0.1351	0.000	0.5619	0.3103	0.0096	0.0989	0.443	0.1125	-0.0751
14.0	0.4359	0.1304	0.000	0.5669	0.3218	0.0070	0.0877	0.444	0.0999	-0.0740
15.2	0.4601	0.1273	0.000	0.5876	0.3526	0.0081	0.0902	0.450	0.1012	-0.0695
16.5	0.4762	0.1171	0.000	0.6000	0.3755	0.0077	0.0960	0.449	0.1057	-0.0768
17.8	0.5009	0.1125	0.000	0.6192	0.3992	0.0066	0.0963	0.456	0.1073	-0.0742
20.3	0.5337	0.1099	0.000	0.6447	0.4245	0.0048	0.0954	0.463	0.1054	-0.0735
22.9	0.5590	0.1055	0.000	0.6672	0.4640	0.0045	0.0978	0.482	0.1104	-0.0735
25.4	0.5798	0.0999	0.000	0.6864	0.4896	0.0019	0.1021	0.498	0.1147	-0.0775
27.9	0.6029	0.1000	0.000	0.6989	0.5006	-0.0022	0.1032	0.523	0.1114	-0.0786
30.5	0.6160	0.1013	0.000	0.7129	0.5194	-0.0067	0.0802	0.545	0.0762	-0.0675
33.0	0.6294	0.1102	0.000	0.7314	0.5271	-0.0015	0.0924	0.523	0.0922	-0.0673
35.6	0.6461	0.1173	0.000	0.7430	0.5299	-0.0011	0.1089	0.550	0.1096	-0.0711
40.6	0.6745	0.1154	0.000	0.7644	0.5619	-0.0101	0.0851	0.586	0.0814	-0.0694
45.7	0.7086	0.1072	0.000	0.7855	0.5979	-0.0164	0.0780	0.625	0.0572	-0.0763
50.8	0.7312	0.1026	0.000	0.8044	0.6362	-0.0145	0.0798	0.629	0.0602	-0.0727

The vita has been removed from the scanned document